Measurement of Beauty Production in Deep Inelastic Scattering at HERA

Volker Michels

Measurement of Beauty Production in Deep Inelastic Scattering at HERA

Dissertation

zur Erlangung des Doktorgrades

des Departments Physik der Universität Hamburg

vorgelegt von

Volker Michels

aus Lüneburg

2008

korrigierte Fassung (30.08.2008)

Gutachter der Dissertation:	Dr. B. List Prof. Dr. R. Klanner
Gutachter der Disputation:	Prof. Dr. P. Schleper Dr. H. Jung
Datum der Disputation:	28.08.2008
Vorsitzender des Prüfungsausschusses:	Dr. M. Martins
Vorsitzender des Promotionsausschusses:	Prof. Dr. J. Bartels
Dekan der Fakultät Mathematik, Informatik, Naturwissenschaften:	Prof. Dr. A. Frühwald

Abstract

A measurement of the beauty production cross section in ep collisions at a centre-of-mass energy of 319 GeV is presented. The data was collected with the H1 detector at the HERA collider in the years 2005-2007 and corresponds to an integrated luminosity of 285 pb^{-1}. Events are selected by requiring the presence of at least one jet together with a muon in the final state. The large mass of b-flavoured hadrons is exploited to identify events containing beauty quarks on a statistical basis. Single and double differential cross sections are measured in deep inelastic scattering, with photon virtualities $3.5 < Q^2 < 100$ GeV^2. The results are compared to perturbative QCD calculations. The next-to-leading order prediction is 1.8σ below the measurement. The deficiencies of the prediction are found in the forward direction of the muon, which is defined by the direction of the proton beam, and at low transverse momenta of the muon and jet. The leading-order predictions, which are augmented by parton showers, describe the shape of the measurements very well, but not the normalization. The predictions are about a factor two too low, which is compatible with the next-to-leading order prediction.

Kurzfassung

Eine Messung des Wirkungsquerschnittes für beauty-Quark Produktion in ep-Kollisionen bei einer Schwerpunktsenergie von 319 GeV wird vorgestellt. Die Daten wurden mit dem H1-Detektor am HERA-Beschleuniger in den Jahren 2005-2007 aufgezeichnet und entsprechen einer integrierten Luminosität von 285 pb^{-1}. Für die Auswahl der Ereignisse wird mindestens ein Jet zusammen mit einem Myon verlangt. Die große Masse von Hadronen mit beauty-Quarks wird ausgenutzt, um Ereignisse mit beauty-Quarks auf einer statistischen Weise zu identifizieren. Einfach- und doppelt-differentielle Wirkungsquerschnitte werden in tief-inelastischer Streuung gemessen, mit Photonvirtualitäten $3,5 < Q^2 < 100$ GeV^2. Die Ergebnisse werden mit perturbativen QCD Berechnungen verglichen. Die Vorhersage in nächst führender Ordnung ist $1,8\sigma$ niedriger als die Messung. Die niedrigeren Werte der Vorhersage werden in Vorwärtsrichtung für das Myon, welche gegeben ist durch die Richtung des Protonstrahls, und bei niedrigen Transversalimpulsen für das Myon und den Jet gemessen. Die Vorhersagen in führender Ordnung, ergänzt durch Partonenschauer, beschreiben die Form der Messungen sehr gut, nicht jedoch die Normierung. Die Vorhersagen sind ungefähr einen Faktor zwei zu niedrig, was kompatibel ist mit der Vorhersage in nächst führender Ordnung.

Contents

Introduction

Quantum Chromo Dynamics (QCD) describes one of the fundamental forces of nature, the strong force. The study of the production of heavy quarks at the electron proton collider HERA gives insight into various aspects of QCD, both at the short distances where perturbative calculations are possible (perturbative regime), and at larger distances where only phenomenological approaches exist (non-perturbative regime).
The large masses of heavy quarks set an energy scale, where perturbative QCD is expected to give reliable predictions. This holds true in particular for the production of beauty quarks which have a mass of about 5 GeV.
In this thesis open beauty production is studied in the region of deep inelastic scattering (DIS) in the range $3.5 < Q^2 < 100$ GeV^2, where Q^2 is the virtuality of the exchanged photon. A muon from a semi leptonic heavy quark decay and a jet are required in the final state. The momentum of the original quark, which is not visible in the final state directly, can be approximated by the energy and direction of the observed jet. The fraction of beauty events of the data sample is determined on a statistical basis, using the large momentum of the muon with respect to the jet axis (p_t^{rel}) for beauty quarks.
In comparison to the photoproduction regime ($Q^2 \approx 0$ GeV^2), the cross section and therefore the statistics of the data sample is small in the DIS regime. On the other hand the structure of the photon is not important for the DIS regime, which helps to reduce the uncertainties of theoretical predictions. Q^2 provides an additional hard scale apart from the jet transverse momentum and the quark mass. This allows a study of the multiscale problem: the QCD predictions may become unreliable if several hard scales are present due to large coefficients in the perturbation series.
In this thesis differential cross sections as a function of different observables are compared to theory predictions. These are available in the form of next-to-leading order calculations of the hard matrix element with respect to α_s, the coupling constant of the strong interaction. Full event generators perform the calculation in leading order, and the long distance, non perturbative regime is modelled using phenomenological approaches. For a further investigation of the interesting regions of phase space where deviations to the predicitons are observed double-differential cross sections are determined.
In the region of phase space investigated in this analysis, both the transverse momentum of the jet and $\sqrt{Q^2}$ are comparable to the beauty quark mass. Therefore the calculations in the massive scheme are expected to give reliable results. In this

scheme the beauty and charm quark are not treated as active flavours inside the proton, but are produced in the hard interaction process (boson-gluon fusion). This process is sensitive to the gluon density of the proton which can be determined from the scaling violations of the inclusive cross sections. Using information gained on the gluon density, predictions of heavy quark production become possible. In this thesis direct measurements of heavy quark production are made thus providing a test of such predictions.

This thesis is organized as follows:
Chapter 1 gives a theoretical introduction to heavy quark production at HERA.
In **Chapter 2** the H1 detector and the relevant subdetectors are introduced.
In **Chapter 3** an overview of experimental methods and previous measurements at HERA and elsewhere is given.
The explanation if the experimental work of this thesis starts with **Chapter 4**, where the event reconstruction is discussed in detail.
In **Chapter 5** the selection of the event samples, in both data and Monte Carlo, is presented, followed by a discussion of the beauty quark measurement in **Chapter 6**. Here the p_t^{rel} method, which is used to obtain the beauty fraction of the data sample together with all correction factors applied to the data to obtain the cross sections as well as systematic studies are discussed in detail.
In **Chapter 7** the results are presented: the total visible cross section for beauty quark production, differential and double differential cross sections as a function of different observables compared to next-to-leading order calculations and two different Monte Carlo predictions.
In **Chapter 8** the summary of the results is given. Some results are compared to other measurements and discussed in a more general context.
The presentation of the analysis is concluded with **Chapter 9** where an outlook is given and some potential improvements of the measurement are discussed.
In **Appendix D** a topic not related to the analysis but part of the work done for this thesis is discussed. A z vertex trigger based on drift chamber signals was implemented as a part of the Fast Track Trigger (FTT) upgrade project of the H1 experiment. The principle and implementation of this trigger and the results thereof are discussed.

Chapter 1

Heavy Flavour Production at HERA

1.1 Kinematics of High-Energy ep Scattering

The scattering process

$$ep \to lX \tag{1.1}$$

is described by the exchange of a virtual gauge boson as illustrated in figure 1.1. For this thesis only the **neutral current** process $ep \to eX$ is relevant where a virtual photon or Z boson is exchanged. The exchange of virtual W bosons leads to the **charged current** process $ep \to \nu_e X$ with a neutrino in the final state.
The photon virtuality Q^2 is given by the squared momentum transfer

$$Q^2 = -\boldsymbol{q}^2 = -(\boldsymbol{k} - \boldsymbol{k'})^2, \tag{1.2}$$

the squared centre-of-mass energy of the reaction is

$$s = (\boldsymbol{p} + \boldsymbol{k})^2. \tag{1.3}$$

The relative energy transfer at the electron-boson vertex in the proton rest frame is given by

$$y = \frac{\mathbf{p} \cdot \mathbf{q}}{\mathbf{p} \cdot \mathbf{k}},\ 0 \leq y \leq 1, \tag{1.4}$$

the Bjorken scaling variable as

$$x = \frac{Q^2}{2\mathbf{p} \cdot \mathbf{q}},\ 0 \leq x \leq 1. \tag{1.5}$$

The Bjorken scaling variable can be interpreted as the fraction of the proton's momentum carried by the interacting quark in the infinite momentum frame. Neglecting the lepton and proton masses, these variables are related by the equation

$$Q^2 = x \cdot y \cdot s. \tag{1.6}$$

The phase space region of small momentum transfers ($Q^2 \approx 0$) is called **photoproduction**, at H1 usually selected by the condition $Q^2 < 1$ GeV^2. The region of larger Q^2 is referred to as **deep inelastic scattering** (DIS).

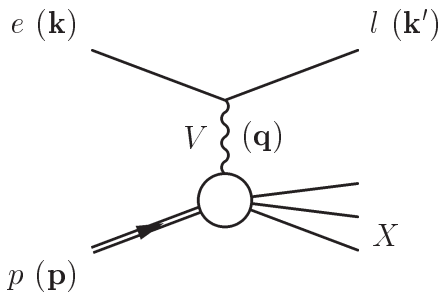

FIGURE 1.1: *Deep inelastic electron-proton scattering at HERA in the single boson exchange picture. For the neutral current process a photon or Z^0 boson is exchanged, resulting in an final state electron. In the case of a charged current process a W boson is exchanged, resulting in an outgoing antineutrino. The four momenta are denoted in parantheses.*

1.2 Quark Parton Model and Proton Structure Functions

In the **Quark Parton Model** (QPM) picture [39, 61] the proton is made of quasi-free, non interacting particles, called **partons**, which can be identified as **quarks**. The double differential cross-section for electron proton scattering can then be described by the incoherent sum of electron parton scatterings

$$\frac{d^2\sigma}{dxdQ^2} = \frac{2\pi\alpha^2}{xQ^4}\left(1+(1-y)^2\right)\sum_i e_i^2 x q_i(x). \tag{1.7}$$

The distribution function $q_i(x)$ gives the probability that the struck quark i carries the momentum fraction x of the proton. The momentum distribution $xq(x)$ is called **parton distribution function** (PDF).
The inelastic electron proton scattering cross-section is given by the general formula

$$d\sigma \sim L^e_{\mu\nu} W^{\mu\nu}, \tag{1.8}$$

where $L^e_{\mu\nu}$ is the tensor describing the leptonic current and $W^{\mu\nu}$ is the tensor describing the hadronic current. For unpolarized neutral current scattering, neglecting parity violating effects due to the weak interaction, the hadronic tensor has the form

$$W^{\mu\nu} = W_1\left(-g^{\mu\nu}\right) + \frac{g^\mu g^\nu}{q^2} + \frac{W_2}{m^2}\left(p^\mu - \frac{p\cdot q}{q^2}q^\mu\right)\left(p^\nu - \frac{p\cdot q}{q^2}q^\nu\right), \tag{1.9}$$

where W_1 and W_2 are structure functions and m is the proton mass.
When ignoring mass terms and redefining the structure functions as $F_1 = W_1$ and $F_2 = (p\cdot q)W_2/m^2$, the double differential cross-section can be expressed as

$$\frac{d^2\sigma}{dx\,dQ^2} = \frac{4\pi\alpha^2 s}{xQ^4}\left(xy^2F_1(x,Q^2) + (1-y)F_2(x,Q^2)\right). \tag{1.10}$$

In terms of F_2 and the longitudinal structure function $F_L = F_2 - 2xF_1$ the cross-section may also be written as

$$\frac{d^2\sigma}{dx\,dQ^2} = \frac{4\pi\alpha^2 s}{xQ^4}\left(Y_+ F_2(x,Q^2) - y^2 F_L(x,Q^2)\right), \tag{1.11}$$

where $Y_+ = 1 + (1-y)^2$. The longitudinal structure function F_L is related to the exchange of a longitudinally polarised photon. This contribution is kinematically suppressed due to the factor y^2 and leads to sizeable effects only for large inelasticities.
When compared to equation (1.7), the quark parton model predicts that the structure function depends only on x and not on Q^2:

$$F_2(x,Q^2) = F_2(x) = \sum_i e_i^2 x q_i(x). \tag{1.12}$$

This effect, known as **scaling**, can be seen for $x \sim 0.1$ for HERA and fixed target data, as shown in figure 1.2. **Scaling violations** become visible at low x, where F_2 rises with increasing Q^2. This can be interpreted by QCD (see section 1.3) due to the parton dynamics and the corresponding rise of the gluon density towards small x.

1.3 Quantum Chromo Dynamics (QCD)

Quantum Chromo Dynamics is a non-Abelian gauge theory that describes the interactions between quarks and gluons. Quarks are spin-1/2 color charged particles building the hadronic matter. Massless spin-1 gluons are the mediators of the strong force between quarks. The interaction is based on a $SU(3)_c$ color symmetry group and three-fold color charges. The symmetry group allows for a rich interaction structure. The exchange quanta itself carry charge, which is the main difference to Quantum Electrodynamics (QED). Loop graphs (see figure 1.3), contributing to higher orders of the expansion of scattering amplitudes in α_s, are divergent. QCD is a renormalizable field theory: to ensure finite results in all orders of the expansion in α_s, a renormalized (redefined) coupling $\alpha_s(\mu_r)$ is defined, that depends on the renormalization scale μ_r. The leading order equation for the **running coupling** is

$$\alpha_s(\mu_r) = \left(b_0 \ln(\frac{\mu_r^2}{\Lambda_{QCD}^2})\right)^{-1}, \text{with } b_0 = \frac{33 - 2n_f}{12\pi}, \tag{1.13}$$

where n_f is the number of active flavours. The scale parameter Λ_{QCD} depends on the renormalization scheme and on the number of active flavours. It was determined experimentally for the $\overline{MS}$ scheme (see section 1.4) to be about 215 MeV [58].
The running coupling is shown in figure 1.4. For μ_r much larger than Λ_{QCD}, the effective coupling is small and a perturbative description is applicable. This region of **asymptotic freedom** corresponds to the quark parton model picture of quasi-free quarks. For μ_r of the order of Λ_{QCD} the strong binding force becomes important, which confines the quarks within hadrons (**confinement**).

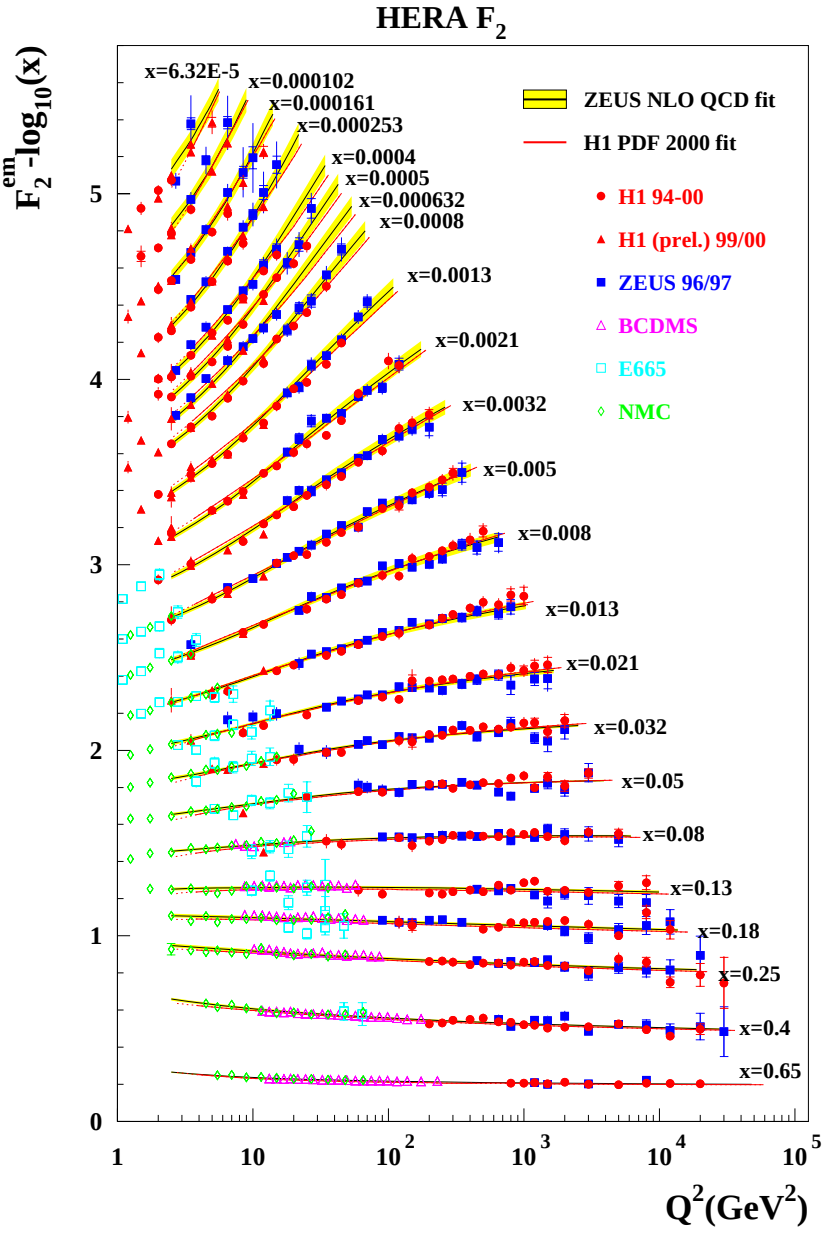

FIGURE 1.2: *Proton structure function F_2 for various fixed values of x, measured by H1, ZEUS and different fixed target experiments together with DGLAP-based fits. For better visibility an offset ($-\log x$) is applied to each data point.*

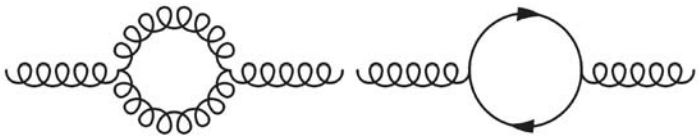

FIGURE 1.3: *Virtual corrections to the gluon propagator: gluon loop (left) and fermion loop (right).*

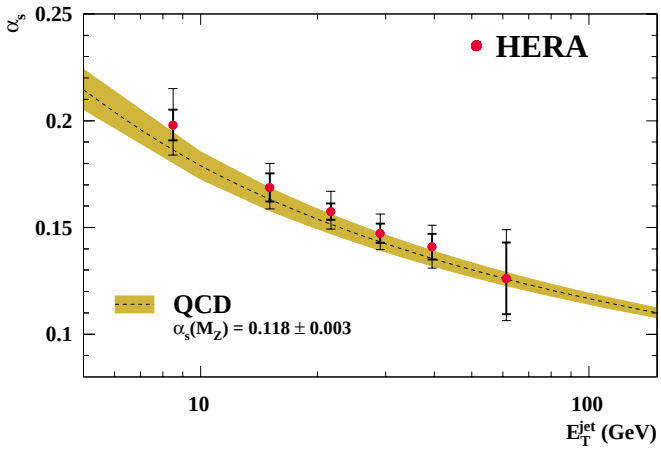

FIGURE 1.4: *Running of the effective coupling constant α_s as a function of the transverse jet energy. Shown is the combined H1 and ZEUS measurement and the QCD prediction [51].*

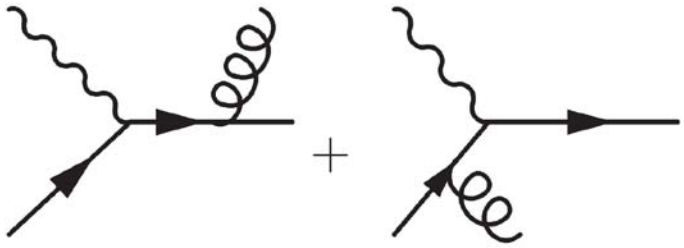

FIGURE 1.5: *Diagrams contributing to $\mathcal{O}(\alpha_s)$ correction to the quark parton model by emission of gluons from the quark line ($\gamma^* q \to gg$). For QCD Compton processes the gluon can either be emitted from the initial or final state quark.*

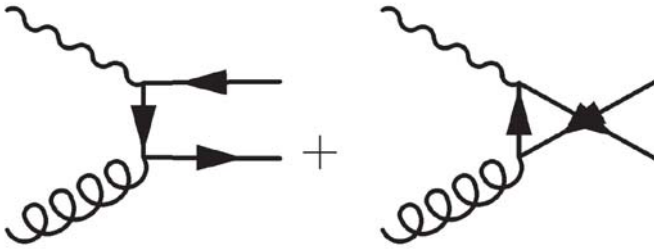

FIGURE 1.6: *$\mathcal{O}(\alpha_s)$ boson gluon fusion process $\gamma^* g \to qq$ (BGF).*

1.4 QCD Improved Parton Model

In QCD the scaling of the structure functions is broken due to $\mathcal{O}(\alpha_s)$ corrections to the parton model result. Diagrams contributing to this corrections by emission of gluons from the quark line ($\gamma^* q \to qg$) are shown in figure 1.5. Therefore in QCD the structure function is Q^2 dependent and given by [59]

$$F_2(x,Q^2) = x \sum_{q,\bar{q}} e_q^2 \left[q_0(x) + \frac{\alpha_s}{2\pi} \int_x^1 \frac{d\xi}{\xi} q_0(\xi) \left\{ P_{qq}\left(\frac{x}{\xi}\right) \ln \frac{Q^2}{\kappa^2} + C\left(\frac{x}{\xi}\right) \right\} + ... \right], \tag{1.14}$$

where $C(x)$ is a calculable function and the splitting function P_{qq} is given in leading order by the equation[1]

$$P_{qq}(x) = \frac{4}{3} \left(\frac{1+x^2}{(1-x)_+} + \frac{3}{2}\delta(1-x) \right). \tag{1.15}$$

[1]This splitting function is always used inside an integral and is therefore a distribution. The plus description is used, the integral with any sufficiently smooth function f is $\int_0^1 dx \frac{f(x)}{(1-x)_+} = \int_0^1 dx \frac{f(x)-f(1)}{1-x}$ and $\frac{1}{(1-x)_+} = \frac{1}{1-x}$ for $0 \le x \le 1$. The singularity for $x \to 1$ is due to emissions of soft gluons.

The scaling is broken by logarithms of Q^2/κ^2, where κ is a cut-off that has to be introduced due to **collinear divergencies**, which arise when the gluon is emitted parallel to the quark. This problem is solved by absorbing these singularities into the quark distribution, which now becomes scale dependent:

$$\begin{aligned} q(x,\mu_f^2) =& q_0(x) + \frac{\alpha_s}{2\pi}\int_x^1 \frac{d\xi}{\xi} q_0(\xi)\left(P_{qq}(\frac{x}{\xi})\ln\frac{\mu_f^2}{\kappa^2} - C_q(\frac{x}{\xi})\right) \\ &+ \frac{\alpha_s}{2\pi}\int_x^1 \frac{d\xi}{\xi} g_0(\xi)\left(P_{qg}(\frac{x}{\xi})\ln\frac{\mu_f^2}{\kappa^2} + C_g(\frac{x}{\xi})\right) + ... \end{aligned} \tag{1.16}$$

In this formula, $\mathcal{O}(\alpha_s)$ contributions from the process $\gamma^* g \to qq$ (see figure 1.6) are included and folded with the **bare gluon distribution** $g_0(x)$, where the corresponding splitting function is

$$P_{qg}(x) = \frac{1}{2}\left(x^2 + (1-x)^2 + (1-x)^2\right). \tag{1.17}$$

The **factorization scale** μ_f defines the scale where the singularities are contributed to the quark density which cannot be calculated perturbatively. The Wilson coefficient functions C_q and C_g depend on the factorization and renormalization schemes, as the amount of finite contributions to the quark density is arbitrary. For the DIS factorization scheme the structure function F_2 has the simple form

$$F_2(x,Q^2) = x\sum_{q,\bar{q}} e_q^2 q(x,Q^2). \tag{1.18}$$

For the $\overline{MS}$ factorization scheme, where not all the gluon contribution is absorbed into the quark distribution, the structure function has the form

$$\begin{aligned} F_2(x,Q^2) =& x\sum_{q,\bar{q}} e_q^2 \int_x^1 \frac{d\xi}{\xi} q(\xi,Q^2)\left(\delta(1-\frac{x}{\xi}) + \frac{\alpha_s}{2\pi}C_q^{\overline{MS}}(\frac{x}{\xi}) + ...\right) \\ &+ x\sum_{q,\bar{q}} e_q^2 \int_x^1 \frac{d\xi}{\xi} g(\xi,Q^2)\left(\frac{\alpha_s}{2\pi}C_g^{\overline{MS}}(\frac{x}{\xi}) + ...\right). \end{aligned} \tag{1.19}$$

The coefficient functions are

$$C_q^{\overline{MS}}(z) = \delta(1-z) + \frac{\alpha_s}{2\pi}C_q^1 + ... \tag{1.20}$$

$$C_g^{\overline{MS}}(z) = \frac{\alpha_s}{2\pi}C_g^1(z) + ..., \tag{1.21}$$

with

$$\begin{aligned} C_q^1(z) =& \frac{4}{3}\Big(\frac{4\ln(1-z)-3}{2(1-z)_+} - (1+z)\ln(1-z) - \frac{1+z^2}{1-z}\ln z \\ &+ 3 + 2z - (\frac{\pi^2}{3} + \frac{9}{2})\delta(1-z)\Big), \end{aligned} \tag{1.22}$$

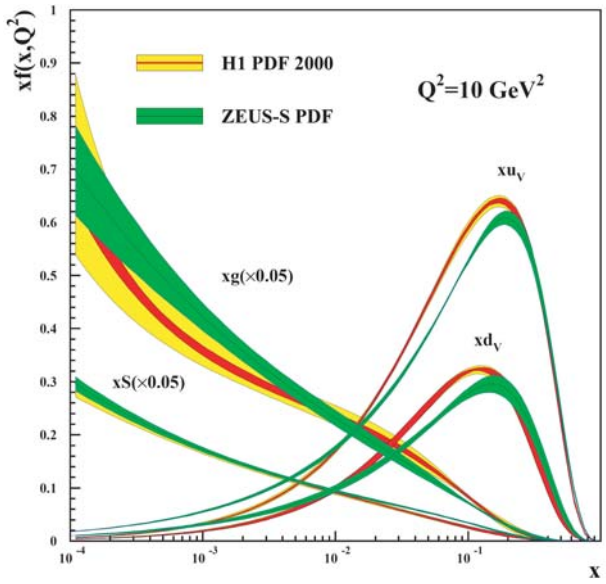

FIGURE 1.7: *Gluon and valence quark densities of the proton as obtained from H1 and ZEUS fits.*

$$C_g^1(z) = \frac{1}{2}\left((z^2 + (1-z)^2)\ln(\frac{1-z}{z}) + 8z(1-z) - 1\right). \tag{1.23}$$

Equations (1.18) and (1.19) are based on the **factorization theorem** [52] which states that the cross-section for DIS may be written as the convolution of a hard scattering cross-section and a non-perturbative parton density.
From fits to the measured F_2 structure functions the parton density functions can be determined. The gluon and valence quark distributions as determined from H1 and ZEUS fits are shown in figure 1.7. The gluon density becomes important and exceeds the quark densities by far for the small x region. This is the reason for the observed scaling violations of the structure functions at low x.

To compare the data measured in this analysis with theory predictions, sets of parton density functions are used that are based on global fits, provided by the CTEQ [89] group.

1.4.1 Parton Evolution Models

The scale dependent parton densities discussed in the previous section include soft processes up to the factorization scale μ_f. They are not calculable by perturbative QCD, nevertheless QCD predicts the scale dependence. If the densities are measured at a scale μ_0, an evolution to a scale $\mu > \mu_0$ is possible. The variations of $q(x,\mu^2)$ and $g(x,\mu^2)$ with respect to $\ln\mu^2$ are given by the **DGLAP**[2] **equations** [25,57,67,68,91]

$$\frac{\partial q_i(x,\mu^2)}{\partial \ln\mu^2} = \frac{\alpha_s}{2\pi}\int_x^1 \frac{d\xi}{\xi}\left(q_i(\xi,\mu^2)P_{qq}(x/\xi) + g(\xi,\mu^2)P_{qg}(x/\xi)\right) \tag{1.24}$$

[2]Dokshitzer, Gribov, Lipatov, Altarelli, Parisi

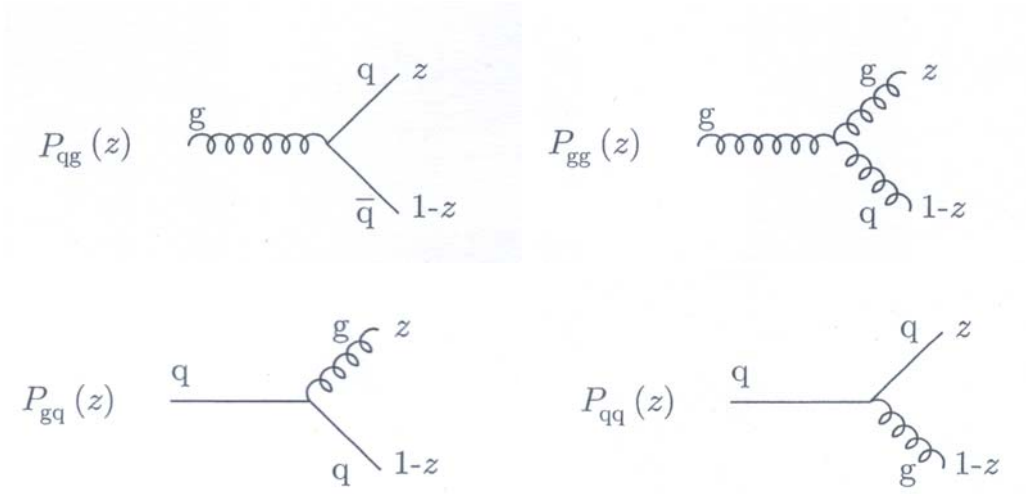

FIGURE 1.8: *Illustration of the four different splitting functions used for the DGLAP equations. z denotes the longitudinal momentum fraction.*

and

$$\frac{\partial g(x,\mu^2)}{\partial \ln \mu^2} = \frac{\alpha_s}{2\pi}\int_x^1 \frac{d\xi}{\xi}\left(\sum_i q_i(\xi,\mu^2)P_{gq}(x/\xi) + g(\xi,\mu^2)P_{gg}(x/\xi)\right). \tag{1.25}$$

These equations depend on the splitting functions P_{qq}, P_{gq}, P_{qg} and P_{gg}, which are illustrated in figure 1.8. They give the probability for a parton j to emit a parton i with momentum $p_i = zp_j$.

The DGLAP approach is based on resumming the leading $\alpha_s \ln(Q^2/\mu^2)$ terms.[3] This leading log approximation (LLA) requires a strong ordering in the transverse momenta of the emitted partons (see figure 1.9):

$$\mu^2 < p_{t,1}^2 < p_{t,2}^2 < ... < p_{t,n}^2 < Q^2. \tag{1.26}$$

This approach describes successfully the scaling violations of the structure functions observed at HERA down to the smallest accessible x. The DGLAP evolution is used to model parton showers for Monte Carlo programs (see section 1.8). The probability for evolving from a virtual mass scale t_1 to t_2 without resolvable branching is given by the ratio $\Delta(t_2)/\Delta(t_1)$, where $\Delta(t)$ is the **Sudakov form factor** (for a deeper discussion see e.g. [54]).

The **CCFM**[4] **approach** [45, 46, 48, 95] is an alternative to the DGLAP approach. It is based on the angular ordering constraint, which is a property of QCD: in a cascade of gluon and quark emissions the angles of the emitted particles decrease when proceeding down one branch. An unintegrated k_t dependent gluon density

[3] This resumming is achieved by replacing α_s by the running coupling.
[4] Ciafaloni, Catani, Fiorani, Marchesini

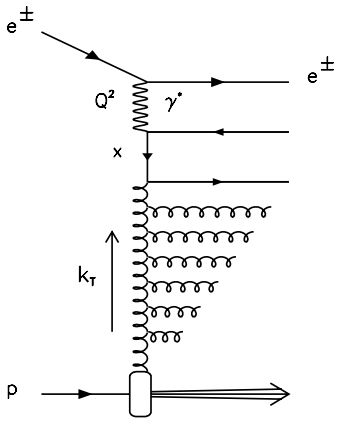

FIGURE 1.9: *Subsequently emitted gluons build a gluon ladder. For the DGLAP approach the emitted gluons are ordered in transverse momenta k_t.*

$\mathcal{A}(x_g, k_t^2, \mu_F^2)$ is used, allowing the partons entering the hard matrix element to be off-shell. The CCFM approach, also called $\boldsymbol{k_t}$ **factorization**, is equivalent to the DGLAP approach, also called **collinear factorization**, for large Q^2 and moderate x. This scheme avoids the problem of $\alpha_s \ln(1/x)$ terms of the DGLAP solution which becomes important for small x and might spoil the convergence of the perturbation series.

1.5 Heavy Quark Production

The production of charm and beauty quark pairs at HERA is an ideal testing ground for QCD as the masses of these heavy quarks set a hard scale which allows the measurements to be compared to perturbative calculations. At scales of the charm mass $m_c \approx 1.5$ GeV and beauty mass $m_b \approx 4.75$ GeV the strong coupling constant α_s gets so small that processes with further gluons involved are expected to be sufficiently suppressed. In the model described so far, only light quarks are considered. Several approaches exist to introduce beauty and charm quarks, they treat these quarks either as massless or massive:

Massive Scheme

As no charm or beauty density for the proton is assumed, this scheme is also called **fixed flavour number scheme** (FFNS). Heavy quarks are only produced perturbatively in the hard interaction. The leading order ($\mathcal{O}(\alpha_s)$) boson-gluon-fusion process and some next to leading order ($\mathcal{O}(\alpha_s^2)$) processes are shown in figure 1.10. The corresponding beauty structure function (the formalism is similar for charm quarks) is given by

$$F_2^b(x, Q^2) = 2 \int_x^1 \frac{dz}{z} x g_3(x/z, \mu^2) C_g^{FF}(z, m_b^2/Q^2, \mu^2), \tag{1.27}$$

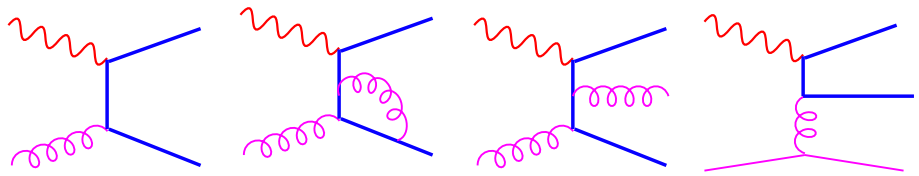

FIGURE 1.10: *Leading order (outer left) and next-to-leading order diagrams for heavy quark production in the massive scheme.*

where g_3 is the gluon density for three light flavours, μ^2 is the used scale (e.g. $\mu^2 = m_b^2 + p_{tb\bar{b}}^2$), and the massive fixed flavour coefficient function is given by

$$C_g^{FF}(z, m_b^2/Q^2, \mu^2) = \frac{\alpha_s(\mu^2)}{2\pi} e_b^2 C_g^{1,FF}(z, m_b^2/Q^2) + ... \tag{1.28}$$

For $Q^2 \gg m_b^2$ the gluon coefficient function is given by

$$C_g^{1,FF}(z, m_b^2/Q^2) = C_g^1 + \frac{1}{2}\left(z^2 + (1-z)^2\right) \ln(\frac{Q^2}{m_b^2}), \tag{1.29}$$

where C_g^1 is the gluon coefficient function from the massless DGLAP formalism (equation (1.23)) and an additional term proportional to $\ln(\frac{Q^2}{m_b^2})$ appears, representing collinear gluon emissions from the heavy quarks.
For $Q^2 \gg m_b^2$, terms proportional to $\left(\alpha_s \ln(\frac{Q^2}{m_b^2})\right)^n$, which are considered up to the order $\mathcal{O}(\alpha_s^2)$, might spoil the convergence of the perturbation series. The same holds for terms proportional to $\left(\alpha_s \ln(\frac{p_t^2}{m_b^2})\right)^n$ for $p_t^2 \gg m_b^2$. If p_t^2 and Q^2 are not too large compared to m_b^2, this method is reliably applicable.
This scheme is used for the theory predictions for this analyis.

Massless Scheme

In this scheme heavy quarks are considered as massless active flavours of the proton by introducing heavy quark structure functions for scales larger than the heavy quark mass. Therefore this scheme is called **zero-mass variable flavour number scheme** (ZM-VFNS). This results in a resummation of the terms representing collinear gluon radiations. The parton dynamics of heavy quarks can then be described by the DGLAP approach in a similar way as for the light quarks. The disadvantage is that the threshold behaviour for low Q^2 can not be described properly by this scheme. Some leading and next to leading order diagrams for this scheme are shown in figure 1.11.
The **variable flavour number scheme** (VFNS) is a mixed scheme that interpolates between the VFNS and the FFNS approach with a correct threshold behaviour at low Q^2 and heavy quark densities for large Q^2.

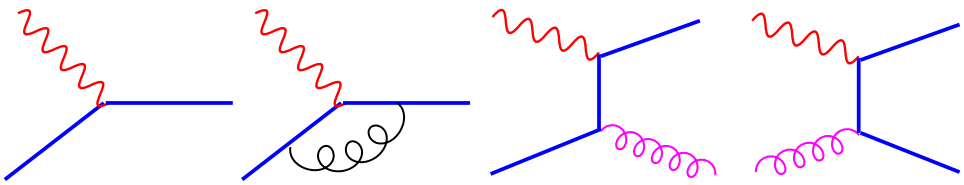

FIGURE 1.11: *Leading order (outer left) and next-to-leading order diagrams for heavy quark production in the massless scheme.*

1.6 Parton Hadronization

As a consequence of the colour confinement (see section 1.3), all experimental results are derived from the observation of hadrons. The hadronization, also called fragmentation process, has to be modelled to allow the comparison to theoretical predictions. This process can be calculated perturbatively above a scale of ≈ 1 GeV. The evolution of a heavy quark from the factorization scale μ_f to this scale via subsequent gluon emissions and splittings is described in Monte Carlo simulations by the parton shower approach. The scale dependence of this evolution is described by the DGLAP evolution (see section 1.4).
For the long distance, non perturbative part of the hadronization process different phenomenological models exist.
For this analysis the **string fragmentation** model [28] is used. In this model strings are formed by $q\bar{q}$ pairs and the colour field between them (see figure 1.12, left). The stored potential energy is proportional to the separation distance of the quarks. When this energy is large enough, the string breaks up and a new $q\bar{q}$ pair is produced out of the vacuum. Gluons are incorporated into this mechanism by kinks in the strings. Finally the string fragments are combined to hadrons. The transverse momentum distribution is assumed to be Gaussian, the longitudinal momentum fraction z is given by the fragmentation function $\mathcal{D}_Q^h(z)$. The **Lund fragmentation function** [28], defined as

$$\mathcal{D}_Q^h(z) \sim \frac{1}{z}(1-z)^a \exp(-bm_t^2/z), \tag{1.30}$$

is used as default for the Monte Carlo simulation for this analysis. Here m_t is the transverse mass $m^2 + p_x^2 + p_y^2$ of the hadron, and a and b are free parameters. For heavy quarks the Lund-Bowler [40] fragmentation function is used, which is a modification of equation (1.30). Another widely used fragmentation function is the **Peterson fragmentation function** [101], given by

$$\mathcal{D}_Q^h(z) \sim \frac{1/z}{\left(1 - 1/z - \epsilon_Q/(1-z)\right)^2}, \tag{1.31}$$

where ϵ_Q is a free parameter which is different for charm and beauty quarks, resulting in a harder fragmentation for beauty quarks. This means that beauty hadrons get

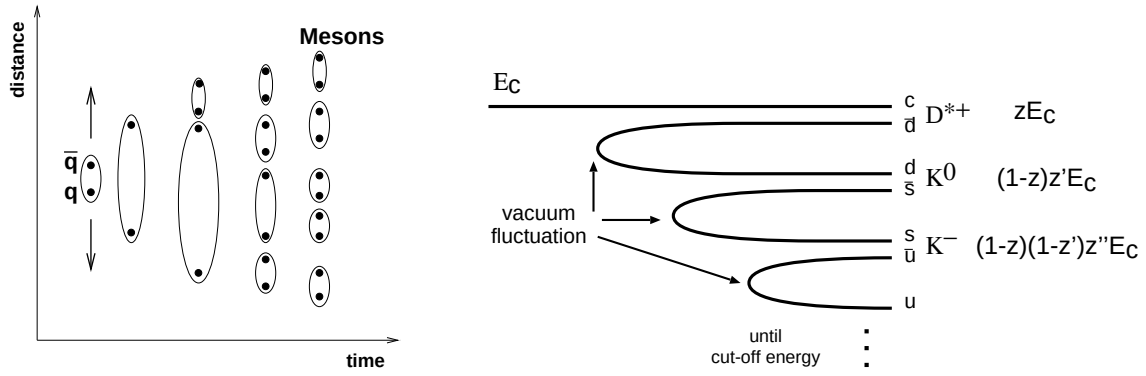

FIGURE 1.12: *Illustration of the String Fragmentation model (left) and the Independent Fragmentation (right).*

on average a larger longitudinal momentum fraction of the initial parton. In this analysis this function is used for the systematic study of the fragmentation of heavy hadrons. A further fragmentation function is the **Kartvelishvili fragmentation function** [84], defined as

$$\mathcal{D}_Q^h(z) \sim z^\alpha (1-z). \tag{1.32}$$

The string fragmentation model is similar to the **independent fragmentation** [62] which is not used anymore. In this model the partons hadronize individually (see figure 1.12, right). For each transition the initial parton is combined with a quark from a vacuum fluctuation. The other quark pair continues the fragmentation process. This cascade is stopped when all the energy is used up.
Another model which is not used for this analysis but mentioned for completeness is the **cluster fragmentation model** [116] where clusters form colour singlets which decay isotropically into hadron pairs.

1.7 Charm and Beauty Hadrons

The most important properties of charm and beauty hadrons that can be exploited as experimental signatures on a statistical basis for heavy quark production are their large mass and lifetime (see section 3.1). The main properties of heavy hadrons are listed in table 1.1. The much smaller CKM (Cabbibo-Kobayashi-Maskawa) matrix element $|V_{cb}|$ responsible for the decay $b \to cW^-$ compared to the matrix element $|V_{cs}|$ responsible for the decay $c \to sW^+$ is the reason for the longer lifetime of beauty hadrons, which is about 1.6 ps, compared to 0.4-1 ps for charm hadrons [58]:

$$|V_{cb}| = 0.0412 \pm 0.0020 \tag{1.33}$$

$$|V_{cs}| = 0.224 \pm 0.016 \tag{1.34}$$

This results in a larger decay length for beauty hadrons, where the lifetime effect is partially compensated by the larger Lorentz-boost of charm hadrons. Due to the

Hadron	quark content	lifetime [ps]	$c\tau$ [μm]	mass [GeV]
D^+	cd	1.051 ± 0.013	315	1869.3 ± 0.5
D^0	$c\bar{u}$	0.412 ± 0.003	123	1864.5 ± 0.5
D_s^1+	$c\bar{s}$	0.490 ± 0.009	147	1968.5 ± 0.6
Λ_c^+	ucd	0.200 ± 0.006	60	2284.9 ± 0.6
B^+	ub	1.674 ± 0.018	502	5279.0 ± 0.5
D^0	$d\bar{b}$	1.542 ± 0.016	462	5279.4 ± 0.5
B_s^0	$s\bar{b}$	1.461 ± 0.057	438	5369.6 ± 2.4
Λ_b^0	udb	1.229 ± 0.080	368	5624 ± 9

TABLE 1.1: *Lifetime, decay length and mass of some selected charm and beauty hadrons.*

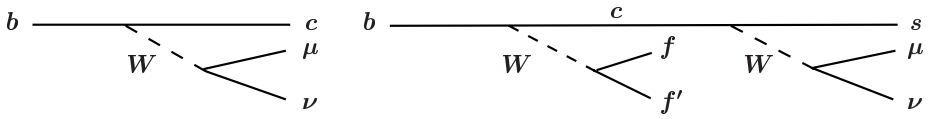

FIGURE 1.13: *Diagrams for semi-leptonic decays of beauty quarks: direct (left) and the cascade decay via a charm quark (right).*

large beauty quark mass the semi-leptonic decay of beauty hadrons can be described by the spectator model [73, 74], where the beauty quark decay is not affected by the light quarks (see figure 1.13). One can distinguish two modes for the decay $B \to \mu X$: for the **direct** process the beauty quark decays into cW and the W subsequently into a muon and neutrino. The branching ratio for this direct decay is about 10.6% [58]. For the **indirect** decay the charm quark decays further into sW, where the W decays into a muon and neutrino. In rare cases two muons can be produced as two W bosons appear in this indirect decay chain. The branching ratio for this indirect decay is about 8% [58]. Other decay chains as $B \to J/\Psi \to \mu\mu$ or $B \to \tau X \to \mu X'$ have much smaller branching ratios.

1.8 Monte Carlo Event Generators

Monte Carlo Generators provide an event-by-event prediction of the full hadronic final state. This is the input of detector simluations needed to study detector effects and to determine detector acceptances and efficiencies. Event generators model the underlying physics using several steps, based on the factorization theorem (see section 1.4). In figure 1.14 the different parts of an event generator are shown. All generators available at present calculate the hard matrix element in leading order α_s. Higher order QCD effects are modelled by the simulation of parton showers before and after the hard interaction. These parton showers are based on parton evolution equations (see section 1.4.1), where a backward evolution from the hard

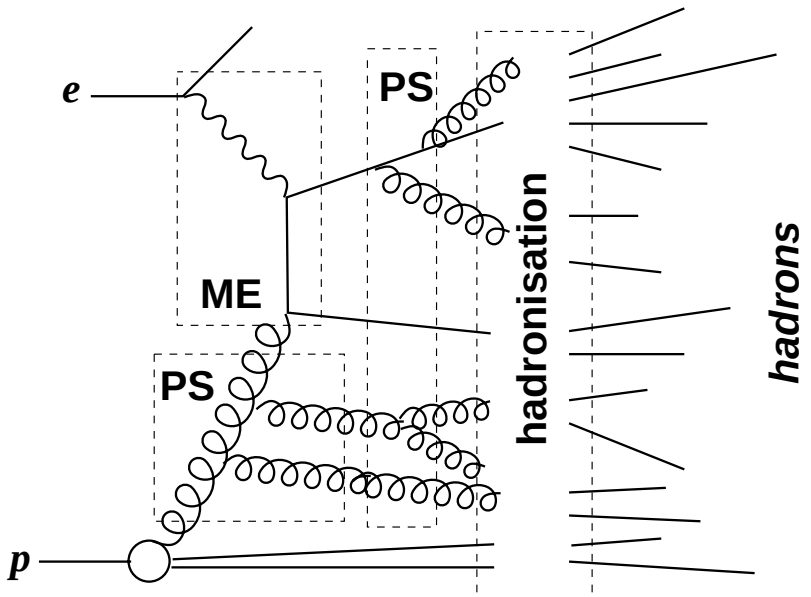

FIGURE 1.14: *Illustration of the perturbative and non perturbative processes implemented in Monte Calo generators: hard matrix element (ME), parton showers (PS) and the hadronization.*

matrix element to the proton is used for performance reasons. As the multi gluon emissions result in observable objects, event generators are in this sense superior to NLO predictions. For the hadronization part of the generators phenomenological fragmentation models (see section 1.6) are implemented. In addition hadron decays are modelled, e.g. semi-leptonic decays of heavy hadrons. After running the jet algorithm this hadron level prediction can be compared to data. For the determination of detector corrections this hadron level information is fed into detector simulations, usually based on the GEANT package [42], which provides particle tracking through the different subdetectors. Decays of long lived particles are simulated at this step. This simulation step is not part of the Monte Carlo generators and not discussed further. Finally the simulated data is subject to the same reconstruction as the data (see section 4).
For this analysis the default event generator is RAPGAP [82], used for a full simulation and in a separate mode to produce beauty events via boson gluon fusion. In both cases the leading order calculation is performed in the massive scheme. The inclusive mode includes a full simulation, including quark parton model and processes of the order α_s, like boson gluon fusion and QCD Compton. Higher order QCD effects are modelled using the DGLAP approach for the initial and final state parton showers. Hadronization and particle decays are implemented using the JETSET part of the PYTHIA code [109–112]. The hadronization is modelled using the Lund string fragmentation, where for heavy quarks the Peterson fragmentation function can be used. RAPGAP is interfaced to the HERACLES program [88], which simu-

lates QED radiative corrections. It generates the $e\gamma^* e$ vertex, including real photon emission from the incoming and outgoing electron and virtual corrections. By incorporating these corrections at this level large correction factors on reconstruction level for the DIS kinematic variables x, Q^2 and y can be avoided.
As an alternative, the Monte Carlo generator CASCADE [81, 83] is used. This program generates the boson gluon fusion process $\gamma^* g^* \rightarrow q\bar{q}$ for light and heavy quarks using an unintegrated gluon density which is obtained from the measured structure function F_2. This model has the advantage that the gluon entering the hard subprocess is allowed to carry a non zero transverse momentum. The backward evolution of the gluon density is based on the CCFM model, final state parton showers are modelled based on the DGLAP approach (see section 1.4.1). The hadronization process is again modelled by the JETSET routine. QED radiation is not implemented in CASCADE.
Details about the Monte Carlo parameters used for the simulated samples and for the samples used for the comparison to the data can be found in section 5.2 and 7.1, respectively.

1.9 NLO Calculation

The Monte Carlo integration program HVQDIS [69] provides the total and differential cross sections for a number of variables for heavy quark production in deep inelastic scattering. The matrix element is calculated in next-to-leading order using the massive approach (see section 1.5) in the $\overline{MS}$ scheme (see section 1.4). The program provides two or three partons for the final state. To allow a comparison to data, an extended version of this program is used. The hadronization of beauty hadrons into beauty flavoured hadrons is modelled by rescaling the three-momentum of the quark using the Peterson fragmentation function. Semileptonic decays into a final state with a muon are modelled using the muon decay spectrum taken from JETSET [109–112]. Parton level jets are reconstructed by applying the k_t algorithm (section 4.4.1) to the outgoing partons. A comparison to data at hadron level requires a correction to the hadron level using a Monte Carlo generator like RAPGAP. This is explained in section 7. The main theoretical uncertainties of the NLO calculation arise from the uncertainty of the beauty quark mass and the renormalization and factorization scales (see section 7).

Chapter 2

The Experiment

2.1 HERA

Two accelerators, one for electrons or positrons and one for protons, are housed in a common ring tunnel of 6.3 km circumference. This HERA collider, the preaccelerators and the location of the four interaction regions are illustrated in figure 2.1, left. The proton ring is equipped with 422 dipole magnets, 224 main quadrupole magnets, 400 correction quadrupoles, 200 correction dipoles, all superconducting. About 100 mA of protons were injected at an energy of 40 GeV and accelerated up to 920 GeV. The magnetic field for the proton ring was 5.1 Tesla for the nominal beam energy produced by a current of 5500 A for the dipoles. The electron ring consists of more than 1000 normal conducting dipole magnets. The injection energy was 12 GeV, the lumi energy 27.5 GeV. The usual beam current was about 45 mA. A maximal longitudinal polarisation of 45% was achieved for the lepton beam using three spin rotator pairs.
The lepton beam and proton beam consisted of up to 180 bunches, where each bunch contained about 10^{10} particles. The bunch length was about 8 mm for the leptons and, much longer, up to $20 - 30$ cm for the protons. The revolution frequency was 47.3 kHz.
Whereas the HERA B and HERMES experiments were using only the proton and lepton beam, respectively, the beams were brought to collison at the collider experiments H1 and ZEUS. Every 96 ns an intersection happened, which defined the HERA bunch crossing rate of 10.4 MHz. The luminosity is given by

$$\mathcal{L} = \frac{1}{4\pi e^2 f_0 n_b} \frac{I_e I_p}{\sigma_x \sigma_y}, \tag{2.1}$$

where f_0 is the revolution frequency, n_b is the number of bunches, I_e and I_p are the electron and proton currents, and $\sigma_x \cdot \sigma_y$ is the spot size at the interaction point, with typical values of 118 μm $\cdot$ 31 μm. Typical parameters of the lepton and proton beams are summarized in table 2.1.
After a shutdown and upgrade program to increase the luminosity, which included the installation of focussing magnets within the H1 and ZEUS detectors, luminosity

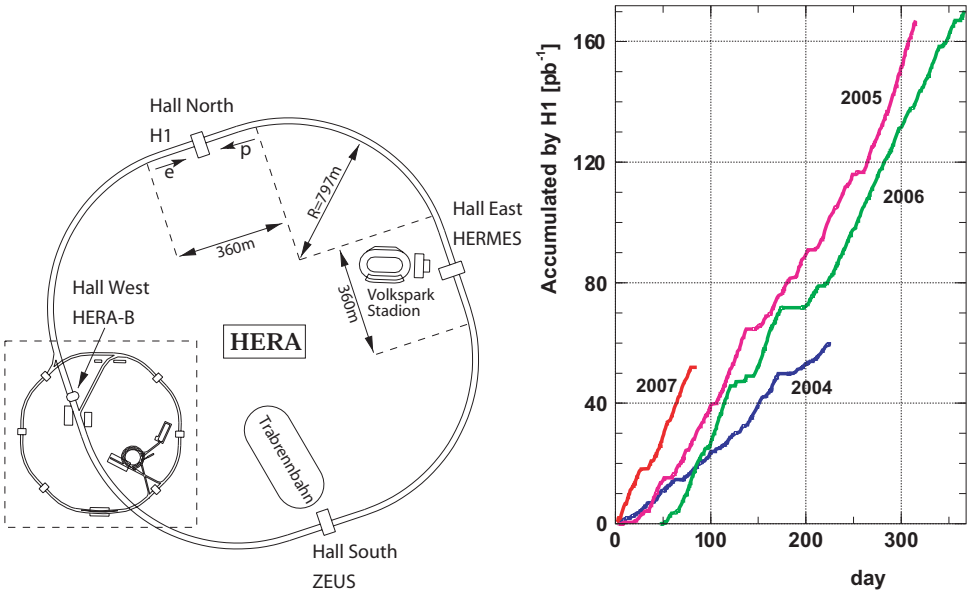

FIGURE 2.1: *HERA accelerator, preaccelerators and the four experiments H1, ZEUS, HERMES and HERA B and accumulated lumi for the H1 experiment for the years 2004-2007* [1].

	Electron-Proton	Positron-Proton
Proton/Electron beam energy	920 GeV/27.6 GeV	
Proton/Electron beam currents	108 mA/41 mA	110 mA/44 mA
Luminosity [$\mathrm{cm}^{-2}\mathrm{s}^{-1}$]	$4.9 \cdot 10^{31}$	$4.0 \cdot 10^{31}$
Specific luminosity [$\mathrm{mA}^{-2}\mathrm{cm}^{-2}\mathrm{s}^{-1}$]	$2.4 \cdot 10^{30}$	$1.7 \cdot 10^{30}$
Spot size $\sigma_x \times \sigma_y$ [$\mu\mathrm{m}^2$]	118×32	

TABLE 2.1: *Parameters of HERA II [53, 107]*

operation resumed in 2002 in the electron-proton mode. In July 2006 the operation switched to positron-proton mode. The accumulated luminosities for the different years are shown in figure 2.1, right. After dedicated low energy runs with a reduced proton beam energy to measure the longitudinal structure function F_L, the HERA operation ended at the end of June 2007.

2.2 H1 Detector

The H1 detector [11], which is currently being dismantled after the shutdown of HERA, was a complex detector consisting of several subdetectors which were arranged in a shell structure around the interaction point at the center of the detector. It was optimized for new particle production, neutral current inclusive measurements

	Detector Component	Abbreviation
	Tracking Detectors	
1	Forward Silicon Detector	FST
2	Central Silicon Detector	CST
3	Backward Silicon Detector	BST
4	Central inner proportional chamber	CIP
5	Central outer z drift chamber	COZ
6	Inner central jet chamber	CJC1
7	Outer central jet chamber	CJC2
8	Backward proportional chamber	BPC
	Calorimeters	
9	Electromagnetic spaghetti calorimeter	SpaCal em.
10	hadronic spaghetti calorimeter	SpaCal hadr.
11	Liquid argon calorimeter (electromagnetic)	LAr em.
12	Liquid argon calorimeter (hadronic)	LAr hadr.
	Muon Detectors	
13	Instrumented iron: Central Muon Detector	CMD
14	Forward Muon Detector	FMD

TABLE 2.2: *List of the main detector components of H1 (legend to figure 2.2).*

and charged current interactions. Therefore the detector covered the whole 4π solid angle with a higher instrumentation in the proton direction to account for the asymmetric beam energies. The main design decisions were the use of liquid argon as detector medium and lead/copper as absorber for the calorimeters and a coil outside the calorimeters.

A drawing of the detector is shown in figure 2.2, the inner part is shown in figure 2.3. The proton beam direction defines the positive z-axis, the $x - y$ plane is perpendicular to this axis, with the x-axis pointing to the center of the ring and the y-axis downward. The nominal interaction point defines the origin of the coordinate system. The polar angle ϕ of a particle trajectory is defined in the $x-y$ plane where $\phi = 0$ defines the x-axis, the azimutal angle θ is defined with respect to the z-axis.
The most inner detectors are tracking detectors used for identifying decay vertices, triggering and reconstruction of tracks. They are surrounded by calorimeters using liquid argon as active material for the measurements of particle energies. A lead-scintillator-fibre detector was used to identify the scattered electron in the backward direction. The superconducting magnet, which was outside the calorimeters, generated a magnetic field of 1.15 Tesla which was needed for the momentum measurement of charged particles. The return yoke of the magnet was instrumented with limited streamer tubes used to detect muons that penetrate the calorimeters. In the forward direction the detector was instrumented with a forward muon detector, which is not used for this analysis.
As part of the HERA II upgrade program many subdetectors and trigger systems were improved, this includes the Fast Track Trigger (FTT), which is used to trigger

	Detector Component	Abbreviation
	Tracking Detectors	
2	Central Silicon Tracker	CST
3	Central inner proportional chamber	CIP
4	Inner central jet chamber	CJC1
5	Central outer z drift chamber	COZ
6	Central outer proportional chamber	COP
7	Outer central jet chamber	CJC2
8	CJC electronics	
9	Forward tracking detector	FTD
10	Superconducting quadrupole magnet	GO
11	Forward tracker cables	
12	Inner wall of LAr vacuum tank	
13	Backward proportional chamber	BPC
14	Electromagnetic spaghetti calorimeter	SpaCal em.
15	Photomultipliers for SpaCal em.	
16	Hadronic spaghetti calorimeter	SpaCal hadr.
17	Photomultipliers for SpaCal hadr.	
18	Superconducting quadrupole magnet	GG

TABLE 2.3: *The main component of the central H1 tracker and backward calorimeters (legend to figure 2.3). Shown is the 2005 configuration without forward and backward silicon detectors (FST, BST). In figure 2.3 '1' denotes the nominal interaction point.*

events based on drift chamber information and a combination with other subdetectors. The FTT is discussed in more detail in section D.

2.3 Tracking System

A radial view of the central tracking system is shown in figure 2.4. The sub-detector closest to the interaction region is the Central Silicon Tracker (CST) used for precise measurements of charged particle tracks close to the event vertex. This detector is surrounded by the Central Inner Proportional Chamber (CIP) used for triggering. The most important tracking detectors are the inner and outer Central Jet chambers, CJC 1 and CJC 2, with the central outer z-chamber between them. They cover the angular range in $20° < \theta < 160°$.
In the forward direction the Forward Tracking Detector FTD delivers track information in the angular range $5° < \theta < 25°$.
The CST is supplemented by silicon detectors in the forward and backward region, the FST and BST, which were only operational for a fraction of the HERA II period due to repair work.
The Backward Proportional Chamber BPC refines the measurement of the scattered electron of the backward calorimeter.

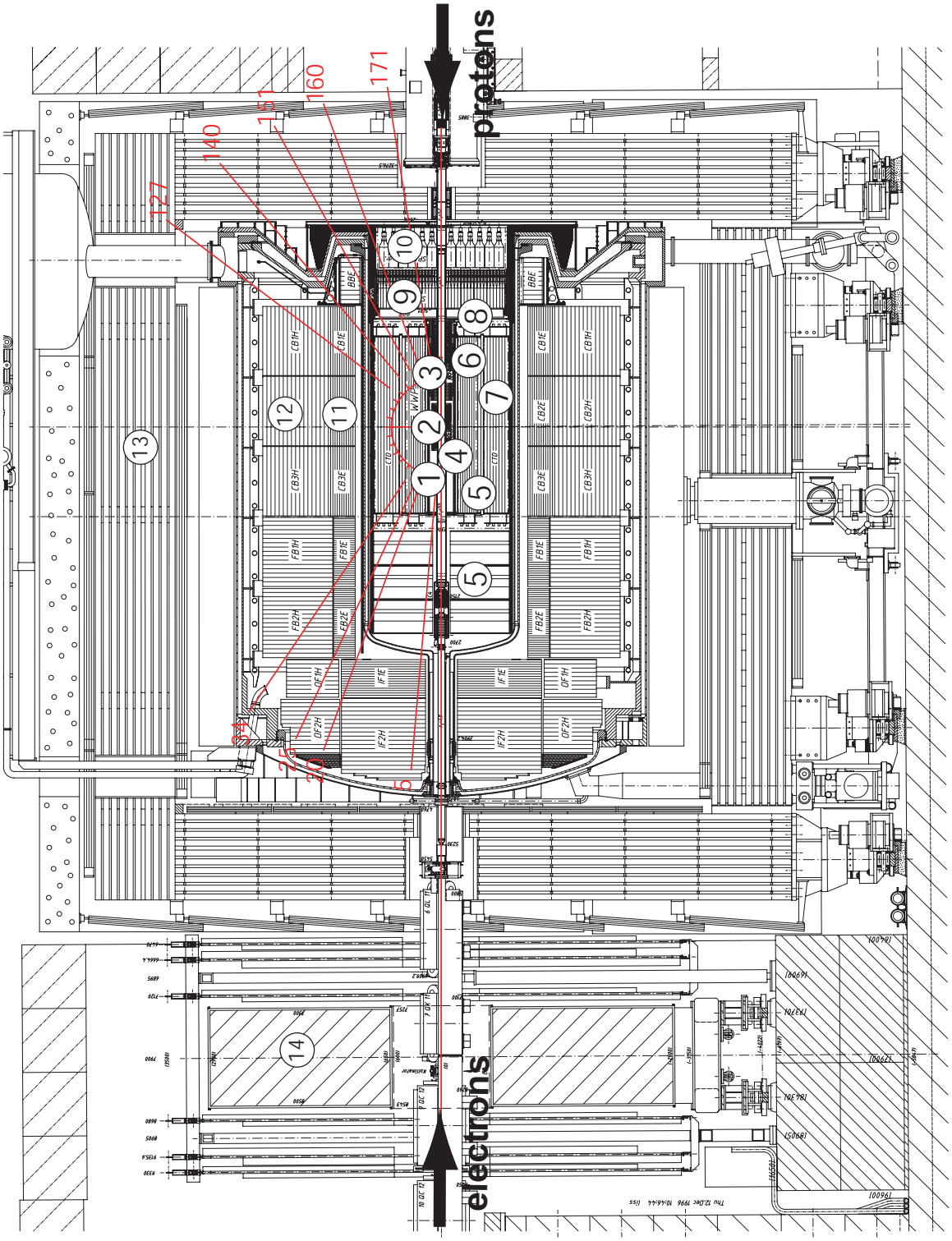

FIGURE 2.2: *Technical drawing of the H1 detector after the luminosity upgrade. For the different subdetectors see table 2.2.*

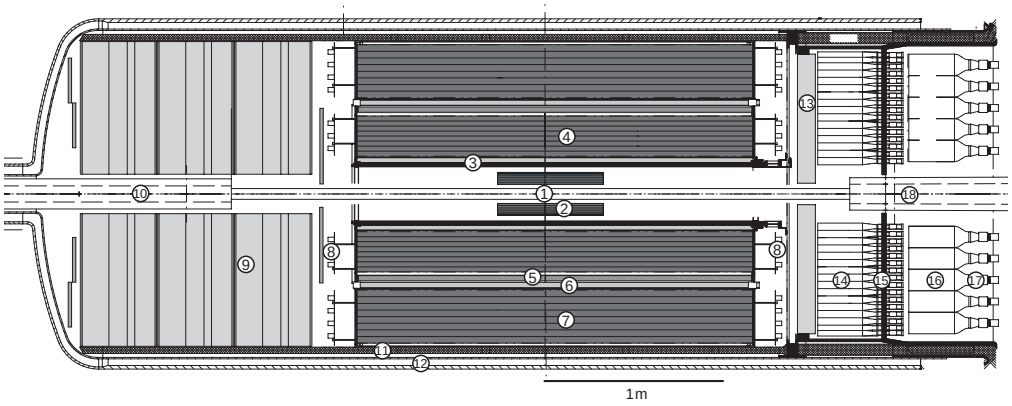

FIGURE 2.3: *The inner part of the H1 detector, consisting of the central tracking system, the forward tracking system and backward calorimeter. The legend to the subdetectors is given in table 2.3. Not shown in this drawing are the forward and backward silicon detectors.*

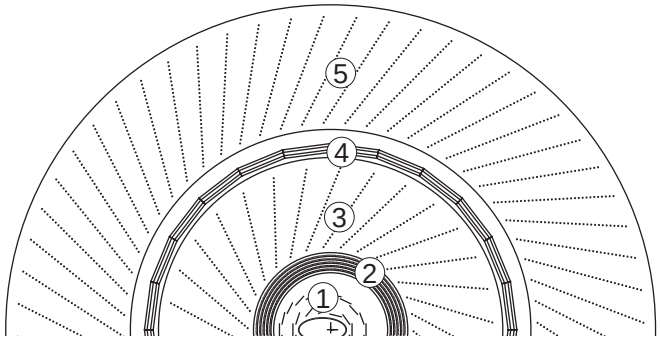

FIGURE 2.4: *Radial view of the central tracking system at H1. Shown are from the inside to outside: CST (1), CIP (2), CJC1 (3), COZ (4), CJC2 (5).*

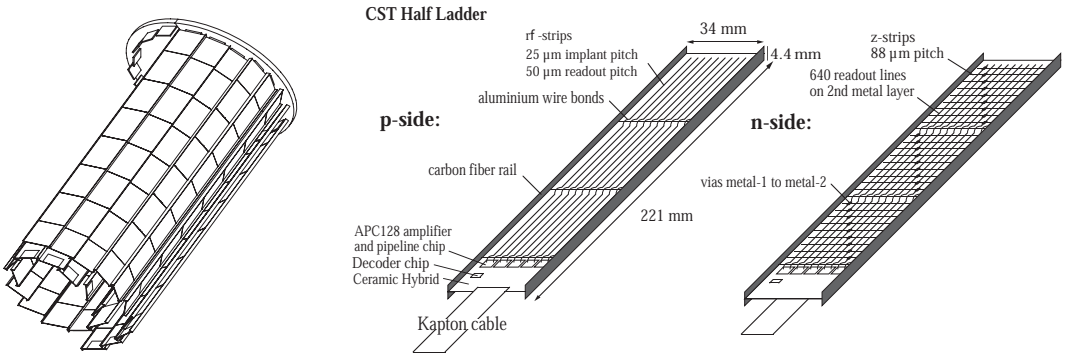

FIGURE 2.5: *Central silicon detector: elliptical arrangement of the two layers of strip sensors (left) and detailed view of the n and p side of the strip sensors (right).*

2.3.1 Central Silicon Tracker (CST)

The CST delivers precise vertex and track information by refining tracks reconstructed in CJC1 and CJC2. Several analyses use this data and exploit lifetime effects of heavy quarks (see section 3.1). For the analysis presented in this thesis this information is not used. This detector consists of double-sided strip sensors which are arranged in two layers around the beam pipe at a distance between 4 and 13 cm due to the elliptical beam pipe in this region for HERA II (see figure 2.3.1, left). The p side of the sensors has strips parallel to the z-axis and delivers information in the $r\phi$ plane, the n side measures the z coordinate. The p and n side of the ladders, made of six sensors each, are illustrated in figure 2.3.1, right. More detailed information on the CST and the two endcap parts (FST, BST) of the H1 silicon tracker can be found in [92].

2.3.2 Central Proportional Chamber (CIP)

The Central Inner Proportional Chamber (CIP) installed for HERA II is a multi-wire proportional chamber with wires parallel to the beam. 5 detector layers enclose the CST at radii between 15 and 20 cm. The chamber covers a range $-112.7 < z < +104.3$ cm and $11^\circ < \theta < 169^\circ$. The 9600 readout pads are arranged in a projective geometry which results in the same pattern for tracks that origin from the same z position. The CIP2000 trigger searches for track patterns, builds a z-vertex histogram from the number of tracks pointing to the bins along the beamline, and evaluates the histogram. A fast trigger decision on Level 1 (see section 2.7) allows an early rejection of background events without introducing dead time for data taking. The trigger decision is based on the total number of entries in the histogram and the fraction of central to backward entries (CIP significance). A similar condition is used for the FTT z-vertex trigger (see section D). The fast response time of the detector also allows for a determination of time of the interaction (event t_0). Details on the detector and the trigger can be found in [115].

2.3.3 Central Jet Chamber (CJC)

The Central Jet Chamber is a drift chamber made of two parts, the inner chamber CJC1 that encloses the CIP at an inner radius of 20.3 cm and the outer chamber CJC2 with an outer radius of 84.4 cm. An angular range $20° < \theta < 160°$ is covered, defined by the acceptance of the CJC2. The inner (outer) chamber is divided in 30 (60) cells, which are tilted with respect to the radial direction. This ensures that high momentum tracks cross the cell boundaries and can be measured within 2 cells. Each cell of CJC1 (CJC2) contains 24 (32) sense wires. The actual positions of these wires are shifted by an amount of ± 150 μm (staggering). The hit position is measured using the drift time of charges to these signal wires (determined in a Qt-analysis of the pulse shape, see section D.3.2), drift velocity and the exact wire position. An ambiguity appears as it is not known from which side the charges drift to the wire resulting in the reconstruction of mirror hits. This left-right ambiguity can be resolved due to the crossing of cell boundaries and the staggering of the sense wires. The single hit resolution in the $r\phi$-plane is about 140 μm, in the z plane only about 22 mm are achieved.
The CJC is the main detector component that provides the data (hit information) used for the reconstruction of tracks in the central detector region. The reconstruction algorithm delivers helix parameters of bent tracks due to the magnetic field, which is a measurement of the transverse momentum of the corresponding particle. The principle is described in some more detail in section 4.2 in the context of the muon track reconstruction.
A fraction of the signal wires deliver information for the Fast Track Trigger (FTT), which is described in some more detail in section D.

2.3.4 Outer Z Chamber

The Central Outer Z Chamber (COZ) is a drift chamber with wires strung perpendicular to the z-axis. It is used to improve the poor z measurement of the CJC and achieved a resolution of about 350 μm. This chamber is installed between the inner and outer jet chambers CJC1 and CJC2 and covers the angular range $25° < \theta < 155°$. The thickness of the chamber is 1.5% X_0, where X_0 is the radiation length. Energy losses and photon conversions between the jet chambers have to be taken into account for the track reconstruction algorithm.

2.3.5 Forward Tracker

An additional tracking system (Forward Tracking Detector, FTD) to identify charged particles is installed in the forward direction. This allows the measurement of heavy quark production for large Q^2 and x, where the hadronic final state is produced in the forward direction.
The detector is designed to detect tracks in the angular range $5° < \theta < 25°$ from the interaction point and was upgraded for HERA II. It consists of three supermodules, where the inner two supermodules (with respect to the interaction point) contain five planar chambers (the three inner denoted as P type, the two outer as Q type).

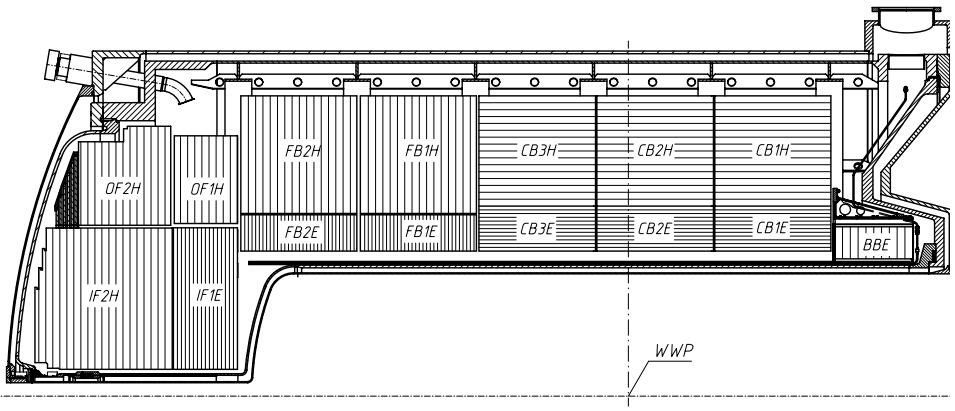

FIGURE 2.6: *r-z view of the upper half of the Liquid Argon Calorimeter. The parts denoted with "E" belong to the electromagnetic section, the parts denoted with "H" belong to the hadronic section. The different orientation of the absorber plates for the different wheels is visible.*

The outer supermodule has only one module of type Q. The drift cells for the P chambers have four wires each, which are rotated with respect to the y-axis for an amount of 0°, +60° and −60°. The cells for the Q type have 8 wires each at angles of +30° and +90°. The identification of tracks in the FTD starts with a search for clusters, which are groups of three or four hits consistent with a straight line, in each of the planar chambers. A cluster defines a plane in space containing the path of the particle. The combination of two planes defines a line segment on the particle's path. A third plane is required to resolve ambiguities due to many different combinations of two planes if several particles pass the chamber. These segments from different submodules are combined to forward tracks. It is also possible to combine these forward tracks with tracks from the central drift chamber CJC for the overlap region.

2.4 Calorimetry

2.4.1 Liquid Argon Calorimeter (LAr)

The Liquid Argon Calorimeter (LAr) (figure 2.6) covers the forward and central region of the H1 Detector in the angular range $4° < \theta < 153°$. The electromagnetic section (ECAL) measures electromagnetic showers using lead absorbers. Hadronic showers which penetrate into the hadronic part (HCAL) are measured using steel absorbers. In both cases the active material is liquid argon, therefore the whole calorimeter is contained in a cryostat. The calorimeter is divided into eight wheels made of eight octants each. The orientation of the absorber plates is such that particles from the interaction point impinge with an angle larger than 45°. The electromagnetic section of the calorimeter has a resolution of $\sigma_E/E \approx 11\%\sqrt{E/\mathrm{GeV}} \oplus 1\%$, the hadronic section has a resolution of $\sigma_E/E \approx 50\%\sqrt{E/\mathrm{GeV}} \oplus 2\%$. The calorime-

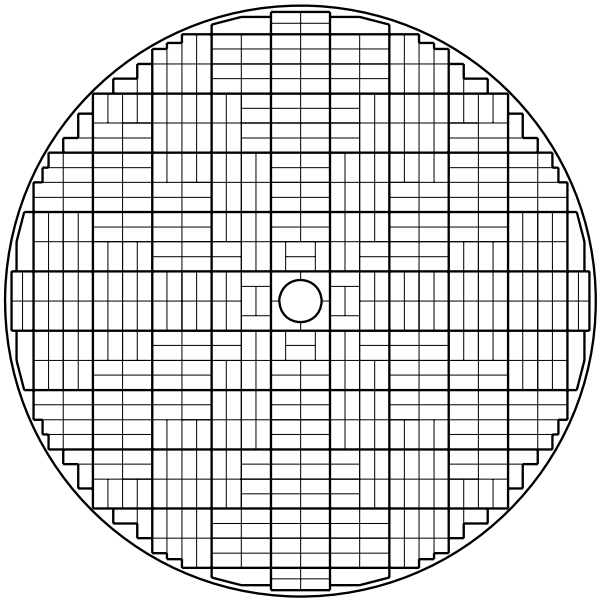

FIGURE 2.7: *Illustation of the electromagnetic SpaCal: each module, indicated by the thick lines, consists of eight submodules (thin lines).*

ter is of non compensating type, which means that the response for electromagnetic particles is higher than for hadrons. The compensation is obtained using offline algorithms.

2.4.2 SpaCal

The backward region of H1 is instrumented with a lead-scintillating fibre Spaghetti Calorimeter (SpaCal). It has a diameter of 160 cm and consists of an electromagnetic (see figure 2.7) and a hadronic section.
The electromagnetic section consists of about 1150 quadratic lead absorber cells with scintillating fibres, pairwise arranged in submodules, where eight submodules build a module. The cells have an active volume of $4 \times 4 \times 25$ cm^3. The thickness corresponds to 27.5 radiation lengths which ensures an only small leakage of the deposited electromagnetic energy to the hadronic section. The fibres with 0.5 mm diameter direct the light through light mixers to photomultiplier tubes (PMT), where the scintillation light is converted into an electrical pulse and amplified. This calorimeter is used to measure the scattered electron in the backward direction, with an energy resolution $\sigma_E/E \approx 7\%\sqrt{E/\mathrm{GeV}} \oplus 1\%$, and the polar angle of the scattered electron can be measured with a resolution of about 2 mrad. In addition this detector is used to trigger on the scattered electron and as a veto to suppress beam gas due to the precise timing information with a resolution of 1 ns.

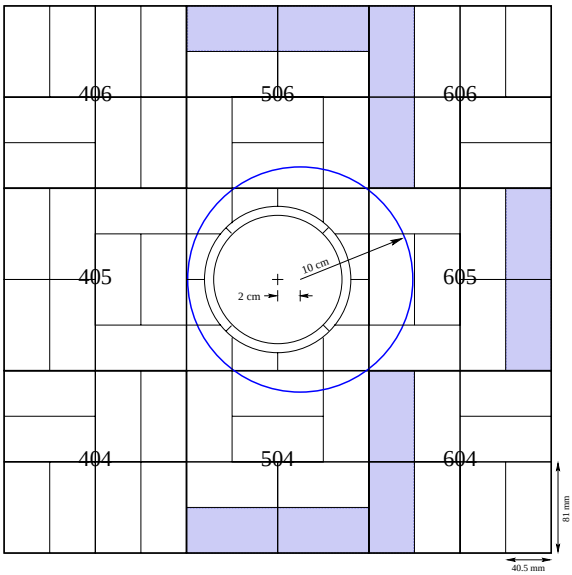

FIGURE 2.8: *Inner SpaCal region: the circle shows the new SpaCal hole, which has a radius of 10 cm. The origin is shifted with respect to the origin of the H1 coordinate system.*

The hadronic section of the SpaCal has a similar structure with larger cells of dimension $12 \times 12 \times 25$ cm^3. The cell depth corresponds to one interaction length. This calorimeter is used as a veto against hadrons.
The installation of the focussing at H1 for the HERA II upgrade required modifications of the inner spacal region. In order to have space for the new elliptical beam pipe, the radius of the spacal hole was extended 10 cm, where the center is shifted with respect to the center of the H1 coordinate system (see figure 2.8). The angular coverage is reduced to $153^\circ < \theta < 173^\circ$, the acceptance in Q^2 is reduced to $\approx 4 < Q^2 < 100$ GeV^2.

2.5 Muon System

The return yoke of the solenoid magnet is instrumented with limited streamer tubes to measure tracks of muons that penetrate the calorimeters. This Central Muon Detector (CMD) is divided into four parts: forward endcap ($4^\circ < \theta < 35^\circ$), backward endcap ($130^\circ < \theta < 171^\circ$), and the barrel region ($35^\circ < \theta < 130^\circ$), made of the backward and forward barrel. The backward barrel region is not used for the analysis presented in this thesis. Each of these parts consists of 16 modules (see figure 2.9). About 103 000 limited streamer tubes with a cross section of 1×1 cm^2 are mounted in the slits between the ten iron plates with a thickness of 7.5 cm, where the slits are on average 2.5 cm wide. Three additional layers of streamer tubes are mounted on the inner and outer surface of the return yoke. The wires are strung parallel (perpendicular) to the beam axis for the barrel (endcap) region. Influence charges

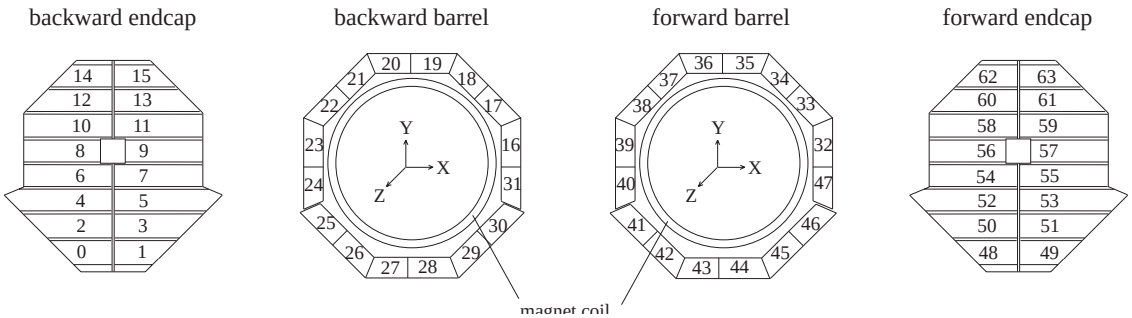

FIGURE 2.9: *Illustration of the four parts of the Central Muon Detector. Each part consists of 16 modules.*

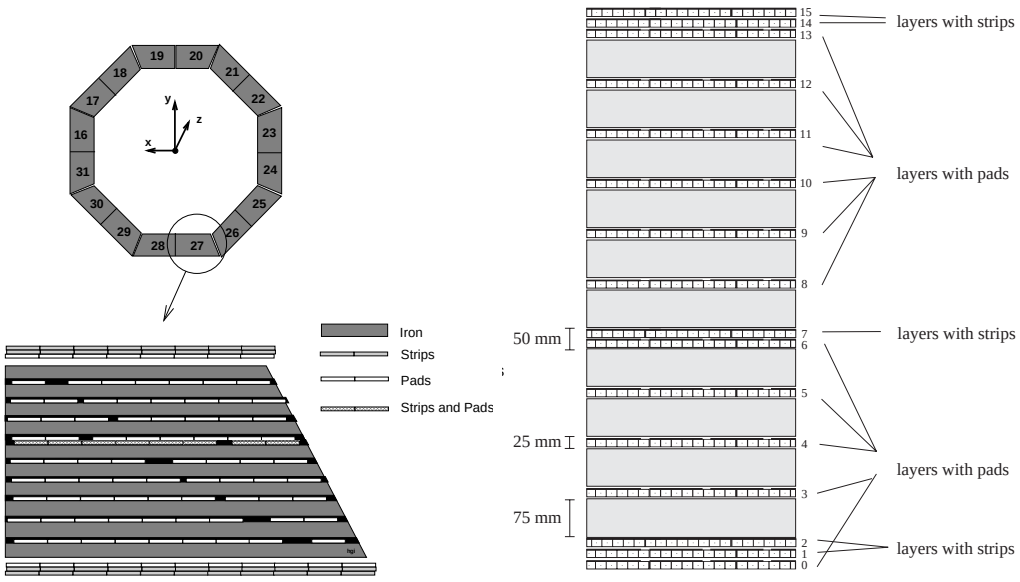

FIGURE 2.10: *Cross section view of an instrumented iron module.*

are induced and measured at electrodes mounted at the top side of the chambers. These electrodes are either strips with a width of 17 mm and 3 mm spacing or pads with a size of 25×25 cm^2 in the endcaps and 50×40 cm^2 in the barrel. The instrumentation of the different layers of a module is shown in figure 2.10. Wires and strips are read out digitally and allow for a two-dimensional space measurement. Five layers (3,4,5,8 and 12) are used in addition for trigger purposes.
The momentum resolution of the CMD is only about 30%. Therefore for this analysis the muon system is only used to identify muons, the momentum measurement is provided by the tracking system. The tracks from the muon system (iron tracks) are combined with the inner tracks from the tracking system (see section 4.2).

2.6 Luminosity Measurement

The rate at which the Bethe-Heitler process $ep \rightarrow ep\gamma$ [37] occurs, is used to measure the luminosity. This process has a large and well known cross section, calculable in Quantum Electro Dynamics (QED). The photons of this process are detected at small angles by a quartz-fibre calorimeter with tungsten absorber located at z=-103 m. A beryllium filter shields the detector against synchrotron radiation background induced by the focusing magnets. The main uncertainty of the measurement is the acceptance of the photon detector. The offline measurement for the HERA II running period is not fully understood when writing this thesis. Therefore an averaged uncertainty of about 4% is assumed for the data period analysed in this thesis, which is higher than the uncertainty for HERA I, which is about 2%.

2.7 Trigger

At the nominal bunch crossing rate of 10 MHz at HERA, electron proton scattering is expected to appear at a rate of several kHz. As the rate of background events (e.g. beam gas and beam wall events) is three orders of magnitude higher and the detector can only be read out at a rate of 50 Hz, a trigger system with a high selectivity is required which selects interesting physics events and rejects background event efficiently. At H1 a four level trigger system was used: the algorithms of the first three levels were running on custom made hardware. The readout of one event takes about 1.4 ms, during which the data taking is stopped. The optimisation goal to keep this dead time reasonably low (about 10%) defined the maximum rate at which the detector can be read out. The computing farm of standard PCs at level four reduced the rate further to about ten events per second which were fully reconstructed and written to tape.

2.7.1 Level 1

The first level trigger is the only trigger level that does not induce deadtime itself, as the data from the subdetectors is written to pipelines and the data taking continues during the calculation of the trigger decision. In total 256 Trigger Elements (TEs)

are formed, based on track signals of the muon system and the central tracker and energy depositions in the calorimeters. These TEs are forwarded to the Central Trigger Logic (CTL) where they are combined to up to 192 Subtriggers (STs). Only if a subtrigger condition is fulfilled, the pipelines are stopped and the dead time starts.
In order to limit the output rate of this trigger level to the predefined target rate and to make best use of the available bandwidth, subtriggers are prescaled, i.e. scaled down.[2] Therefore some subtriggers "see" only a fraction of the luminosity. This is not the case for the subtrigger relevant for the analysis presented in this thesis.
Subdetectors with precise timing information (SpaCal and CIP) deliver t_0 trigger signals, which define the bunch crossing of the triggered interaction and mark therefore the positions in the pipelines that has to be read out by the subdetectors.

2.7.2 Level 2

After a positive level 1 decision dead time is accumulated as the pipelines are stopped. The level 1 decision is validated using three trigger systems: the topological trigger and the neural network trigger combine information from trackers, calorimeters and the muon system. The FTT refines the level decision and reaches a track resolution comparable to the offline reconstruction. The total time available for the level 2 decision is 20 μs. 96 trigger elements are forwarded to the Central Trigger Logic and combined. If no level one trigger could be validated by level two, the data taking resumes, otherwise the readout of the detector begins. Many level one triggers did not have level two conditions and were validated by default.

2.7.3 Level 3

The readout started after a positive level two decision with an average readout time of 1.3 ms per event. This time could be much larger, depending on the event size. The level 3 trigger, which was part of the FTT system (see section D), could stop the readout after 100 μs and therefore reduce the deadtime of the detector. The level 3 system performed a partial event reconstruction based on level two track information on commercial processors. In addition information from the muon system and calorimeter information is used. 48 trigger elements are provided to the Central Trigger Logic, which rejects the event if no trigger element could be validated, where some subtriggers with no level 3 condition are validated by default. The level 3 system must ensure a maximum output rate of about 50 Hz.

2.7.4 Level 4

After readout the full event information was assembled at the event builder. The full event reconstruction was performed at a PC farm, followed by an event classification.

[2]Events are rejected in a deterministic way: for subtriggers with prescale factor n only each n-th positive decision is taken into account.

Based on this decision events which fall into one of the event classes and in addition a fraction of rejected events were stored with a rate of about 10-20 Hz.

Chapter 3

Previous Experimental Results

In this section an experimental review about beauty quark production at HERA and elsewhere is given. After a short introduction of the experimental methods used for the measurements at the HERA experiments, the results are discussed for the photoproduction and the DIS region. This is complemented by a discussion of measurements at other colliders.
A discussion of charm quark production can be found in [33].

3.1 Experimental Methods

The different taggig methods used at H1 and ZEUS to select heavy flavour enriched samples are illustrated in figure 3.1. A full reconstruction of heavy flavoured hadrons is only done for charmed hadrons, where e.g. the golden decay channel ($D^{*+} \rightarrow D^0\pi_s^+ \rightarrow (K^-\pi^+)\pi_s^+$) is used. For beauty hadrons, no similar decay channel without neutral particles and large enough branching ratios exists. Instead usually a **lepton tag** is used. The muons and electrons from semileptonic decays of beauty hadrons have large enough momenta and can therefore be well reconstructed.
For the **muon+jet** analyses, jets are required in addition to the lepton (dijets for the photoproduction region and only one jets due to the lower statistics for the DIS region). The jets estimate the quark direction. This information is needed to determine the fraction of beauty events on a statistical basis using the $\boldsymbol{p_t^{rel}}$ **tag**. p_t^{rel} is the relative transverse momentum of the lepton with respect to the jet axis. The large mass of beauty hadrons is exploited which results in large values of p_t^{rel}. An event display of a dijet event with an identified muon is shown in figure 3.2. Figure 3.3 shows the p_t^{rel} distributions used for the first H1 measurement [10], the H1 measurement using the full HERA 1 statistics [8], and for the analysis presented in this thesis.
In [8] the p_t^{rel} tag is combined with a **lifetime tag** which exploits the long lifetime of beauty hadrons. The **signed impact parameter** distribution δ of a track is defined as the shortest distance to the primary event vertex. To define a signed impact parameter the jet axis is needed. In figure 3.4 the δ distribution for the muon track is shown. The position of the muon track at the primary vertex is measured

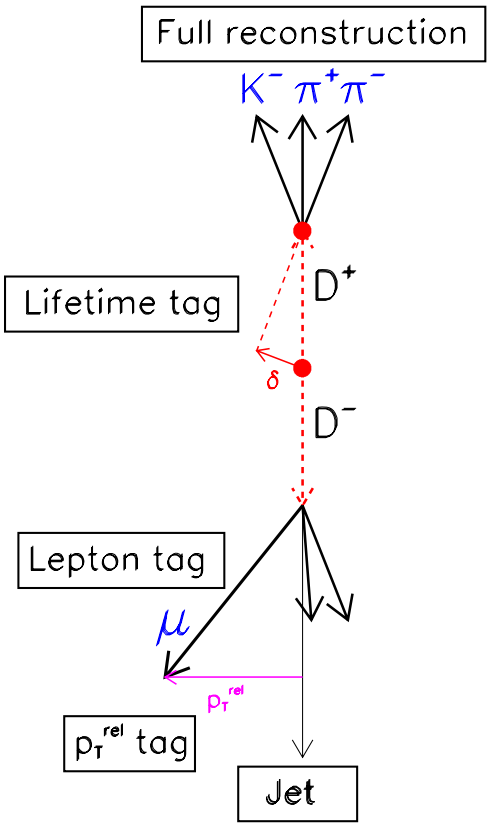

FIGURE 3.1: *Tagging methods used at H1 and ZEUS to select heavy flavour enriched samples (from [33]).*

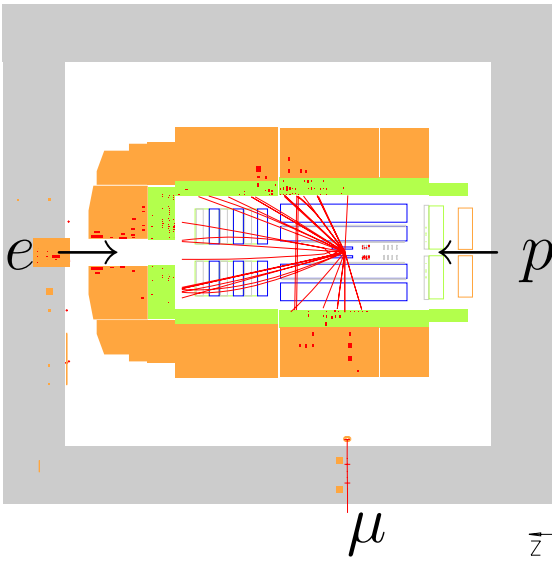

FIGURE 3.2: *Event display of a dijet event with an muon identified in the Central Muon Detector.*

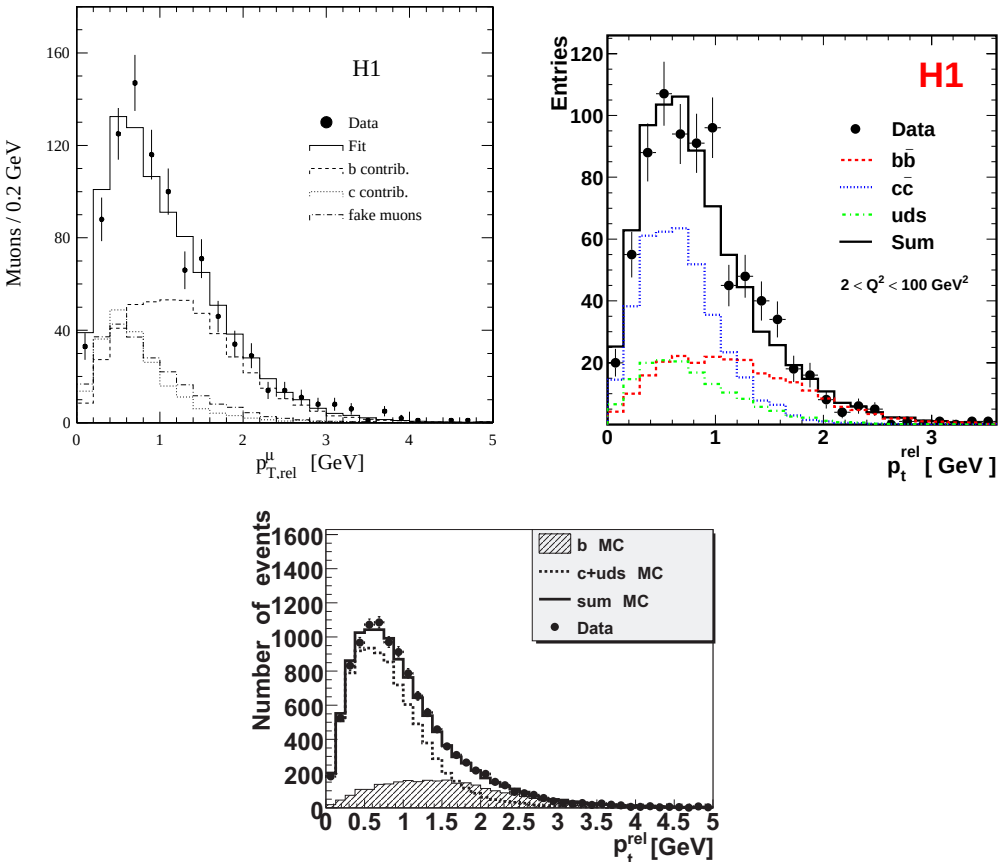

FIGURE 3.3: *P_t^{rel} distribution from the first H1 measurement [10] based on 7 pb^{-1} from 1996 photoproduction data (upper left plot), from the measurement [8], based on about 50 pb^{-1} of DIS data recorded in 1999/2000 (upper right plot) and from the measurement presented in this thesis, based on about 285 pb^{-1} HERA II data (lower plot). The upper right and lower plot show the distribution for electroproduction data. The increased statistics of the 1999/2000 data and the HERA II data allow the measurement of differential cross sections and double differential cross sections, respectively.*

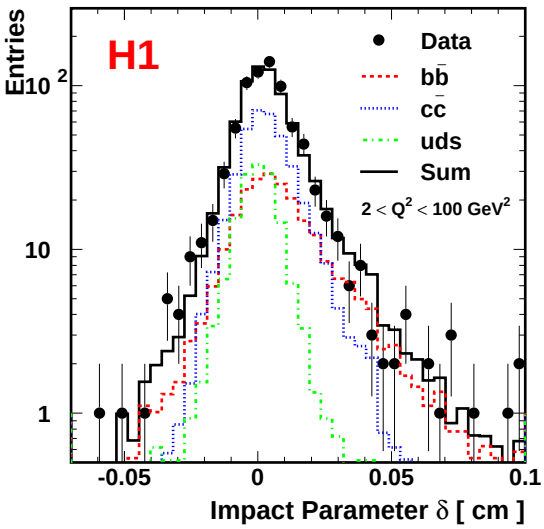

FIGURE 3.4: *δ distribution of the muon track, which is defined as the distance to the primary vertex, for the DIS sample of the H1 muon+jet analysis [8].*

using the innermost tracking detector, the Central Silicon Tracker (see section 2.3.1). This additional information allows a separation of light flavour, charm and beauty events on a statistical basis. This is not possible when using p_t^{rel} alone, as the light flavour and charm quark distributions are very similar. The main disadvantage of methods using jets is the lower energy cut at about 5 GeV, which is necessary to reconstruct a stable jet axis. This cut limits the measured range of the beauty quark transverse momentum.

A measurement at threshold is possible when requiring a second heavy quark tag besides the muon, either a D^* or a second muon. For the ***D**** analyses [9, 18] the charm and beauty content of the sample can be disentangled on a statistical basis using charge and angular correlations (see figure 3.5). For the **dimuon** analyses [50] it is exploited that for the beauty signal there are significantly more muon pairs with unlike-sign charges. This method has the advantage that low beauty quark momenta can be measured but the disadvantage of a low statistics data sample compared to other methods.

An alternative method is the **inclusive lifetime tagging method**, based on the displaced impact parameter of tracks in dijet events [7, 63]. This method has the advantage that highest transverse jet momenta up to 35 GeV can be reached, because of the larger available statistics.

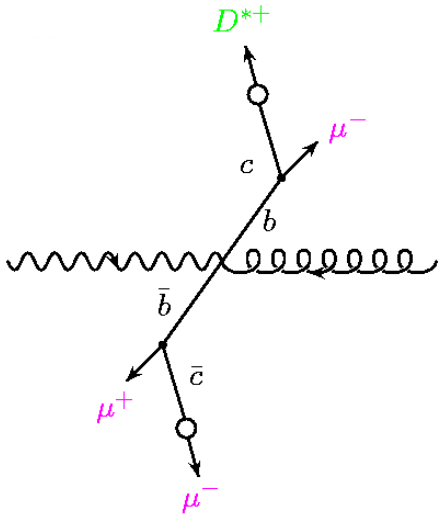

FIGURE 3.5: *Possible production of a muon and a D^* meson in a beauty quark event (from [33]).*

3.2 Measurements at HERA

Beauty production is measured at HERA in photoproduction and deep inelastic scattering by the collider experiments H1 and ZEUS using the different methods explained in the previous section and covering different kinematic regions. The largest statistics is available for the photoproduction region. In addition, beauty production was measured at the fixed target experiment HERA B.

3.2.1 Photoproduction

In figure 3.6 a summary of ZEUS results, based on HERA I data, is shown. This includes the very recent results from the analysis using decays into electrons [17], an older measurement using the same method [22], the measurement using decays into muons [16, 19] and the D^* muon measurement [18]. The measured cross sections with respect to the beauty quark momentum are compared to the NLO prediction. For the jet measurements the transverse quark momentum is given by the transverse jet momentum, the lowest momentum is accessible for the D^* muon measurement. In [17] it is stated that "the measurements agree well with the previous values, giving a consistent picture of b-quark production in ep collisions in the photoproduction regime and are well reproduced by the NLO calculations". The interesting region of low transverse momenta will be further explored by an H1 measurement at threshold using electrons and muons triggered by the Fast Track Trigger [103].
The NLO prediction predicts a less steep behaviour than the H1 HERA I analysis based on events with muon and jets, which combines p_t^{rel} tag and the lifetime tag [8] (see figure 3.7). The prediction "is lower than the data in the lowest momentum bin by roughly a factor of 2.5". When extrapolated to the inclusive beauty quark cross

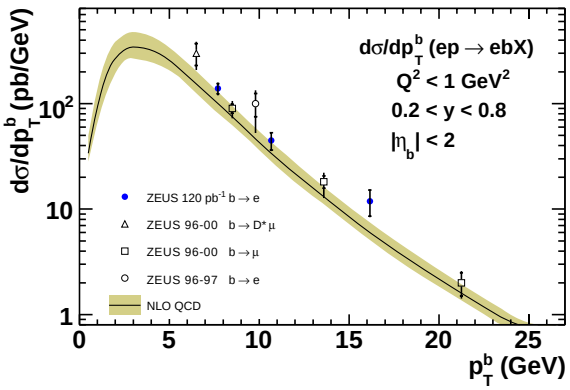

FIGURE 3.6: *Summary of ZEUS photoproduction results, obtained from HERA I data. Besides the latest results using decays into electrons [17], the results from [22], [16, 19] and [18] are given.*

section, the result is 2.3 standard deviations below the result obtained in the first H1 measurement using the p_t^{rel} tag [10]. The analogue ZEUS measurement [16] did not verify this result and agrees with the NLO prediction (see figure 3.7). The higher statistics of the HERA II data and the better understood CST detector allows a measurement of higher precision [85].

Also for the dijet analysis based on the inclusive lifetime tag [7] the data is above the NLO prediction (see figure 3.8).

3.2.2 Deep Inelastic Scattering

The beauty production cross section at a median transverse momentum value for the b-quark of 6.5 GeV was measured as well for deep inelastic scattering in [18]. It is concluded that "[...] the measured cross sections exceed the NLO predictions, but they are compatible within errors." Some results of the ZEUS HERA I measurement at higher transverse momenta using the p_t^{rel} tag are shown in figure 3.10. The jet selection is performed in the Breit frame (see section 4.4.2). It is concluded that "the differential cross sections are in general consistent with the NLO QCD predictions; however at low values of Q^2, Bjorken x, and muon transverse momentum, and high values of jet transverse energy and muon pseudorapidity, the prediction is about two standard deviations below the data." A similar measurement was performed at H1 for HERA I data, in a more restricted phase space. Also for this measurement jets are selected in the Breit frame, and in addition to the p_t^{rel} tag the lifetime tag is used. For this measurement it is concluded that also for DIS "the total cross section measurements are somewhat higher than the predictions.[...]the observed excess is pronounced at large muon pseudo-rapidities." Preliminary results for a ZEUS measurement using a fraction of the HERA II statistics, again using only the p_t^{rel} tag, are shown in figure 3.11. This time the jet selection is done in the laboratory

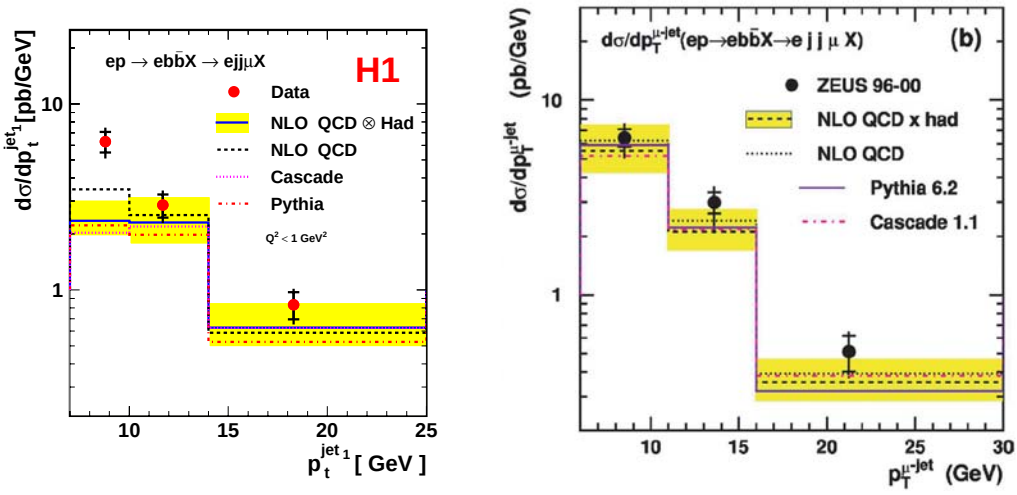

FIGURE 3.7: *Differential photoproduction cross section as a function of the jet transverse momentum for the highest transverse momentum jet for the H1 muon+jets HERA I measurement [8] (left) and the ZEUS muon+jets HERA I measurement [16] (right).*

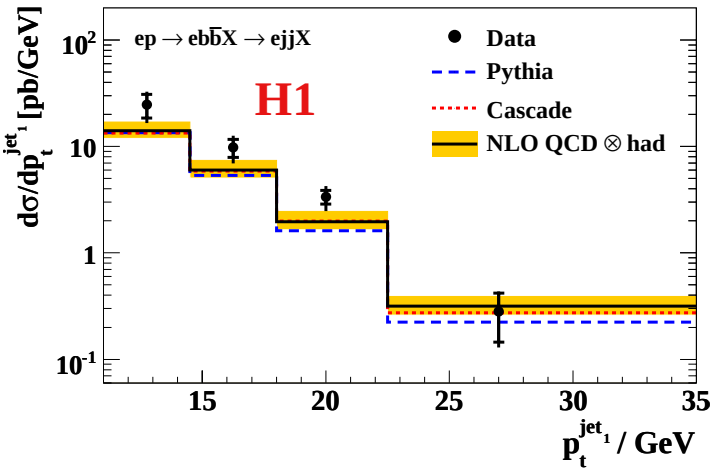

FIGURE 3.8: *Differential photoproduction cross section as a function of the jet transverse momentum for the highest transverse momentum jet for the H1 HERA I dijet analysis using the inclusive lifetime tag [7].*

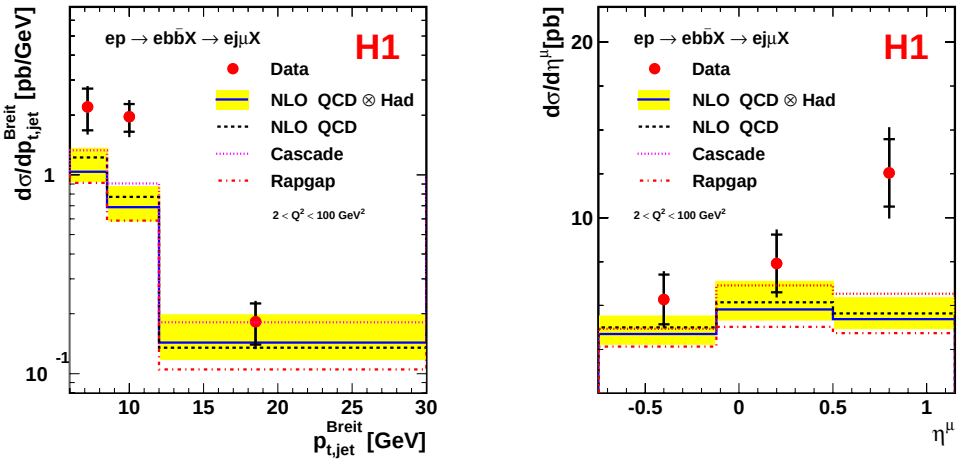

FIGURE 3.9: *Differential cross sections as a function of the jet transverse momentum and the muon pseudorapidity for the H1 HERA I DIS analysis [8] using a combination of the p_t^{rel} tag and the lifetime tag.*

frame and the measurement was extended to the forward region and supplemented by double differential cross sections. It is concluded that "the total visible cross section is 2σ higher than the NLO prediction. [...]In all distributions the data are described in shape by the MC and by the NLO QCD calculation."
For the analysis presented in this thesis the well established p_t^{rel} method is applied to a large fraction of the HERA II data. In comparison to the H1 HERA-1 analysis, the phase space is extended towards larger pseudorapidities and smaller momenta of the muon and the jet selection is performed in the laboratory frame. As a cross check, the analysis is repeated for the same phase space region as for the HERA I anaysis[1], selecting the jets in the Breit frame.

3.2.3 Fixed Target

Fixed target beauty production at HERA-B, where the proton beam halo interacts with wires of different materials, allows a measurement at threshold complementary to the collider experiments. The result of a combined measurement based on the decay channels $b\bar{b} \rightarrow J/\Psi X$ and $b\bar{b} \rightarrow \mu\mu X$ [5, 6] is shown in figure 3.12. The conclusion is that the combined result "is consistent with the latest QCD predictions [...] based on NLO calculations and resummation of soft gluons."

[1]Due to the modified SpaCal detector the lower part of the Q^2 phase space is only accessible by an extrapolation based on the Monte Carlo prediction

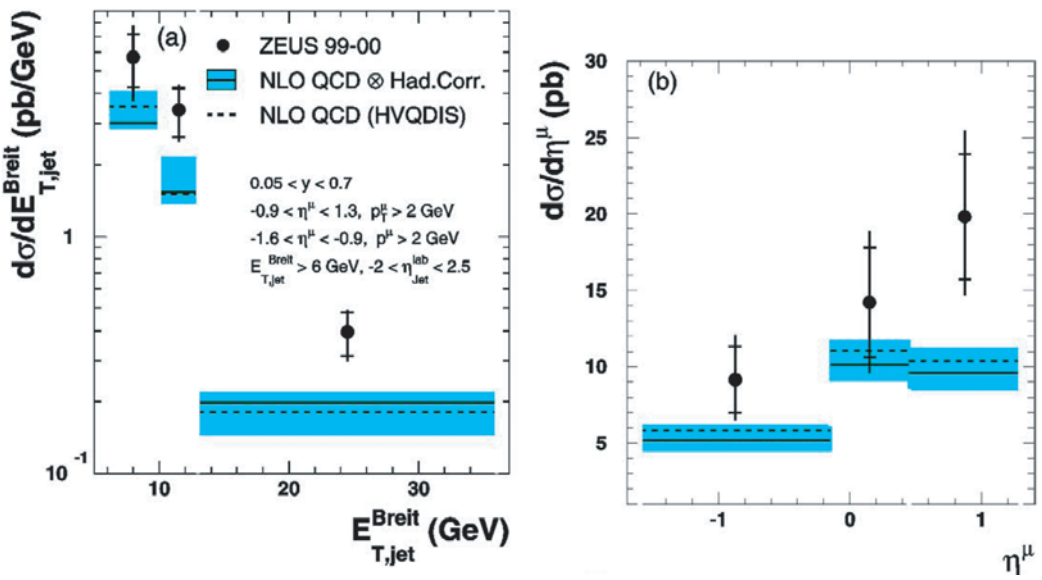

FIGURE 3.10: *Differential cross sections as a function of the jet transverse momentum and the muon pseudorapidity for the ZEUS HERA I DIS analysis [21] using the* p_t^{rel} *tag.*

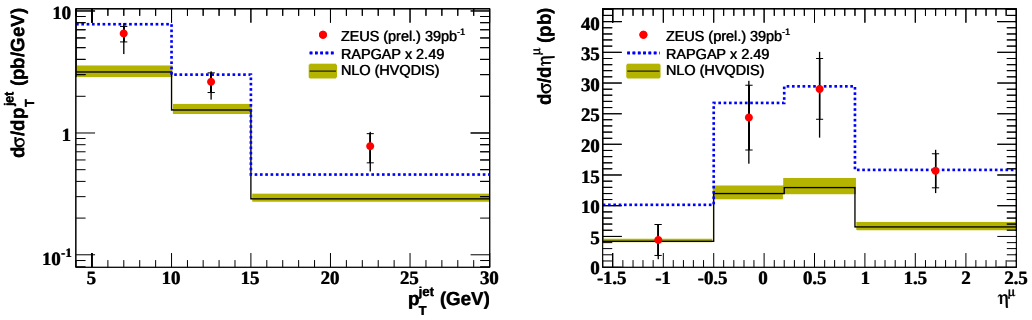

FIGURE 3.11: *Differential cross sections as a function of the jet transverse momentum and the muon pseudorapidity for the ZEUS HERA II DIS analysis [20] using the* p_t^{rel} *tag.*

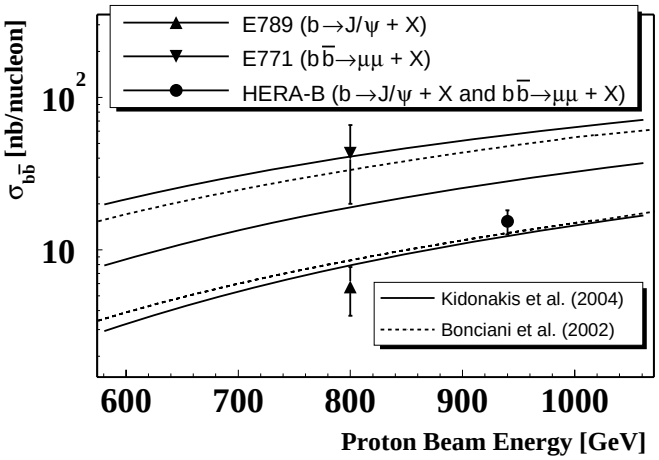

FIGURE 3.12: *Cross section for $b\bar{b}$ production as a function of the proton energy in fixed target collisions. Shown is the result of a combined HERA B measurement [5,6], lower energy Fermilab experiments [24, 78] and NLO predictions.*

3.3 Measurements at Other Colliders

3.3.1 $p\bar{p}$ Collisions

Beauty production in hadron collisions was first measured at the $Sp\bar{p}S$ collider at CERN. In [14, 15] the UA1 collaboration finds "good agreement with an [NLO] QCD prediction over the whole measured transverse-momentum range"(figure 3.13 left). Also this measurement is based on a p_t^{rel} fit to the muon decay spectrum (see figure 3.13, right). Over the last years the Tevatron collider is the main source for beauty quark production measurements in $p\bar{p}$ collisions. The measurements were performed at an centre of mass energy of 1800 GeV for Run I and 1960 GeV for Run II. For the final Run I measurements based on beauty hadron decays, both collaborations, D0 and CDF, come to the conclusion that the measurements do not agree very well with NLO predictions (see figure 3.14). For a measurement in the forward region [3], the D0 collaboration states that they "find that next-to-leading order QCD calculations underestimate b quark production by a factor of four in this region." For the measurement [2] CDF comes to the conclusion that "the differential cross section is measured to be 2.9 [...] times higher than the NLO QCD predictions with agreement in shape."
In contrast, a D0 measurement based on beauty jets [4] is well described by the NLO QCD prediction.
The results of a CDF measurement based on Run II data [1] are shown in figure 3.15. The data is in good agreement with QCD predictions using a fixed-order approach with a next-to-leading-log resummation, using updated determinations of proton parton densities and beauty quark fragmentation functions.

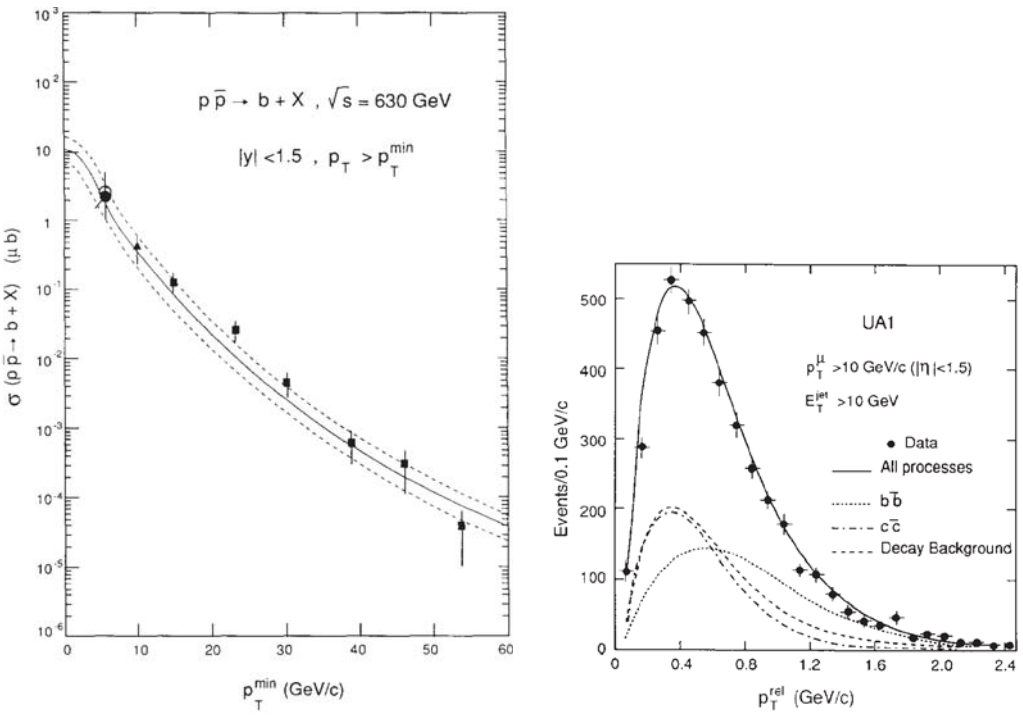

FIGURE 3.13: *Results from the UA1 measurement at the SpS collider (left) and the p_t^{rel} distributions used to measure the beauty fraction.*

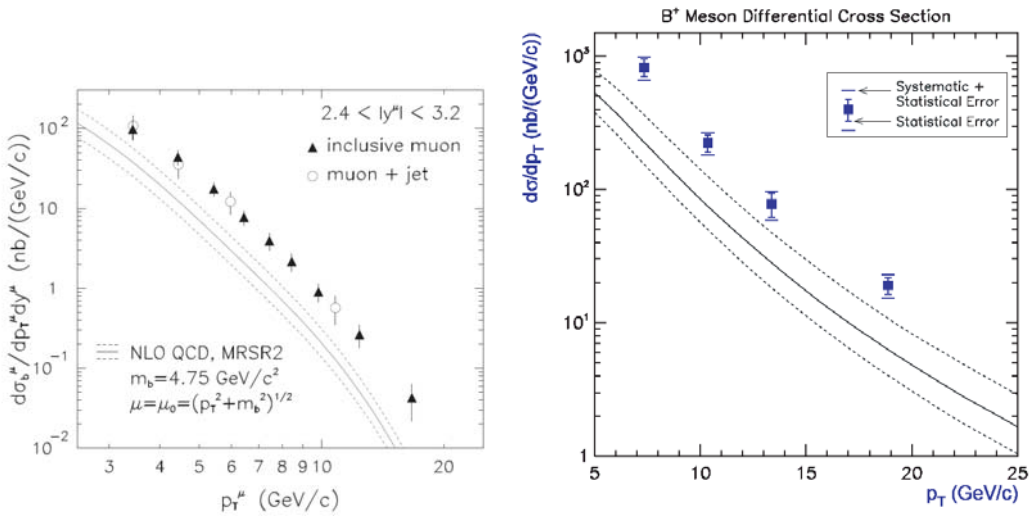

FIGURE 3.14: *Tevatron Run I measurements of beauty quark production from D0 (left) [3] and CDF (right) [2].*

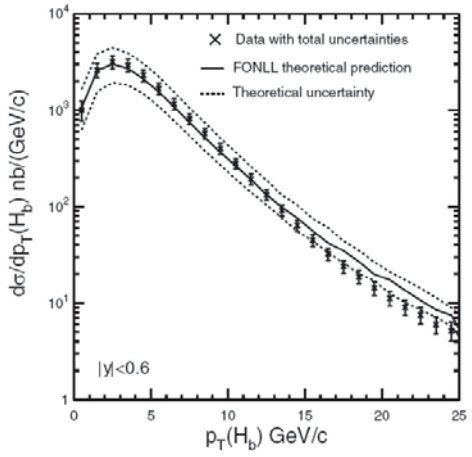

FIGURE 3.15: *Recent measurement of beauty quark production from CDF for Run II data [1]. The data is compared to improved QCD calculations.*

3.3.2 $\gamma\gamma$ Collisions

Beauty quark production in photon-photon collisions was measured at the LEP experiments. The L3 collaboration published final results based on the whole data sample, where events containing b quarks are identified through their semileptonic decay into electrons or muons [13]. The result is shown in figure 3.16 and compared to NLO QCD predictions. The results are "found to be in significant excess with respect to Monte Carlo predictions and next-to-leading order QCD calculations." The measurement is a factor of three, and three standard deviations, higher than the prediction.

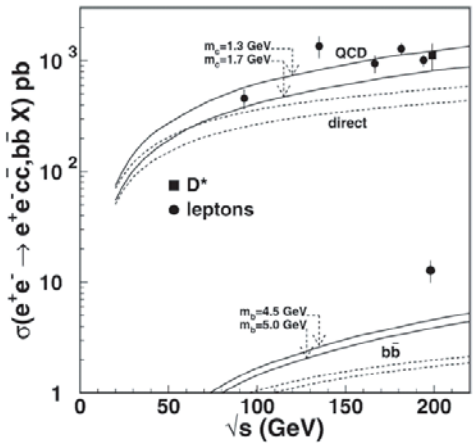

FIGURE 3.16: *Beauty quark production measurement at the LEP collider [13]. The data is compared to NLO QCD calculations. For completeness also measurements of charm quark production are compared to the predictions.*

Chapter 4

Event Reconstruction

This analysis is based on the reconstruction of the scattered electron[1] and the hadronic final state, in particular muons and jets. This will be discussed in this chapter in detail, focussing on the subdetectors and algorithms involved.

4.1 Identification and Reconstruction of the Scattered Lepton

The main detector for measuring the kinematics of the scattered lepton in the kinematic range of this analysis is the electromagnetic part of the SpaCal calorimeter. Due to the high granularity of the calorimeter, the scattered lepton deposits energy in several neighbouring cells, which comprise a cluster. The cluster having the highest energy is taken as the scattered electron, where only clusters with a minimum energy of 8 GeV and a maximal radius[2] of 4 cm are taken into account. The cell energies are calibrated using the double-angle method, which was introduced in [71] and [34] and has become the standard method to perform the electron calibration [66]. This method makes use of the fact that the kinematics of the scattered lepton is overconstrained and can be determined from the measurement of the hadronic final state.
The polar and azimuthal angle of the lepton with respect to the event vertex is determined from the cluster position[3] taking into account the position of the event vertex. In addition tracks measured from the BPC detector are extrapolated to the SpaCal. If the distance of the track impact point to the cluster centre is smaller than 4 cm, this extrapolated value is used. Finally beam tilt corrections are applied. This ensures that the angles are measured with respect to the beam axis which is tilted against the nominal axis.

[1] From now on only the term electron is used for electrons and positrons.

[2] The radius is defined using logarithmic weighting.

[3] The z position of the cluster is not measured directly but calculated from the cluster energy E_{cl} using the formula $z = 0.002 \cdot E_{cl} + 0.853 \log(2479 \cdot E_{cl})$. The parameters of this formula are determined from simulations of the longitudinal shower distribution.

4.2 Identification and Reconstruction of the Muon

The reconstruction of the muon kinematics is done using the information from tracks in the inner tracking chambers. The CMD, which is the outermost part of the H1 detector, is used to identify the muon. Muons in the energy range considered in this analysis are minimal ionising particles. In addition they do not produce electromagnetic or hadronic showers in the calorimeters (The average energy loss in lead is only about 10 MeV per traversed cm). The energy deposits are concentrated within a narrow cone around the muon track. Muons need an energy of about 1.5 GeV to pass the superconducting coil surrounding the calorimeter and reach the CMD. Here they loose an energy of about 90 MeV per iron plate.
For this analysis only muons are considered whose inner track fulfills certain quality criteria ("Lee West Tracks", [117]) and can be extrapolated and linked to the outer track with a minimal link probability. The latter is derived from the χ^2 value which is determined from the track parameters of both the inner and outer track and their covariance matrices. Details concerning this procedure as well as the reconstruction of inner tracks (inner chambers) and outer tracks (CMD) can be found e.g. in [106]. The track reconstruction will be outlined briefly in the following.

4.2.1 Track Reconstruction in the Inner Drift Chambers

In the **Central Jet Chamber** a track finding in the plane perpendicular to the beam axis is perfomed. This track finding is based on charge and drift time information of single hits. Triplets of hits are connected to curved tracks using a χ^2 fit. The curvature κ allows the determination of the muon momentum since the magnetic field is known. In the r-z-plane the z-position is determined from the charge division between the wire ends. In addition information from the COZ drift chamber is used to increase the resolution. The values determined for the track include the helix parameters κ, θ, ϕ, and z_0. θ and ϕ denote the track direction and z the position at the DCA, which is the point of closest approach to the event vertex. After the track reconstruction a vertex fit is performed yielding refined helix parameters. This leads to a momentum resolution of $\sigma_{p_t}/p_t = 0.005\ p_t/\mathrm{GeV} \oplus 0.015$.
Track segments of the radial and planar drift chambers of the **Forward Tracking Detector** are combined to tracks and fitted to the reconstructed vertex.
In the overlap region ($15^\circ \leq \theta \leq 25^\circ$) a combination of forward and central tracks is performed.

4.2.2 Track Reconstruction in the Instrumented Iron

Tracks in the Central Muon Detector are searched for using up to 16 wire layers and 3 pad layers (see section 2.5). A pattern matching is performed separately for the forward and central parts. Only patterns with a sufficient hit number and not matching to particle showers are considered as tracks. Inner tracks are extrapolated to the CMD, taking into account energy loss, multiple scattering and variations of the magnetic field. Then the extrapolated parameters are compared to the parameters

measured by the CMD using a χ^2 method. The following parameters of the iron track (outer track) are used:

- the z-coordinate of the first point on the iron track
- the azimuthal angle of the connection of the first measured point on the iron track to the event vertex
- the azimuthal angle of the reconstructed iron track

From the χ^2 value a linking probability is determined. Events with a low linking probability are rejected (see section 5.5).

4.3 Reconstruction of the Hadronic Final State

The reconstruction of the kinematics of the hadronic final state is based on **Hadronic Final State (HFS) Objects**. These are also input objects to the jet finding algorithm (see section 4.4). The HFS objects are constructed by a energy flow algorithm (**Hadroo2** [100]) making use of information from charged particle tracks and calorimetric energy clusters. Their respective resolution and overlap are taken into account, while double counting of energy is avoided [70, 99]. In the following the selection of input objects to the algorithm and the basic principles of the algorithm will be described.

4.3.1 Selection of Input Objects

Input to the algorithm are **tracks** and **clusters**. The tracks have to be well measured with the central detectors, see section 4.2 for the track reconstruction. Tracks are supposed to originate from a pion, the energy is given by

$$E_{track}^2 = p_{track}^2 + m_\pi^2, \tag{4.1}$$

the error is obtained from error propagation using the output of the track fit:

$$\frac{\sigma_{E_{track}}}{E_{track}} = \frac{1}{E_{track}} \sqrt{\frac{P_{t,track}^2}{\sin^4\theta} \cos^2\theta \sigma_\theta^2 + \frac{\sigma_{P_{t,track}}^2}{\sin^2\theta}}, \tag{4.2}$$

with σ_{P_t} and σ_θ being the corresponding errors on $P_{t,track}$ and θ.
The other input to the algorithm are clusters. They are built by a clustering algorithm from neighbouring cells after applying noise reduction and dead material corrections. Clusters can be classified as **electromagnetic** or **hadronic**. All clusters with at least 95% of their energy in the electromagnetic part of the calorimeter and with also 50% of it in the first two layers are defined as electromagnetic clusters [100]. Since the LAr calorimeter is non compensating, a reweighting of the corresponding cells has to be applied to hadronic clusters. Details on the cell selection, clustering and reweighting can be found e.g. in [90]. Finally a noise suppression is applied to the clusters by running several background finders. This includes the suppression of low energy isolated clusters, halo muons, cosmic muons and coherent noise.

4.3.2 Hadroo2 Algorithm

The Hadroo2 algorithm is a modified energy flow algorithm in the sense that both track and calorimetric information is used without a one-to-one attribution of tracks to individual clusters. The basic idea of the algorithm is to decide whether the track or the calorimeter clusters behind the track are preferred, i.e. better measured. If the track information is preferred, this information is taken to define the HFS object and the clusters are locked to avoid double counting.
Tracks are extrapolated to the surface of the calorimeter as a helix, inside the calorimeter a straight line extrapolation is performed. A calorimetric volume is defined by an overlapping volume of a 67.5° cone and two cylinders of radius 25 cm for the electromagnetic part and 50 cm for the hadronic part of the calorimeter. A calorimetric energy $E_{cylinder}$ is defined as the sum of all cluster energies within this volume. The expected relative error on the energy measurement in the calorimeter is estimated, only using the measured track energy, since the contribution of neutral particles to the cluster is not known:

$$\left(\frac{\sigma_E}{E}\right)_{LAr,exp.} = \frac{\sigma_{E,LAr,expectation}}{E_{track}} = \frac{0.5}{\sqrt{E_{track}}}. \tag{4.3}$$

The track measurement is preferred either if the track measurement is better compared to the expected calorimeter measurement,

$$\frac{\sigma_{E,track}}{E_{track}} < \frac{\sigma_{E,LAr,expectation}}{E_{track}}, \tag{4.4}$$

or the calorimetric energy is larger than the energy measured from the track,

$$E_{track} < E_{cylinder} - 1.96 \cdot \sigma_{E_{cylinder}}. \tag{4.5}$$

In the latter case one assumes calorimetric energy from neutral particles, upward calorimetric energy fluctuations are taken into account.
If the track measurement is preferred, clusters behind the track are locked to avoid double counting. The maximum locked energy is given by the calorometric energy $E_{cylinder}$, also in this case upward energy fluctuations with respect to the track energy are taken into account.
If the calorimetric energy is prefered, the HFS object is defined from this energy and the track is locked. The remaining clusters after treating all tracks are considered to be massless. They are assumed to originate from neutral hadrons with no measured track or charged particles with a badly measured track.
As discussed in [100], the calorimetric measurement is better than the track measurement in the central region for energies larger than 25 GeV. In this detector region the cluster contribution to the total hadronic transverse momentum is about 40%.

4.3.3 Treatment of Calorimetric Energy Deposition for Muons

Muons are part of the hadronic final state but as minimal ionizing particles subject to a special treatment. An **isolation criterium** is applied to the muons. A muon

is classified as **isolated** if the calorimeter energy in a cone around the extrapolated track is less than 5 GeV, but not larger than $p^{\mu} + 1$ GeV. The cone radius is 35 cm in the electromagnetic and 75 cm in the hadronic section of the LAr calorimeter. The muon fourvector is not altered, but depending on the isolation the clusters along the muon track in the calorimeter are treated differently. If the muon is isolated, those clusters are **locked** and are no longer visible for the HFS algorithm.[4] This avoids double counting of energy belonging to the muon. If the muon is not isolated, no locking of clusters is applied. This avoids locking of energy depositions of other particles which would lead to an underestimation of the jet energy. This method results in an overestimation of the jet energy for non isolated muons, which is corrected by applying the same algorithm for the simulated samples. As the calorimetric energy deposition of muons is not described very well the sensitivity of the algorithm to modifications concerning the isolation and locked energy has to be checked. This is described in more detail in section 6.6 where an estimation for the systematic uncertainty is given.

4.4 Jet Reconstruction

Jets on detector level are reconstructed by a jet algorithm, using the HFS objects and the muon as input. Jets are complex objects constructed to define and perform the measurement. Therefore the results of the measurement and the definition of the cross sections depend on the used algorithm. To correct detector level jets for detector effects like reconstruction efficiencies and to predict cross sections, the algorithm has to be applied on hadron level as well. It is also possible to apply the algorithm on parton level before hadronization corrections to obtain parton level cross sections. The requirement of a sound definition on these different levels implies that the construction of such an algorithm is a non trivial task. The Snowmass Convention [72] gives some basic properties such an algorithm has to fulfill. The algorithm has to be well defined on each level. From the experimental point of view the jets have to be easily measured from the hadronic final state. From the theoretical point of view this means that the jets have to be easily calculated from the partonic state. Furthermore there has to be a close connection between the jet distributions on detector level and on parton level. The experimental and theoretical requirements the algorithm has to fulfill are closely connected:

- The results of the algorithm have to be independent of the detector granularity, this means the angular resolution of the detector. Therefore the results should not depend on resolving two particles which are almost collinear. An analogue requirement has to be fulfilled on parton level, the result should not change when replacing one particle by two almost collinear particles. This reflects the fact that in perturbative QCD **collinear divergencies** are cancelled by virtual corrections.

[4] This locking is performed for clusters within a smaller **inner cone** of radius 25 cm and 50 cm for the electromagnetic and hadronic section, respectively.

- The results of the algorithm have to be independent from noise and thresholds of the individual calorimeter cells. The analogue requirement on parton level is the insensitivity to the emission of low energy particles. The resulting **infrared divergencies** are guaranteed to be cancelled in perturbative QCD by virtual corrections.

Two types of algorithms are used:

- Cone algorithms define jets on a simple geometric basis by maximizing the energy flow into a cone with a fixed radius $R = \sqrt{\Delta\eta^2 + \Delta\Phi^2}$, where η is the pseudorapidity[5] and ϕ the angle position of the particle. Algorithms of this type are used for hadron-hadron collisions. Despite the advantage of a simple intuitive interpretation and simple implementation, they have several disadvantages. The main problem is the treatment of overlapping jets since the assignment of particles to jets is ambiguous.
- Clustering algorithms find pairs of particles based on a closeness criteria and merge them to pseudoparticles in an iterative procedure. These pseudoparticles are the constituents of the jets. Jets created this way have no geometrical definition but the advantage of an unambigous assignment of particles to jets. Algorithms of this type have been used for e^+e^- collisions and are also used for hadron collisions today after solving problems of the treatment of the hadron remnant and underlying events.

The algorithm used for this analysis is the longitudinally invariant k_T-clustering algorithm [44], which will be described in the following section in more detail.

4.4.1 Longitudinally Invariant k_T-Clustering Algorithm

This is the algorithm most frequently used at HERA. It starts with a list of particle fourvectors and proceeds as follows:

1. For each pair of particles a closeness parameter $d_{i,j}$ is calculated, where

$$d_{i,j} = \min[p_{t,i}^2, p_{t,j}^2] \left[(\eta_i - \eta_j)^2 + (\Phi_i - \Phi_j)^2\right] \tag{4.6}$$

   and for each particle a closeness to the beam particles is defined by $d_i = p_{t,i}^2$. For small opening angles the "distance" $d_{i,j}$ is proportional to k_t, which is the momentum of the softer particle to the axis of the harder:

$$\min[p_{t,i}^2, p_{t,j}^2](\Delta\Phi^2 + \Delta\eta^2) \approx k_t^2. \tag{4.7}$$

2. The minimum d_{min} of all values $d_i, d_{i,j}$ is determined, if $d_{min} = d_{i,j}$ the two particles are combined to form a new one, if $d_{min} = d_i$ then that particle is removed from the list and added to the list of *protojets*.
3. New values for $d_i, d_{i,j}$ are determined and step 2 is repeated. This iteration continues until all particles are assigned to protojets.

[5]The pseudorapidity is defined as $\eta = -\ln(\tan\frac{\theta}{2})$, where θ is the polar angle of the particle.

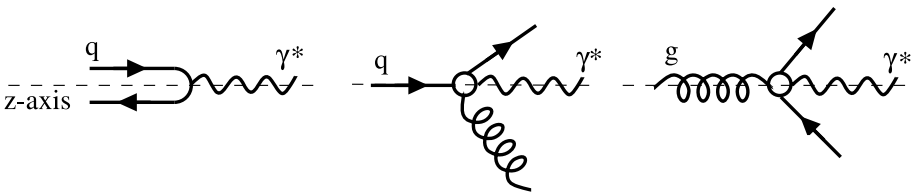

FIGURE 4.1: *Quark Parton Model (left), QCD Compton (middle) and Boson Gluon Fusion (right) processes in the Breit frame (from [47]).*

The way how two objects are merged is defined by the **recombination scheme** which is a prescription how to calculate the parameters of the new particle from the two merged particles. For this analysis the **p_t-weighted recombination scheme** is used:

$$\eta_k = \frac{1}{p_{t,k}}(p_{t,i}\eta_i + p_{t,j}\eta_j), \tag{4.8}$$

$$\Phi_k = \frac{1}{p_{t,k}}(p_{t,i}\Phi_i + p_{t,j}\Phi_j), \tag{4.9}$$

$$\text{with } p_{t,k} = p_{t,i} + p_{t,j}. \tag{4.10}$$

4.4.2 Jets in the Breit Frame

In the **Breit frame** [60] for the lowest order process $\gamma^* q \rightarrow q'$ (Quark Parton Model) there is no energy transfer between the virtual photon and the initial state quark. They collide head on and the quark momentum is reversed (see figure 4.1). If the z-axis is chosen such that $q = (0, 0, 0, -Q)$, the incoming quark has the four momentum $p = (Q/2, 0, 0, Q/2)$ and the outgoing scattered quark has the four momentum $p' = (Q/2, 0, 0, -Q/2)$. The transformation to the Breit frame requires rotations and a boost and is explained in detail in appendix B.
The Breit frame is an appropriate frame for the investigation of leading order QCD processes like boson gluon fusion and QCD Compton. Jets reconstructed from these processes usually have large p_t, whereas for quark parton model processes there is no transverse momentum in either the initial or final state on parton level and only limited transverse momentum on hadron level due to fragmentation.
Despite the advantage of a better separation of BGF processes from QPM processes, the jet selection is performed in the laboratory frame for this analysis. This selection results in a higher statistics event sample and allows a measurement of the beauty contribution to the proton structure function F_2. The selection of jets in the Breit frame is performed as a cross check to compare to published results (see section 6.6).

4.5 Kinematic Variables

This measurement is defined in terms of the properties η and p_t of the jet and muon and in addition in terms of the event variables x, Q^2 and y which are related via

$Q^2 = x \cdot y \cdot s$.
The quantities Q^2 and y can be determined from the kinematics of the scattered electron, this is called the **electron method**:

$$y_e = 1 - \frac{E'_e(1 - \cos\theta_e)}{2E_e} \tag{4.11}$$

$$Q^2_e = 2E'_e E_e(1 + \cos\theta_e) = \frac{E'^2_e \sin^2\theta_e}{1 - y_e}. \tag{4.12}$$

Here E'_e and θ_e denote the energy and polar angle of the scattered electron.
The resolution of the y_e measurement is given by

$$\frac{\delta y_e}{y_e} = \left(\frac{1}{y_e} - 1\right) \frac{\delta E'}{E'} \oplus (\frac{1}{y_e} - 1) \cot\left(\frac{\theta_e}{2}\right) \delta\theta_e. \tag{4.13}$$

For $y > 0.3$ the resolution is dominated by the resolution of the energy measurement ($\delta E'_e/E'_e < 4\%$). Due to the $1/y_e$ term the resolution gets worse for smaller y. One advantage of the HERA kinematics is that the measurement of the DIS variables is overconstrained and can be performed by using the properties of the hadronic final state alone. When using conservation of energy and longitudinal momentum,

$$(E^{in}_P - P^{in}_{z,P}) + (E_e - P_{z,e}) = 2E_e = E'_e(1 - \cos\theta_e) + \sum_a E_a(1 - \cos\theta_a), \tag{4.14}$$

y can be expressed in terms of the hadronic final state alone:

$$y_h = \frac{2E_e - E'_e(1 - \cos\theta_e)}{2E_e} = \frac{\Sigma}{2E_e}, \tag{4.15}$$

where $\Sigma = \sum_a E_a(1 - \cos\theta_a)$ and the sum is performed over all final state particles neglecting their masses. This method is called **hadron method**, it was introduced by Jacquet and Blondel [76].
The resolution of y reconstructed by the hadron method is given by the hadronic energy resolution:

$$\frac{\delta y_h}{y_h} = \frac{\delta\Sigma}{\Sigma}. \tag{4.16}$$

This method can also be used for lower values of y since the resolution does not diverge at low y.
The reconstruction of y can be further improved. Emissions of collinear real photons from the incoming electron before the interaction with the proton (QED initial state radiation) lead to large corrections because in equation (4.15) the electron energy is fixed to E_e. This can be avoided by replacing E_e by the "measured" incoming electron energy using the relation given by (4.14):

$$y_\Sigma = \frac{\Sigma}{\Sigma + E'_e(1 - \cos\theta_e)}. \tag{4.17}$$

This **sigma method** [32] has a similar resolution as the hadron method.

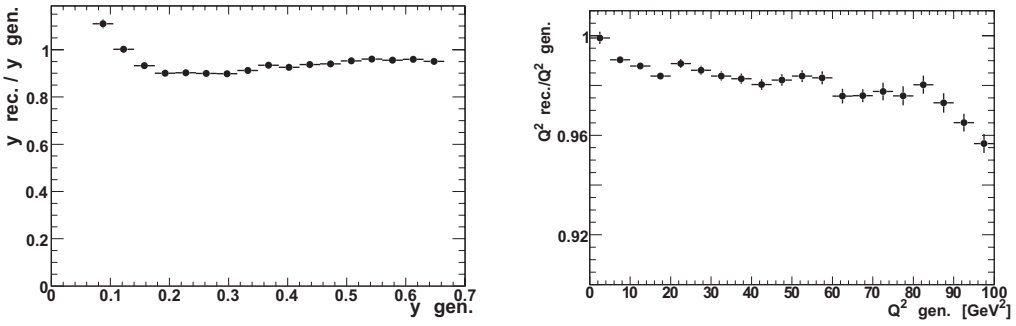

FIGURE 4.2: *Ratio of reconstructed to generated values as a function of the generated value for y_Σ (left) and Q_e^2 (right).*

To summarize, for this analysis a combination of the electron method and the sigma method is used, Q^2 is reconstructed using the electron method and y using the sigma method due to its better resolution at low y and its insensitivity to radiative effects. As a cross check the analysis is repeated using the electron method for the reconstruction of y as well (see section 6.6). The Bjorken scaling variable x is given by

$$x = \frac{Q_e^2}{y_\Sigma \cdot s}. \tag{4.18}$$

The resolution plots for Q_e^2 and y_Σ are shown in figure 4.2.

Chapter 5

Event Selection

This measurement is based on the selection of a **heavy quark enriched sample** where beauty, charm and light quarks contribute with respective fractions of 25%, 55% and 20% [8]. The exact measurement of the beauty fraction and the determination of detector correction factors applied to the data requires a precise description of the data using simulated Monte Carlo samples. In the case of discrepancies additional corrections or the introduction of systematic errors have to be considered.
This chapter is organized as follows: first the requirements the analysed data sample has to fulfill are discussed, including the online trigger selection and the corresponding correction factors. After this the signal and background Monte Carlo samples are presented. Finally the selection cuts that are applied both to the data and the Monte Carlo samples are discussed in detail, including the selection of DIS events, muon events and jet events. **Control distributions** are shown for each selection cut.

5.1 Data Sample

Data from the years 2005-2007, taken at a center of mass energy of 320 GeV, is analysed. The analysed part of the HERA II data has to fulfill several requirements on the selected runs, the status of subdetectors and the online trigger selection. This will be discussed in the following. The data sample consists of three different run periods, the corresponding run ranges and luminosities are summarized in table 5.1. The total luminosity of the analysed data is 285.1 pb^{-1}.

Run Period	Run Range	Luminosity [pb^{-1}]
2005 e-	401617-436893	101.4
2006 e-	444094-466997	54.3
2006/07 e+	468531-492541	129.4

TABLE 5.1: *Different run ranges and corresponding luminosities.*

s 61: ((SPCLe_IET>2)||SPCLe_IET_Cen_3)&&(FTT_mul_Td>0)&&VETO &&CIPVETO	
SPCLe_IET>2	Spacal inclusive electron trigger, outer part
SPCLe_IET_Cen_3	Spacal inclusive electron trigger, central part
FTT_mul_Td>0	at least one FTT L1 track with $p_t > 900$ MeV
VETO	Veto wall, Time of flight detectors
CIPVETO:(CIP_mul>11)&&(CIP_sig==0)	CIP veto

TABLE 5.2: *Trigger elements of subtrigger s61*

5.1.1 Run Selection and Detector Status

A **run selection** is applied to the data, taking into account the running conditions of the machine and the detector. Only runs with an assigned quality of **good and medium** are included in the data sample, in addition several run ranges are excluded due to problems and malfunctions of detector compoments relevant to the analysis. The list of **excluded runs** is summarized in appendix A.
In addition detector status information which is stored every 10 seconds is used. Only events where all relevant subdetectors are fully functional are selected. The high voltage status of the sub detectors has to be controlled since a lower than the nominal value leads to a significant loss of efficiency. The relevant subdetectors are the forward and central tracking chambers, the SpaCal calorimeter, the muon system, the luminosity system, Time of Flight detectors and the Fast Track Trigger. The condition of the CIP detector is not taken into account for the run selection as it is only used as a veto condition.
The run ranges and the corresponding corrected luminosites are summarized in table 5.1[1].

5.1.2 Trigger selection

The data sample and its luminosity is defined by the applied online selection criterions (trigger condition). The used data sample was triggered by the DIS subtrigger s61, which requires a scattered electron detected by the backward calorimeter (SpaCal) and in addition a high momentum track measured by the central drift chambers and found online by the Fast Track Trigger. Background events originating from beam gas events are rejected online using the timing condition of the SpaCal and additional veto conditions from the Veto Wall, different time of flight detectors and CIP trigger elements. The subtrigger elements are summarized in table 5.2. The online selection of DIS events is only fully efficient for electron energies above 17 GeV. Therefore a correction has to be applied for lower energy electrons. The energy dependence of this subtrigger was measured using a sample of events containing an offline selected scattered electron detected by the SpaCal but triggered independently. The fraction of events fulfilling the online SpaCal condition

[1]The given run range for the 2005 e^- does not include the period before the FTT was active. For this period the track trigger condition is not fully efficient and has to be investigated.

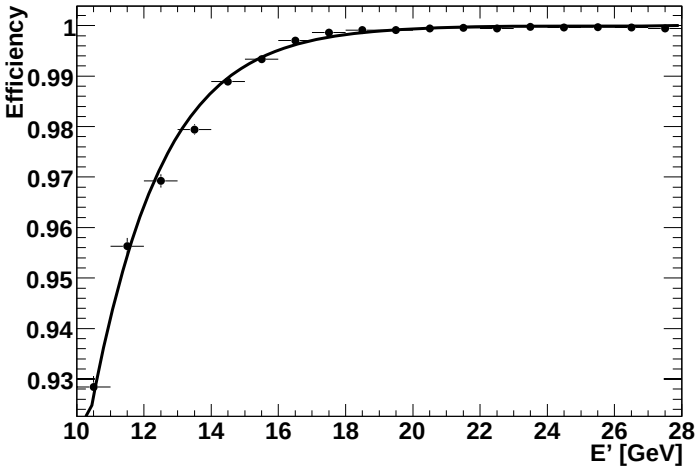

FIGURE 5.1: *Energy dependence of the SpaCal trigger efficiency.*

as well determines the efficiency as shown in figure 5.1. A Fermi function of the form $1/(1+\exp(-a \cdot E' + b))$, where a and b are free parameters, is fitted to these data points. This additional detector inefficiency was incorporated to the analysis by applying a weight to each simulated event according to the measured electron energy.
The online track condition does not lead to an inefficiency. This was checked using an independently triggered data sample. The loss of events due to the additional CIP veto condition, which was applied from run 474479 on, is negligible.

5.2 Monte Carlo Samples

The simulated event samples, used to determine detector efficiencies and acceptances and to describe signal and background distributions, are generated using RAPGAP as the default event generator, supplemented by the Heracles program [23] to generate radiative events.
The luminosity of the **inclusive event samples**, generated using the full mode IPRO 1200 [82], including light flavour, charm and beauty events, corresponds to about 6 times the data luminosity (see table 5.3). The kinematic range for the event generation is restricted to $Q^2 > 1$ GeV^2 and $y > 0.01$. Heavy quarks are produced in the massive mode, the decision whether to generate a quark parton model process or a first order α_s process is based on the cross section for the particular process at a given x and Q^2. The charm and beauty quark masses are set to 1.5 GeV and 4.75 GeV, respectively. The GRV LO [65] sets for the parton density functions are used. The scale is set to Q^2 for light flavour events and $Q^2 + m_Q^2$ for heavy quark production, where m_Q is the heavy quark mass. Lund String fragmentation is used, with the Peterson fragmentation function for light quarks and the Lund-Bowler frag-

MC type	runperiod	number of events	$\mathcal{L}$ $[pb^{-1}]$
inclusive	$05e^-$	$20.4 \cdot 10^6$	~ 500
inclusive	$06e^-$	$9.5 \cdot 10^6$	~ 220
inclusive	$06/07e^+$	$39.1 \cdot 10^6$	~ 970
beauty	$05e^-$	510054	850.8
beauty	$06e^-$	1089269	1701.0
beauty	$06/07e^+$	254404	425.8

TABLE 5.3: *Monte Carlo sets: given are the number of events that are reconstructed and simulated and the luminosities for the different run periods.*

mentation function for heavy quarks (see section 1.6). Due to the large cross section only a fraction of the generated events is simulated: events that do not contain at least one jet with a minimum transverse momentum of 4 GeV and a charged particle with transverse momentum of at least 1.9 GeV in the range $10° < \theta < 165°$ are rejected. In total about 69 Mio. events are simulated.
The luminosity of the **beauty event samples**, generated using mode IPRO 1400 [82], corresponds to about 10 times the data luminosity (see table 5.3), where the kinematic range is again restricted to $Q^2 > 1$ GeV^2 and $y > 0.01$. The MRST 2004FF4lo [96] set of parton density functions is used. The beauty mass is set to 4.75 GeV, the scales are set to $Q^2 + m_b^2$ and the Lund string fragmentation with the Lund-Bowler fragmentation function is used. Also for the beauty sample only a fraction of the generated events is simulated. At least one charged particle with a minimum transverse momentum of 1.9 GeV in the range $10° < \theta < 165°$ is required. No muon is demanded to allow fake muon studies. In total about 1.9 Mio. events are simulated.

5.2.1 Background Sources

Each selected event requires the detection of a muon candidate. If the muon arises from the decay of a hadron or τ-lepton, but no beauty hadron is produced, the event is regarded as a background event. The muon candidate of a background event may either be a real muon or a misidentified hadron. In the case of a real muon this may come from a charm quark decay or from the decay of a light hadron, usually a pion or a kaon, which are predominantly produced. Almost every pion decays into a muon and a neutrino (the branching fraction is almost 100%). The branching fraction the decay of a kaon into a muon and a neutrino is $(63.43 \pm 0.17)\%$ [58]. Due to the large decay lengths $c\tau$ (7.8 m for pions and 3.7 m for kaons), these particles are usually stopped inside the LAr calorimeter before decaying. Because of the abundance of these particles and the large branching fractions, light hadrons that decay during the passage through the detector volume in the inner detector are an important contribution to the background (**inflight decays**).
The other important contribution to the background are misidentified hadrons. This source of background can be further distinguished:

- The hadrons that are interacting in the calorimeter do not necessarily deposit their entire energy inside the calorimeter. Energy leakage passing some iron layers may lead to the misidentification of these hadrons (denoted as **punch through**).

- Hadrons may reach the muon detector without strongly interacting inside the calorimeter volume. The maximum probability for this is 0.6%, depending on the polar angle [97]. These hadrons contribute to the background because the muon system in some cases falsely identifies the resulting hadronic showers as muons. This contribution is denoted as **sail through** background.

Misidentified hadrons (punch through, sail through) and inflight decays are summarized as **fake muons**. According to the Monte Carlo simulation, for about 21% of the selected charm events and about 18% of the selected beauty events, the selected muon candidate is a fake muon, and for about 30% of the selected light flavour events the selected muon comes from an inflight decay.

5.3 Z Vertex Distribution

A precise measurement of the kinematic variables and modelling of the detector acceptance requires a well described distribution of the z position of the event vertex. The longitudinal bunch structure of the protons is reflected in a Gaussian z vertex distribution. A cut on the minimal distance of the z position of the event vertex to the nominal vertex is applied ($|z_{vtx}| < 35$ cm). Events not fulfilling this cut are most probably background events, e.g. due to beam gas interactions. The z vertex distribution is on purpose simulated broader than the data distribution, and the average z vertex position is different for the simulation. The widths and median values of the z vertex distributions are determined from the simulated distributions and summarized in table 5.4. The simulated distributions are reweighted individually for each run period. The reweight factor is determined from the ratio of the Gaussian functions obtained from the fits which are evaluated for each event. Both the reweighted and non reweighted z vertex distributions are compared to the data distributions in figure 5.2, where all selection cuts as described in the following sections are applied. As for all control plots presented in the following, the beauty fraction is set to 24%, which is the beauty fraction for the total sample as obtained from the measurement (see section 6.3). The reweighting leads to an improvement of the description.

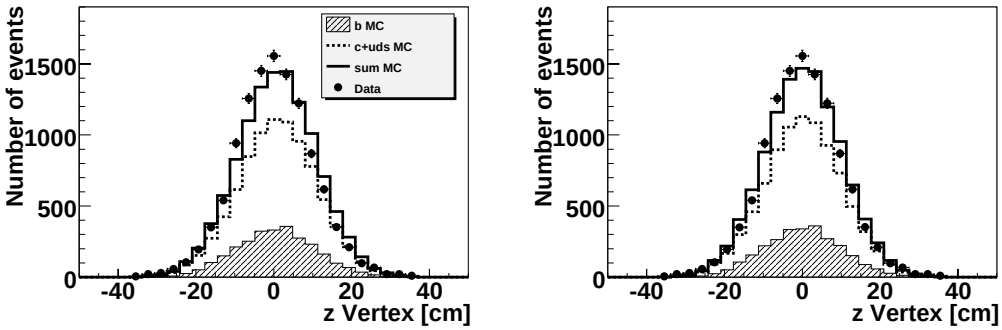

FIGURE 5.2: *Comparison of the simulated z vertex distributions to the data before (left) and after (right) reweighting.*

Run Period	Data		Monte Carlo	
	σ_z [cm]	μ_z [cm]	σ_z [cm]	μ_z [cm]
$05e^-$	10.01	0.57	10.33	1.34
$06e^-$	9.99	0.31	10.10	0.07
$06/07e^+$	9.20	-0.40	9.49	-0.55

TABLE 5.4: *Parameters of the z vertex distributions for the different run periods for data and Monte Carlo as obtained from a Gaussian fit. The Monte Carlo parameters are determined from the beauty sample which do not differ to the inclusive sample within the errors.*

5.4 Selection of DIS Events

The polar angle of the scattered electron is required to be larger than 155°, ensuring a reconstruction by the backward calorimeter (SpaCal) and avoiding the overlap region with the LAr calorimeter. For efficient triggering the electron energy has to be larger than 10 GeV. Misidentified electrons, which lead to **photoproduction background** in the sample, are rejected by requiring a cluster radius smaller than 4 cm because hadronic clusters are usually broader. As shown in figure 5.3 the distribution is shifted towards smaller values for the simulation, but otherwise described well in shape. Possible remaining photoproduction background is rejected by a cut $E - p_z > 45$ GeV, with

$$E - p_z = \sum_h E_a(1 - \cos\theta_a), \tag{5.1}$$

where a summation over the whole final state is done. For photoproduction events, where the scattered electron is not detected but a hadron misidentified as an electron, smaller values of $E-p_z$ are measured. The distribution, which peaks at 55 GeV due to momentum conservation, is shown in figure 5.3. A loss of hadrons and of photons from initial final state radiation in the backward direction leads to a broad asymmetric distribution.

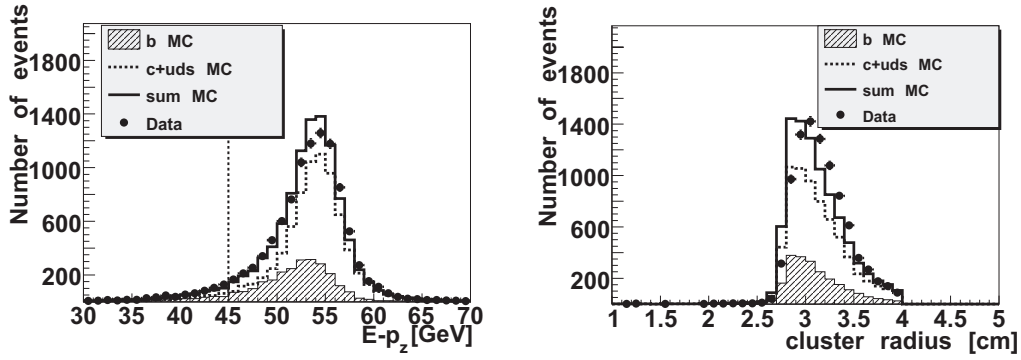

FIGURE 5.3: *Control distributions for $E - p_z$ and the cluster radius. For the Monte Carlo distribution the contribution from beauty quarks is fixed to* 24.6%. *The $E - p_z$ cut applied for the selection is indicated by the dashed line.*

In addition, several **fiducial cuts** have to be fulfilled:

- In the course of the HERA II upgrade program the beampipe was modified and focussing magnets had to be inserted within the detector region. This implied modifications like a new elliptical shape of the beam pipe and a larger SpaCal hole, where the center is shifted horizontally with respect to the nominal beam axis and the center of the H1 coordinate system. At the SpaCal edge the electron energy and scattering angle cannot be measured correctly since the shower is only partly contained in the SpaCal. Therefore the inner SpaCal region, which

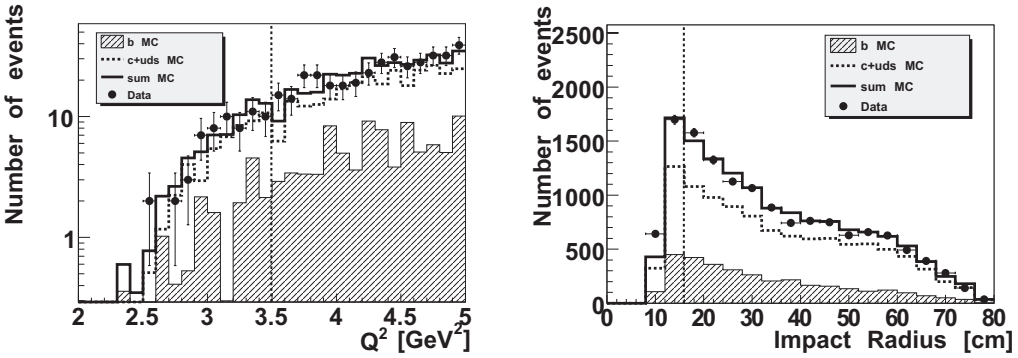

FIGURE 5.4: *Q^2 distribution for small values of Q^2 and impact parameter distribution for the inner SpaCal region, where the contribution from beauty quarks is fixed to 25% for the Monte Carlo distribution. For the Q^2 distribution the radial cut is applied, for the impact parameter distribution no lower Q^2 cut is applied. The data is compared to the Monte Carlo simulation. The cuts used for the analysis are indicated as dashed lines.*

corresponds to low Q^2 events, is not very well described by the Monte Carlo simulation. The shift of the SpaCal hole leads to an asymmetric acceptance as a function of Q^2.

To avoid these problems, a **radial cut** is applied, and only clusters with a minimal radial distance of 16 cm are accepted[2]. This distance is determined with respect to the intersection of the electron beam with the SpaCal plane, taking into account a possible beam tilt (**beam coordinates**)[3]. This ensures a symmetric acceptance and allows for a lower Q^2 cut of 3.5 GeV^2. The radial cluster distribution and the distribution for low values of Q^2 between 2 GeV^2 and 5 GeV^2 are shown in figure 5.4. Both distributions are well descibed by the Monte Carlo simulation. The loss of acceptance due to the radial cut is clearly visible for the Q^2 distribution. No events below 2.5 GeV^2 pass the selection. To avoid too large correction factors, a lower Q^2 cut of 3.5 GeV^2 is applied. For HERA I low Q^2 DIS analyses a lower cut of 2 GeV^2 was usually applied. The analysis is stable with respect to variations of this cut. The radial cut was modified by an amount of ± 0.5 cm, the cross section deviation obtained this way is negligible.

- A fraction of the inner SpaCal region is hit by the synchrotron radiation fan of the electron beam. The corresponding cells are taken out of the trigger. Therefore these cells are excluded from the selection by applying a **box cut** which covers the corresponding SpaCal region. Also in this case the coordinates

[2]This radial cut is much more conservative than the cut applied in [29], where the distance of the cluster to the SpaCal center has to be larger than 12 cm. For that analysis a larger Q^2 cut of 5 GeV^2 was chosen to ensure a symmetric acceptance.

[3]Technically this is done by recalculating the position of the cluster using the angular parameters of the scattered electron which are corrected for beam tilts.

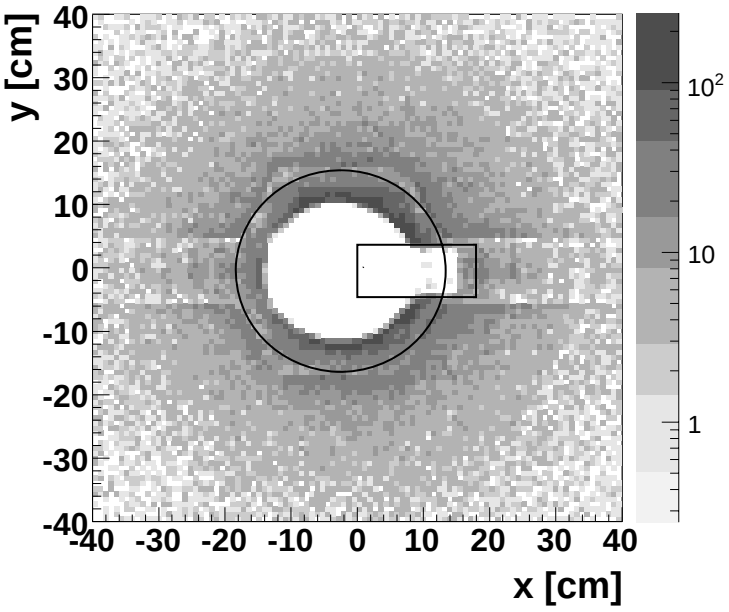

FIGURE 5.5: *Distribution of the reconstructed impact position of electrons in the SpaCal plane for data events. No fiducial cuts are applied. The circle and box applied in the selection are shown. Additional cell cuts are not shown. Due to reconstruction artefacts the shadow of the BPC is visible.*

for this cut are defined in beam coordinates.

- Additional **cell cuts** are applied. Some cells do not deliver trigger signals due to electronic problems, others cannot be used for the energy measurement due to a defect photomultiplier. An investigation for these problematic cells for different run periods was done in [29] and [94]. All these cells are excluded from the selection.[4]

The distribution of impact points for the scattered electron in the SpaCal plane for data events is shown in figure 5.5. The SpaCal hole, the area which is taken out of the trigger and the increase of selected events towards the inner region are clearly visible. The radial and the box cut are also depicted.
Control plots for all relevant distributions are shown in figures 5.7 and 5.8. In addition to the DIS selection cuts the muon and jet selection cuts as explained in the following sections are applied as well. For all plots the contribution from beauty quarks is fixed to 24%, as measured from the data (see section 6.3.3). The Monte Carlo distributions are normalized to the number of data events.
The polar angle of the scattered electron is reweighted since the distribution does not

[4]In the case of a defect photomultiplier it is demanded that clusters of neighbouring cells have a minimum distance of 1 cm to the defect cell to achieve a good description of the acceptance by the simulation.

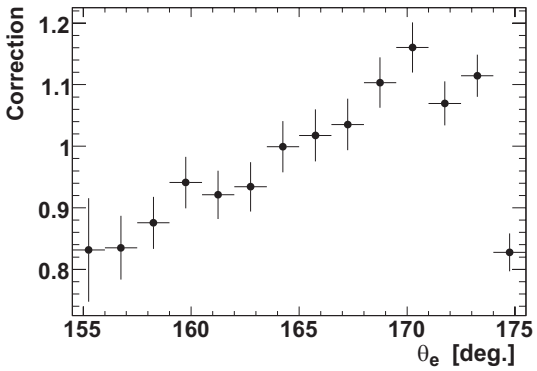

FIGURE 5.6: *Reweight factor applied to the Monte Carlo simulation as a function of θ_e.*

cut	value
Scattering angle	$\theta_e > 155°$
Electron energy	$E' > 10$ GeV
Cluster radius	< 4 cm
Impact radius	> 16 cm
Virtuality	$3.5 < Q^2 < 100$ GeV^2
Inelasticity	$0.1 < y_\Sigma < 0.7$

TABLE 5.5: *DIS selection cuts. The cuts that define the kinematic range of this analyis are in bold letters.*

describe the data very well. This distribution is reweighted by applying a bin-wise factor that is determined from the comparison of this distribution for data and the inclusive Monte Carlo sample. This reweighting factor as a function of θ_e is shown in figure 5.6. This reweighting leads to an improvement for Q^2 and E', as shown in figure 5.7, where all distributions are shown before and after reweighting.
In figure 5.9 the azimuthal angular distribution of the scattered electron is shown, which is flat and well described by the Monte Carlo simulation.
The y distribution is not described very well for low y (see figure 5.9, left). Since this variable is measured from the hadronic final state (see section 4.5), a reweighting of the pseudorapidity distribution of the muon as discussed in section 5.5 leads to a significant improvement (see figure 5.9, right). The $\log x$ distribution which is measured from Q^2 and y (see section 4.5) is shown in figure 5.10. Also this distribution is well described by the Monte Carlo simulation.
All DIS selection cuts are summarized in table 5.5.

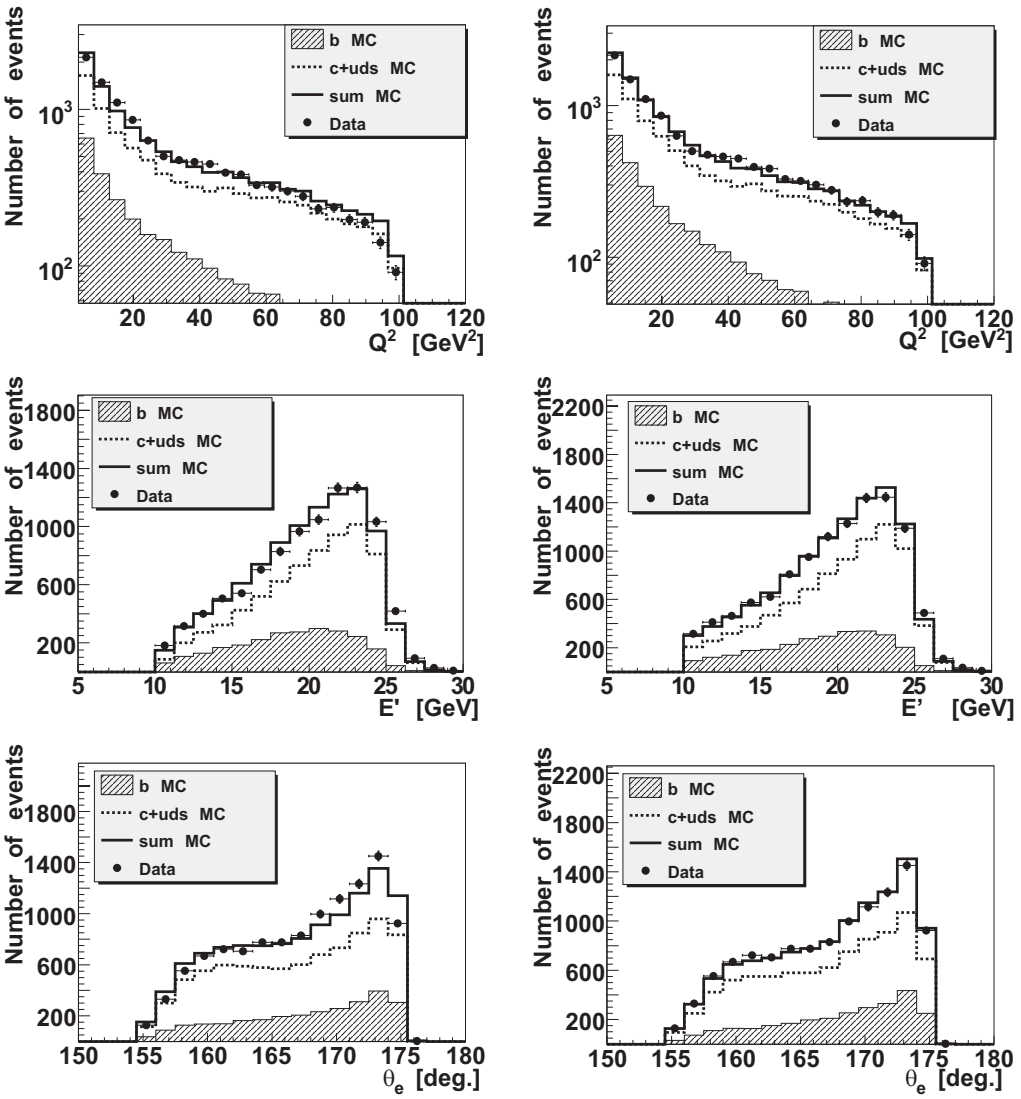

FIGURE 5.7: *Control distributions for variables determined from the scattered electron. The cuts applied for the selection are indicated as dashed lines. The plots are shown before (left column) and after (right column) reweighting in θ_e.*

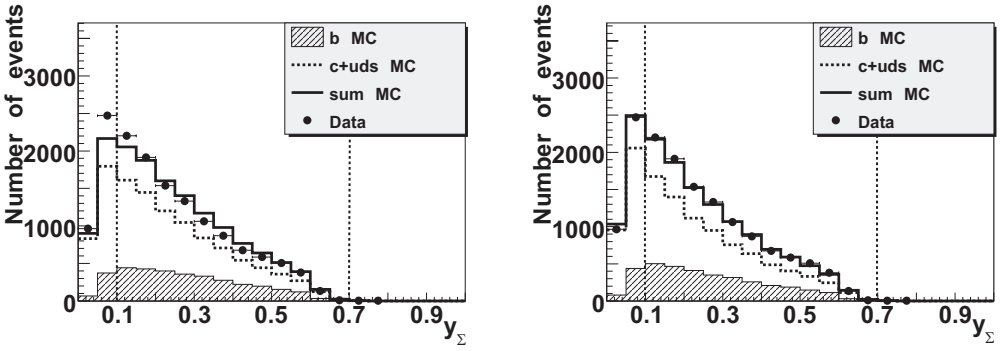

FIGURE 5.8: *Control distribution for the variable y, before (left) and after (right) reweighting in η^μ. The cuts applied for the selection are indicated as dashed lines.*

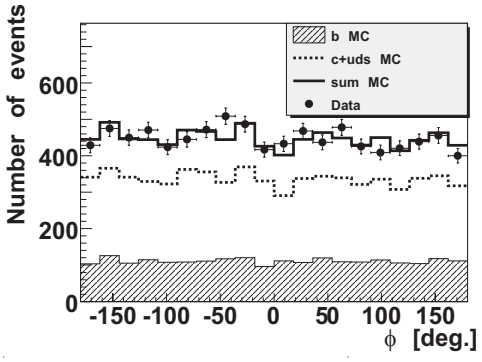

FIGURE 5.9: *ϕ distribution of the scattered electron.*

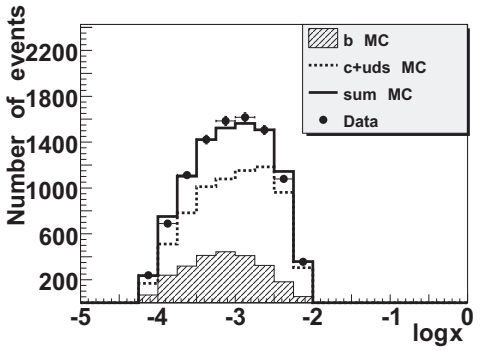

FIGURE 5.10: *Distribution of the Bjorken scaling variable.*

5.5 Selection of Muons

As explained in section 4, muons have to be identified as **iron muons** by the outer central and forward muon detector (**outer track**). This track has to be linked with a certain probability to an **inner track** measured by the central and forward tracking chambers. The muon is required to have a minimum transverse momentum of 2 GeV, the allowed pseudorapidity range is $-0.75 \leq \eta\mu \leq 2$, which corresponds to an angular range $15.4^\circ \leq \theta_\mu \leq 129.4^\circ$ and is an extension in phase space compared to the previous analysis [8]. In the overlap region between the central region (CJC) and the forward region (FTD), a small fraction of the selected muon tracks are reconstructed using information from both detectors (combined tracks) or the FTD alone (forward tracks). This fraction is small (about 8%).
In addition, the muon has to be assigned to a jet fulfilling the jet selection criteria as described in the next section. This assignment of muons to jets is an intrinsic property of the used jet algorithm as described in section 4 since every particle is assigned to exactly one jet. In rare cases a second muon is found fulfilling the selection criteria. Then the muon having the highest transverse momentum is selected and required to be assigned to a selected jet.
The **detector cuts** applied to the muon have an influence on the efficiency of the muon selection and the purity of the sample. As the kinematic range of this analysis is extended with respect to the pseudorapidity and momentum range of the muon, the influence of these cuts is studied in detail. The studied cuts are the **linking probability** of the outer to the inner muon track (see section 4.2) and the number of muon layers having a muon signal separatly for the central and forward region.
The linking probability is shown in figure 5.11. For all distributions shown in this section, in addition to the muon selection, the DIS selection and the jet selection, as explained in the following section, are applied to data and Monte Carlo simulation. The distribution is flat and increases for small probabilities as expected. The Monte Carlo simulation describes the data reasonably well. In addition the distribution of background events is shown for the simulated samples and compared to data. Background events are defined as misidentified hadrons (fake muons) and real muons coming from inflight decays as defined in section 5.2.1. According to the simulation, the background is dominated by misidentified hadrons both from events with no heavy quark or a charm quark involved. The amount of events with a produced beauty quark and a misidentified hadron or events with a real muon coming from an inflight decay is small. As expected, the fraction of background increases for small linking probabilities. The linking probability cut is scanned, the result for the selection efficiency and the purity of the sample is also shown in figure 5.11. The selection efficiency is defined with respect to a sample with no linking probability cut applied. Whereas the selection efficiency decreases from 85% for a linking probability of 2% to 75% for a linking probability of 20%, the fraction of background events stays constant at 30%. The cut applied for this analysis is at 2%. The influence of this cut on the cross section is studied as a cross check in section 6.6.
The same investigation is done for the cut on the number of muon layers with a

cut	value
transverse momentum	$p_t^\mu > 2.0$ GeV
pseudorapidity	$-0.75 \leq \eta^\mu \leq 2.0$
linking probability	$\geq 2\%$
number of muon layers	≥ 3

TABLE 5.6: *Muon selection cuts. The cuts that define the kinematic range of this analyis are in bold letters.*

muon signal. The results are shown in figure 5.12 for the central region and figure 5.13 for the forward region. For this study, no other muon detector cut is applied. The maximum number of layers is 10, the inner and outer muon boxes (see section 2.5) are not taken into account. The distributions of the number of layers are not described very well by the simulation because the single hit efficiency is too low for the simulation after a high voltage increase. Therefore only a loose cut of at least three muon layers is possible. As can be seen in the plot comparing the efficiency and purity of the sample, no significant reduction of background is possible by using a harder cut, whereas the efficiency decreases significantly from almost 100% at a cut of at minimum three layers. Again the efficiency is defined with respect to a sample with no cut on the number of muon layers applied. The same holds for the forward region. The distribution of the number of muon layers with a muon signal is not described very well, the fraction of events having a signal from less than six layers is negligible. Applying a cut on the number of layers does not lead to a significant reduction of the background, whereas the efficiency decreases rapidly. For a cut of less than six layers the background fraction is about 35%, which is a bit higher than for the central region.
Another quantity for rejecting background is the number of layers between the first and the last muon layer having a muon signal. This distributions are shown in figures 5.15 and 5.14 for the forward and central region. Again, the distribution for the forward region is well described, the distribution for the central region is not described very well. A cut on this distribution does not lead to any additional background rejection, therefore no cut is applied.
The pseudorapidity distribution of the muon is shown in figure 5.16. The fraction of events in the forward region ($\eta^\mu > 0.5$) is overestimated by the simulation. A reweighting is applied, where the reweighting factors are determined bin-wise from the ratio of the data to the inclusive Monte Carlo distribution. The reweighting factor as a function of the pseudorapidity is shown in figure 5.17.
The polar angle and transverse momentum distributions are shown in figure 5.18. No further reweighting has to be applied, the transverse momentum distribution is well described by the simulation.
All cuts concerning the muon selection are summarized in table 5.6.

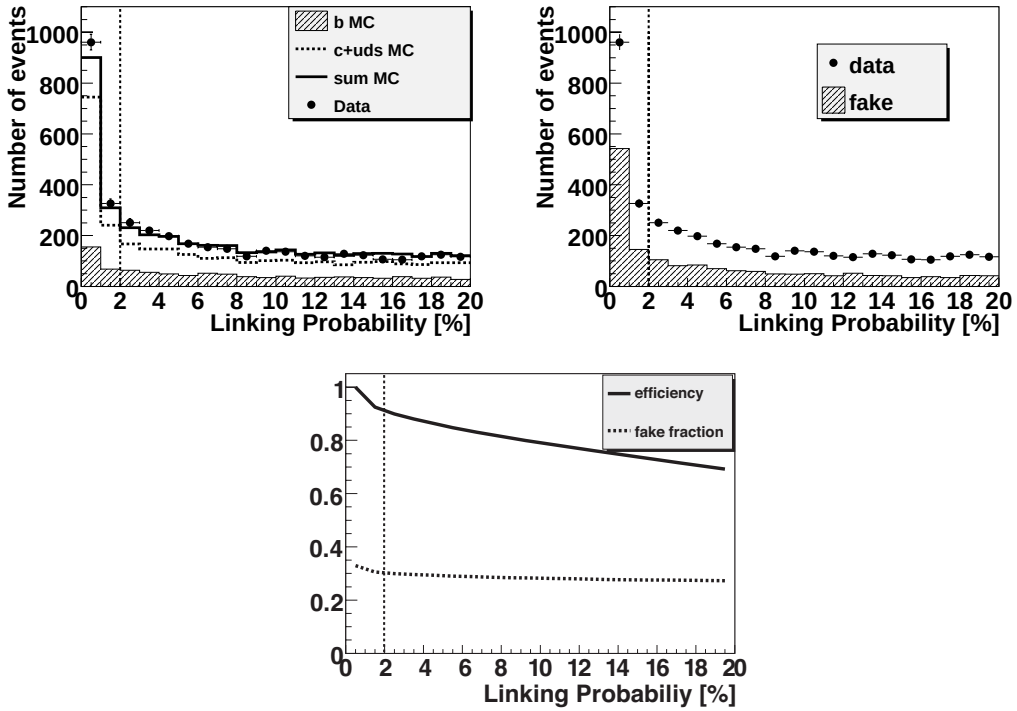

FIGURE 5.11: *Linking probability between central track and iron track: in the upper left plot the data distribution is compared to the simulation, in the upper right plot the data distribution and the distribution from background events as determined from the simulation is shown. In the lower plot efficiency and fake fraction are shown as explained in the text.*

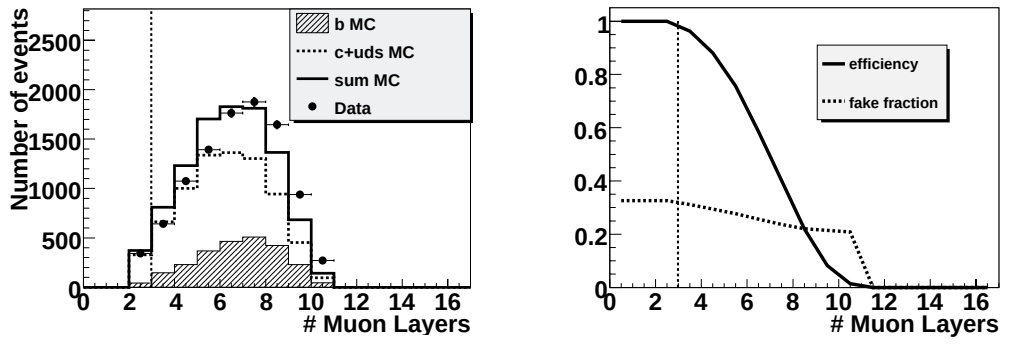

FIGURE 5.12: *Distribution of the number of muon layers with a hit for the central region: in the left plot the data distribution is compared to the simulation, in the right plot efficiency and fake fraction are shown as explained in the text.*

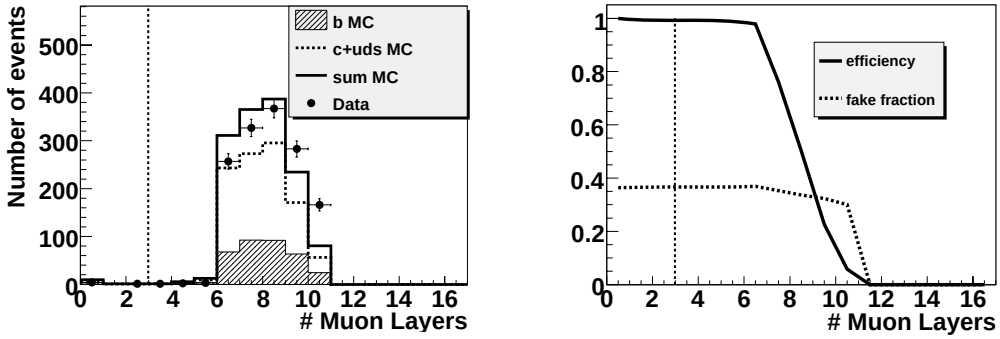

FIGURE 5.13: *Distribution of the number of muon layers with a hit for the forward region: on the left plot the data distribution is compared to the simulation, on the right plot efficiency and fake fraction are shown as explained in the text.*

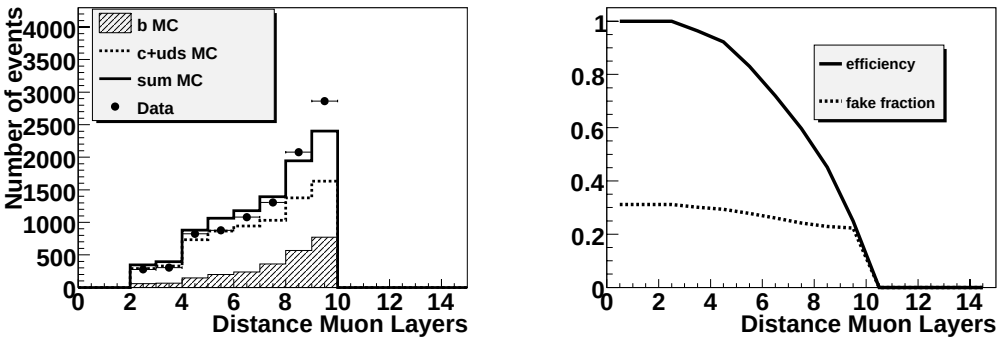

FIGURE 5.14: *Distribution of the distance between first and last hit layer for the central region: on the left plot the data distribution is compared to the simulation, on the right plot efficiency and fake fraction are shown as explained in the text.*

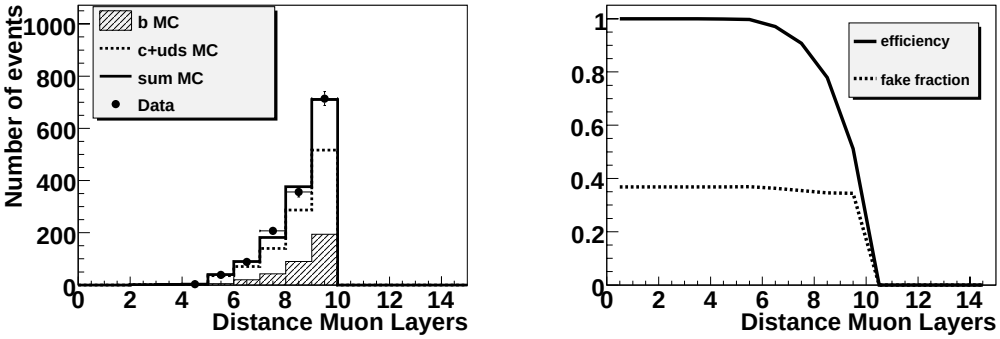

FIGURE 5.15: *Distribution of the distance between first and last hit layer for the forward region: on the left plot the data distribution is compared to the simulation, on the right plot efficiency and fake fraction are shown as explained in the text.*

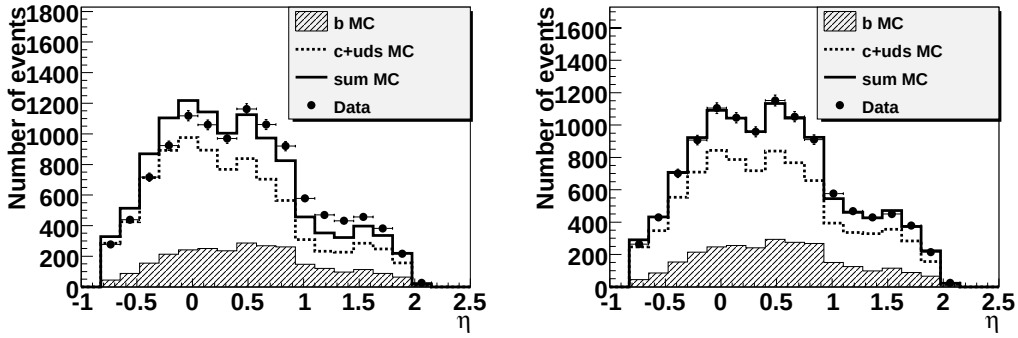

FIGURE 5.16: *Pseudorapidity distribution for the selected muon, before (left) and after (right) reweighting.*

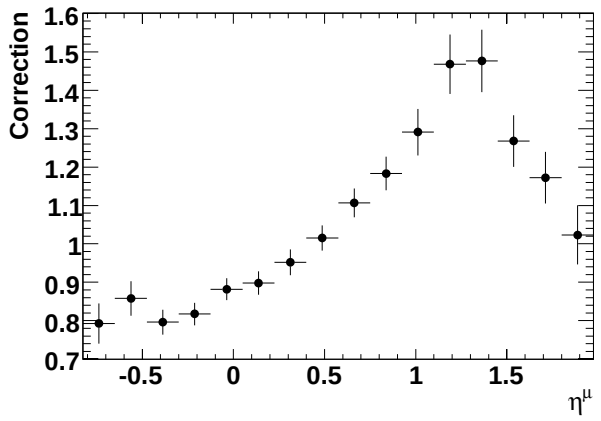

FIGURE 5.17: *Reweight factor applied to the Monte Carlo simulation as a function* η^{μ}.

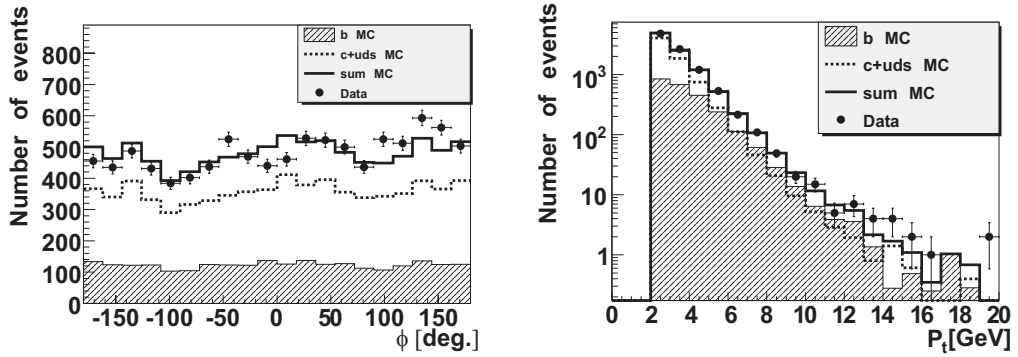

FIGURE 5.18: *Azimuthal angle (left) and transverse momentum (right) distribution of the muon.*

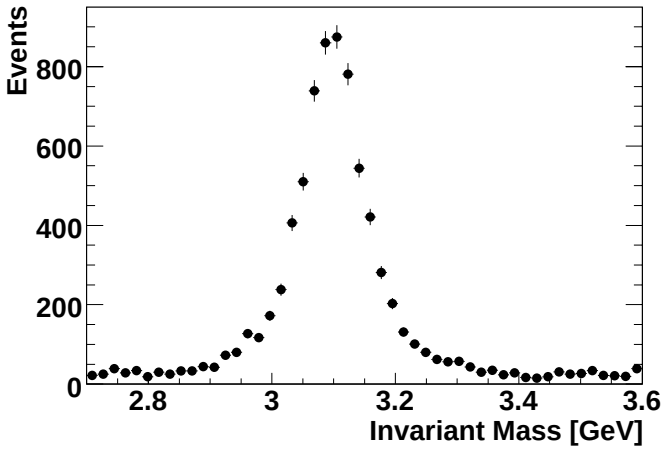

FIGURE 5.19: *Invariant mass distribution of the elastic J/ψ sample*

5.5.1 Muon Identification Efficiency

The performance of the muon identification with respect to the efficiency and misidentification depends on the detector cuts applied to the event selection. Since the data is corrected for these detector effects using Monte Carlo simulations, the identification efficiency of muons in the iron implemented in the simulation has to be checked with real data. Correction factors have to be applied to account for a not perfect simulation of the muon identification. A clean sample of muon events is used for this check, the muons origining from decays of elastically produced J/ψ mesons. Exactly two well measured tracks are demanded, their invariant mass has to lie within the J/ψ mass window, which is defined as the mass range from 2.8 GeV to 3.2 GeV. If in addition at least one of these tracks is identified as a muon in the calorimeter, this event sample is almost background free. The sample was triggered by an independent subtrigger which has no iron muon condition and consists of 1321 muon candidates, the invariant mass distribution is shown in figure 5.19. The cuts for selecting this sample are summarized in table 5.8. The muon identification efficiency can be checked by considering the second muon. The detector cuts for the iron muon correspond to the final selection cuts discussed in section 5. The p_t dependence of the identification is determined for three detector regions: the forward and backward of the barrel region and the forward endcap. For each region the efficiency determined from the data is compared to the efficiency determined from a sample of simulated elastic J/ψ events[5] where the same selection is applied. The results are shown in figures 5.20 to 5.22. For each efficiency measurement a fit of a Fermi function of the form $\epsilon(p_t) = \epsilon_{max}/(1 + \exp(-a\,x + b))$ with three free parameters is performed. The important parameter is ϵ_{max}, which denotes the efficiency for the plateau region. Since the Fermi function is not able to describe both the low and

[5]This sample is generated using the DIFFVM [93] Monte Carlo generator.

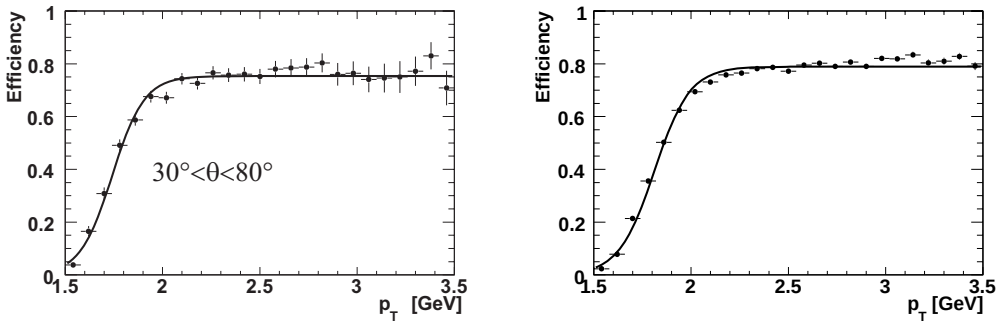

FIGURE 5.20: *Muon reconstruction and identification efficiency for the forward barrel determined from data (left) and Monte Carlo simulation (right).*

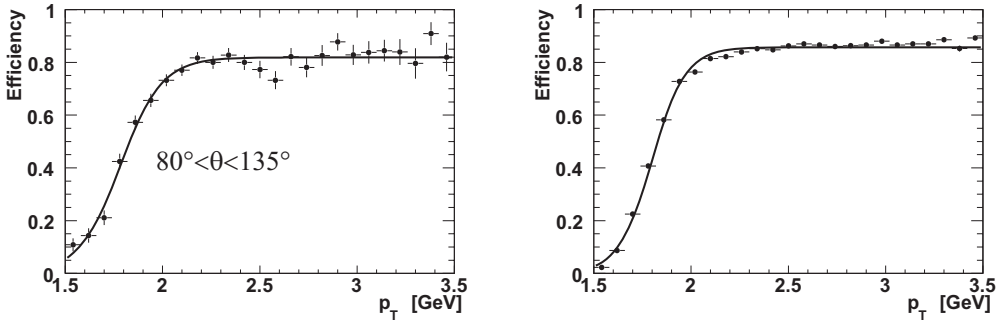

FIGURE 5.21: *Muon reconstruction and identification efficiency for the backward barrel determined from data (left) and Monte Carlo simulation (right).*

high p_t part, the fit is only performed for the region with $p_t > 2.0$ GeV. Only muons in this region are used for this analysis. In general, the efficiency is overestimated by the simulation. It is assumed that the reconstruction efficiency is the same for muons from elastic J/ψ decays and muons in a jet environment.
The p_t dependent correction function is given in figure 5.23. The correction factor is in the range from -9% to -5% for the backward part of the barrel region and from -5% to $+3\%$ for the forward part of the barrel region. For the forward endcap a constant correction factor of 20% is used for the region $p > 4$ GeV which corresponds to $p_t > 2$ GeV. The Monte Carlo simulation is corrected by applying these correction factors. Technically this is done by applying a momentum dependent reweighting of the simulated events for each of the three investigated detector regions. The results of this investigation are summarized in table 5.7. The limited statistics of the data sample, especially in the high momentum region, leads to a non negligible systematic uncertainty introduced by this method. This uncertainty is estimated by the relative error of the parameter ϵ_{max} determined from the fit. A conservative overall uncertainty of 3% is estimated for the muon identification.

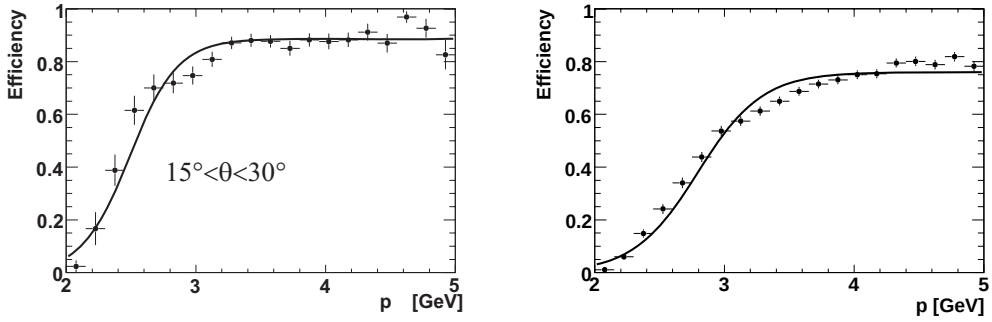

FIGURE 5.22: *Muon reconstruction and identification efficiency for the forward endcap determined from data (left) and Monte Carlo simulation (right).*

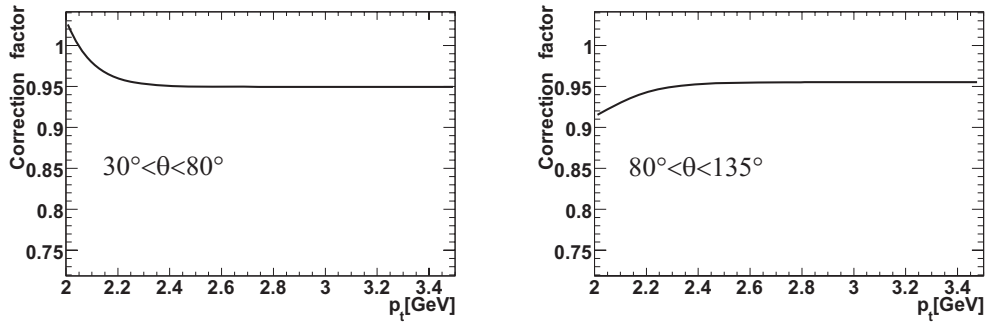

FIGURE 5.23: *Correction factors for the muon reconstruction and identification efficiencies for the forward barrel (left) and the backward barrel (right).*

Detector region	Polar angle	efficiency	rel. correction
backward barrel	$80° \leq \theta \leq 135°$	82%	-9% to -5%
forward barrel	$30° \leq \theta \leq 80°$	75%	-5% to $+3\%$
forward endcap	$15° \leq \theta \leq 30°$	89%	$+20\%$

TABLE 5.7: *Muon reconstruction and identification efficiencies as determined from data for the different detector regions. Also given is the range of correction factors. The efficiency denotes the value ϵ_{max} for the plateau region.*

Elastic J/ψ selection
two well measured primary vertex fitted tracks of opposite charge
invariant mass 2.8 GeV $\leq m_{\mu\mu} \leq$ 3.2 GeV
one identified muon in the calorimeter (Quality ≥ 2)
$20° \leq \theta_\mu \leq 30°$, $30° \leq \theta_\mu \leq 80°$, $80° \leq \theta_\mu \leq 135°$
$\lvert z_{vtx} \rvert < 35$ cm

TABLE 5.8: *Cuts for the J/ψ selection.*

cut	value
transverse momentum	$p_t^{jet} > 6.0$ GeV
pseudorapidity	$\|\eta^{jet}\| \leq 2.5$
number of associated particles	> 2

TABLE 5.9: *Jet selection cuts. The cuts that define the kinematic range of this analyis are in bold letters.*

5.6 Selection of Jets

Using the output of the jet algorithm, a **muon jet association** is performed. The selected muon has to be part of a jet that fulfills the jet selection criteria (denoted as muon jet in the following). The minimum transverse momentum of the jet is 6 GeV, the pseudorapidity range is restricted to the detector region $|\eta^{jet}| \leq 2.5$. To reject possible background from cosmic muons, the number of particles associated to the jet has to be larger than two.
The polar angle distribution of the muon jet is shown in figure 5.24, both before and after reweighting of the muon pseudorapidity distribution (see section 5.5). As expected, also this distribution is well described after the reweighting. In addition, in figure 5.25 the transverse momentum distribution, the jet multiplicity distribution and the distribution for the number of associated particles are shown. The transverse momentum distribution is well described, no further reweighting has to be applied. For the jet multiplicity distribution, only jets fulfilling the jet selection criteria (table 5.9) are counted. The distribution is reasonably well described, the majority of events having one or two reconstructed jets, only a small fraction of events having three reconstructed jets. Also the multiplicity distribution of particles belonging to the selected jet is reasonably well described.
This measurement relies on a precise understanding of the jet structure. Therefore the **energy flow** of the jets is studied in more detail. The results are shown in figure 5.26. For all selected events of the heavy quark enriched sample, the average transverse momentum summed over all hadronic final state particles close in azimuthal angle ($\Delta\phi < 1$) to the jet axis is determined with respect to the distance in pseudorapidity. In an analogous way this is done for all particles close in pseudorapidity ($\Delta\eta < 1$) with respect to the azimuthal distance. Both distributions are compared to the Monte Carlo simulation, an excellent agreement for these distributions is achieved.
For all the jet control distributions shown, the full event selection including the DIS selection and the muon selection was performed. The jet selection cuts are summarized in table 5.9.

5.7 Summary of the Selection

All the cuts defining the kinematic range of this analysis are summarized in table 5.10. In total, 11420 events are selected. The run dependence of the selection (event

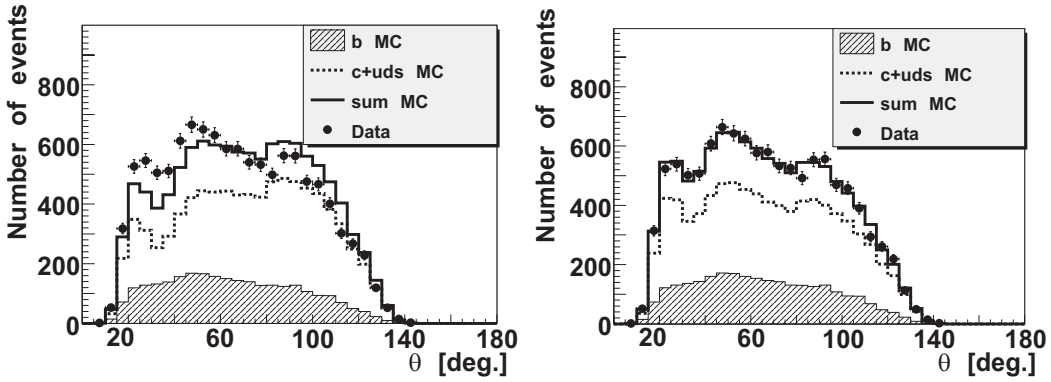

FIGURE 5.24: *Polar angle distribution for the jet selection. The left plot is before, the right plot after reweighting the pseudorapidity distribution of the selected muon.*

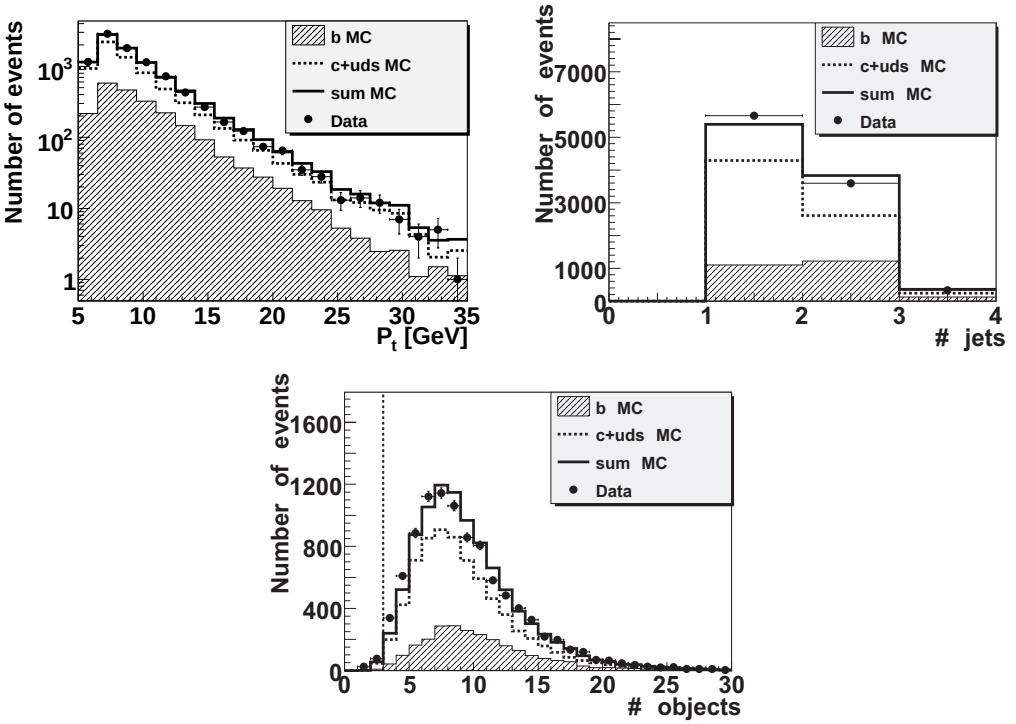

FIGURE 5.25: *Transverse momentum of the muon jet (upper left), multiplicity for jets fulfilling the jet selection criteria (upper right) and number of particles belonging to the muon jet (bottom).*

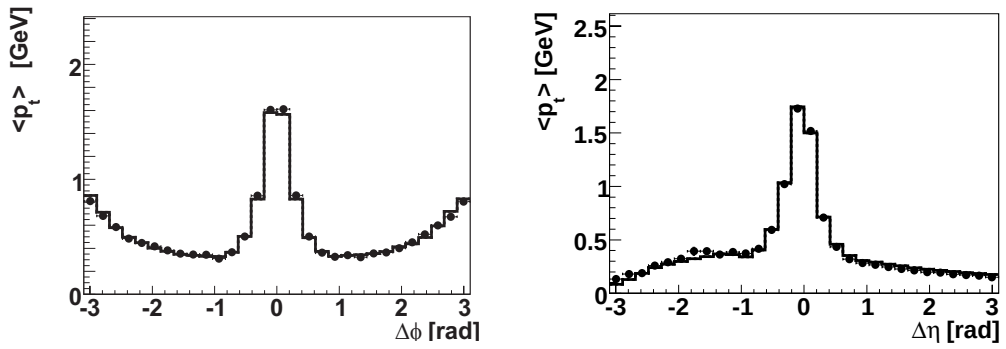

FIGURE 5.26: *Energy flow distributions for the selected jet*

cut	value
Virtuality	$3.5\ \text{GeV}^2 < Q^2 < 100\ \text{GeV}^2$
Inelasticity	$0.1 < y_s < 0.7$
muon transverse momentum	$p_t^{\mu} > 2.0$ GeV
muon pseudorapidity	$-0.75 \leq \eta^{\mu} \leq 2.0$
jet transverse momentum	$p_t^{jet} > 6.0$ GeV
jet pseudorapidity	$\lvert\eta^{jet}\rvert \leq 2.5$

TABLE 5.10: *Summary of all selection cuts that define the kinematic range of this analysis.*

yield) is shown in figure 5.27. No time dependence is observed, the event yield is flat within errors with respect to the run number. On average 40 events are selected per inverse picobarn luminosity.

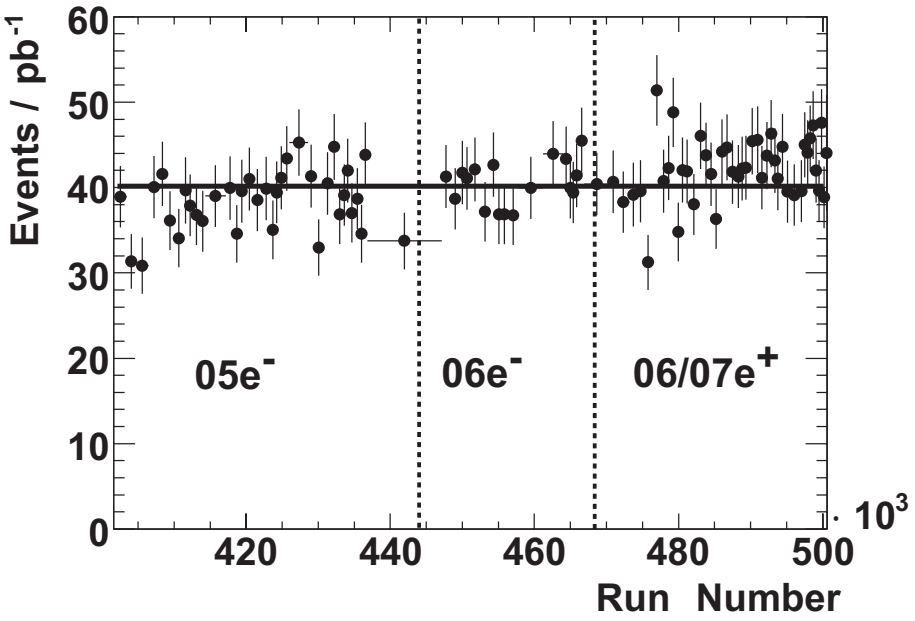

FIGURE 5.27: *Number of selected events per inverse picobarn luminosity. The different run periods are indicated.*

Chapter 6

Measurement

In this chapter the measurement of the cross section for beauty quark production in deep inelastic scattering is discussed. The measurement of the beauty content of the event sample is presented, followed by a discussion of correction factors that have to be applied to the measured number of beauty events. Finally the systematic studies are explained in detail.

6.1 Cross Section Definition

In this thesis, the cross section is measured for beauty quark production with a muon and a jet in the final state, $ep \to eb\bar{b}X \to ej\mu X'$ in the range 3.5 GeV$^2 \leq Q^2 \leq$ 100 GeV^2, $0.1 < y < 0.7$ with $p_t^\mu > 2.0$ GeV, $-0.75 < \eta^\mu < 2$ and $p_t^{jet} > 6.0$ GeV. The jets are defined using the k_T-algorithm on all final state particles after the decay of charmed or beauty hadrons. Muons coming from both direct and indirect b decays (including τ and J/Ψ decays) are considered to be part of the signal. Muons from decays of light flavoured hadrons (inflight decays, see section 5.2.1) are regarded as background.

6.2 Cross Section Determination

In general, the cross section measurement is a counting experiment: the total visible cross section $\sigma_b^{vis}(ep \to eb\bar{b}X \to ej\mu X')$ is determined from the number of measured beauty events for this process, N_b, and the luminosity $\mathcal{L}$,

$$N_b = \mathcal{L} \cdot \sigma_b^{vis}. \tag{6.1}$$

For the measurement of bin averaged differential cross sections the number of selected events $N_b(x_i)$ for each bin x_i has to be divided by the bin width Δx_i,

$$\frac{N_b(x_i)}{\Delta x_i} = \mathcal{L} \cdot \frac{\Delta \sigma_b^{vis}}{\Delta x}|_{\text{Bin i}}. \tag{6.2}$$

The different variables x investigated in this analysis are Q^2, the scaling variable x, the transverse momentum of the muon and the jet, and the pseudorapidity of the

muon.[1] The different binnings for these variables are given in the result tables in appendix C.
Double differential cross sections are determined in an analogous way

$$\frac{N_b(x_i, y_i)}{\Delta x_i \cdot \Delta y_i} = \mathcal{L} \cdot \frac{\Delta \sigma_b^{vis}}{\Delta x \Delta y}|_{\text{Bin i,j}}, \tag{6.3}$$

where y is a second variable. In this analysis double differential cross sections are measured as a function of the transverse momentum of the jet for different muon pseudorapidity regions and as a function of $\log(x)$ for different Q^2.
The measured number of beauty events N_b is determined from the number of observed beauty events N_b^{obs}:

$$N_b = N_b^{obs} \cdot \epsilon^{-1}, \tag{6.4}$$

where ϵ is the factor that corrects for the limited acceptance, efficiency and resolution of the detector, for events with muons from inflight decays and not direct or indirect decays, and for events that do not carry a muon at all but are selected due to a misidentified hadron. This correction factor is discussed in section 6.4.
The number of observed beauty events N_b^{obs} is determined from the total number of observed events N^{obs} by measuring the fraction of beauty events f_b for the event sample:

$$N_b^{obs} = N^{obs} \cdot f_b \tag{6.5}$$

This measurement is discussed in the following section.

6.3 Measurement of Beauty Fractions

The main experimental challenge of this analysis is the measurement of the fraction of selected events originating from decays of beauty mesons. The cross production rates of light, charm and beauty quarks at HERA roughly scale like $\sigma(uds) : \sigma(charm) : \sigma(beauty) = 2000 : 200 : 1$. Beauty production is strongly suppressed due to the limited kinematic phase space and the smaller electric charge of the down type beauty quark compared to the up type charm quark. When requiring a high p_t muon, heavy quarks are enriched, the ratio is then about $\sigma(uds) : \sigma(charm) : \sigma(beauty) = 2 : 5 : 3$.[2] Light flavour events still give a large contribution to the sample due to the large cross section for light quarks.
To measure the beauty fraction, a statistical method is used, based on a fit of template distributions derived from Monte Carlo simulations to the data. Only the transverse momentum distribution of the muon with respect to the jet axis p_t^{rel} as an input for this method.
In the following, the definition of the variable used to determine the beauty fraction is presented, the statistical method is discussed and the fit results are presented.

[1] For the cross section plots the bin averaged cross sections are denoted as $\frac{d\sigma}{dx}$ and shown at the middle of the bin. No bin-centre correction is performed.

[2] This ratio was determined in [8], where the charm and beauty fractions could be disentangled, which is not possible for this analysis (see section 9).

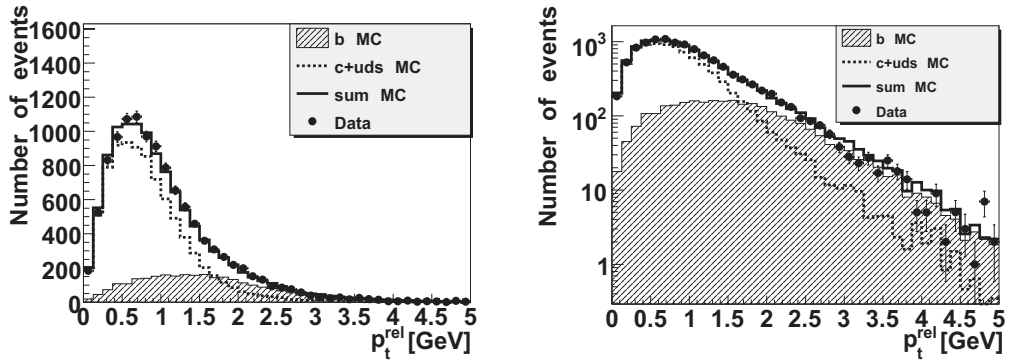

FIGURE 6.1: *p_t^{rel} distribution for the selected events shown in linear (left) and logarithmic (right) scale, compared to the simulation, which is the sum of the two template distributions, weighted according to the fit result. The fraction of the beauty sample as obtained from the fit is 24.6%.*

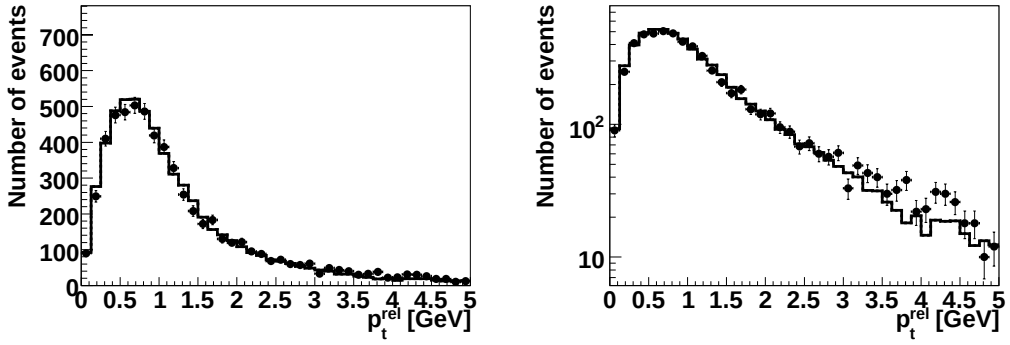

FIGURE 6.2: *Shown is the p_t^{rel} distribution for the highest momentum track with respect to the jet axis for a sample with no muon requirement, compared to the simulation shown in linear (left) and logarithmic (right) scale.*

6.3.1 Relative Transverse Momentum

The transverse momentum of the muon with respect to the jet axis is determined as follows:

$$p_t^{rel} = \frac{|\mathbf{p}_\mu \times (\mathbf{p_{jet}} - \mathbf{p}_\mu)|}{|\mathbf{p_{jet}} - \mathbf{p}_\mu|} \tag{6.6}$$

Following the procedure adapted in the previous analysis [8], the muon momentum is subtracted from the jet momentum. The alternative definition of this variable where the muon momentum is not subtracted is discussed in section 6.6 in the context of the systematic studies. The difference in the fit results for both methods is the major contribution to the systematic uncertainty of this analysis.
The measured distribution of p_t^{rel} is shown in figure 6.1 together with the Monte Carlo predictions. The beauty fraction is set to 24% which is the result of the fit

of the different template distributions to the data. This method is only valid if the contribution from light quark events, which are mainly misidentified hadrons, is well described. This is indeed the case, as shown in figure 6.2. For this check a light quark sample was selected by omitting the muon requirement. In this case p_t^{rel} is defined as the transverse momentum of the highest momentum track with respect to the jet axis, analogue to (6.16).

6.3.2 Binned Likelihood Fit

The p_t^{rel} distributions for the different Monte Carlo sources are used as templates to determine the fraction of beauty events in the data. Since the shapes of the distributions are not given by a smooth function, the data as predicted from the simulation has to be binned and a **binned likelihood fit** has to be performed where the distributions for each bin content is assumed to be a Poisson distribution both for data and simulation. For this analysis an extended method is used as proposed in [31] where as an additional degree of freedom for each template component also fluctuations of the number of simulated events are taken into account. This is necessary if the Monte Carlo statistics is limited which is the case for this analysis. In addition, this method is applicable for Monte Carlo templates with empty bins and weighted Monte Carlo templates. The implementation used for this anlysis is provided by the Root analysis package [41] and uses the MINUIT minimization library [77]. In the following a short outline of this fit method is given.
When using m templates, the number of events in bin i as predicted from the simulation is

$$f_i = \sum_{j=1}^{m} p_j a_{ji}, \tag{6.7}$$

where p_j are the strength factors[3] one is interested in and a_{ji} are the number of Monte Carlo events from source j in bin i. Assuming a Poisson distribution for the bin contents, the logarithm of the likelihood is given by

$$\ln \mathcal{L} = \sum_{i=1}^{n} d_i \ln f_i - f_i, \tag{6.8}$$

where d_i is the number of measured events in bin i, and n is the number of bins.
To take into account fluctuations of the number of Monte Carlo events, the number of data events in a bin is not given by equation 6.7, but

$$f_i = \sum_{j=1}^{m} p_j A_{ji}, \tag{6.9}$$

[3]The actual fractions P_j are obtained when considering the normalization of the template samples with N_j events to the data sample with N_D events: $P_j = p_j N_j / N_D$.

where A_{ji} is the unknown expected number of events for source j in bin i. The corresponding likelihood that has to be maximized is

$$\ln \mathcal{L} = \sum_{i=1}^{n} (d_i \ln f_i - f_i) + \sum_{i=1}^{n} \sum_{j=1}^{m} (a_{ji} \ln A_{ji} - A_{ji}). \tag{6.10}$$

This method results in one additional free parameter A_{ji} for each template bin in which one is not interested in. A simplification is possible by solving the m differentials of equation (6.10) with respect to p_j in an interative procedure. For each step of the iteration and given values for p_j, a set of n equations

$$\frac{d_i}{1 - t_i} = \sum_j \frac{p_j a_{ij}}{1 + p_j t_i}, \tag{6.11}$$

is solved for t_i. The new values of A_{ji} for the next step of the iteration are then given by the relation

$$A_{ji} = \frac{a_{ji}}{1 + p_j t_i}. \tag{6.12}$$

This method has the advantage that it can also be used for reweighted Monte Carlo distributions. This is important for this analysis for several reasons, including the study of systematic effects (see section 6.6). In this case eqs. (6.11) and (6.12) have to be modified by

$$\frac{d_i}{1 - t_i} = \sum_j \frac{p_j w_{ji} a_{ji}}{1 + p_j w_{ji} t_i} \tag{6.13}$$

and

$$A_{ji} = \frac{a_{ji}}{1 + p_j w_{ji} t_i}, \tag{6.14}$$

where w_{ji} is the average weight for source j in bin i.[4]

6.3.3 Fit Results

The p_t^{rel} distributions obtained from the beauty Monte Carlo sample and the inclusive Monte Carlo samples are used as input templates to the fit procedure as described above. Although this method is sensitive to the amount of light quark events, it is not able to distinguish the charm and the light quark fractions. Therefore the fit is performed using two input templates, the beauty template sample and the charm/light quark template. The latter template is based on the inclusive sample where the events originating from beauty quarks are removed. In this way a Monte Carlo dependency is introduced, since it is assumed that the ratio of events originating from light quarks and charm quarks is correctly described. The shapes for the light and charm quark distribution are compared in figure 6.3. The light

[4]To obtain this average weight for each bin, a template histogram with no weights applied to the events is filled. The average weight for a bin is then given by the ratio of entries for the weighted and unweighted template.

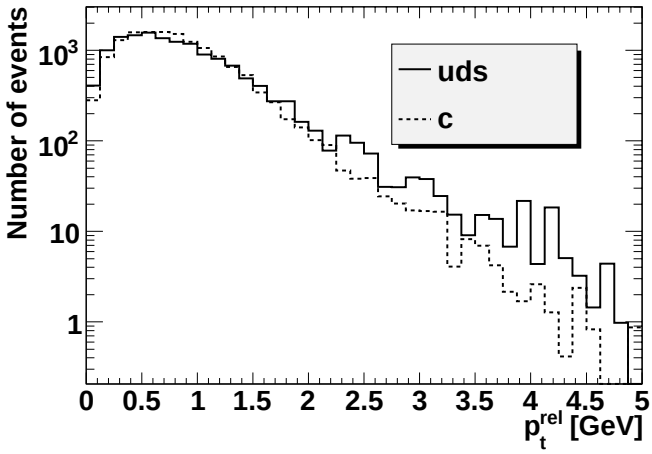

FIGURE 6.3: *Comparison of the p_t^{rel} shape for light and charm quark events.*

quark distribution has a slightly more pronounced tail for high p_t^{rel}. The corresponding systematic uncertainty, which is of the order of the statistical uncertainty of the fit, is discussed in section 6.6.

The fit yields a fraction of 24% beauty events for the selected data sample, which is measured with a statistical relative uncertainty of 4%. The statistical error of the fit is the major contribution to the statistical uncertainty. As expected, the statistical error is larger for the differential measurements. Due to the reduced statistics of both data and simulated samples the error reaches values up to 15%, which is comparable to the total systematic uncertainty of this measurement (see section 6.6). The fractions and corresponding values for χ^2 obtained from the fit for the different binnigs are shown in figures 6.4 and 6.5. For most bins, the χ^2 value (per degree of freedom) is between 1 and 2.

To check the stability of the fit, the number of bins is modified from 40 bins to 20 and 10 bins. No deviation of the fit result within the errors and the fit quality is observed.

The main features of the beauty fraction measurement are as follows:

- The dependency on Q^2 and $\log x$ is flat within the errors.
- A strong dependency on the transverse muon momentum is observed, the measured beauty fraction increases towards higher momentum and reaches a maximum value of about 50%. This is expected as the light quark cross section rises very fast towards low jet transverse momenta, whereas the rise is slower for heavy quarks due to their mass.

  This momentum dependence is reflected in the measurement with respect to the transverse jet momentum. The p_t^{rel}-spectra for data and Monte Carlo for the different bins of the muon transverse momentum are shown in figure 6.6.
- The measurements show a dependency on the polar angle of the muon. The background contribution to the selected sample is highest for the central region

of the detector and decreases towards the forward region. This can be explained by the fact that the amount of material the hadrons have to traverse is lowest for the central region.

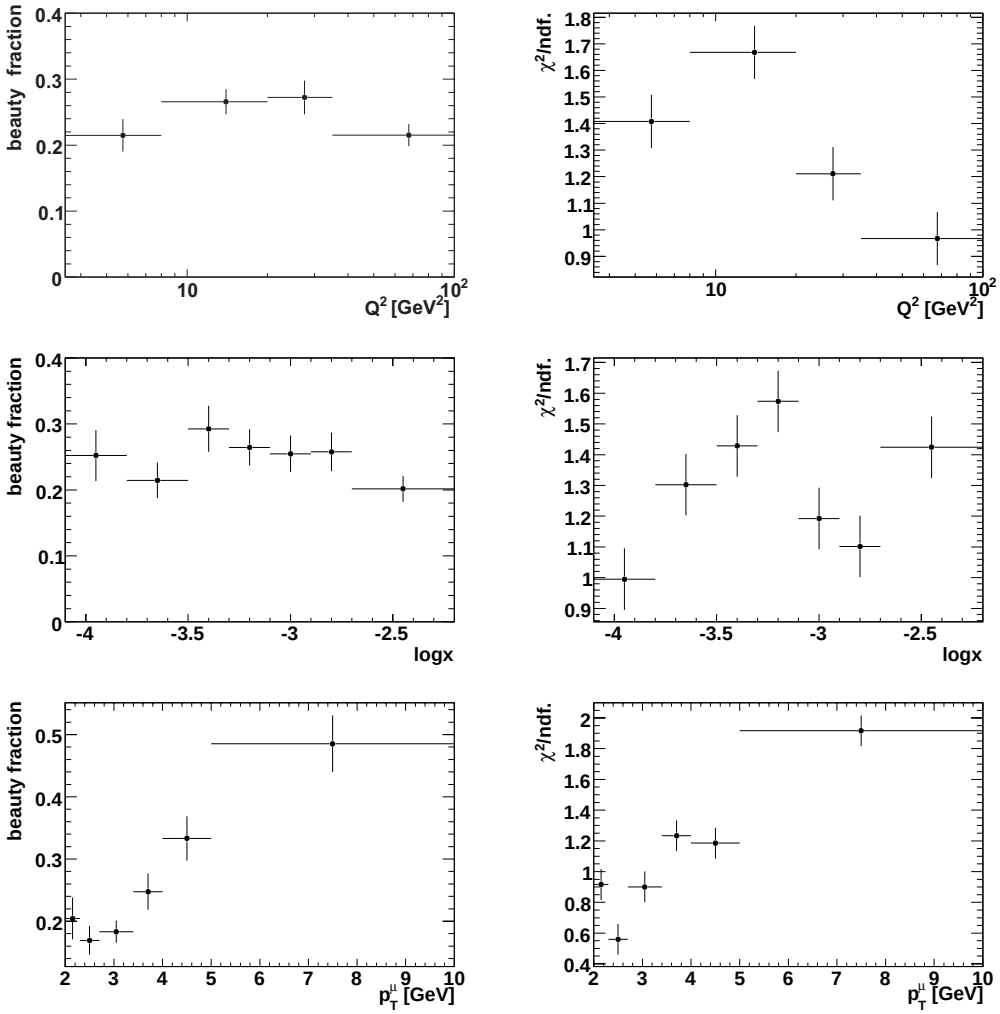

FIGURE 6.4: *Results of the p_t^{rel} fits (left column) and the corresponding χ^2/ndf. (right column) for the different analysis intervals.*

To summarize, the p_t^{rel} method gives stable results with small errors and very good χ^2 values for the fit. This justifies the use of this variable for a one dimensional fit without additional lifetime information. Nevertheless a large dominating systematic error has to be applied due to a possible bias of this method (see section 6.6).

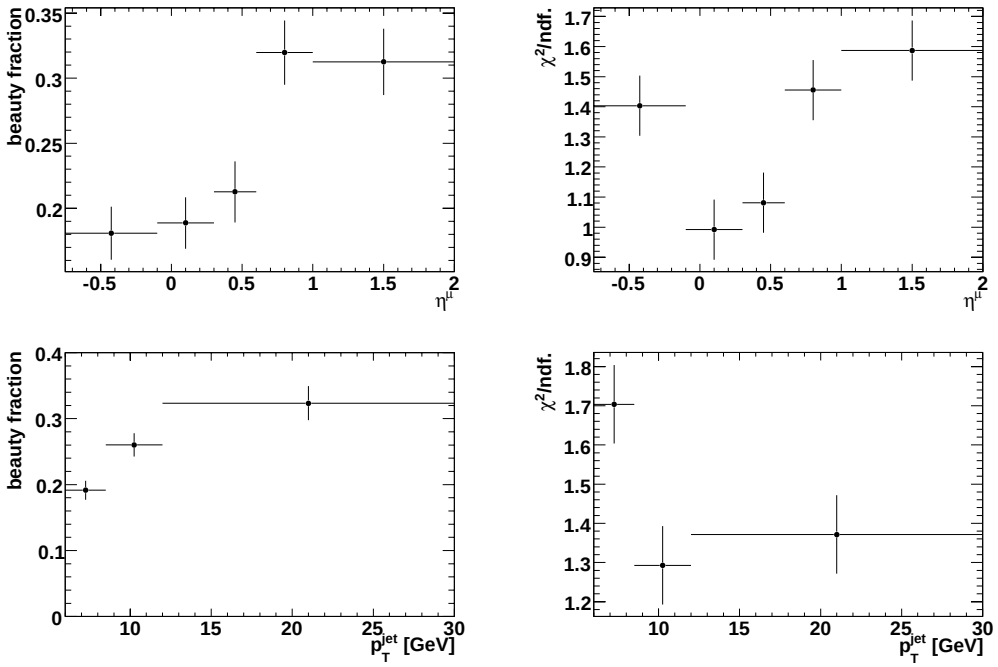

FIGURE 6.5: *Results of the p_t^{rel} fits (left column) and the corresponding χ^2/ndf. (right column) for the different analysis intervals.*

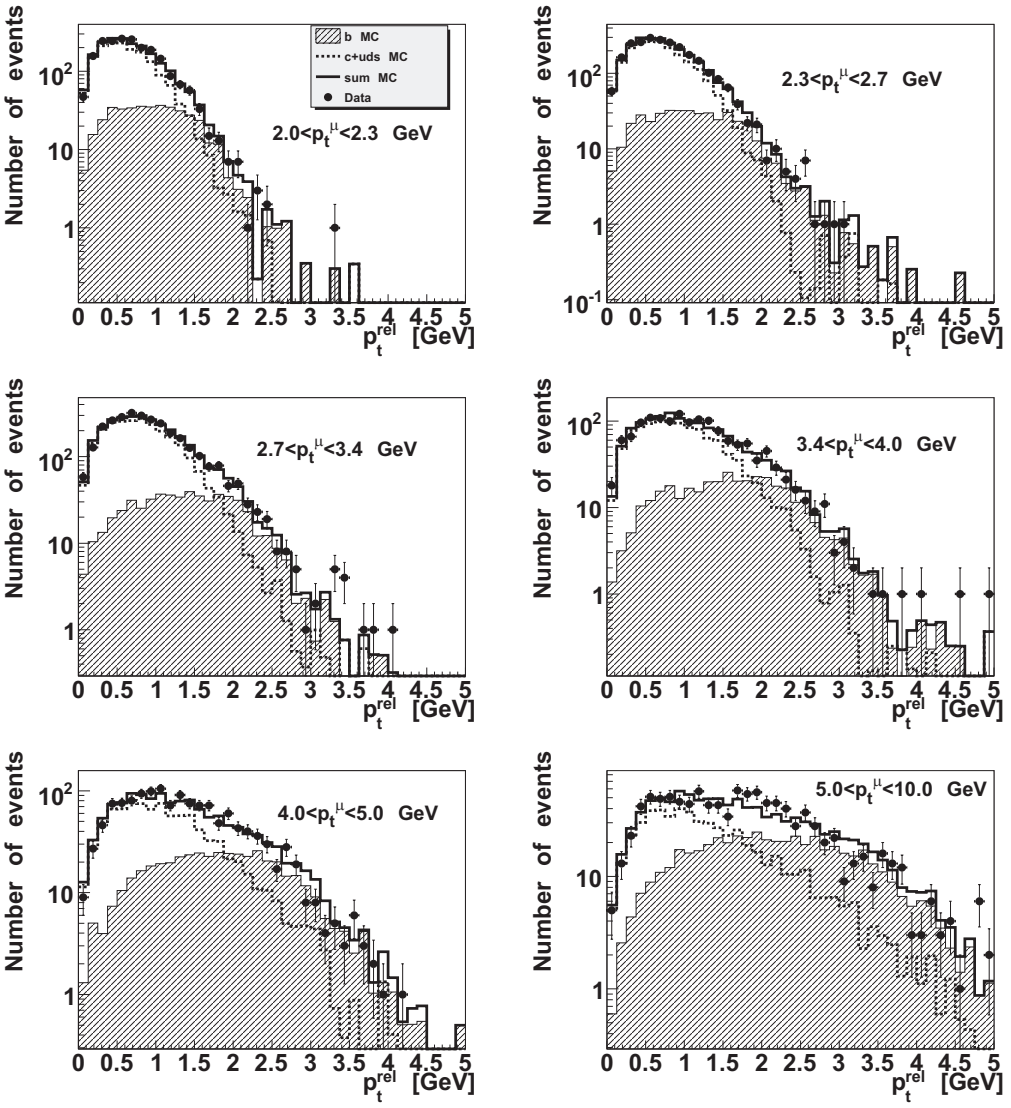

FIGURE 6.6: p_t^{rel}*-fits for different bins of the muon transverse momentum. The beauty fraction increases towards high momenta.*

6.4 Efficiency and Acceptance Corrections

The Monte Carlo simulation of beauty events is used to correct the measurement for detector effects, which includes the resolution, limited efficiency and geometric acceptance of the detector[5]. For this measurement, a bin wise correction is applied where for each bin the number of generated events N^{gen} and the number of reconstructed events N^{rec} is determined. The correction factor ϵ_i for each analyzed bin i is given by the ratio N_i^{rec}/N_i^{gen}. This method also takes into account migrations: an event reconstructed in a certain bin may not necessarily be generated in the same bin. The most common source for migrations is the detector resolution. Therefore the bin widths have to be adapted to the resolutions. This method is only applicable if the detector is fully understood and the Monte Carlo simulations describe the relevant distributions well.
The effect of migrations can be estimated by the **purity**, which is determined from the simulation for each analysis bin as the ratio $N_i^{rec,gen}/N_i^{rec}$, where $N^{rec,gen}$ is the number of reconstructed events that were as well generated in the same bin. A high purity is desirable for each analysis bin to reduce the correction due to migration effects.

The overall detector efficiency for the analyzed kinematic range is 32%, with a purity of 86%. The efficiencies and purities for the bins used for the differential cross section measurement are shown in figures 6.8 and 6.9, and are tabularized in appendix C.
As expected, the efficiency increases towards higher p_t of the muon and reaches a maximum value of almost 60%. On the other hand, the efficiency decreases towards higher transverse momentum of the jet. This is accompanied by a small purity of only $20\% - 30\%$. Both can be explained by migrations into the lower bins. The reason for this is a lower reconstructed than generated jet energy due to the neutrino energy which escapes the detection but is part of the generated jet. In figure 6.7 the resolution of the transverse jet momentum is shown, the average loss of energy is about 20%. In the case of a double semileptonic decay ($b \to cl\nu, c \to sl\nu$) the energy loss is highest due to two neutrinos which escape the detection.
The drop of the efficiency for the lowest Q^2 bin can be explained by the reduced acceptance due to the radial SpaCal cut (see section 5.4).

[5]Separate correction factors were also determined for each run period, no difference is observed within the errors.

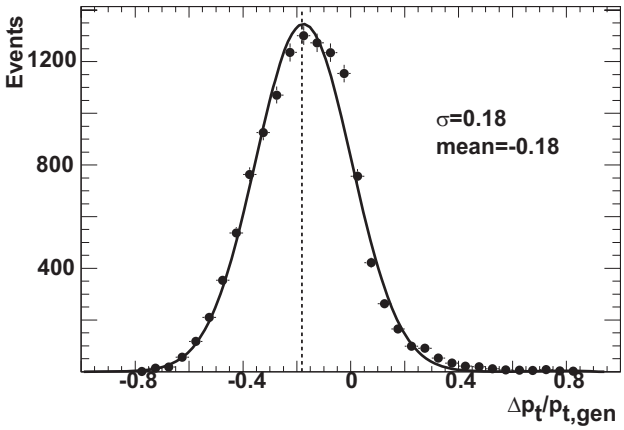

FIGURE 6.7: *Resolution of the measured transverse momentum of the jet according to the Monte Carlo simulation. The momentum is systematically reconstructed about 20% too low due to the missing neutrino energy.*

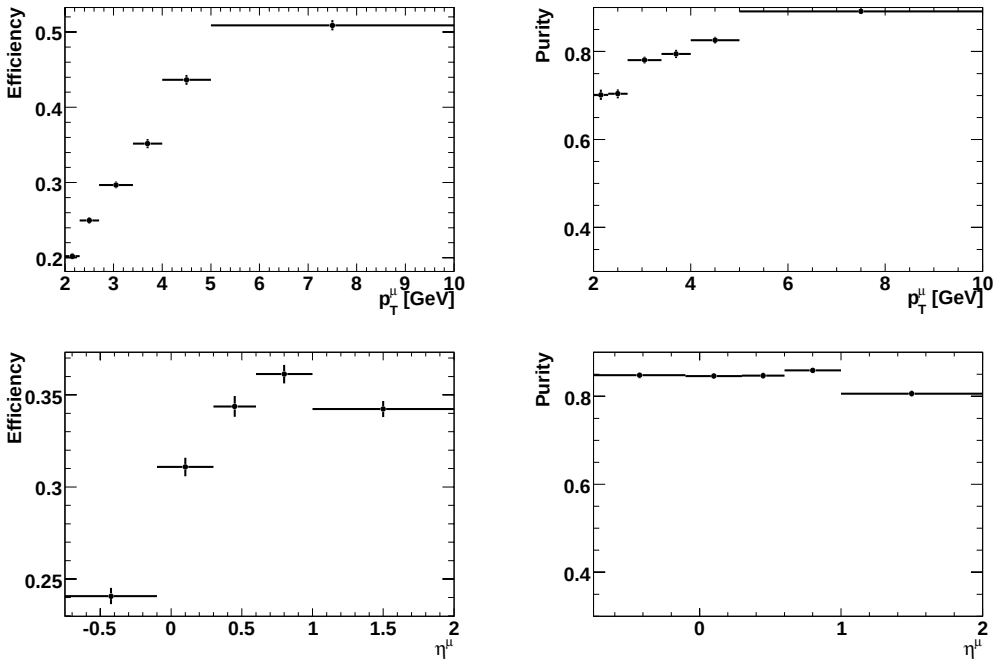

FIGURE 6.8: *Efficiencies (left column) and purities (right column) for the different analysis intervals.*

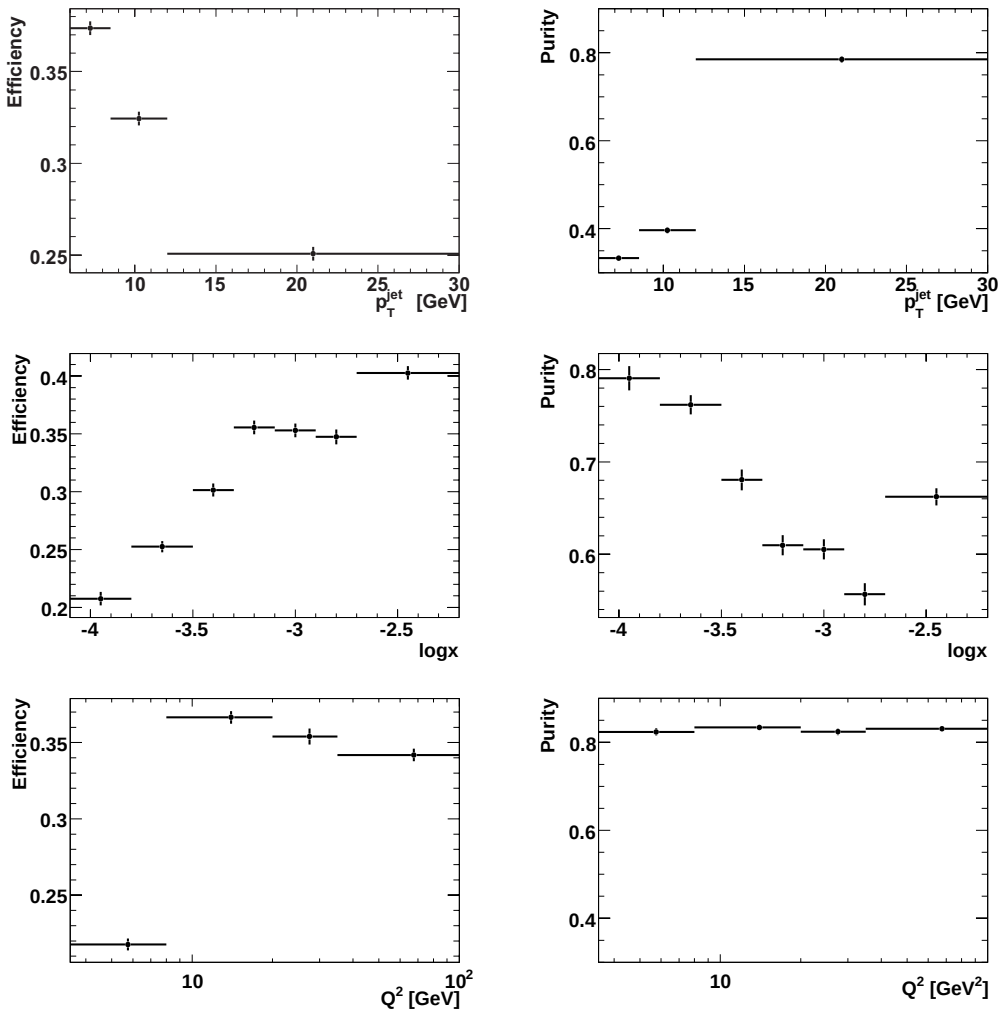

FIGURE 6.9: *Efficiencies (left column) and purities (right column) for the different analysis intervals.*

6.5 QED Corrections

As the NLO calculation does not contain QED corrections, the data is corrected to the QED Born level. Therefore a second Monte Carlo sample is generated, where radiative effects are switched off. An additional correction factor $1 + \delta_{rad}$ is calculated,

$$1 + \delta_{rad} = \sigma^{total}/\sigma^{born} = \frac{N^{total}/\mathcal{L}^{total}}{N^{born}/\mathcal{L}^{born}}, \tag{6.15}$$

where σ^{total} (σ^{born}) is the cross section determined for each analysis bin based on the event numbers and luminosity for the Monte Carlo with (without) QED radiative effects.
The correction factors, which are small and negligible for most bins, are tabularized in appendix C.
All cross sections discussed in the following are cross sections corrected to Born level.

6.6 Systematic Uncertainties and Cross Checks

A number of systematic studies have been performed, the dominant systematic error sources are the uncertainty due to the fit method and model uncertainties. These studies are performed separately for each bin of the cross section measurement. The total systematic uncertainty, which is found to be of similar size for all bins, is estimated to 14%. The different sources contributing to this uncertainty are presented in this chapter in the order of importance and listed in table 6.1.
In addition, cross checks that have been made and that are not presented in other sections, are discussed.

6.6.1 Systematic Uncertainties

p_t^{rel} Definition

The fits are repeated using a different definition of the p_t^{rel} variable:

$$\tilde{p}_t^{rel} = \frac{|\mathbf{p}_\mu \times \mathbf{p_{jet}}|}{|\mathbf{p_{jet}}|} \tag{6.16}$$

Both distributions are compared in figure 6.10. The default definition is broader per definition, nevertheless the separation power for signal and background, determined from the fit quality, is the same for both methods. The fit results obtained from the modified definition $\tilde{p}_t^{rel}$ are systematically below the default value. The reason for this deviation is not well understood. If the model describes the data, no difference for both methods is expected. A p_t-dependent model uncertainty for the charm fraction is one possible explanation as the fit is sensitive to the charm fraction. Therefore the deviation of 8.5% is taken as a systematic uncertainty.

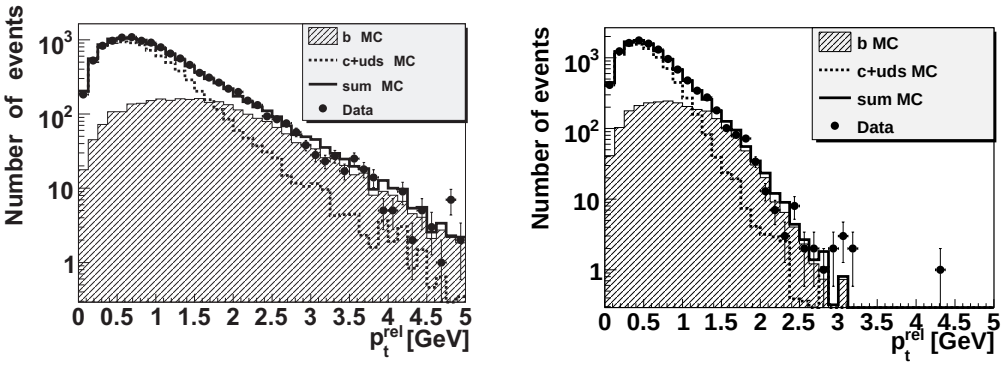

FIGURE 6.10: *Comparison of p_t^{rel} (left) and $\tilde{p}_t^{rel}$ (right)*

Physics Model

To study the dependence on the physics model, the complete analysis chain is repeated using CASCADE Monte Carlo samples for the signal and charm background. Again a common fit of the charm and light flavour background is performed. The charm Monte Carlo is scaled to the luminosity of the inclusive Monte Carlo which is used to extract the light flavour background. For consistency, this modified fitting procedure is repeated using RAPGAP Monte Carlo sets. A difference of 5% for the total cross section is estimated this way.

Fake Muon Background

The method used for this analysis does not allow a direct measurement of the fraction of light flavour induced background. The fraction of light flavour to charm background used for the combined fit of both components is taken from the prediction of the inclusive Monte Carlo. A systematic uncertainty is estimated by scaling the fraction of fake events 50% up and 50% down and repeating the whole analysis chain. This large rescaling is assumed to cover the uncertainty. As explained in section 5.2.1, also beauty and charm events are a source of fake background. The rescaling affects the fake component from all sources. A maximum cross section deviation of about 5% was obtained this way.

Fragmentation Model

The same procedure as explained above is repeated comparing Monte Carlo sets generated with Peterson fragmentation instead of Lund fragmentation which is used as default. This comparision yields a difference of 4%.

Luminosity

A systematic uncertainty has to be assigned to the luminosity measurement, the main source of the uncertainty is the acceptance of the photon detector. For the running periods 2005 e^- and 2006 e^- the uncertainty is 2.5%. For the 2006/2007 e^+ running period a larger systematic uncertainty of 5% has to be applied due to a not fully understood increase of event yields observed for several analyses[6].
The total uncertainty is estimated to 3.6% where the errors are weighted according to the corresponding luminosities of the running periods.

Muon Identification and Reconstruction

The muon reconstruction efficiency is composed of the identification efficiency and the track reconstruction efficiency.
The uncertainty for the muon identification is estimated to 3%. This uncertainty is due to the limited number of J/Ψ events in the data sample used to extract the correction (see section 5.5).
The track reconstruction efficiency is known to a precision of 2%.
The total uncertainty for the muon reconstruction is therefore estimated to 3.6%.

Hadronic Energy Scale

The hadronic energy scale is known up to 4% [87]. The influence of this uncertainty was investigated by rescaling the jet energy and the hadronic final state energy 2% up and down for the beauty Monte Carlo. The variation is only 2% since about half of the energy measurement is determined from track measurements and not affected by this uncertainty [100]. All kinematic variables depending on the energy of the hadronic final state are recalculated in a consistent way. The maximum deviation of the cross section determined from the recalculated detector efficiency is 3.3%.

Jet Axis

The influence of the jet axis measurement on the p_t^{rel} measurement is investigated by increasing the polar angle resolution for the simulation by 10%. The polar angle resolution of the jet according to the Monte Carlo simulation is about 4° (see figure 6.11)[7]. For each simulated event the polar angle is modified on a random basis using a Gaussian distribution with a width of 0.4°, and the whole analysis chain is repeated, including the fit. This yields a cross section deviation of 2%.

[6] This problem was still under investigation at the time writing this thesis.
[7] This resolution cannot be described by a Gaussian profile.

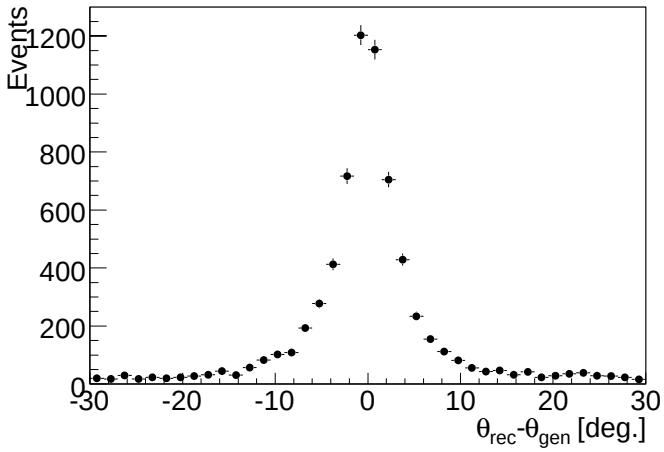

FIGURE 6.11: *Polar angle resolution of the jet according to the Monte Carlo simulation. As a systematic study the width of this distribution is increased by 10% for the simulated events.*

Radiative Corrections

The radiative correction factors are determined using limited Monte Carlo statistics. The uncertainty is estimated to 1.5%.

Calorimetric Energy Deposition of Muons

Muons as minimal ionising particles deposit some energy in the calorimeters. As explained in section 4.3.3, a double counting of energy is avoided for isolated muons by locking all clusters within a cone around the muon track. The distribution of the locked energy for muons is compared to the Monte Carlo prediction in figure 6.12. The simulation does not describe this distribution for energies below 1.5 GeV. Also shown in figure 6.12 is that the fraction of the muon energy that is locked is not described by the simulation. The energy deposition is overestimated by about 40%. For nonisolated muons no calorimetric energy is locked and therefore energy is double counted. The amount of energy double counted is different for data and simulation. This effect is studied by reprocessing the complete data sample and a smaller subset of the Monte Carlo samples using a modified algorithm where even for nonisolated muons double counting of energy is avoided by locking calorimetric energy around the muon track. The complete analysis chain is repeated for these reprocessed samples. The result is compared to the default samples, where for consistency also a subset of the Monte Carlo samples is used. A systematic shift of about 1% for the differential cross sections is determined this way.

Trigger Efficiency

To get an estimate for the uncertainty of the trigger efficiency, the analysis is repeated with no correction factor for the SpaCal trigger (see section 5.1.2) applied.

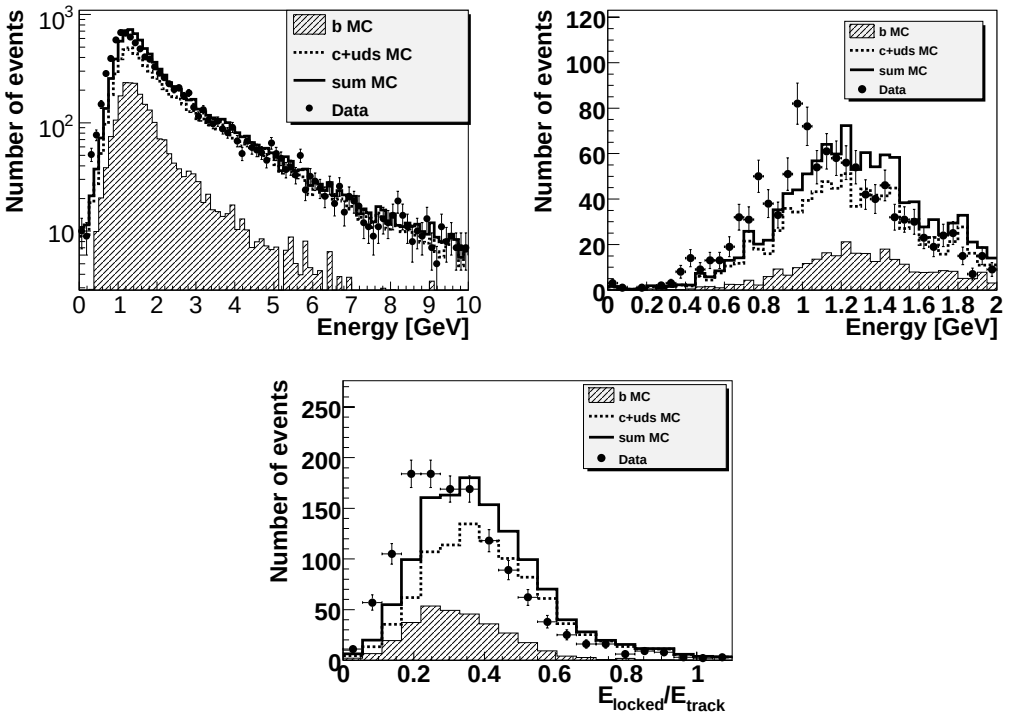

FIGURE 6.12: *Calorimetric energy that is attributed to isolated and nonisolated muons inside a cone around the muon track (upper left), calorimetric energy that is attributed to isolated muons inside a cone around the muon track for the low energy region on linear scale (upper right) and the ratio of locked cluster energy to the track energy for isolated muons (lower plot).*

The cross section deviation is less than 1% for all analysis bins.

Electron Reconstruction

The uncertainty of the electron reconstruction is investigated by varying the polar angle of the scattered electron by an amount of 1 mrad and the energy of the scattered electron by an amount of 1%. The efficiencies are recalculated, whereas the p_t^{rel} fit is not repeated. The change of the cross section estimated this way is negligible.

Source	$\Delta\sigma/\sigma$[%]
Monte Carlo model uncertainties	
p_t^{rel} definition	8.5%
RAPGAP vs. CASCADE	5%
Fake muon background	5%
Fragmentation (Peterson vs. Lund)	4%
Radiative corrections	1.5%
Energy deposition of muons	1%
Detector Efficiencies	
Luminosity	3.6%
Muon identification	3%
Track reconstruction	2%
Trigger efficiency	1%
Scattered electron	negligible
Jet reconstruction	
Hadronic energy scale	3.3%
Jet axis	2%
Sum	14%

TABLE 6.1: *Summary of the different error sources contributing to the systematic uncertainty. The total uncertainty sums up to* 14%.

6.6.2 Cross Checks

HFS algorithm

The HFS algorithm (see section 4.3) includes a locking mechanism for energy deposition of muons in the calorimeter. As a cross check this algorithm was modified and the data sample and subsets of the Monte Carlo samples were reprocessed. The maximum amount of locked energy per muon was reduced from 5 GeV to 2 GeV. Muons with an assigned energy of more than 2 GeV within an cone around the muon track are therefore classified as nonisolated and no energy is locked at all, leading to a double counting of energy. The calorimetric energy distribution is well described above 2 GeV. As expected, no deviation of the total and differential coss sections is observed. In addition, samples were produced using a modified algorithm with an reduced radius for the inner cone of half the default size. Only clusters within this inner cone around the muon track are locked. This is sketched in figure 6.13. No deviation for the cross section measurement is observed. Finally the radius of the outer cone was increased to 50 cm for the electromagnetic part of the calorimeter and 100 cm for the hadronic part. In this case more muons are classified as non isolated with the consequence of energy double counting. Also in this case no deviation for the cross section measurement is observed.

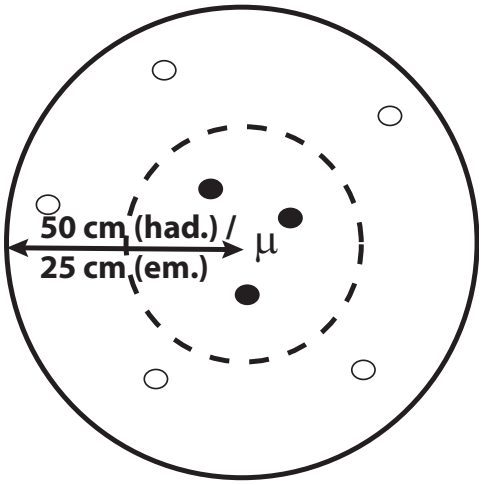

FIGURE 6.13: *Two cones around the muon track in the calorimeters are defined, the inner cone (dashed circle) has half the radius of the outer cone. The cone size is different for the electromagnetic and the hadronic part of the calorimeter. Clusters within the inner cone are locked if the muon is isolated. The isolation depends on the deposited energy within the outer cone.*

Measurement in different quadrants

The total cross section is measured for four different quadrants of the SpaCal. The result is shown in figure 6.14, as expected no ϕ dependence of the cross section is observed within the errors.

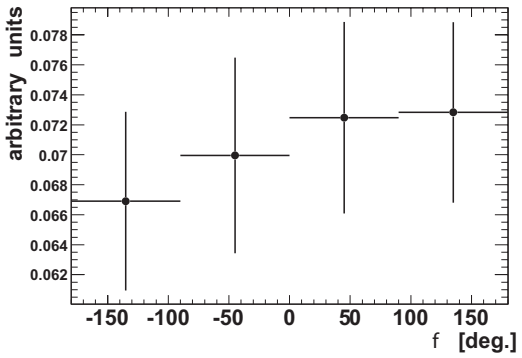

FIGURE 6.14: *Total cross section for four different quadrants of the SpaCal. The numbers are arbitrary units.*

Reconstruction method for y

The default reconstruction method for this analysis is the sigma method (see section 4.5). As a cross check this variable is reconstructed from the scattered electron kinematics alone (y_e). The cross sections obtained this way are consistent with the default cross sections within the errors.

Muon reconstruction

A linking probability cut of 5% instead of 2% is applied for the muon selection. The change of the cross section measurement obtained this way is negligible.

Chapter 7

Results

In this section the results of the cross section measurement for beauty quark production in deep inelastic scattering are discussed. The total cross section, differential and double differential cross sections are presented and compared to theory predictions. As a cross check, the analysis is repeated with the jet selection performed in the Breit frame, which allows a comparison to the published results of [8].

7.1 Theoretical Models

The results are compared to predictions from the next-to-leading order plus parton shower Monte Carlo generators RAPGAP and CASCADE, which use the DGLAP and CCFM evolution, respectively. The parameters are given in table 7.1. As the data is corrected to Born level, QED radiation is not used in the Monte Carlo generation.
The next-to-leading order prediction is calculated using the HVQDIS program (see section 1.9), which provides a prediction on parton level. To estimate the theoretical uncertainties of the NLO calculations, the beauty quark mass and the renormalization and factorisation scales are varied simultaneously from $m_b = 4.5$ GeV and $\mu_r = \mu_f = m_T/2$ to $m_b = 5$ GeV and $\mu_r = \mu_f = 2m_T$, where $m_T^2 = m_b^2 + p_t^2$. The typical change of the cross sections for this variation is about -10% to -20% for the upward variation and +40% to +50% for the downward variation. Another proton structure function is used (CTEQ6l), this leads to a typical variation of about +20%. The uncertainty due to variations of the fragmentation parameter ϵ by 25% is negligible. These cross section variations are added in quadrature to estimate the total systematic uncertainty of the NLO predictions for each bin of the measurement.
A correction from the parton to the hadron level prediction is performed using the RAPGAP Monte Carlo: in each bin of the measurement the parton and hadron level cross sections are calculated and applied as a correction factor to the NLO prediction. At hadron level the jets are reconstructed by applying the jet algorithm to all final state particles, after the decay of beauty or charm hadrons. On parton level the jet algorithm is applied to the generated quarks and gluons after the parton showering step. The typical correction to the hadron level is -10%, with the excep-

	RAPGAP	CASCADE	HVQDIS
Version	3.1	1.2	1.4
Proton PDF	CTEQ6L [102]	JS2001 [81, 83]	CTEQ5F3 [12]
$\mathcal{O}(\alpha_s)$	LO(+PS)	LO(+PS)	NLO
Λ_{QCD} [GeV]	0.25 ($\Lambda^{(5)}_{QCD}$)	0.2 ($\Lambda^{(4)}_{QCD}$)	0.309 ($\Lambda^{(4)}_{QCD}$)
Renorm. scale μ_r^2	$Q^2 + p_t^2$	$4m_b^2 + p_t^2$	$m_b^2 + p_t^2$
Factor. scale μ_f^2	$Q^2 + p_t^2$	$4m_b^2 + p_t^2$	$m_b^2 + p_t^2$
m_b [GeV]	4.75	4.75	4.75
Fragmentation	Lund(+Bowler)	Peterson	Peterson
Lund a	0.4		
Lund b	1.03		
Peterson ϵ_b		0.0069	0.0033

TABLE 7.1: *Parameters used for the different theoretical predictions for beauty quark production from LO Monte Carlo generators and a NLO program.*

tion of the highest jet transverse momentum bin which has a positive correction of about +10%. These correction factors are tabularized in appendix C.

7.2 Total Visible Cross Section

The measurement of beauty electroproduction in the kinematic range

- $3.5 < Q^2 < 100$ GeV^2
- $0.1 < y < 0.7$
- $p_t^\mu > 2.0$ GeV
- $-0.75 < \eta^\mu < 2$
- $p_t^{jet} > 6$ GeV
- $|\eta^{jet}| < 2.5$

yields a cross section of

$$\sigma_{vis}(ep \to eb\bar{b}X \to ej\mu X') = 29.3 \pm 1.3(stat.) \pm 4.1(sys.) \text{ pb}. \tag{7.1}$$

The uncertainty of the measurement is dominated by the systematic uncertainty of about 14% which is approximately three times larger than the statistical uncertainty. This measurement is compared to predictions from the RAPGAP and CASCADE Monte Carlo programs. The prediction from RAPGAP is

$$\sigma_{vis}^{RAPGAP}(ep \to eb\bar{b}X \to ej\mu X') = 14.0 \text{ pb}, \tag{7.2}$$

from CASCADE

$$\sigma_{vis}^{CASCADE}(ep \to eb\bar{b}X \to ej\mu X') = 17.7 \text{ pb}. \tag{7.3}$$

The RAPGAP Monte Carlo prediction is about 3σ lower than the measurement, the CASCADE Monte Carlo prediction is about 1.8σ lower.
The prediction from the NLO calculation, corrected to hadron level, is

$$\sigma_{vis}^{NLO}(ep \to eb\bar{b}X \to ej\mu X') = 14.4^{+7.3}_{-1.1} \text{ pb.} \tag{7.4}$$

This prediction is compatible with both Monte Carlo predictions, but about 1.8σ lower than the data.

7.3 Differential Cross Sections

Differential cross sections are determined in bins of the transverse momentum of the muon and jet, pseudorapidity of the muon, Q^2 and $\log x$ and compared to the NLO and Monte Carlo predictions in the following sections. The measured cross sections and NLO predictions are given in appendix C.

7.3.1 Comparison to NLO Prediction

The NLO prediction lies below the data for most of the measured bins, with the difference at most 2 to 3σ.
A steep rise towards small Q^2 is measured (see figure 7.1). The NLO prediction for the lowest bin is compatible with the data, but the shape of the distribution is not described very well. The deviation of the prediction to the data increases towards higher Q^2, with about 2.9σ difference for the highest bin. The differential cross section as a function of the scaling variable x is shown in figure 7.2, the shape of the distribution is described reasonably well, the prediction is below the data for most of the bins.
The cross section as a function of the pseudorapidity of the muon is shown in figure 7.3. The cross section rises towards the forward region and falls for the most forward bin. The rise of the cross section is not described by the prediction. The differential cross sections as a function of the muon and jet transverse momentum fall steeply towards higher transverse momenta. The data show a steeper behaviour than the predictions, with a difference of about 2σ for the lowest bins.

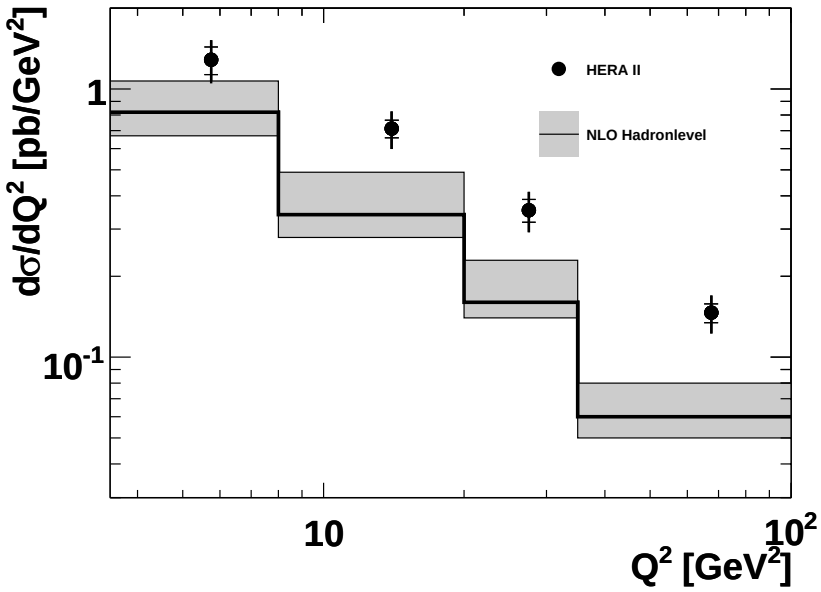

FIGURE 7.1: *Differential Born level cross section as a function of Q^2. The data is compared to the HVQDIS NLO prediction.*

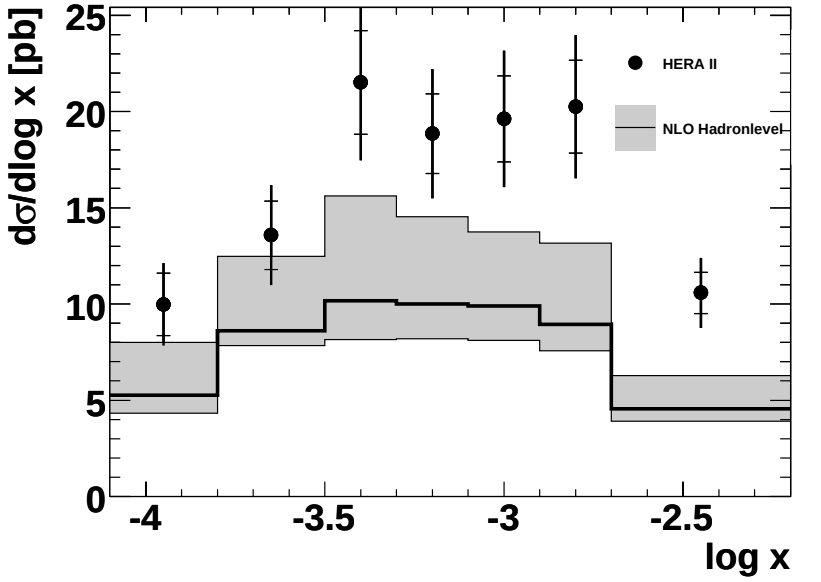

FIGURE 7.2: *Differential Born level cross section as a function of* $\log x$*. The data is compared to the HVQDIS NLO prediction.*

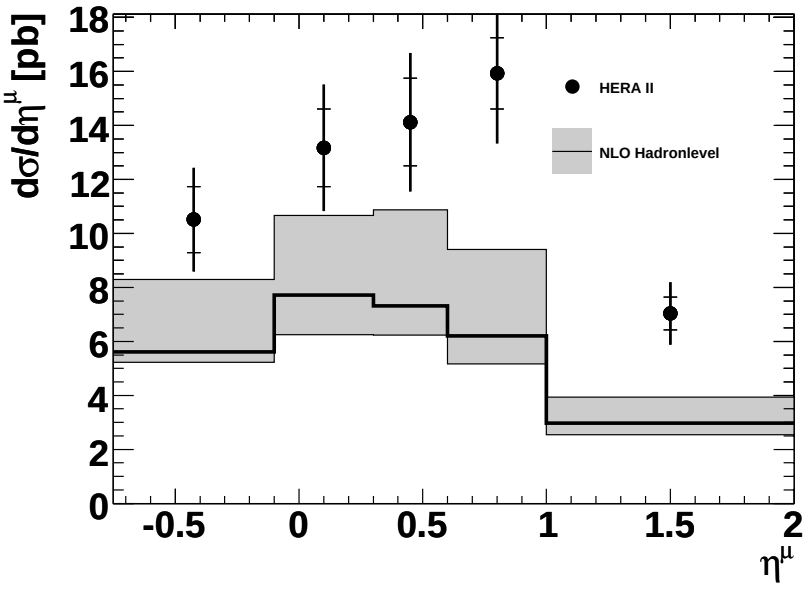

FIGURE 7.3: *Differential Born level cross section as a function of η^{μ}. The data is compared to the HVQDIS NLO prediction.*

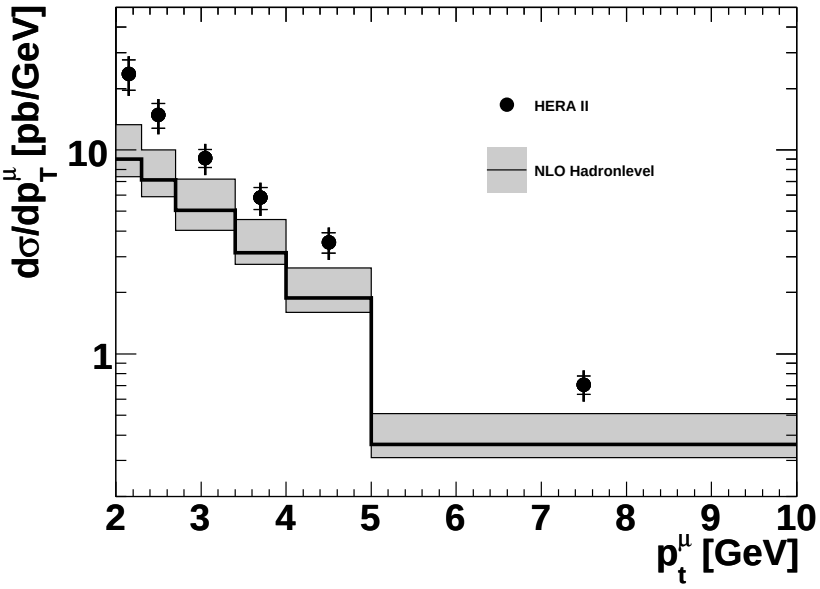

FIGURE 7.4: *Differential Born level cross section as a function of p_t^{μ}. The data is compared to the HVQDIS NLO prediction.*

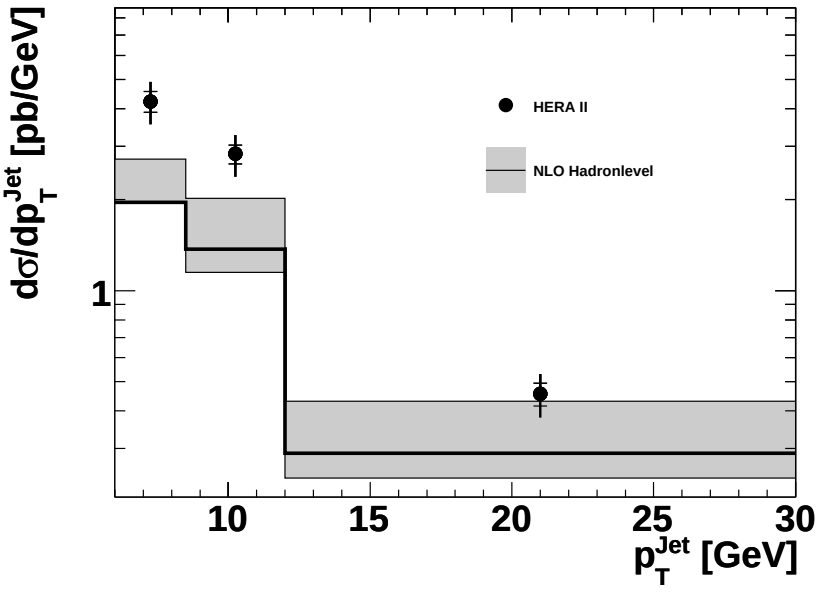

FIGURE 7.5: *Differential Born level cross section as a function of p_t^{jet}. The data is compared to the HVQDIS NLO prediction.*

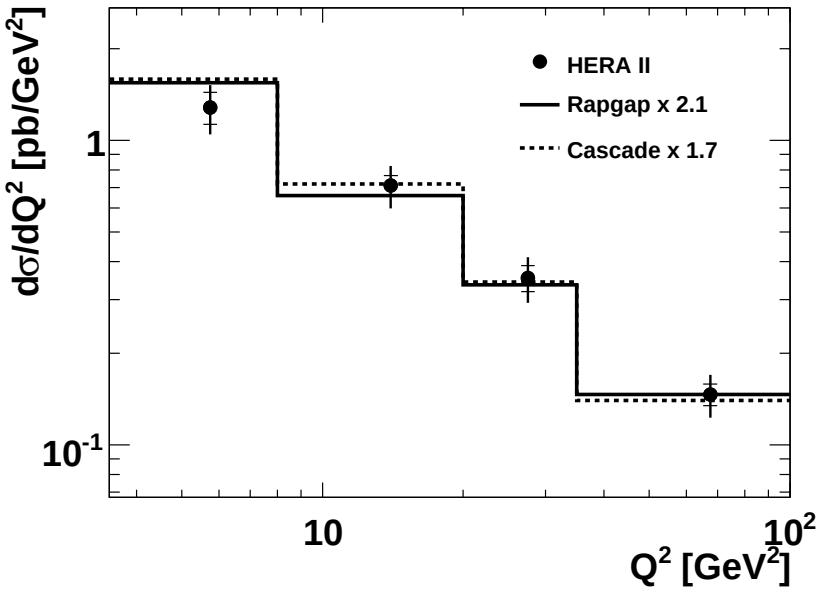

FIGURE 7.6: *Differential Born level cross section as a function of Q^2. The data is compared to RAPGAP and CASCADE Monte Carlo predictions.*

7.3.2 Comparison to Monte Carlo Prediction

The cross section measurements are compared to the predictions of the RAPGAP and CASCADE Monte Carlo generators (see figures 7.6-7.10). The predictions are scaled with a factor 2.1 and 1.7 for RAPGAP and CASCADE respectively. The scaling factors are determined from the predictions and measurements for the total visible range. With exception of the lowest Q^2 bin, where the scaled prediction is below the data, all distributions are well described in shape by the predictions. Both RAPGAP and CASCADE describe the steep rise of the cross section towards small transverse momenta (see figure 7.9). The rise of the cross section towards the forward direction of the muon is better described by the CASCADE prediction (see figure 7.8).

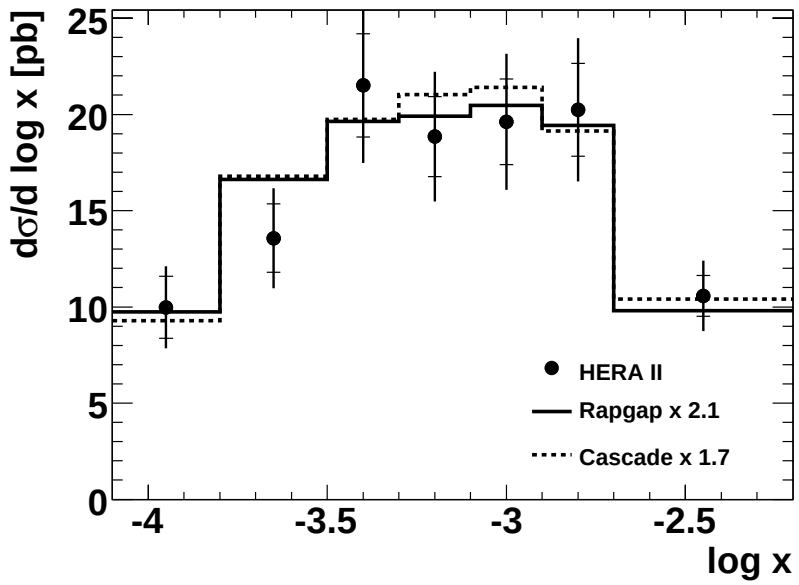

FIGURE 7.7: *Differential Born level cross section as a function of* $\log x$. *The data is compared to RAPGAP and CASCADE Monte Carlo predictions.*

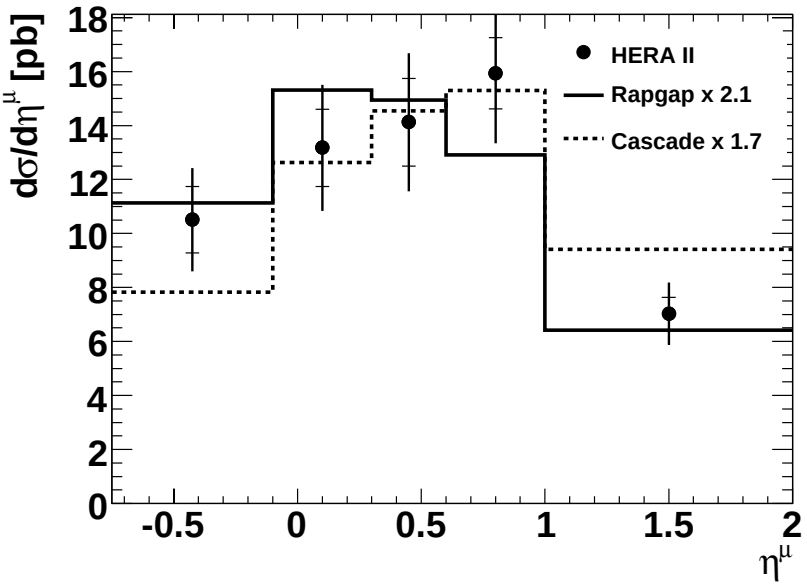

FIGURE 7.8: *Differential Born level cross section as a function of* η. *The data is compared to RAPGAP and CASCADE Monte Carlo predictions.*

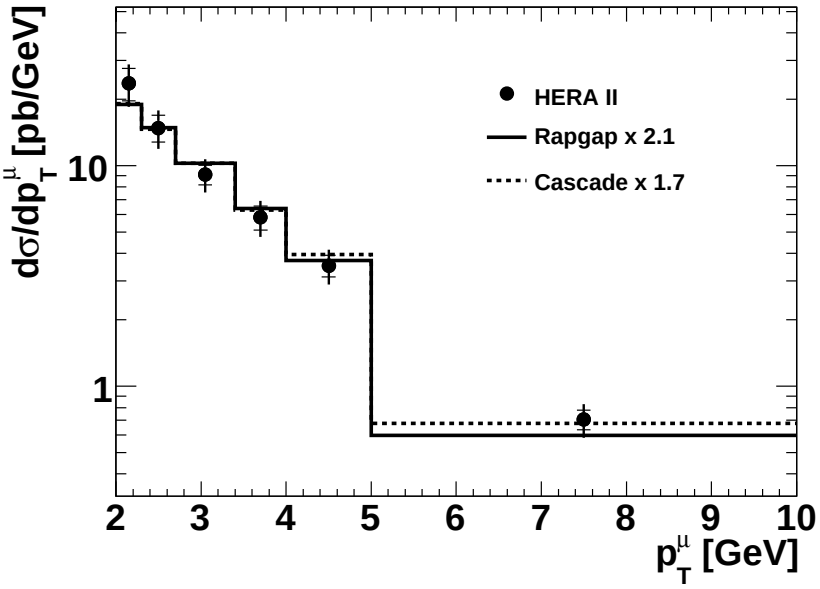

FIGURE 7.9: *Differential Born level cross section as a function of p_t^μ. The data is compared to RAPGAP and CASCADE Monte Carlo predictions.*

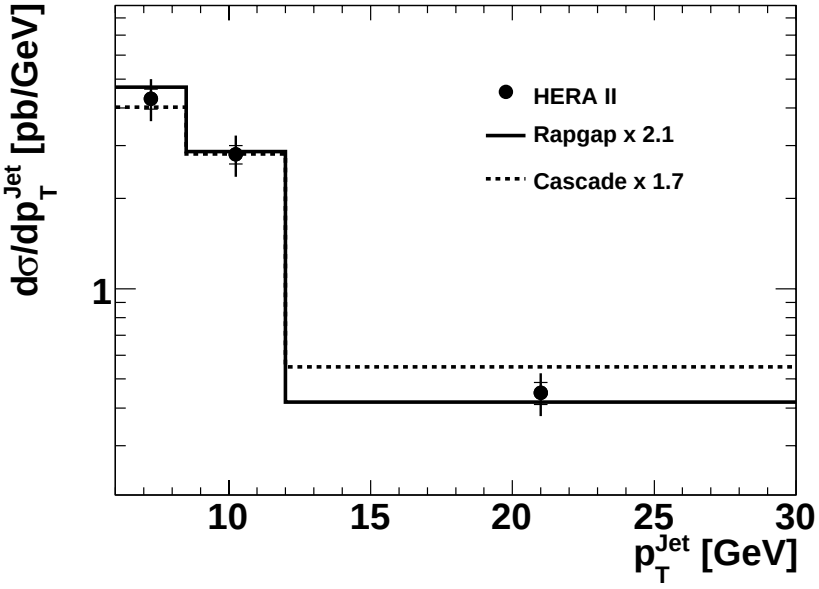

FIGURE 7.10: *Differential Born level cross section as a function of p_t^{jet}. The data is compared to RAPGAP and CASCADE Monte Carlo predictions.*

7.4 Double Differential Cross Sections

To clarify the measurements of the cross sections as a function of the jet transverse momentum, the measurement is performed double differentially for three regions of the muon pseudorapidity:

- $-0.75 < \eta < 0$
- $0 < \eta < 0.5$
- $0.5 < \eta < 2$

In addition the differential cross sections with respect to $\log x$ are measured for five Q^2 ranges:

- $3.5 < Q^2 < 7$ GeV^2
- $7 < Q^2 < 13$ GeV^2
- $13 < Q^2 < 25$ GeV^2
- $25 < Q^2 < 50$ GeV^2
- $50 < Q^2 < 100$ GeV^2

The results are tabularized in appendix C and compared to the theory predictions in the following sections.

7.4.1 Comparison to NLO Predictions

In figure 7.11 the measurements as a function of the jet transverse momentum are compared to the NLO prediction for three different bins of the muon pseudorapidity. Whereas shape and normalization are well described for the central region, the steep rise of the cross section for the forward region is not predicted by the NLO calculation. The prediction lies below the data with a difference of about 3.1σ for the lowest bin of the jet transverse momentum, but agrees within errors for large jet transverse momenta.
The measurements as a function of the scaling variable x are compared to the NLO prediction for five different bins of Q^2. In general the prediction is too low, with a deviation of at most 2.2σ.

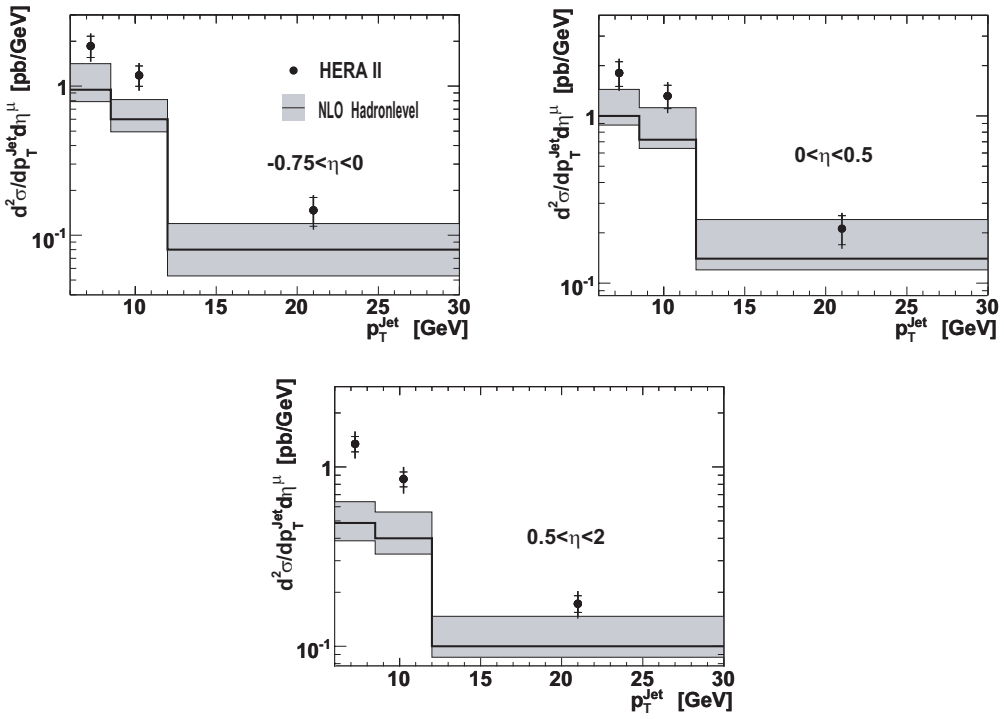

FIGURE 7.11: *Double differential Born level cross section as a function of p_t^{jet} for three different ranges of the muon pseudorapidity. The data is compared to the HVQDIS NLO prediction.*

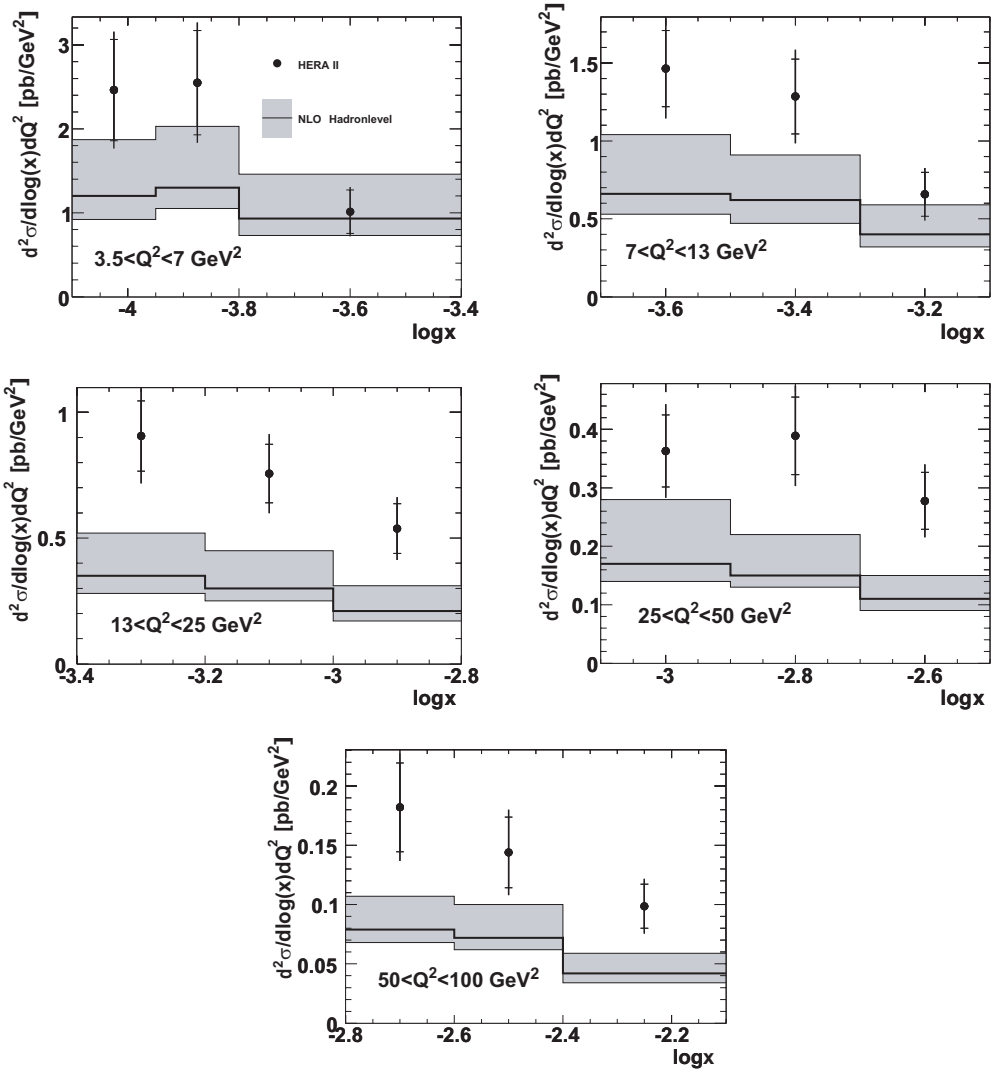

FIGURE 7.12: *Double differential Born level cross section as a function of the scaling variable x for five different Q^2 ranges. The data is compared to the HVQDIS NLO prediction.*

7.4.2 Comparison to Monte Carlo Predictions

In figure 7.13 the double differential measurements as a function of the jet transverse momentum are compared to the scaled Monte Carlo predictions. Both Monte Carlo predictions describe the data well in shape for the central and forward regions.

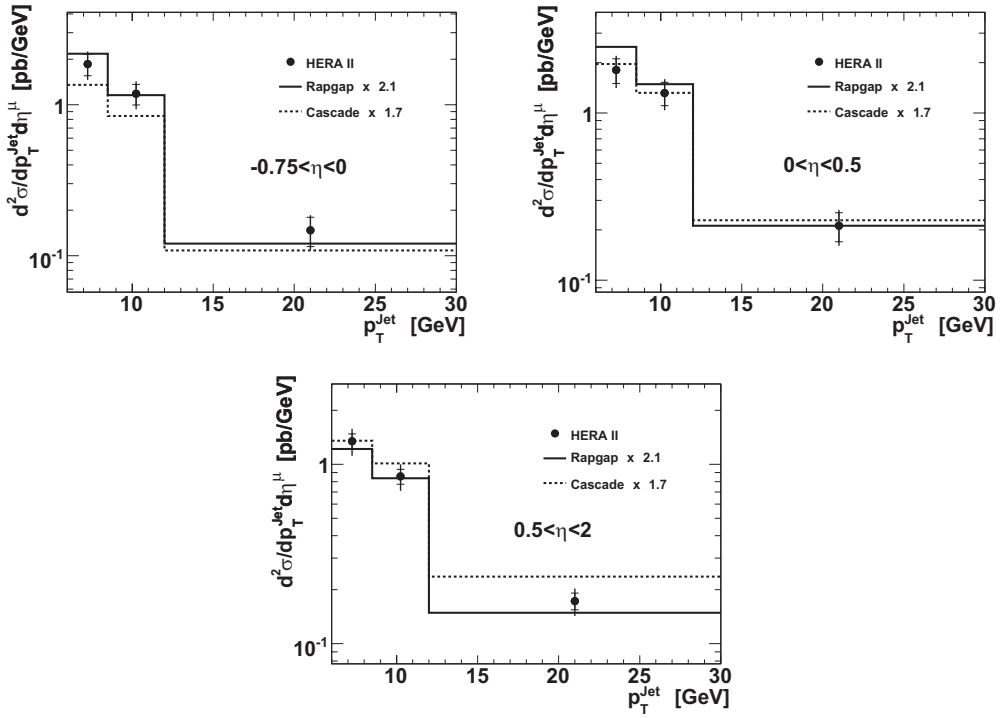

FIGURE 7.13: *Double differential Born level cross section as a function of p_t^{jet} for three different ranges of the muon pseudorapidity. The data is compared to RAPGAP and CASCADE Monte Carlo predictions.*

In figure 7.14 double differential cross sections as a function of the scaling variable x for five different Q^2 regions are shown. Both Monte Carlo predictions describe the data well in shape, with the exception of the lowest Q^2 range, where for one bin the scaled prediction is above the data.

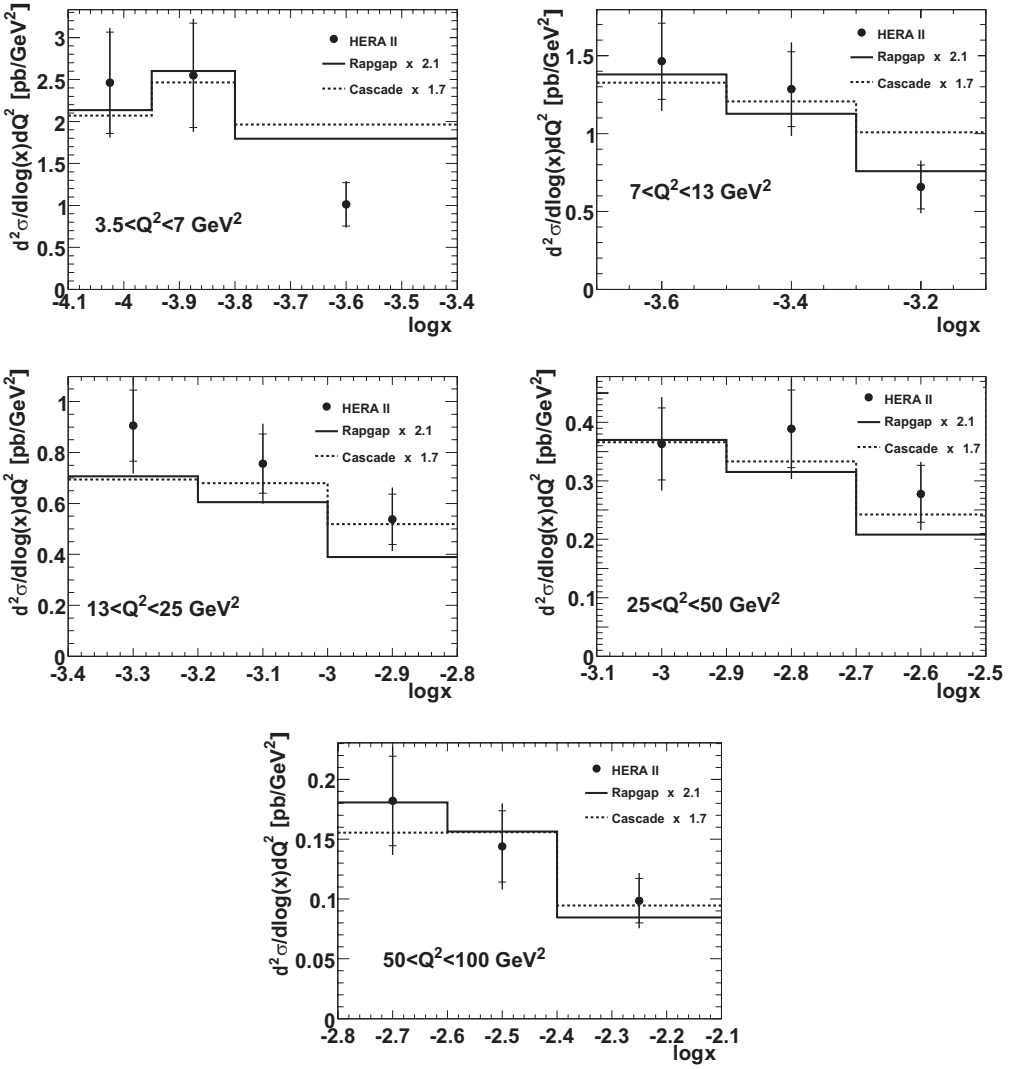

FIGURE 7.14: *Double differential Born level cross sections as a function of* $\log x$ *for five different* Q^2 *ranges.*

7.5 Analysis in the Breit Frame

To compare this measurement to a previous H1 publication [8], this analysis is repeated with a jet selection performed in the Breit frame (see section 4.4.2). Therefore all hadronic final state objects are boosted to the Breit frame (see appendix B) and the hadronic final state finder is rerun. Only the transverse momentum selection cut of the jet is performed in the Breit frame, all other cuts in the laboratory frame. To perform the pseudorapidity cut of the jet in the laboratory frame and to calculate p_t^{rel}, the Breit frame jets are boosted back to the laboratory frame.
The result for the kinematic range

- $3.5 < Q^2 < 100$ GeV^2
- $0.1 < y < 0.7$
- $p_t^\mu > 2.5$ GeV
- $-0.75 < \eta^\mu < 1.15$
- $p_t^{jet,Breit} > 6$ GeV
- $|\eta^{jet}| < 2.5$

is

$$\sigma_{vis}^{Breit}(ep \to eb\bar{b}X \to ej\mu X') = 13.4 \pm 0.9(stat.) \pm 1.9(sys.) \text{ pb}. \qquad (7.5)$$

Only about half of the events compared to the laboratory frame analysis are selected, leading to a higher statistical uncertainty of 6.7%. The same systematic uncertainty of 14% is assumed. The result of this measurement is 60% higher than the RAPGAP Monte Carlo prediction, corresponding to a deviation of about 3σ. The differential cross sections and the comparison to the RAPGAP Monte Carlo prediction are shown in figure 7.16. The RAPGAP prediction is scaled by a factor of 1.6 to account for the normalization difference. The shapes of all differential distributions are reasonably well described by the Monte Carlo prediction, no significant deviations are observed.
This Breit frame measurement is compared to the published H1 measurement by extrapolating the cross sections from the kinematic range $Q^2 > 3.5$ GeV^2 to $Q^2 > 2$ GeV^2 using the Monte Carlo prediction. The measured total cross section is scaled up by 17%, yielding

$$\sigma_{vis}^{Breit}(ep \to eb\bar{b}X \to ej\mu X') = 15.7 \pm 1.1(stat.) \pm 2.2(sys.) \pm 0.5(extrapol.) \text{ pb} \quad (7.6)$$

for the kinematic range

- $2 < Q^2 < 100$ GeV^2
- $0.1 < y < 0.7$
- $p_t^\mu > 2.5$ GeV
- $-0.75 < \eta^\mu < 1.15$
- $p_t^{jet,Breit} > 6$ GeV
- $|\eta^{jet}| < 2.5$.

The statistical error is 6.7% and a systematic uncertainty of 14% as determined in the laboratory frame analysis is assumed. The uncertainty in the extrapolation

due to the limited Monte Carlo statistics is taken into account by an additional uncertainty of 3.5% on the measurement. The result quoted in the publication is

$$\sigma_{vis}^{Breit,publication}(ep \to eb\bar{b}X \to ej\mu X') = 16.3 \pm 2.0(stat.) \pm 2.3(sys.) \text{ pb.} \quad (7.7)$$

This new HERA II measurement is in good agreement with the published result. The systematic uncertainty of this measurement is of comparable size and the statistical uncertainty is reduced due to the larger data sample.
The differential cross sections are compared in figure 7.15. Also in this case a scaling factor is applied for each individual bin according to the Monte Carlo prediction. All new HERA II data points agree even within statistical errors with the published results, except for the most forward bin of the muon pseudorapidity. A deviation of about 2σ suggest an upward fluctuation of the HERA I measurement. The lowest bins of the muon and jet transverse momenta are systematically lower for the new measurement but still in agreement within errors.

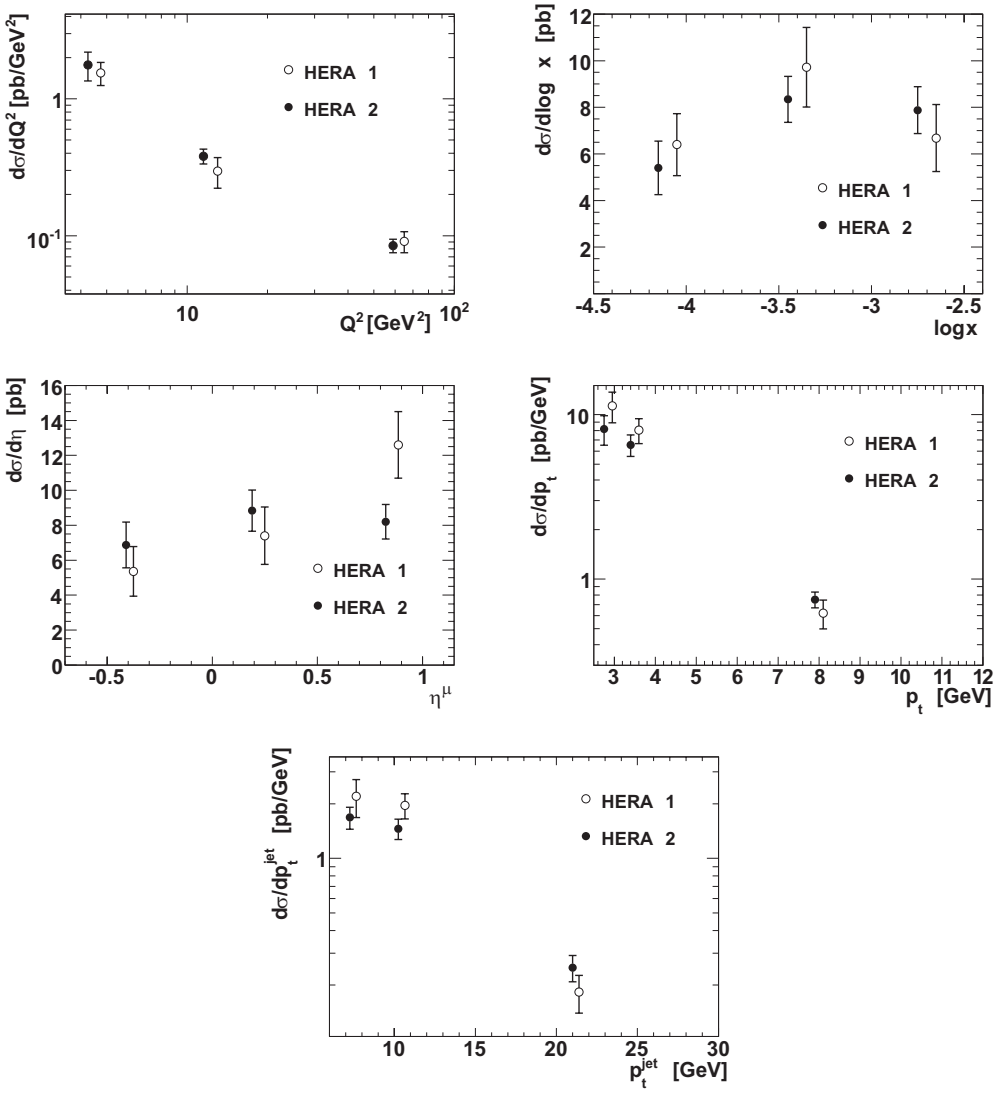

FIGURE 7.15: *Comparision of double differential cross sections measured in the Breit frame to the published HERA I measurement. Only the statistical errors are shown. For better visibility, the data points of the HERA I measurement are shifted horizontally.*

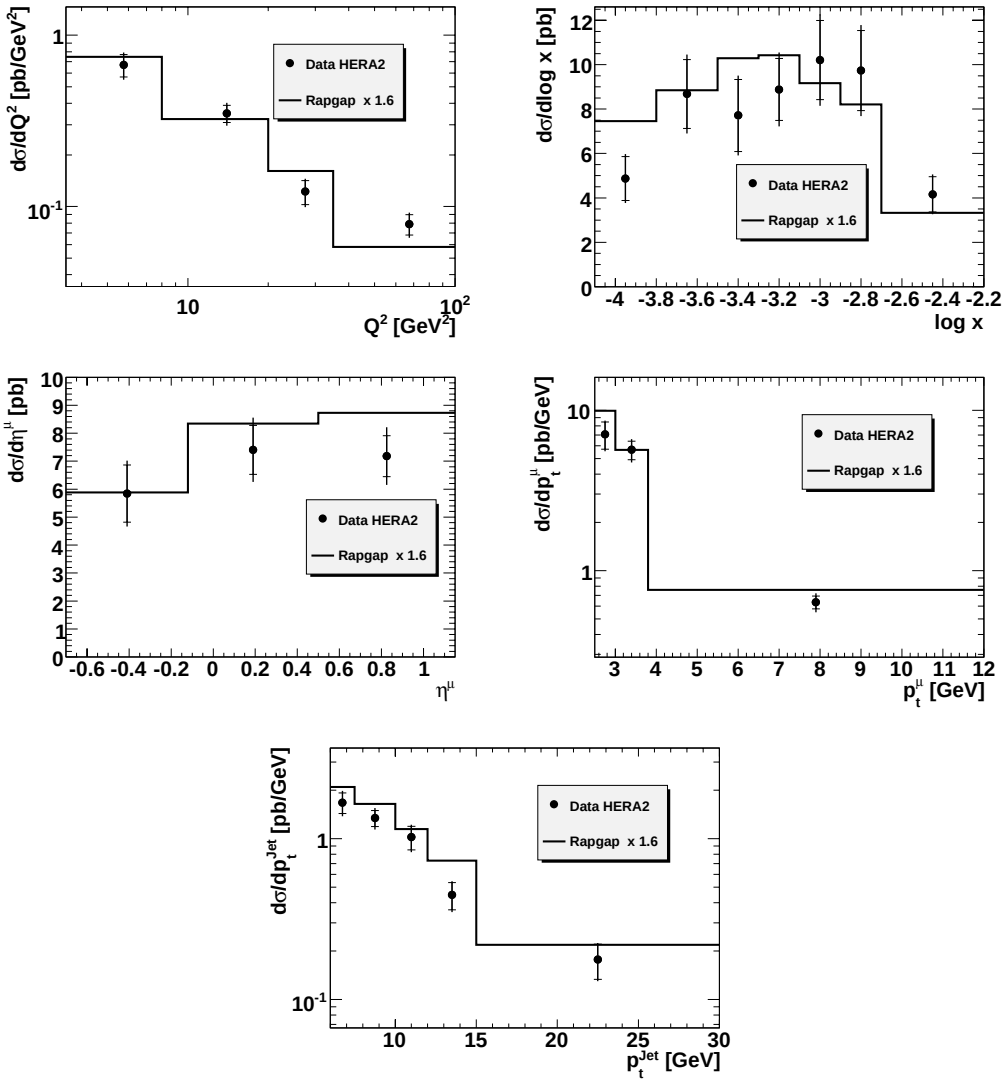

FIGURE 7.16: *Comparision of double differential cross sections measured in the Breit frame to the RAPGAP Monte Carlo prediction.*

Chapter 8

Summary and Discussion of the Results

In this analysis, open beauty quark production in deep inelastic scattering with a muon and a jet in the final state was measured with the H1 detector using approximately 285 pb^{-1} of HERA II data taken in the years 2005-2007. The beauty fraction of the event sample was determined on a statistical basis using the p_t^{rel} method which exploits the large transverse momentum with respect to the jet axis of the muon for beauty quark events. The phase space was extended to the forward region and lower transverse muon momenta compared to the previous H1 analysis [8]. All relevant systematic uncertainties were reevaluated, and the detector cuts of the muon system were optimized to obtain a high selection efficiency and a small background contribution to the sample.
For the visisble range $3.5 < Q^2 < 100$ GeV^2, $0.1 < y < 0.7$, $p_t^\mu > 2.0$ GeV, $-0.75 < \eta^\mu < 2$, $p_t^{jet} > 6$ GeV and $|\eta^{jet}| < 2.5$ where the jet is reconstructed using the inclusive k_t algorithm and selected in the laboratory frame, the total cross section was measured to be

$$\sigma_{vis}(ep \to eb\bar{b}X \to ej\mu X') = 29.3 \pm 1.3(stat) \pm 4.1(sys.) \text{ pb}. \tag{8.1}$$

The total uncertainty of the measurement was reduced compared to the previous measurement from about 19% to 15% due to the higher statistics of the data sample. The statistical uncertainty was reduced from 14% to 4.5%. Therefore it was also possible to obtain the same systematic uncertainty of 14% although no additional lifetime information as in the previous analysis was used.
The results are compared to theory predictions. The prediction of the next-to-leading order calculation in the massive scheme, using the program HVQDIS, corrected to hadron level, is

$$\sigma_{vis}^{\text{NLO}}(ep \to eb\bar{b}X \to ej\mu X') = 14.4^{+7.3}_{-1.1} \text{ pb}, \tag{8.2}$$

with a much larger uncertainty than the measurement, dominated by scale uncertainties. This prediction is about 1.8σ below the measurement, which is compatible

with the findings of the previous H1 and ZEUS measurements in DIS. Due to the large beauty mass one would expect a much better agreement.
The predictions of the Monte Carlo programs RAPGAP and CASCADE, which calculate the matrix element in leading order in the massive scheme (augmented by parton showers) and use different parton evolution schemes, are compatible with the NLO prediction. The normalization factors are 2.1 and 1.7 for RAPGAP and CASCADE respectively.

Differential cross section measurements are performed as a function of Q^2, Bjorken x, the muon pseudorapidity, and the muon and jet transverse momenta. For the forward direction, at large pseudorapidities of the muon and large Bjorken x, and small muon and jet transverse momenta, the next-to-leading order prediction is up to 2σ below the data. The rise of the cross section towards small transverse momenta is steeper than that predicted by the calculations. These results are compatible with the H1 and ZEUS HERA I measurements and the latest ZEUS HERA II results (see figures 8.1 and 8.2). The interpretation is not clear: possible explanations for this deficiency being missing higher order effects or insufficient modelling of the fragmentation process.
The next-to-leading order calculation does not describe the shape of the Q^2 distribtion very well for the small and medium Q^2 region covered in this analysis. The prediction is below the data for all bins of this measurement. This is also observed in the latest ZEUS measurement, which covers an extended Q^2 region up to 10 000 GeV^2 (see figure 8.3). The prediction agrees only for Q^2 much larger than m_b^2 and p_t^2. This may indicate that the interplay of the different scales is not fully understood.
With exception of the lowest Q^2 bin, both Monte Carlo generators describe the shape of all measured distributions very well. The rise of the cross section as a function of the muon pseudorapidity is better described by the CASCADE Monte Carlo.

The large statistics of the data sample allowed a measurement of double differential distributions. The measurement of the cross section as a function of the jet transverse momentum for three regions of the muon pseudorapidity confirms that the excess at low transverse momenta is most significant in the forward region, where the next-to-leading order calculation predicts a less steeper rise of the cross section towards small transverse momenta. The prediction is about 3σ below the data. In contrast, both Monte Carlo generators describe the shape of the distributions very well for all detector regions.
Additionally a double differential measurement of the cross section as a function of the scaling variable x is performed for different Q^2 regions. With exception of the lowest Q^2 region (which is compatible with the single differential Q^2 measurement), the shape of the distribution is well described by the prediction for all other Q^2 ranges.

As a cross check, the measurement is repeated with the reconstruction and selection performed in the Breit frame. This allows a direct comparison to the previous

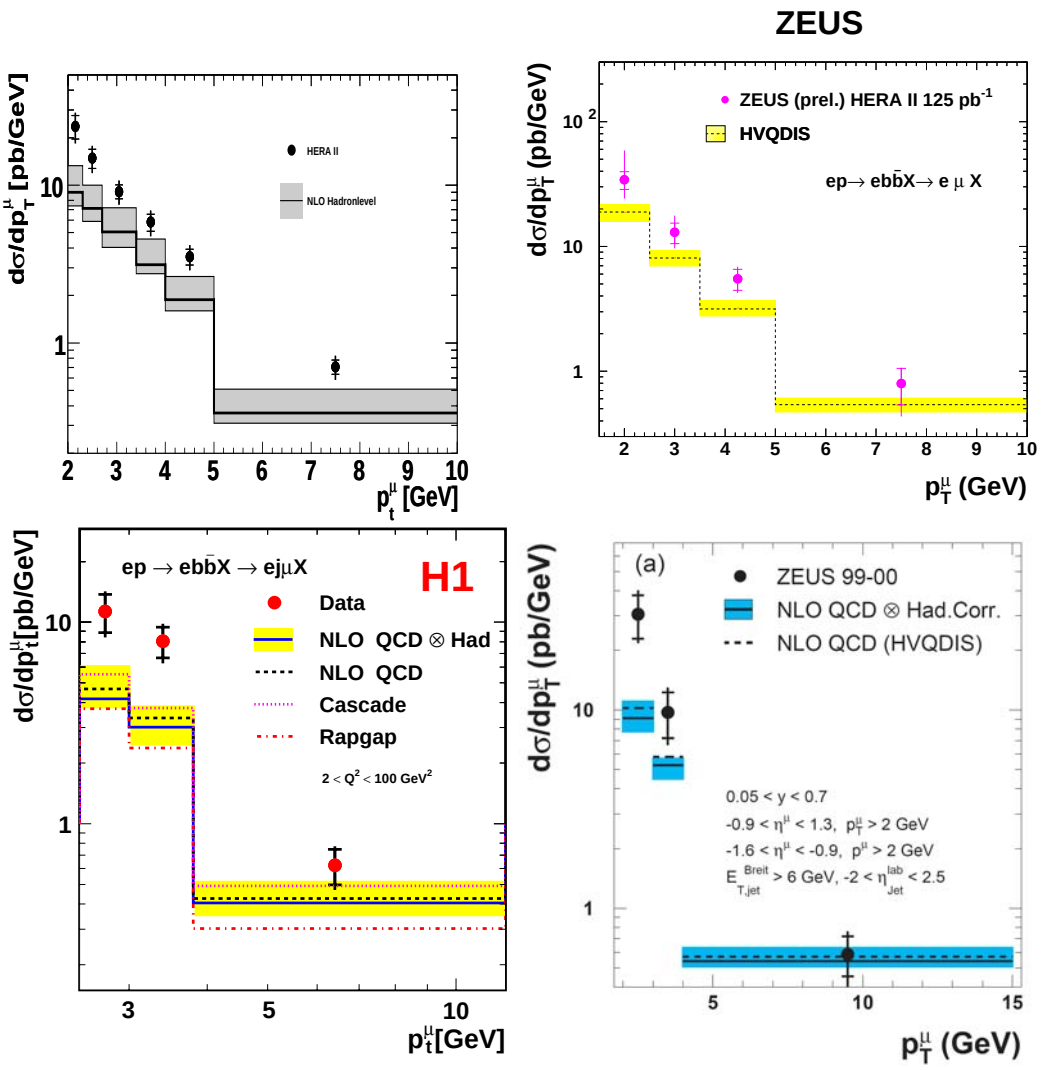

FIGURE 8.1: *Cross section measurements as a function of the muon transverse momentum. Shown are the results of the analysis presented in this thesis (upper left), of the latest ZEUS HERA II measurement using decays into a muon and a jet [38] (upper right), and of the previous H1 (lower left) [8] and ZEUS (lower right) [21] HERA I measurements.*

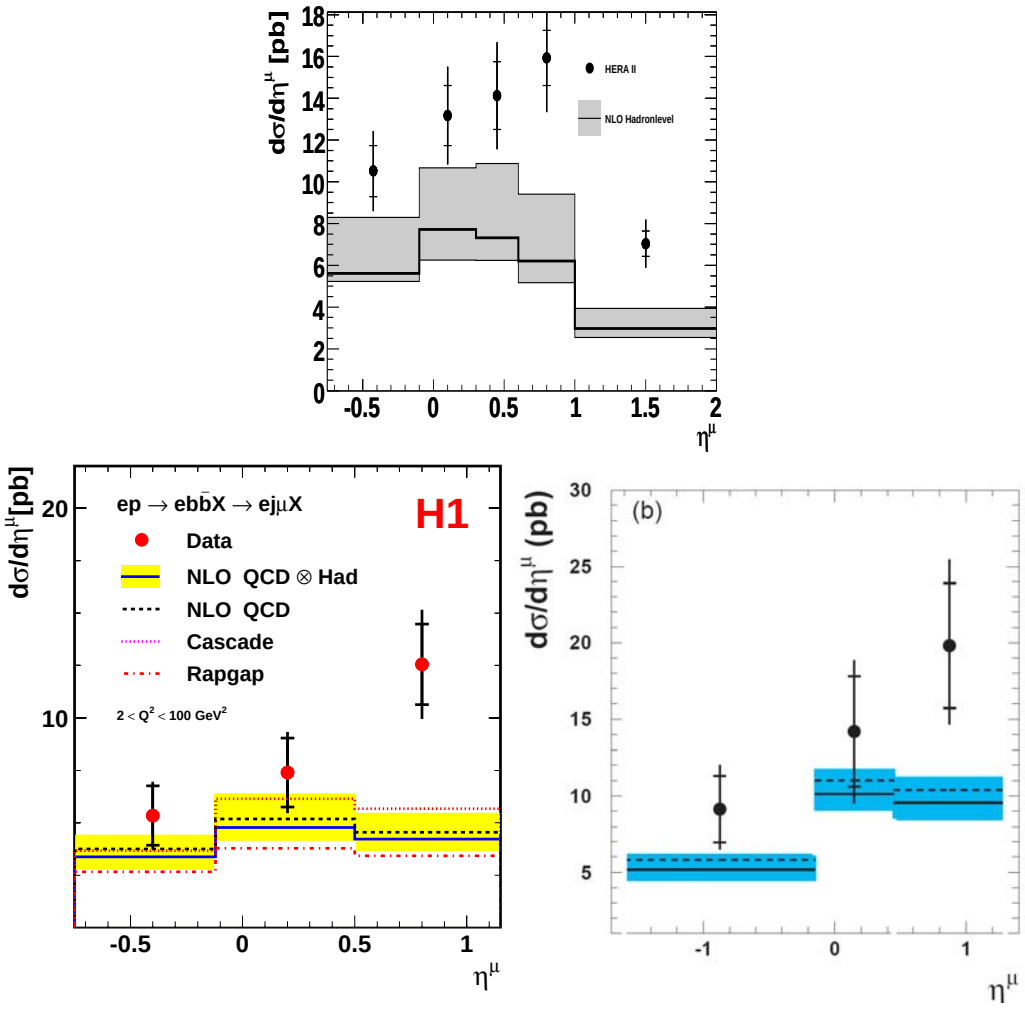

FIGURE 8.2: *Cross section measurements as a function of the muon transverse momentum. Shown are the results of the analysis presented in this thesis (upper) and of the previous H1 (lower left) [8] and ZEUS (lower right) [21] HERA I measurements.*

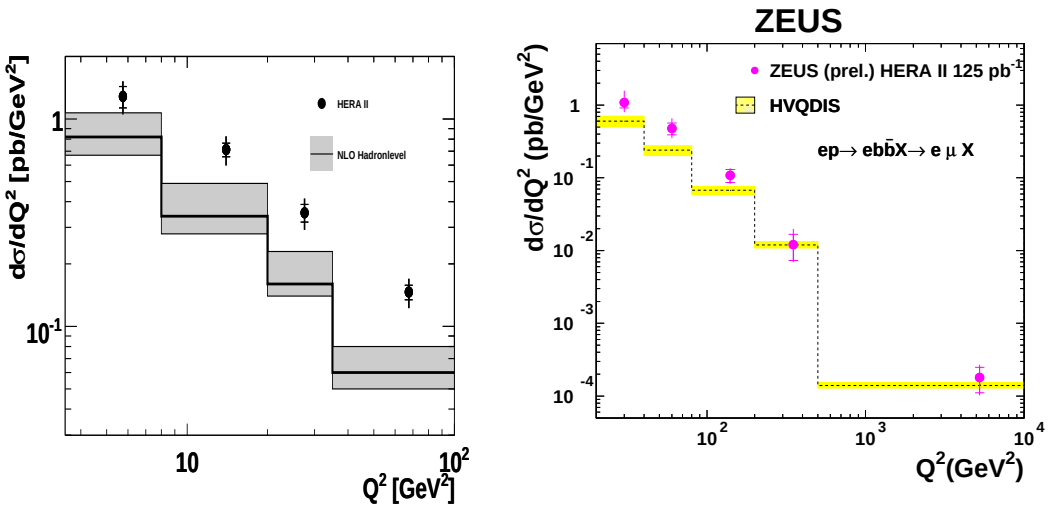

FIGURE 8.3: *Cross section measurements as a function of Q^2. Shown are the results of the analysis presented in this thesis (left) and of the latest ZEUS HERA II muon+jet measurement. [38] (right), which covers a larger Q^2 region.*

H1 results and requires only an extrapolation to lower Q^2. For the total and differential cross section measurements, both analyses agree within the statistical errors.

Chapter 9

Outlook

The measurements presented in this thesis are another step towards a better understanding of beauty quark production at HERA in deep inelastic scattering. From the experimental point of view, the high statistics and precision of the HERA II data, which will remain the last ep-data for the next few decades, has not yet been fully exploited.
Whereas a combination with HERA I data and the inclusion of the 2004 run period of HERA II will not lead to a significant increase of the statistical precision of the measurement, there is still potential to decrease the systematic uncertainties (compared to the HERA I measurements). The next step in this direction would be the additional use of lifetime information. The CST tracking detector is very well understood and delivered high precision data for a large fraction of the HERA II run period [85, 86]. Although additional sources of systematic uncertainty have to be considered, it is possible to reduce the total systematic uncertainty of the measurement by combining both p_t^{rel} and lifetime information and perfoming a two-dimensional fit to determine the beauty fraction. As an estimation of the charm and light quark content of the event sample is possible when lifetime information is used, the measurement of the contribution from light quark events is possible which allows a reduction of the model uncertainties. Furthermore, a measurement of charm quark cross sections is possible in parallel.
The results of this and other analyses show that the forward region (defined by the proton direction) is the most interesting phase space region to study. Due to the limited acceptance of the CST detector, lifetime information is not available for this region and one has to rely on the p_t^{rel} information alone. Despite the stability of this method and the good agreement between the results obtained from both methods [85], it is necessary to get an understanding of the remaining deficits in the modelling of the p_t^{rel} distribution, which were seen in this analysis. A step in this direction would be a detailed study of the jet axis resolution for different detector regions.
Besides a reduction of the systematic uncertainties, a further extension of the measured phase space region is possible. By extending the measurement to regions where the scattered electron is located in the central region, the large Q^2 domain can be

investigated. As the momentum transfer is much larger than the beauty mass and the transverse momentum of the beauty quark, a comparison to the theory predictions in this region allows a better understanding of the multi scale problem.
It was shown in this analysis that the double differential measurement is possible due to the high statistics of the data sample. It has to be investigated whether the precision is sufficient to contribute to the measurement of the beauty quark structure function F_2^b, which depends on the double differential cross sections as a function of the scaling variable x and Q^2.
As the uncertainties of the theoretical predictions are large compared to the systematic uncertainties of the measurements, also from the theory side further progress is needed to complete the picture of beauty quark production. It would be interesting to compare the data to next-to-leading order predictions. This MC@NLO [64] is not available at present. Next to next to leading order calculations (NNLO) are available from the MRST [114] group in the mixed flavour number scheme, but there are no programs existing yet for calculating single or double differential cross sections.

The focus of interest in High Energy Physics will move to the LHC (Large Hadron Collider) at CERN very soon, which is expected to discover new physics beyond the Standard Model. Nevertheless, the interpretation of the new data relies on a good understanding of standard model processes, in particular the production of heavy quarks. This is where the legacy of HERA, which has delivered the last data on electron-proton scattering for the next decades, will contribute to the exploration of the new energy frontier.

Appendix A

Run Selection

Run range	Reason
421402	FTT problem
422787-422790	FTT timing tests
422799-422811	FTT timing tests
445534-445553	FTT wrongly configured
452556-452560	FTT RO problem
458838-459181	FTT level 1 topologies not loaded
466189-466227	FTT problem (CJC2)
475320-476029	FTT level 1 problems
483626-483763	FTT problem (low efficiency)
486648-486672	FTT RO problem
487728-487812	FTT RO problem
496354-496372	FTT problem (low efficiency)
496410-496480	FTT problem (low efficiency)

TABLE A.1: *List of excluded runs*

Mnemonic	Detector component
FTP	forward tracker
CJC1	inner jet chamber
CJC2	outer jet chamber
LAr	LAr calorimeter
FTT	Fast Track Trigger
LUMI	lumi system
SPAC	SPACAL calorimeter
IronClusters	Central Muon Detector
TOF	Time of flight system

TABLE A.2: *List of requested detector components for the run selection. The mnemonics as used for the steering of the executable to perform the run selection [113] are given.*

Appendix B

Transformation to the Breit Frame

The transformation from the laboratory frame to the Breit frame requires rotations and a boost. The complete transformation that contains the boost and rotates the z axis from the laboratory frame to the Breit frame can be written in the matrix form

$$\mathcal{L}(L \to B) = R_y(\alpha')\Lambda(\beta)R_y(\alpha). \tag{B.1}$$

All components can be written in terms of the components of $q = (q_0, q_1, 0, q_3)$ which is the four momentum of the exchanged virtual photon in the laboratory frame. When defining

$$D_1^2 = q_1^2 + \left(q_3 + \frac{Q^2}{q_0 - q_3}\right)^2 \tag{B.2}$$

and

$$D_2^2 = Q^2 q_1^2 + q_0^2(q_0 - q_3)^2, \tag{B.3}$$

the Lorentz parameter is given by

$$\beta = \frac{D_1}{q_0 + Q^2/(q_0 - q_3)}, \tag{B.4}$$

the rotation about the y-axis in the HERA frame is given by

$$\sin\alpha = -\frac{q_1}{D_2}, \qquad \cos\alpha = \frac{q_3 + Q^2/(q_0 - q_3)}{D_1} \tag{B.5}$$

and the final rotation about the y axis in the Breit frame is given by

$$\sin\alpha' = \frac{Qq_1}{D_2}, \qquad \cos\alpha' = -\frac{q_0(q_0 - q_3)}{D_2}. \tag{B.6}$$

Details can be found in [54].
The overall transformation matrix takes the simple form

$$\mathcal{L}(L \to B) = \begin{pmatrix} \frac{q_0}{Q} + \frac{Q}{q_0 - q_3} & -\frac{q_1}{Q} & 0 & -\frac{q_3}{Q} - \frac{Q}{q_0 - q_3} \\ -\frac{q_1}{q_0 - q_3} & 1 & 0 & \frac{q_1}{q_0 - q_3} \\ 0 & 0 & 1 & 0 \\ \frac{q_0}{Q} & -\frac{q_1}{Q} & 0 & -\frac{q_3}{Q} \end{pmatrix}. \tag{B.7}$$

Appendix C

Cross Section Tables

		Measurement	Experimental errors		Correction factors		
η^μ-range		$d\sigma/d\eta^\mu$	stat.	sys.	f_b	ϵ_{rec}	δ_{rad}
		[pb]	[pb]	[pb]	[%]	[%]	[%]
-0.75	-0.1	10.5	1.2	1.5	18.1 ± 2.0	24.1	-1
-0.1	0.3	13.2	1.4	1.9	18.9 ± 2.0	31.1	-1
0.3	0.6	14.1	1.6	2.0	21.3 ± 2.3	34.4	-1
0.6	1.0	15.9	1.3	2.2	32.0 ± 2.5	36.1	+2
1.0	2.1	7.03	0.61	0.98	31.3 ± 2.5	34.2	+1
p_t^μ-range		$d\sigma/dp_t^\mu$	stat.	sys.	f_b	ϵ_{rec}	δ_{rad}
[GeV]		[pb/GeV]	[pb/GeV]	[pb/GeV]	[%]	[%]	[%]
2.0	2.3	23.6	4.0	3.3	20.5 ± 3.4	20.2	+1
2.3	2.7	14.8	2.1	2.1	16.9 ± 2.3	25.0	-2
2.7	3.4	9.11	0.92	1.28	18.3 ± 1.8	30.0	+2
3.4	4.0	5.83	0.72	0.82	24.8 ± 2.9	35.2	-1
4.0	5.0	3.52	0.40	0.49	33.3 ± 3.6	43.6	+2
5.0	10.0	0.706	0.072	0.100	48.5 ± 4.5	50.9	-2
p_t^{jet}-range		$d\sigma/dp_t^{jet}$	stat.	sys.	f_b	ϵ_{rec}	δ_{rad}
[GeV]		[pb/GeV]	[pb/GeV]	[pb/GeV]	[%]	[%]	[%]
6.0	8.5	4.30	0.33	0.60	19.1 ± 1.4	37.4	+2
8.5	12.0	2.80	0.20	0.39	26.0 ± 1.8	32.4	-1
12.0	30.0	0.450	0.038	0.063	32.3 ± 2.6	25.1	+1
Q^2-range		$d\sigma/dQ^2$	stat.	sys.	f_b	ϵ_{rec}	δ_{rad}
[GeV^2]		[pb/GeV^2]	[pb/GeV^2]	[pb/GeV^2]	[%]	[%]	[%]
3.5	8.0	1.28	0.15	0.18	21.5 ± 2.5	21.8	-2
8.0	20.0	0.712	0.054	0.100	26.6 ± 1.9	36.5	-2
20.0	35.0	0.353	0.035	0.050	27.2 ± 2.5	35.4	0
35.0	100.0	0.146	0.012	0.020	21.5 ± 1.7	34.2	+1
$\log x$-range		$d\sigma/d\log x$	stat.	sys.	f_b	ϵ_{rec}	δ_{rad}
		[pb]	[pb]	[pb]	[%]	[%]	[%]
-4.1	-3.8	9.98	1.62	1.40	25.2 ± 3.9	20.8	-1
-3.8	-3.5	13.6	1.8	1.9	21.4 ± 2.7	25.2	0
-3.5	-3.3	21.5	2.7	3.0	29.3 ± 3.5	30.1	+1
-3.3	-3.1	18.8	2.1	2.6	26.4 ± 2.8	35.6	+2
-3.1	-2.9	19.6	2.2	2.7	25.5 ± 2.8	35.3	-1
-2.9	-2.7	20.2	2.4	2.8	25.8 ± 2.9	34.7	+2
-2.7	-2.2	10.6	1.1	1.5	20.2 ± 2.0	40.3	-1

TABLE C.1: *Differential cross sections for the process* $ep \to eb\bar{b}X \to ej\mu X'$ *in the kinematic range* $3.5 < Q^2 < 100$ GeV^2, $0.1 < y < 0.7$, $p_t^\mu > 2$ GeV, $-0.75 < \eta^\mu < 2.0$, $p_t^{jet} > 6$ GeV and $|\eta^{jet}| \leq 2.5$. *Also given are correction factors as obtained from the Monte Carlo simulation and the beauty fractions of the event sample.*

		Measurement	Experimental errors		Correction factors		
p_t^{jet}-range [GeV]		$d\sigma/(dp_t^{jet}d\eta^{\mu})$ [pb/GeV]	stat. [pb/GeV]	sys. [pb/GeV]	f_b [%]	ϵ_{rec} [%]	δ_{rad} [%]
6.0	8.5	1.86	0.30	0.26	14.6 ± 2.3	30.4	+2
8.5	12.0	1.18	0.18	0.17	23.8 ± 3.5	24.6	-4
12.0	30.0	0.147	0.032	0.021	34.3 ± 6.9	15.8	-1

TABLE C.2: *Differential cross sections as a function of the transverse momentum of the jet in the kinematic range* $3.5 < Q^2 < 100$ GeV^2, $0.1 < y < 0.7$, $p_t^{\mu} > 2$ GeV, $\mathbf{-0.75 < \eta^{\mu} < 0}$, $p_t^{jet} > 6$ GeV and $|\eta^{jet}| \leq 2.5$. *Also given are correction factors as obtained from the Monte Carlo simulation and the beauty fractions of the event sample.*

		Measurement	Experimental errors		Correction factors		
p_t^{jet}-range [GeV]		$d\sigma/(dp_t^{jet}d\eta^{\mu})$ [pb/GeV]	stat. [pb/GeV]	sys. [pb/GeV]	f_b [%]	ϵ_{rec} [%]	δ_{rad} [%]
6.0	8.5	1.81	0.30	0.25	14.6 ± 2.4	38.1	0
8.5	12.0	1.32	0.21	0.18	22.0 ± 3.3	32.1	-1
12.0	30.0	0.211	0.042	0.030	26.5 ± 4.9	22.3	-2

TABLE C.3: *Differential cross sections as a function of the transverse momentum of the jet in the kinematic range* $3.5 < Q^2 < 100$ GeV^2, $0.1 < y < 0.7$, $p_t^{\mu} > 2$ GeV, $\mathbf{0 < \eta^{\mu} < 0.5}$, $p_t^{jet} > 6$ GeV and $|\eta^{jet}| \leq 2.5$. *Also given are correction factors as obtained from the Monte Carlo simulation and the beauty fractions of the event sample.*

		Measurement	Experimental errors		Correction factors		
p_t^{jet}-range [GeV]		$d\sigma/(dp_t^{jet}d\eta^{\mu})$ [pb/GeV]	stat. [pb/GeV]	sys. [pb/GeV]	f_b [%]	ϵ_{rec} [%]	δ_{rad} [%]
6.0	8.5	1.35	0.13	0.19	28.4 ± 2.7	41.6	+3
8.5	12.0	0.856	0.082	0.120	28.6 ± 2.6	36.6	+1
12.0	30.0	0.173	0.018	0.024	34.3 ± 3.4	28.5	-2

TABLE C.4: *Differential cross sections as a function of the transverse momentum of the jet in the kinematic range* $3.5 < Q^2 < 100$ GeV^2, $0.1 < y < 0.7$, $p_t^{\mu} > 2$ GeV, $\mathbf{0.5 < \eta^{\mu} < 2}$, $p_t^{jet} > 6$ GeV and $|\eta^{jet}| \leq 2.5$. *Also given are correction factors as obtained from the Monte Carlo simulation and the beauty fractions of the event sample.*

		Measurement	Experimental errors		Correction factors		
$\log x$-range		$d\sigma/(d\log x dQ^2)$	stat.	sys.	f_b	ϵ_{rec}	δ_{rad}
		[pb]	[pb]	[pb]	[%]	[%]	[%]
-4.1	-3.95	2.46	0.60	0.34	26.7 ± 6.2	19.8	-2
-3.95	-3.8	2.55	0.62	0.36	23.9 ± 5.6	20.1	-1
-3.8	-3.4	1.01	0.26	0.14	15.1 ± 3.7	16.2	-1

TABLE C.5: *Differential cross sections as a function of the scaling variable x in the kinematic range* $\mathbf{3.5 < Q^2 < 7.0\ GeV^2}$, $0.1 < y < 0.7$, $p_t^\mu > 2$ GeV, $-0.75 < \eta^\mu < 2.0$, $p_t^{jet} > 6$ GeV and $|\eta^{jet}| \leq 2.5$. *Also given are correction factors as obtained from the Monte Carlo simulation and the beauty fractions of the event sample.*

		Measurement	Experimental errors		Correction factors		
$\log x$-range		$d\sigma/(d\log x dQ^2)$	stat.	sys.	f_b	ϵ_{rec}	δ_{rad}
		[pb/GeV^2]	[pb]	[pb]	[%]	[%]	[%]
-3.7	-3.5	1.46	0.25	0.20	24.9 ± 3.9	33.9	-6
-3.5	-3.3	1.29	0.24	0.18	31.3 ± 5.6	39.0	0
-3.3	-3.1	0.658	0.141	0.092	22.3 ± 4.6	45.8	-1

TABLE C.6: *Differential cross sections as a function of the scaling variable x in the kinematic range* $\mathbf{7.0 < Q^2 < 13.0\ GeV^2}$, $0.1 < y < 0.7$, $p_t^\mu > 2$ GeV, $-0.75 < \eta^\mu < 2.0$, $p_t^{jet} > 6$ GeV and $|\eta^{jet}| \leq 2.5$. *Also given are correction factors as obtained from the Monte Carlo simulation and the beauty fractions of the event sample.*

		Measurement	Experimental errors		Correction factors		
$\log x$-range		$d\sigma/(d\log x dQ^2)$	stat.	sys.	f_b	ϵ_{rec}	δ_{rad}
		[pb/GeV^2]	[pb]	[pb]	[%]	[%]	[%]
-3.4	-3.2	0.906	0.140	0.127	32.2 ± 4.7	34.1	0
-3.2	-3.0	0.756	0.116	0.106	29.3 ± 4.2	39.5	-3
-3.0	-2.8	0.538	0.100	0.075	27.8 ± 4.8	44.8	-8

TABLE C.7: *Differential cross sections as a function of the scaling variable x in the kinematic range* $\mathbf{13 < Q^2 < 25\ GeV^2}$, $0.1 < y < 0.7$, $p_t^\mu > 2$ GeV, $-0.75 < \eta^\mu < 2.0$, $p_t^{jet} > 6$ GeV and $|\eta^{jet}| \leq 2.5$. *Also given are correction factors as obtained from the Monte Carlo simulation and the beauty fractions of the event sample.*

		Measurement	Experimental errors		Correction factors		
$\log x$-range		$d\sigma/(d\log x dQ^2)$	stat.	sys.	f_b	ϵ_{rec}	δ_{rad}
		[pb]	[pb]	[pb]	[%]	[%]	[%]
-3.1	-2.9	0.363	0.062	0.051	27.0 ± 4.3	32.9	-1
-2.9	-2.7	0.389	0.066	0.054	26.6 ± 4.3	38.0	-5
-2.7	-2.5	0.278	0.049	0.039	24.6 ± 4.1	46.5	-9

TABLE C.8: *Differential cross sections as a function of the scaling variable x in the kinematic range* $\mathbf{25 < Q^2 < 50\ GeV^2}$, $0.1 < y < 0.7$, $p_t^\mu > 2$ GeV, $-0.75 < \eta^\mu < 2.0$, $p_t^{jet} > 6$ GeV and $|\eta^{jet}| \leq 2.5$. *Also given are correction factors as obtained from the Monte Carlo simulation and the beauty fractions of the event sample.*

		Measurement	Experimental errors		Correction factors		
$\log x$-range		$d\sigma/(d\log x dQ^2)$	stat.	sys.	f_b	ϵ_{rec}	δ_{rad}
		[pb]	[pb]	[pb]	[%]	[%]	[%]
-2.8	-2.6	0.182	0.037	0.025	27.1 ± 5.3	28.3	+5
-2.6	-2.4	0.144	0.030	0.020	16.2 ± 3.3	37.1	-2
-2.4	-2.1	0.099	0.019	0.014	19.2 ± 3.5	46.9	-2

TABLE C.9: *Differential cross sections as a function of the scaling variable x in the kinematic range* $\mathbf{50 < Q^2 < 100\ GeV^2}$, $0.1 < y < 0.7$, $p_t^\mu > 2$ GeV, $-0.75 < \eta^\mu < 2.0$, $p_t^{jet} > 6$ GeV and $|\eta^{jet}| \leq 2.5$. *Also given are correction factors as obtained from the Monte Carlo simulation and the beauty fractions of the event sample.*

		NLO prediction	Theor. uncertainty	Correction to hadron level
η^μ-range		$d\sigma/d\eta^\mu$	Sys.	$C_h - 1$
		[pb]	[pb]	[%]
-0.75	-0.1	5.61	$^{+2.69}_{-3.81}$	-10.0
-0.1	0.3	7.72	$^{+2.94}_{-1.47}$	-9.2
0.3	0.6	7.31	$^{+3.56}_{-1.07}$	-8.6
0.6	1.0	6.21	$^{+3.20}_{-1.04}$	-8.0
1.0	2.1	2.97	$^{+0.97}_{-0.42}$	-8.2
p_t^μ-range		$d\sigma/dp_t^\mu$	Sys.	$C_h - 1$
[GeV]		[pb/GeV]	[pb/GeV]	[%]
2.0	2.3	9.00	$^{+4.30}_{-1.63}$	-11.5
2.3	2.7	7.12	$^{+2.89}_{-1.22}$	-11.0
2.7	3.4	5.05	$^{+2.15}_{-1.02}$	-10.5
3.4	4.0	3.13	$^{+1.43}_{-0.38}$	-8.5
4.0	5.0	1.88	$^{+0.76}_{-0.28}$	-6.0
5.0	10.0	0.36	$^{+0.15}_{-0.05}$	-0.5
p_t^{jet}-range		$d\sigma/dp_t^{jet}$	Sys.	$C_h - 1$
[GeV]		[pb/GeV]	[pb/GeV]	[%]
6.0	8.5	1.96	$^{+0.76}_{-0.00}$	-17.0
8.5	12.0	1.37	$^{+0.65}_{-0.22}$	-10.5
12.0	30.0	0.29	$^{+0.14}_{-0.05}$	+10.0

TABLE C.10: *Predictions from next-to-leading order QCD calculations in the kinematic range* $3.5 < Q^2 < 100$ GeV^2, $0.1 < y < 0.7$, $p_t^\mu > 2$ GeV, $-0.75 < \eta^\mu < 2.0$, $p_t^{jet} > 6$ GeV and $|\eta^{jet}| \leq 2.5$.

		NLO prediction	Theor. uncertainty	Correction to hadron level
Q^2-range		$d\sigma/dQ^2$	Sys.	$C_h - 1$
[GeV^2]		[pb/GeV^2]	[pb/GeV^2]	[%]
3.5	8.0	0.82	$^{+0.25}_{-0.15}$	-9.0
8.0	20.0	0.34	$^{+0.15}_{-0.06}$	-10.0
20.0	35.0	0.16	$^{+0.07}_{-0.02}$	-9.5
35.0	100.0	0.06	$^{+0.02}_{-0.01}$	-7.5
$\log x$-range		$d\sigma/d\log x$	Sys.	$C_h - 1$
		[pb]	[pb]	[%]
-4.1	-3.8	5.26	$^{+2.74}_{-0.93}$	-7.2
-3.8	-3.5	8.61	$^{+3.87}_{-0.77}$	-9.4
-3.5	-3.3	10.17	$^{+5.45}_{-2.03}$	-9.6
-3.3	-3.1	10.01	$^{+4.53}_{-1.82}$	-9.0
-3.1	-2.9	9.90	$^{+3.85}_{-1.80}$	-10.0
-2.9	-2.7	8.95	$^{+4.22}_{-1.34}$	-8.2
-2.7	-2.2	4.55	$^{+1.72}_{-0.64}$	-9.0

TABLE C.11: *Predictions from next-to-leading order QCD calculations in the kinematic range* $3.5 < Q^2 < 100$ GeV^2, $0.1 < y < 0.7$, $p_t^\mu > 2$ GeV, $-0.75 < \eta^\mu < 2.0$, $p_t^{jet} > 6$ GeV and $|\eta^{jet}| \leq 2.5$.

		NLO prediction	Theor. uncertainty	Correction to hadron level
p_t^{jet}-range [GeV]		$d\sigma/(dp_t^{jet}d\eta^{\mu})$ [pb/GeV]	sys. [pb/GeV]	$C_h - 1$ [%]
6.0	8.5	0.95	$^{+0.47}_{-0.15}$	-17
8.5	12.0	0.60	$^{+0.22}_{-0.11}$	-9
12.0	30.0	0.09	$^{+0.04}_{-0.02}$	+13

TABLE C.12: *Predictions from next-to-leading order QCD calculations in the kinematic range* $3.5 < Q^2 < 100$ GeV^2, $0.1 < y < 0.7$, $p_t^{\mu} > 2$ GeV, $\mathbf{-0.75 < \eta^{\mu} < 0}$, $p_t^{jet} > 6$ GeV and $|\eta^{jet}| \leq 2.5$.

		NLO prediction	Theor. uncertainty	Correction to hadron level
p_t^{jet}-range [GeV]		$d\sigma/(dp_t^{jet}d\eta^{\mu})$ [pb/GeV]	sys. [pb/GeV]	$C_h - 1$ [%]
6.0	8.5	1.00	$^{+0.45}_{-0.13}$	-17
8.5	12.0	0.72	$^{+0.40}_{-0.08}$	-11
12.0	30.0	0.14	$^{+0.09}_{-0.02}$	+11

TABLE C.13: *Predictions from next-to-leading order QCD calculations in the kinematic range* $3.5 < Q^2 < 100$ GeV^2, $0.1 < y < 0.7$, $p_t^{\mu} > 2$ GeV, $\mathbf{0 < \eta^{\mu} < 0.5}$, $p_t^{jet} > 6$ GeV and $|\eta^{jet}| \leq 2.5$.

		NLO prediction	Theor. uncertainty	Correction to hadron level
p_t^{jet}-range [GeV]		$d\sigma/(dp_t^{jet}d\eta^{\mu})$ [pb/GeV]	sys. [pb/GeV]	$C_h - 1$ [%]
6.0	8.5	0.49	$^{+0.16}_{-0.10}$	-17
8.5	12.0	0.40	$^{+0.16}_{-0.07}$	-11
12.0	30.0	0.10	$^{+0.04}_{-0.01}$	+8

TABLE C.14: *Predictions from next-to-leading order QCD calculations in the kinematic range* $3.5 < Q^2 < 100$ GeV^2, $0.1 < y < 0.7$, $p_t^{\mu} > 2$ GeV, $\mathbf{0.5 < \eta^{\mu} < 2.0}$, $p_t^{jet} > 6$ GeV and $|\eta^{jet}| \leq 2.5$.

		NLO prediction	Theor. uncertainty	Correction to hadron level
$\log x$-range		$d\sigma/d\log x$	Sys.	$C_h - 1$
		[pb]	[pb]	[%]
-4.1	-3.95	1.20	$^{+0.67}_{-0.18}$	-7
-3.95	-3.8	1.30	$^{+0.73}_{-0.25}$	-8
-3.8	-3.4	0.93	$^{+0.53}_{-0.20}$	-12

TABLE C.15: *Predictions from next-to-leading order QCD calculations in the kinematic range* $\mathbf{3.5 < Q^2 < 7.0\ GeV^2}$, $0.1 < y < 0.7$, $p_t^\mu > 2$ GeV, $-0.75 < \eta^\mu < 2.0$, $p_t^{jet} > 6$ GeV and $|\eta^{jet}| \leq 2.5$.

		NLO prediction	Theor. uncertainty	Correction to hadron level
$\log x$-range		$d\sigma/d\log x$	Sys.	$C_h - 1$
		[pb]	[pb]	[%]
-3.7	-3.5	0.66	$^{+0.38}_{-0.13}$	-9
-3.5	-3.3	0.62	$^{+0.29}_{-0.15}$	-9
-3.3	-3.1	0.40	$^{+0.19}_{-0.08}$	-13

TABLE C.16: *Predictions from next-to-leading order QCD calculations in the kinematic range* $\mathbf{7 < Q^2 < 13\ GeV^2}$, $0.1 < y < 0.7$, $p_t^\mu > 2$ GeV, $-0.75 < \eta^\mu < 2.0$, $p_t^{jet} > 6$ GeV and $|\eta^{jet}| \leq 2.5$.

		NLO prediction	Theor. uncertainty	Correction to hadron level
$\log x$-range		$d\sigma/d\log x$	Sys.	$C_h - 1$
		[pb]	[pb]	[%]
-3.4	-3.2	0.35	$^{+0.17}_{-0.07}$	-8
-3.2	-3.0	0.30	$^{+0.15}_{-0.05}$	-10
-3.0	-2.8	0.21	$^{+0.10}_{-0.04}$	-13

TABLE C.17: *Predictions from next-to-leading order QCD calculations in the kinematic range* $\mathbf{13 < Q^2 < 25\ GeV^2}$, $0.1 < y < 0.7$, $p_t^\mu > 2$ GeV, $-0.75 < \eta^\mu < 2.0$, $p_t^{jet} > 6$ GeV and $|\eta^{jet}| \leq 2.5$.

		NLO prediction	Theor. uncertainty	Correction to hadron level
$\log x$-range		$d\sigma/d\log x$	Sys.	$C_h - 1$
		[pb]	[pb]	[%]
-3.1	-2.9	0.17	$^{+0.11}_{-0.03}$	-9
-2.9	-2.7	0.15	$^{+0.07}_{-0.02}$	-10
-2.7	-2.5	0.11	$^{+0.04}_{-0.02}$	-11

TABLE C.18: *Predictions from next-to-leading order QCD calculations in the kinematic range* $\mathbf{25 < Q^2 < 50\ GeV^2}$, $0.1 < y < 0.7$, $p_t^\mu > 2$ GeV, $-0.75 < \eta^\mu < 2.0$, $p_t^{jet} > 6$ GeV and $|\eta^{jet}| \leq 2.5$.

		NLO prediction	Theor. uncertainty	Correction to hadron level
$\log x$-range		$d\sigma/d\log x$	Sys.	$C_h - 1$
		[pb]	[pb]	[%]
-2.8	-2.6	0.08	$^{+0.03}_{-0.01}$	-7
-2.6	-2.4	0.07	$^{+0.03}_{-0.01}$	-8
-2.4	-2.1	0.04	$^{+0.02}_{-0.01}$	-9

TABLE C.19: *Predictions from next-to-leading order QCD calculations in the kinematic range* $\mathbf{50 < Q^2 < 100\ GeV^2}$, $0.1 < y < 0.7$, $p_t^\mu > 2$ GeV, $-0.75 < \eta^\mu < 2.0$, $p_t^{jet} > 6$ GeV and $|\eta^{jet}| \leq 2.5$.

Appendix D

Level 1 Z-Vertex Trigger

D.1 Overview

The successfull HERA II physics program is based on the four to five times higher instantaneous luminosity that was delivered to the experiments. The upgrade of the storage ring required an upgrade of the detectors. For the H1 detector it was decided to keep the reliable data acquisition electronics and to increase the sensitivity of the experiment to interesting events instead. Therefore new trigger electronics and algorithms were developed, based on signals from different subdetectors. The jet trigger was designed to recognise local energy depositions in the liquid argon calorimeter. The DCRPhi trigger [119] was replaced by the Fast Track Trigger (FTT) [30, 49], both processing drift chamber information.
One important part of the trigger upgrade was the replacement of the CIP detector by an improved detector consisting of five instead of three layers and new trigger electronics [115]. Only by rejecting beam induced background, like beam gas and beam wall events (see figure D.1), at an early stage at level 1, an efficient use of the trigger bandwith for all other physics triggers was possible. Nevertheless, at the beginning of the HERA II data taking the CIP was still in the commissioning phase

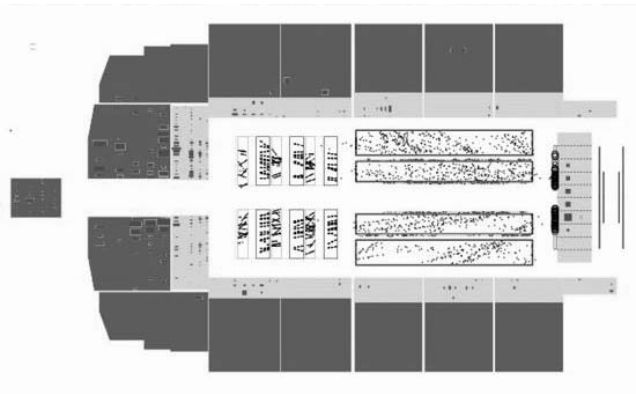

FIGURE D.1: *Event display of a beam gas induced background event.*

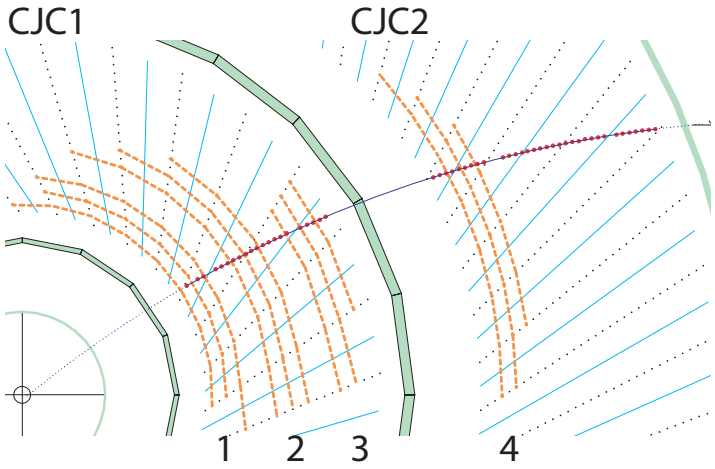

FIGURE D.2: *A radial view of the FTT, the CJC wires used by the FTT are indicated as dashed lines. Only the three inner FTT layers of CJC1 are used for the z vertex trigger.*

and only three out of five layers were operational. This was accompanied by very high beam induced backgrounds. It was highly desirable to have a backup solution for the CIP trigger, therefore studies were conducted that demonstrated the feasibility of a z vertex trigger based on drift chamber signals at level 1 by extending the FTT functionality [36]. For this only a minimum of additional hardware was necessary. The corresponding interfaces for this upgrade were introduced from the beginning in the design of the FTT data flow and the algorithms were finally implemented within the work of this thesis.
In the following a brief overview of the FTT is given followed by a discussion of the z vertex trigger algorithm.

D.1.1 Fast Track Trigger

In order to cope with the higher rates after the HERA II upgrade and to increase the selectivity, the Fast Track Trigger was built to replace the DCRPhi trigger. Of special interest is a high selectivity in the photoproduction region where the rate of signal and background events is high and no suppression based on triggering on the scattered electron is possible. Therefore a purely track based trigger is necessary, using information from the central drift chambers. The drift chamber signals allow for a standalone track reconstruction, the achieved resolution of $2\% \, p_t/$ GeV is comparable to the offline resolution. The FTT allows for a low momentum threshold of 100 MeV, compared to a threshold of 400 MeV for the DCRPhi trigger. This is of special interest for the study of soft physics, e.g. production of mesons at the production threshold (very low transverse momenta). The large dynamic range of track momenta and the pattern recognition on a short timescale within 500 ns are a major challenge. In addition the algorithms had to be designed to deal with the large drift times of 10-12 bunchcrossings within the drift chambers.

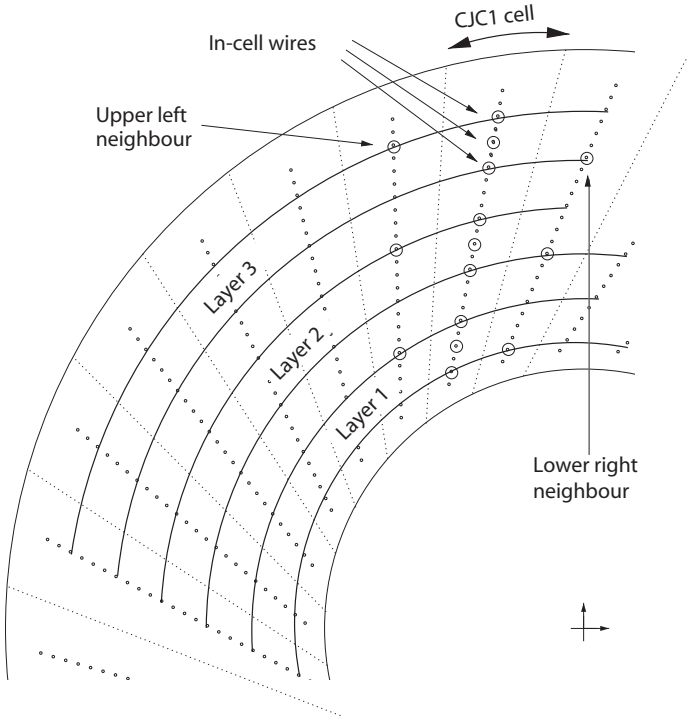

FIGURE D.3: *Geometry of the CJC with wires marked used for the FTT (from [36]). Each group consists of three wires, the upper left and lower right neighbour wire are included in the processing of each group.*

The FTT uses only a fraction of 450 from 2440 wires of the drift chambers. A radial slice of the drift chambers is shown in figure D.2. As indicated, the FTT wires are arranged in four trigger layers, three for the inner chamber and one for the outer chamber. The inner and outer layers consist of 30 and 60 trigger cells, respectively. Each trigger group is made of three FTT wires. The cell geometry for the inner layers is depicted in figure D.3. The local pattern matching is performed within these trigger cells.
The FTT provides trigger information on all three trigger levels, where the first two levels are solely based on drift chamber signals.
At **level 1** track segments are linked in the transverse plane, yielding coarse track parameters. Finally the trigger decision is determined, in total a set of 32 trigger elements (TEs) is forwarded to the Central Trigger Logic. These trigger elements are based on the number of tracks above a certain momentum threshold, the total charge of the tracks and the arrangement of tracks in the $r - \phi$ plane. All these calculations have to be performed within the *level 1 latency* of 2.3 μs (24 bunch crossings). Details can be found in [35]. The z vertex trigger, that is described in this thesis, is part of level 1.
At **level 2** track segments are linked based on refined segment information. A 3-dimensional primary vertex constrained fit is performed. This consists of a circle fit in the transverse plane, which is able to fit four track segments within 2.25 μs. In the longitudinal plane a straight line fit is performed, combining up to 12 hits and the z vertex position. This fit can be performed within 1.12 μs. The level 2-linker algorithm is described in detail in [35], the 3-dimensional fit in [118]. The vertex position in z that is used for the fit in the longitudinal plane is determined by the FTT on an event-by-event basis [35]. In addition it was possible to perform an invariant mass reconstruction already on Level 2 using the parameters determined by the track fits [35]. Finally 64 internal FTT trigger elements [105] are generated making use of the higher precision and resolution at level 2. These trigger elements are combined to 24 physics triggers that are sent to the central trigger logic. The internal trigger elements are based on track multiplicities above a certain threshold, track topologies in the transverse plane and the total charge in the event. Level 2 does not only verify and refine level 1 information but also delivers information based on the z vertex and additional kinematic quantities like the E_t and p_t, which is the scalar and vectorial sum of charged particle momenta, V_p and V_{ap}, which is the amount of momentum parallel and antiparallel to the direction of missing momentum, and the invariant mass of two track combinations. The total time available on level 2 is 20 μs.
At **level 3** a partial event reconstruction is performed by determining invariant masses based on the high precision tracks delivered from level 2. For this purpose physics algorithms like the selection of D^* candidates run on commercial processors [79, 80, 98]. At level 3 it is possible to combine track information with information from other detectors, like the muon system [103] and the liquid argon calorimeter. The latter allows the search for electronic decays of beauty mesons at low momenta [43, 103]. The total time available for level 3 is 100 μs.

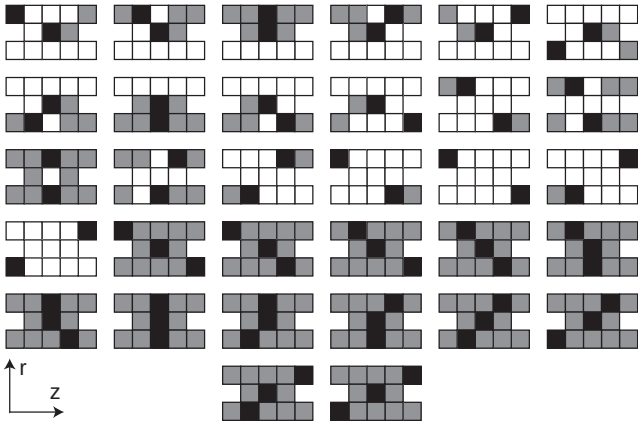

FIGURE D.4: *Mutually exclusive valid patterns for the segment finding (from [35]). Each pattern defines a local search neighbourhood, consisting of five hit positions for the outer and inner wire and three hit positions for the middle wire. For the positions marked in black a hit is required, for positions marked in white no hit is allowed. The grey patterns denote "Don't care" positions.*

D.1.2 Z Vertex Trigger

The z vertex trigger algorithm consists of the following steps:

- For each FTT-wire a **hit finding** algorithm is applied, followed by a calculation of the z-coordinate of the hit. The hit finding is common for the z vertex algorithm and the r-ϕ part of the FTT. The result of the z measurement is given in two representations, with a resolution of 62 bins for the level 2 system and a resolution of 40 bins (11 cm per bin) for the level 1 z vertex part due to bandwith limitations[1]. The hit finding and the z measurement are explained in more detail in section D.3.2.
- For each of the 90 trigger cells of the inner three FTT layers a **search for track segments** is performed. The pattern matching algorithm is based on hitpatterns along the z-coordinate, where five bins of each inner and outer wire[2] and three bins of the middle wire build a local search neighbourhood. The valid patterns are summarized in figure D.4. All 32 patterns are mutually exclusive and also patterns consisting of only two hits are valid to account for the limited hit finding efficiency. The result of this part of the algorithm are z-segments for each of the trigger cells.
- In the **linking step** all combinations of two segments belonging to different layers are extrapolated to the beamline, and the intercept is entered into a histogram. This extrapolation is done separately for 10 different ϕ-sectors (see

[1]Technically an internal representation of 124 bit is used, which is converted to a 62 and 40 bit representation.

[2]The hit information of the outer wires is combined with the information from neighbour wires.

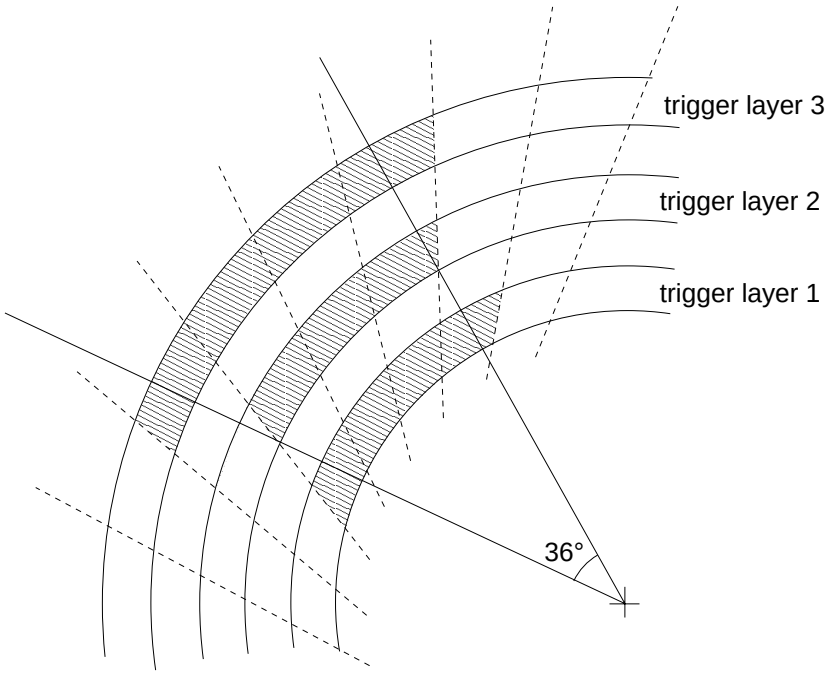

FIGURE D.5: *Illustration of a ϕ sector. The vertex histogram is calculated for each sector seperately. Within the overlap region cells contribute to both sectors.*

figure D.5). The final vertex histogram is the sum of these 10 individual histograms and consists of 40 bins with a binwidth of 11 cm, covering the range from -2 m to 2 m. This has to be compared to a much coarser binning of about 16 cm for the CIP, where the number of bins is only 15. The extrapolation method is illustrated in figure D.6.

- Finally this vertex-histogram is evaluated by counting the histogram entries and performing a peak search. The **trigger decision** is based on the peak position and the number of entries in the signal region of the histogram compared to the total histogram contents.

Several aspects make the implementation of the z vertex algorithm a challenging task:

- The algorithm has to account for the large drift times up to 10-12 bunch crossings. A hit might constitute a valid segment combined with a hit detected later due to a larger drift time. Therefore hits have to be held in pipelines of sufficient length. A large fraction of the available time at level 1 is spent for waiting for the latest hits. This latency is about five times larger than the hit finding itself.
- Due to the limited time available at level one, the z vertex algorithm has to run in parallel to the r-ϕ-part. Since large parts of the algorithms run in parallel on the same hardware, a large fraction of the resources for the individual FPGAs has to be shared. This implies complications concerning the timing constraints of the final design at register transfer level. In addition the bandwidth for signal

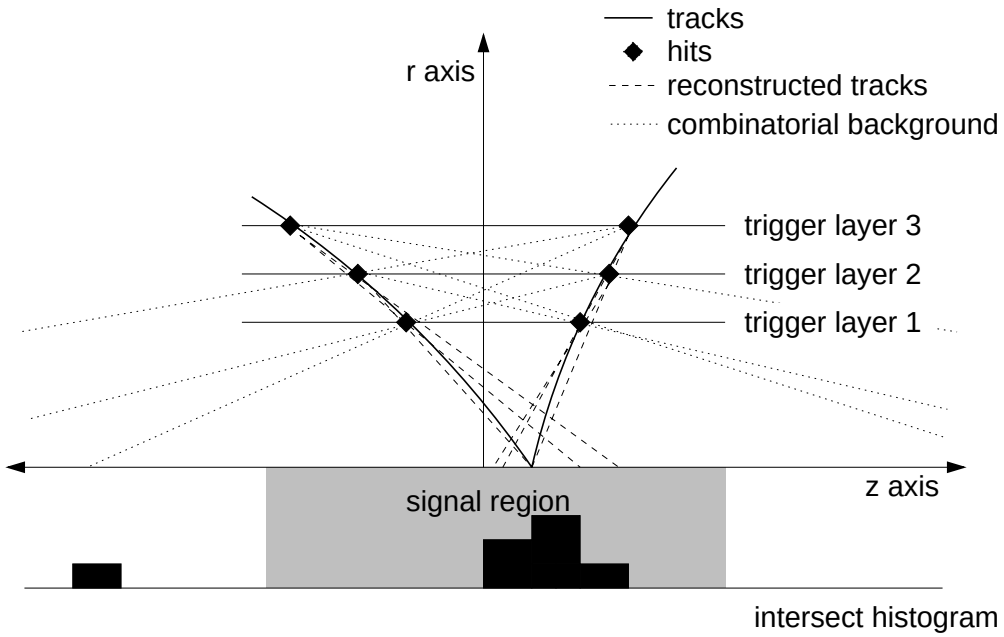

FIGURE D.6: *Sketch of the z-linking process (from [35]). All combinations of two segments are extrapolated to the beamline, leading to entries in the vertex histogram. The entries are weighted and smeared according to the different precision depending on the layer combination.*

transmission between the different hardware components is limited.

- In comparision to the z vertex algorithm at level 2, not only r-ϕ linked segments are considered for the extrapolation, but all segments for the inner three layers. Therefore the algorithm suffers from a much larger number of z-segments and z-segment combinations, resulting in a smaller signal to noise ratio. This problem is enhanced by the fact that the outer FTT layer is not used for the algorithm due to hardware limitations. Combining segments from the inner and the outer layer (CJC2), which is possible at level 2, allows for a large lever arm and a much higher precision for the peak measurement.

D.2 Data Flow and Hardware

The FTT level 1 trigger system is distributed over a large number of hardware boards, most of them are used for level 2 functionality as well. An illustration of the level 1 system is given in figure D.7.
The processing of the drift chamber data starts at the **Front End Modules (FEM)**. Each FEM processes the data coming from 5 trigger cells (15 wires times two wire ends). In total the system consists of 30 FEMs, each of the three inner trigger layers is connected to 6 FEMs. The outer layer is not used by the Level 1 z vertex trigger. After digitization the hit finding and z measurement is performed, followed by the segment finding in the r-ϕ and $r-z$ plane, which is done in parallel.

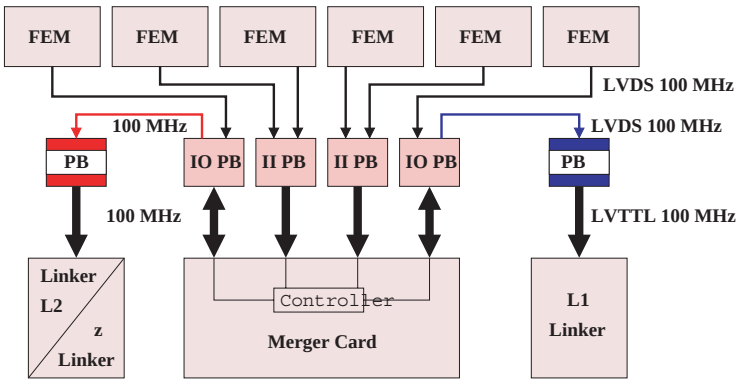

FIGURE D.7: *Overview of the FTT L1 Trigger system, showing the data flow from the FEMs to the various linker cards via the merger cards.*

In addition, the segment finding at level 2 with a higher resolution is performed on the FEMs.
The FEMs transmit the data to the **Merger Card** at a rate of 100 MHz via **LVDS**[3] **channel links**. Therefore the Merger Cards are equipped with four **Piggy Back Cards** that receive the data. Two different types of Piggy Back Cards are used, the II-type has two input channels, the IO-card one input and one output channel. Merger and Piggy Back Cards are operated at a frequency of 100 MHz. The merger collects the r-ϕ and z data from 6 FEMs and forwards this information to the linker and z linker, respectively (see figure D.7). The z data is organized in 10 sectors (5 or 6 groups each) and sent out in sequence. One of the IO-Piggy Back Cards sends the merged r-ϕ segments to the **linker card** via one LVDS Channel Link, the other IO-piggy back card sends $r - z$ segments to the **z linker card** via a second LVDS channel link. In addition, r-ϕ segments for level 2 are sent, therefore Merger and Piggy Back Cards switch between **level 1 mode** and **level 2 mode**. In level 2 mode, the z linker Piggy Back Card, that is receiving the data from the merger, is forwards the data to the **L2 linker card**. The Merger card and the different linker cards are **Multipurpose Processing Boards (MPBs)**. Both, the MPBs and the FEM hardware and the used key technologies are presented in more detail in the following subsections.

D.2.1 Front End Modules and Multipurpose Processing Boards

For the FTT level 1 and level 2 hardware two types of boards are used: 30 Front End Modules (FEMs, figure D.8), built by Rutherford Appleton Laboratory, and several Multipurpose Processing Boards (MBPs, figure D.9), built by Supercomputing Systems (SCS). Each Front End Module is equipped with 15 dual 10 bit Analogue to Digital Converters (ADCs) of type AD9218-80 [55] for sampling the analogue signal

[3]Low Voltage Differential Signaling [108]

of 5 trigger groups at a rate of 80 MHz. The further digital processing is performed on 6 FPGAs of type Altera APEX20K400E [27]. Five of them, the so-called Front FPGAs, perform the hit finding, z measurement and segment finding in the r-ϕ plane. To include information from neighbour wires, these FPGAs are cross-linked with the neighbour FPGAs. The Front FPGAs are clocked with a frequency of 80 MHz. The sixth FPGA of this type (so called Back FPGA) synchronizes and collects the track segments from the Front FPGAs and forwards them to the Merger system. The five Front FPGAs and the Back FPGA are connected via a 40 bit bus. In level 2 mode a validation of the track segments is performed, using higher granularity masks stored in RAM. (For the level two verification and lookup the board is equipped with a 4 MB Zero Bus Turnaround (ZBT) memory.) The segment finding in the r-z plane at level 1 is an extension of the trigger functionality using the remaining hardware resources. In addition this board is equipped with a FPGA of type ALTERA FLEX which provides a VME[4] interface for configuration and readout.
Many components of the FTT, including the merger system and different linkers, are implemented on Multiporpose Processing Boards using different firmware implementations. Each MPB hosts up to four Piggy Back cards providing two 5 GBit/s channel links each, controlled by an Altera APEX20K60E FPGA. The corresponding buses are collected on the main board by the **Data Controler FPGA**, which hosts the linker algorithms for the linker cards and the merger algorithm for the merger card. The FPGAs are of type Altera APEX20KC600E for the linker boards and Altera APEX20K400E for the merger boards. A FPGA of type Altera FLEX EPF10K30A is used to control the VME interface. At level 2 fitter boards are used for track fits, which are in addition equipped with four floating point DSPs and a corresponding DSP controller FPGA.

D.2.2 Key Technologies

The implementation of fast and parallel algorithms and the successful commissioning of the FTT was only possible by the use of fast and flexible programmable hardware on level 1 and level 2. As the FTT is based on pattern matching algorithms a dedicated memory technology is used. Both key technologies are briefly presented in the following.

Field Programmable Gate Arrays (FPGAs)

FPGAs are programmable integrated circuits (ICs). They are used for complex applications, where flexibility and reprogrammable redesign are important. This is especially important during the commissioning phase.
An overview of the APEX20K device is shown in figure D.10. This device incorporates LUT-based logic[5], product-term-based logic and memory. These components are organized in groups consisting of logic array blocks (LABs) and embedded sys-

[4]Vesa Module Europe

[5]LUT stands for look-up-table, which is a function generator that implements any function of four variables.

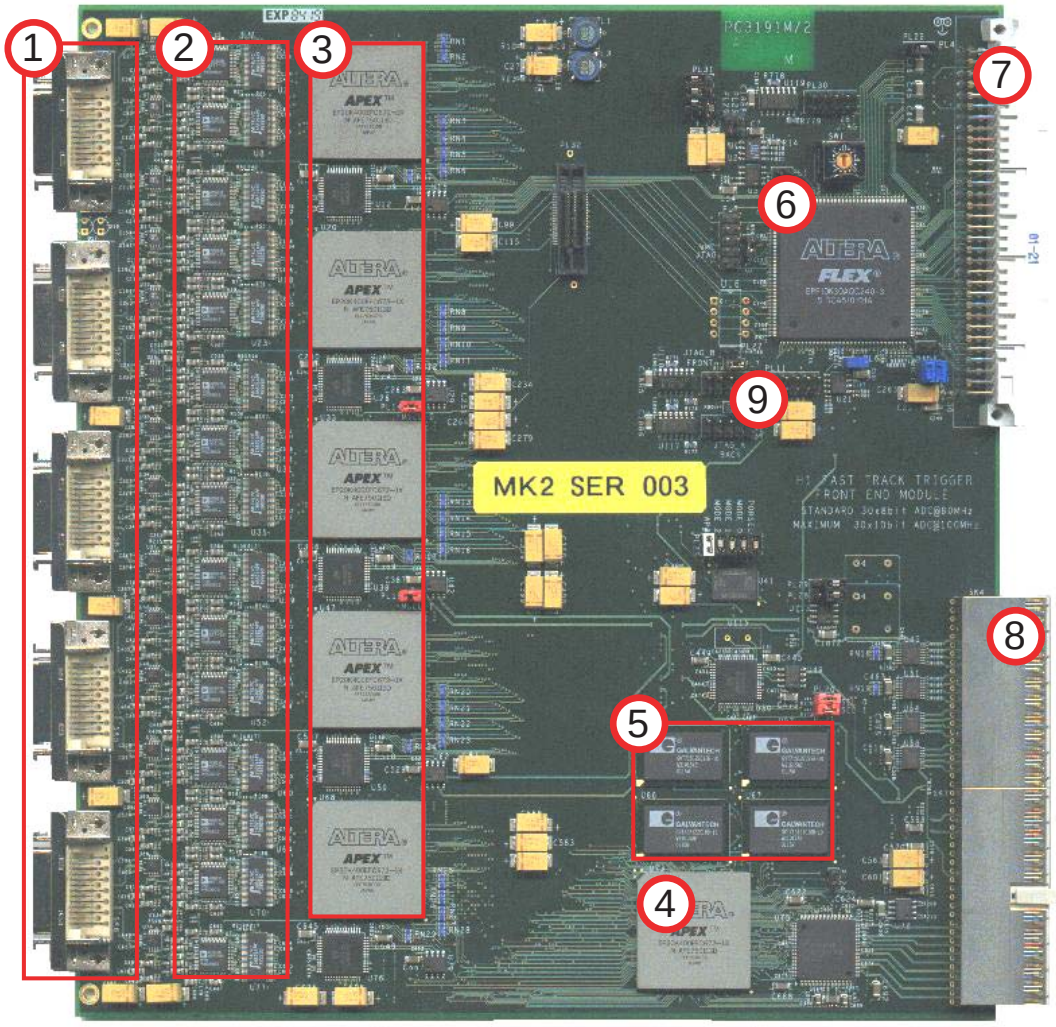

FIGURE D.8: *Photo of a front end module (from [35]).* ***1****: Connector for analogue signal cables* ***2****: ADCs* ***3****. Front FPGAs* ***4****: Back FPGAs* ***5****: ZBT RAM* ***6****: VME Interface FPGA* ***7****: VME Connector J1* ***8****: Custom backplane connector* ***9****: JTAG Connectors.*

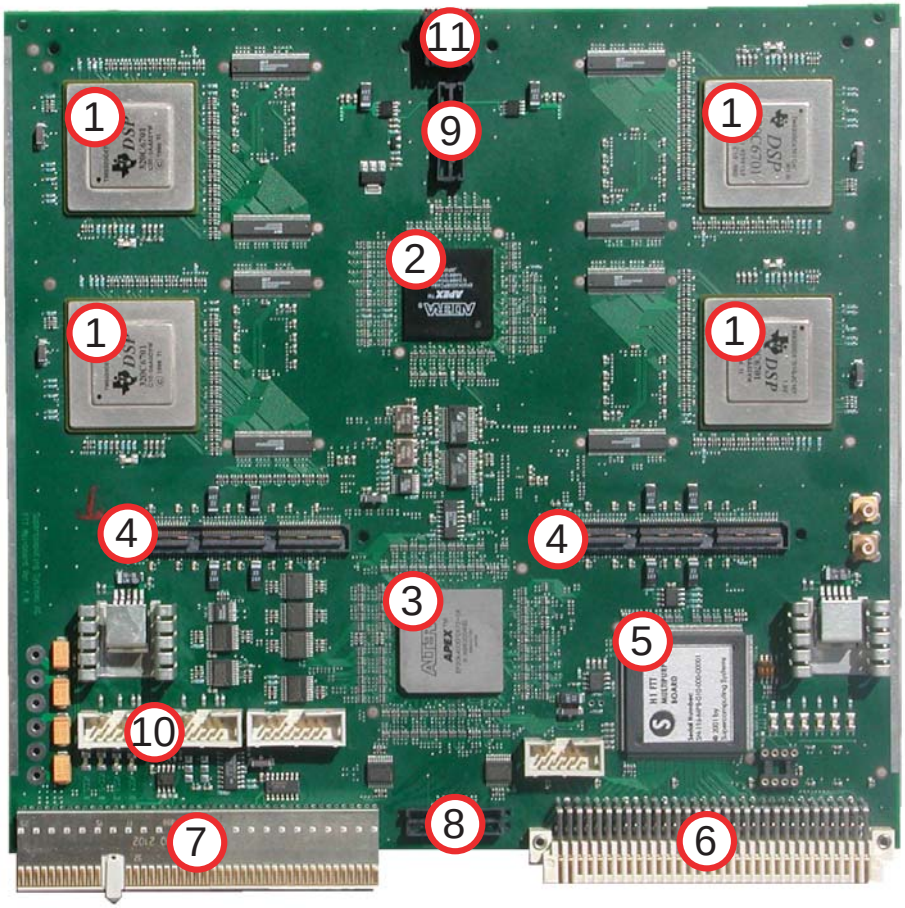

FIGURE D.9: *Picture of a Multipurpose Processing Board (from [35]).* ***1****: DSPs* ***2****: DSP Controller FPGA* ***3****: Data Controller FPGA* ***4****: Piggy Back connectors* ***5****: VME Interface FPGA* ***6****: VME Connector J1* ***7****: Custom backplane connector* ***8****: Logic analyser connector for Data Controller FPGA* ***9****: Logic analyser connector for DSP Controller FPGA* ***10****: JTAG connectors 11: Status LEDs. For the z linker a simplified version is used without DSPs and DSP Controller FPGA. Not visible are two more Piggy Back connectors, a dual ported RAM and DPRAM Controller FPGA on the back side.*

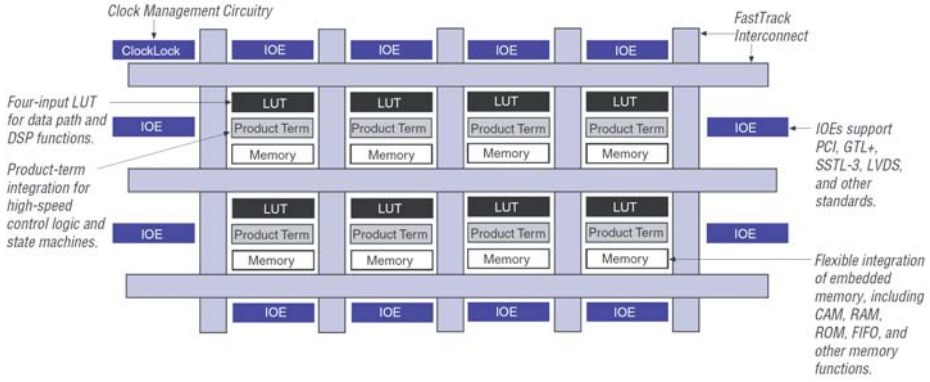

FIGURE D.10: *APEX 20K Device Block Diagramm (from [27]). Shown are the logic array blocks, consisting of LUT-based logic, product-term-based logic, and memory. These blocks are connected via fast interconnections (FastTrack Interconnect).*

tem blocks (ESBs) and connected via fast interconnections. The smallest units of this architecture are logic elements (LEs). Each LE contains a four-input LUT, a programmable register and carry and cascade chains[6]. Product-term logic is implemented using ESBs. In this mode, each ESB contains 16 macrocells consisting of two product terms and a programmable register each. The ESB can implement various types of memory blocks, including dual-port RAM, ROM, FIFO, and CAM blocks. The latter is discussed in the following subsection in more detail due to the importance for the used algorithms.

Content Adressable Memories (CAMs)

Content Adressable Memories are associative memories based on RAM technology. Instead of receiving the address and supplying the data as in conventional RAM memory, a data word is compared to a list of pre-loaded data words, and the address of the matching data word(s) is signaled. The search through all memory locations is done in parallel. CAMs are used for implementing high-speed search applications, e.g. pattern matching algorithms. The used APEX 20KE device contains on-chip CAM which is built into the ESB blocks [56].
The core task of the z vertex trigger and the FTT in general is a fast pattern matching of drift chamber hits. All valid patterns shown in figure D.4 are used to pre-load the CAMs during configuration. The CAM units allow for a third matching state, the "Don't care" state (ternary CAM). As all patterns are disjoint, the single match mode can be used. For this mode only one clock cycle is needed to read the stored data.

[6]Carry chain logic is used to implement counters, adders and comparators. Cascade chain logic is used to implement functions with a very wide fan-in.

D.3 Implementation of the Z Vertex Trigger

In this chapter the implementation of the z vertex trigger is discussed in detail. Since this is based on the programming of FPGAs using the hardware description language VHDL, this chapter begins with a brief discussion of VHDL and the development process. After this the different steps of the algorithm are presented.

D.3.1 VHDL

The algorithm is implemented using the hardware description language VHDL[7]. The use of this high level language allows a high level of abstraction for the system design, including top-down and bottom-up design approaches and reusable components. A common modelling for the simulation and the synthesis of the design can be used. Digital hardware is described in VHDL using concurrent assignments, concurrent processes, and local signals for the communication between them. For processes the use of sequential statements is allowed. This way it is possible to implement not only combinatorical logic but sequential logic using storage components like flip flops. More details can be found e.g. in [75].
For the implementation the Quartus II design software [26] is used. This is an integrated development environment for all design steps, including the compilation, simulation, synthesis, placement and routing. During the synthesis step a netlist is produced. The last step, the mapping of the netlist to the hardware and connecting the components is a very time consuming step. For complex designs this step has to be repeated several times to fulfill the timing requirements.

D.3.2 Hit finding and Z Measurement

Both hit finding and the z measurement are performed on the Front FPGAs of the Front End Modules. Therefore the digitized signal of 10 channels (both ends of 5 wires, 3 wires of the corresponding cell plus two neighbour wires) is fed into the Front FPGA at a rate of 80 MHz. This results in a total input rate of 720 Gbit/s. The hitfinding and the z measurement, performed by the **Qt Algorithm** and a **charge division** algorithm, are described in the following.

Qt Algorithm

A difference of samples (DOS) method is used to measure the hit timing. Therefore for each time slice n the difference of the digitized wire value to the previous time slice $n-1$ is calculated,

$$\delta_n = s_n - s_{n-1}, \tag{D.1}$$

where s_n is the sum of both wire ends. A hit is found at a time slice n if the following conditions are fulfilled:

- The difference δ_n is above a certain threshold, which implies a minimum slope for the rising edge of the hit.

[7] **V**ery High Speed Integrated Circuit **H**ardware **D**escription **L**anguage

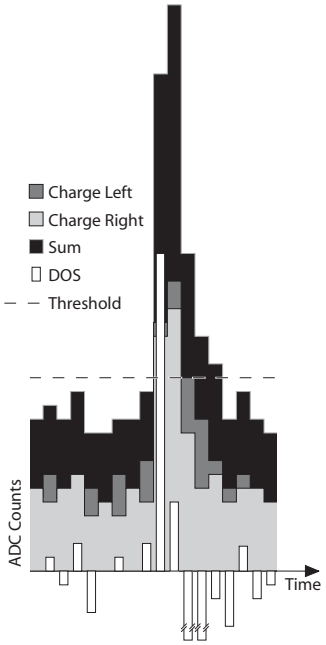

FIGURE D.11: *Illustration of the Difference of Samples method (from [35]).*

- The difference δ_n is larger than the difference for the next time slice δ_{n+1}.

This DOS technique is illustrated in figure D.11. By applying these conditions a hit finding with high efficiency and purity, high precision of the hit timing measurement and high accuracy of the charge measurement is possible. This step of the algorithm takes only three 80 MHz clock cycles. With the availability of the hit information, the segment finding in r-ϕ can proceed.

Charge Division

To determine the z value, a charge integration is performed for both wire ends. The principle of the charge integration is illustrated in figure D.12. The integration is performed for six clock cycles and starts as soon as the difference of samples is above the threshold. A noise substraction is performed, therefore a pedestal integration of six clock cycles is performed eight clock cycles before the hit (in phase with the HERA clock to reduce the influence of correlated noise). For a time period of 20 clock cycles after the hit integration, no pedestal integration is allowed. The values q_L and q_R for the measured charges are then entered into the simple formula

$$z = L_{eff} \frac{q_L - q_R}{q_L + q_R}, \tag{D.2}$$

where L_{eff} is the effective wire length, which is not only determined by the physical wire length but also by electronics at the wire ends (see figure D.13). If the values for the charges at both wire ends are equal, the formula yields a value $z = 0$ for the hit position, which is the center of the wire.

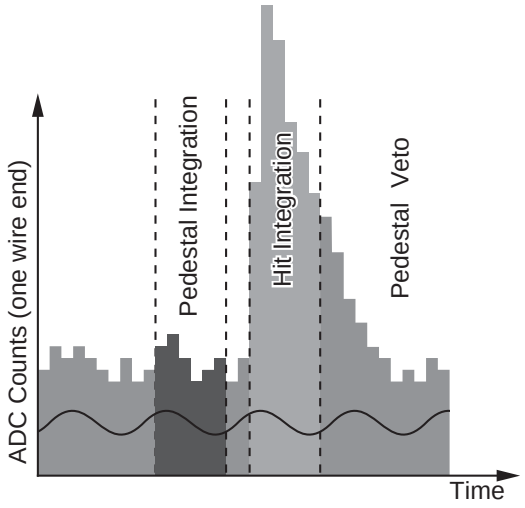

FIGURE D.12: *Illustration of the charge integration method (from [35]). Shown are the interval for the signal integration, the interval for the background integration (pedestal) and the veto region, where no pedestal integration is allowed.*

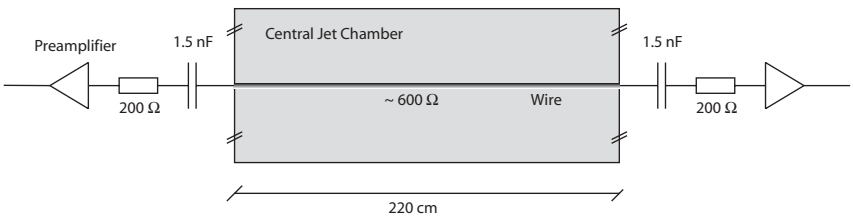

FIGURE D.13: *Illustration of CJC wires (from [35]). For the Qt algorithm an effective wire length is used, which accounts for the impedance due to electronics at both wire ends.*

Data line	L1/Monitor mode
40	80 MHz Clk inverted
39	0
38	κ enable
37	z enable
36	BC half
35	monitor enable
34..19	monitor data
18..17	z(17..16)
16..1	z(15..0)/κ(15..0)

TABLE D.1: *Front FPGA to back FPGA protocol. Only the protocol for the level 1 and monitor mode is shown.*

D.3.3 Segment Finding

The segment finding in $r-z$ is performed on the back FPGA. The functional design of the VHDL implementation is shown in figure D.15. The data is processed by three different units:

Synchronizer

The first step is the synchronization of five 80 MHz 40 bit data streams (one data stream for each trigger cell) to the 100 MHz clock of the back FPGA. For the synchronization the inverted 80 MHz clock is transmitted via the data stream. As a result only 8 of the 10 clock cycles per bunch crossing contain valid data. Three different protocols are used: level 1 mode, level 2 mode and read-out control mode. In level 1 mode, the z data is sent two times per bunch crossing. For each half bunch crossing 5 times 6 bit encoded z data is transmitted, which takes two clock cycles. For these clock cycles the z-enable bit of the data stream is set, the bunch crossing half is indicated by another bit. The front FPGA to back FPGA protocol for level one is shown in table D.1.

Pipeline Units

To account for the large drift times of the detector, the hit information is fed into five pipeline units, one for each cell, and stored for 10 bunch crossings. Therefore it is possible to form hit patterns consisting of hits detected at different bunch crossings but belonging to the same event. Each pipeline unit contains five counter units, three for the cell wires and two for the left and right neighbour wire. Each counter unit uses 40 counters to model one pipeline per z position. Twice a bunch crossing it is checked whether a hit was detected for each z position. In this case the counter is set to 10 and the bit corresponding to this z position is enabled. The counters are decremented per bunch crossing, and the corresponding bit is disabled if the counter is at zero.

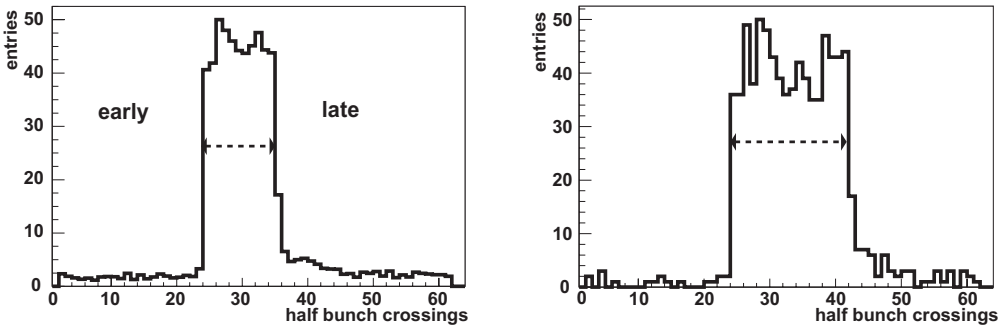

FIGURE D.14: *Drift spectrum for z hits for the innermost layer and the outermost layer. This data was read out from the back FPGA.*

For each cell 120 bit (40 z positions per wire) are written to a cyclic memory which is used to feed the data to the CAM unit.
In addition, the hit information is written to a dedicated cyclic memory twice per bunch crossing for timing studies. This memory has a depth of 31 bunch crossings and can be read out via VME. The number of z hits with respect to the half bunch crossing is shown in figure D.14 for the innermost layer and the outermost layer, ordered from earlier to later bunch crossings. The first hits are written to the memory 20 bunch crossings before the pipelines are stopped by the central trigger decision. The rising edges for all trigger layers show that the pipelines are stopped at the same time with respect to the central trigger signal for each event. The width of this distribution denotes the maximum drift time, which is about 6 bunch crossings for the innermost layer and about 10 bunch crossings for the outermost layer. The latest hits are available only about 10 bunch crossings before the pipelines stop. As all subsequent processing and transmission steps exceed this time constraint, only the fraction of hits that are available early enough is processed and included to the trigger decision. To maximize this fraction, all steps of the algorithm have to be optimized with regard to processing time and parallelism.

CAM Unit

The CAM Unit performs the search for track segments in a local search neighbourhood. 10 bit of z-information from three wires is presented to 38 CAMs (one for each z position, omitting the edge positions) in parallel and compared to predefined patterns. This principle and the z-patterns are illustrated in figure D.16 and D.4. The data from five groups has to be processed, but due to limited resources only one CAM unit is available. Therefore the data from each group is presented to the CAM unit in sequence using a state machine. The result of this pattern matching is represented by five 40 bit vectors, where each component represents a z-bin. These vectors become available in sequence for each group. To reduce the amount of data to be transmitted and processed, a reduction to three 40 bit vectors is necessary by merging these vectors. Three groups of 40 bit z data are defined, which belong to

FEM	PB card	PB type	group	layer 1		layer 2		layer 3	
0	1	M1KO	0		0-1		0-1		0-2
			1	(5)	1-4	(1)	2-4	(6)	2-4
			2		4*				
1	2	M1II1a	0						5
			1	(5)	5-7	(1)	5-7	(6)	5-8
			2		7-9		8-9		8-9
2	3	M1II2a	0		10		10		10-11
			1	(5)	10-13	(1)	11-13	(6)	11-14
			2		13-14		14		14
3	2	M1II1b	0		15-16		15-16		15-17
			1	(5)	16-19	(1)	17-19	(6)	17-19
			2		19				
4	3	M1II2b	0						20
			1	(5)	20-22	(1)	20-22	(6)	20-23
			2		22-24		23-24		23-24
5	4	M1ZO	0		25		25		25-26
			1	(5)	25-28	(1)	26-28	(6)	26-29
			2		28-29		29		29

TABLE D.2: *CJC 1 Merger Input. Only the z data is shown, in addition κ information is sent. The Merger receives three groups of z data for each of the five FEMs for one layer. The data denoted with * is not transmitted due to bandwidth limitations.*

one sector (see figure D.5). For each group a bitwise *or* of three or four vectors is performed, depending on the FEM type and layer. This is summarized in table D.2. Finally the z data is sent out to the merger cards in three groups of 40 bit. The sequence of data sent to the merger card is summarized in table D.3. Three cycles are needed for the z data, two cycles for the r-ϕ data.

D.3.4 Merging

The amount of data is further reduced by merging the z segments on three merger boards, one for each layer. 10 sectors are defined, with overlap regions between them (figure D.5).
As the implementation of the merger algorithms is not part of this thesis, only a brief overview of the merger functionality is given. The merging scheme is complicated because r-ϕ data and z data are processed on the same merger. A detailed description including the detailed merging scheme and r-ϕ functionality can be found in [104].
The FEM-Merger channel links are operated at 100 MHz. The protocol is given in table D.4. Five bytes are available for the unencoded z position per group, dedicated header bits are used to denote the group number. In addition *r-ϕ* information is sent via these channel links. Control words are used for switching between the level 1 and level 2 mode. For each bunch crossing the *BeginTriggerData* control word is

Step	word	HClk FEM
1	control word	$0 \rightarrow 1$
2	5 lower bytes $r\phi$ segments	1
3	5 higher bytes $r\phi$ segments	1
4	empty word	1
5	empty word	1
6	40 bits z segments group 0	$1 \rightarrow 0$
7	40 bits z segments group 1	0
8	40 bits z segments group 2	0
9	empty word	0
10	empty word	0

TABLE D.3: *Sequence of sending data at 100 MHz (10 cycles per bunchcrossing) from the FEM to the Merger Cards.*

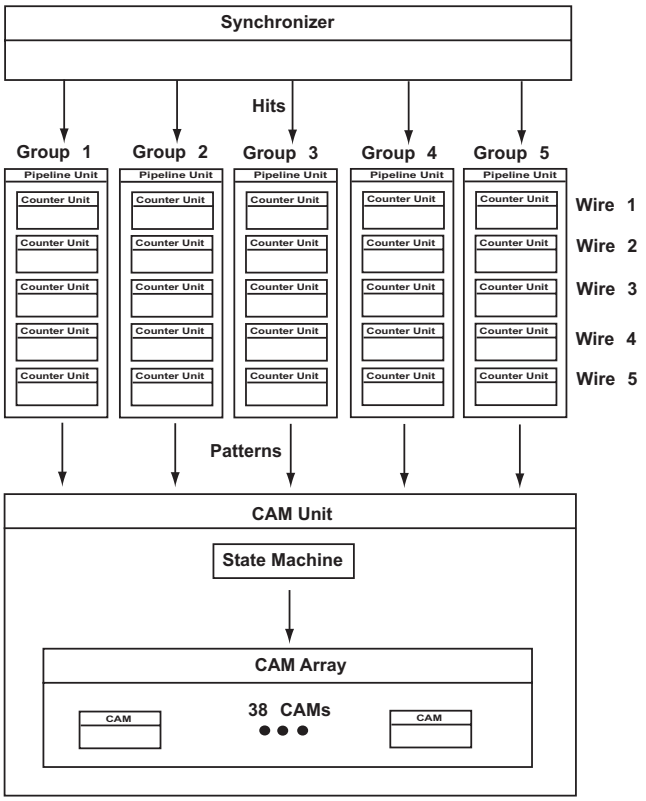

FIGURE D.15: *Functional design of the segment finding unit of the back FPGA. Hits from each trigger group are fed to the Pipeline Units. Each Pipeline Unit consists of 5 counter units, one for each FTT wire. The CAM Unit consists of 38 CAM memories, one for each z position.*

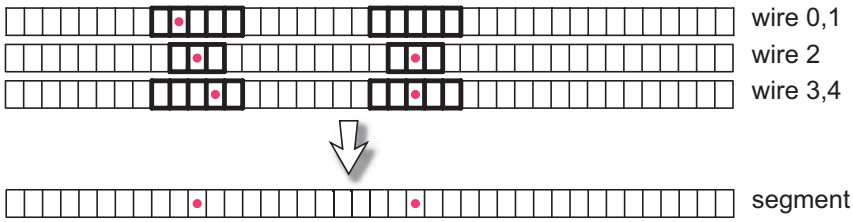

FIGURE D.16: *Principle of the pattern matching performed on the back FPGA. For each z position a local pattern matching is performed, resulting in a segment array.*

Data type	byte 5	byte 4	byte 3	byte 2	byte 1	byte 0
Invalid/no data	0 0 0 0 0 X X X	load	load	load	load	load
Track segments	cell#(7..3)load(2..0)	load	load	load	load	load
L1 mode	header	cell 5	cell 4	cell 3	cell 2	cell 1
empty word	0 0 0 0 1 0 0 P	ignored	ignored	ignored	ignored	ignored
$r\phi$ segments (low)	0 0 0 0 1 0 1 P	lower byte	lower byte	lower byte	lower byte	lower byte
$r\phi$ segments (high)	0 0 0 0 1 1 0 P	higher byte	higher byte	higher byte	higher byte	higher byte
z segment group 0	0 0 0 1 0 0 1 P	unencoded z position				
z segment group 1	0 0 0 1 0 1 0 P	unencoded z position				
z segment group 2	0 0 0 1 1 0 0 P	unencoded z position				
Control words	1 1 1 1 1 X X P					
BeginTriggerData	1 1 1 1 1 0 0 P	FEM#	0x00	#HCLK	#HCLK	#HCLK
SwitchTol2Mode	1 1 1 1 1 0 1 P	FEM#	0x00	#L1Keep	#L1Keep	#L1Keep
NoMoreSegments	1 1 1 1 1 1 1 P	FEM#	0x00	0x00	0x00	#sent segments
SwitchToL1Mode	1 1 1 1 1 1 0 P	FEM#	0x00	#L2Keep	#L2Keep	#L2Keep

TABLE D.4: *FEM-Merger Protocol. P stands for parity bit. The control words contain counter information for monitoring purposes.*

sent along with the actual HERA clock counter. For each of the three trigger layers used by the z-trigger, one merger receives z data data via four Piggy Back cards. One of these cards forwards the data to the z linker. 22 clock cycles after receiving the *BeginTriggerData* control word, the last z sector is sent to the z linker card. The channel link to the z linker is operated at 100 MHz, the protocol is summarized in table D.5. The sequence of data and control words from the merger to the z linker card is summarized in table D.6. The *BeginTriggerData* control word is sent only once at the beginning of the level 1 mode.

D.3.5 Linking and Trigger Decision

The linking of the segments is the essential part of the algorithm. This is performed on a dedicated MPB-board, the z linker, operated at 100 MHz. The z data is received by the z linker via three LVDS channel links, one for each layer. The linking step is followed by the evaluation of the resulting vertex histogram and the generation of trigger elements which are sent to the Central Trigger. The different modules of the implementation are discussed in the following.

Data type	byte 5	byte 4	byte 3	byte 2	byte 1	byte 0
Invalid/no data (L2 mode)	0 0 0 0 0 0 0 0					
Track segments	cell#(7..3)load(2..0)	load	load	load	load	load
L1 mode	header	byte 4	byte 3	byte 2	byte 1	byte 0
z segment	0 sector+1 0 0 S	unencoded z position				
Control words	1 1 1 1 1 X X P					
BeginTriggerData	1 1 1 1 1 0 0 P	FEM#	0x00	#HCLK	#HCLK	#HCLK
SwitchTol2Mode	1 1 1 1 1 0 1 P	FEM#	0x00	#L1Keep	#L1Keep	#L1Keep
NoMoreSegments	1 1 1 1 1 1 1 P	FEM#	0x00	0x00	0x00	0x00
SwitchToL1Mode	1 1 1 1 1 1 0 P	FEM#	0x00	#L2Keep	#L2Keep	#L2Keep

TABLE D.5: *Merger-z-Trigger protocol. P stands for parity bit. The control words contain counter information for debugging purposes. For the sector which is sent first in a sequence (sector 2) the startbit S is set high. In level 2 mode track segments are sent.*

Step	word	HClk Merger
1	*BeginTriggerData*	$0 \rightarrow 1$
2	sector 2 z segment	1
3	sector 3 z segment	1
4	sector 4 z segment	1
5	sector 5 z segment	1
6	sector 6 z segment	$1 \rightarrow 0$
7	sector 7 z segment	0
8	sector 8 z segment	0
9	sector 9 z segment	0
10	sector 0 z segment	0
11	sector 1 z segment	$0 \rightarrow 1$
...	...	...
...	*SwitchToL2Mode*	...
...	...	...
...	L2 track segments	
...	...	...
...	*NoMoreSegments*	...
...	...	...
...	*SwitchToL1Mode*	...

TABLE D.6: *Sequence of data sent from the merger to the z linker.*

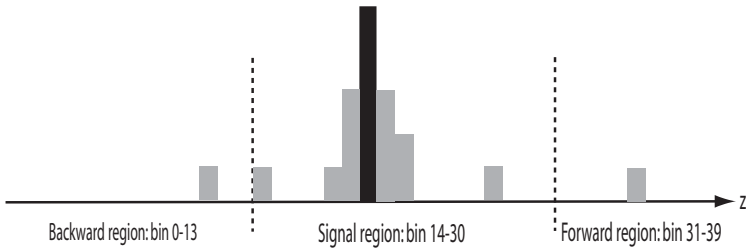

FIGURE D.17: *Illustration of the vertex histogram, divided into backward, signal and forward region.*

Parameter	Value
length CJC	220 cm
centre CJC	110 cm
radius inner layer R0	22.0 cm
radius middle layer R1	33.0 cm
radius outer layer R2	44.0 cm
#histogram bins	40
histogram length	440 cm
histogram centre	220 cm

TABLE D.7: *CJC and vertex histogram parameters used for the extrapolation of z segments.*

Receiver Unit

This unit synchronizes the data from three trigger layers. The incoming data is written to input buffers, implemented as cyclic memories. The synchronization step is performed by a final state machine that writes the data to three z buses, one for each trigger layer. The data of one sector is written per clock cycle to each bus. In total ten clock cycles are needed for all ten sectors.

Histogram Unit

The Histogram Unit performs the linking step of the algorithm by extrapolating segment pairs linearly to the beam line. It consists of three linking units, corresponding to the three possible combinations of two layers. Each of these linking units fills a 40 bin z vertex histogram with a binwidth of 11 cm.
The linear extrapolation of segment pairs to the beamline using the geometric CJC parameters given in table D.7[8] is performed offline. For each histogram bin all segment combinations, that can be extrapolated to that bin (**links**) are calculated offline, and the corresponding VHDL code is generated.
The algorithm is pipelined, the linking is performed for each of the ten sectors in sequence sharing the same hardware. Each link gives an entry for the corresponding bin. The vertex histogram is calculated by summing up the number of links for each bin. This cannot be done in one clock cycle due to timing constraints. For each bin an adder with a large fan-in would be required. Instead, the addition is done in several steps within five clock cycles using a chain of adders. The sum unit is used to add the individual histograms for each layer combination. The algorithm is pipelined, therefore one tenth of the histogram is processed for each clock cycle. The vertex histograms for all ten sectors become available in sequence and are summed up to the final vertex histogram. After ten clock cycles the data from the next bunch crossing is processed. To take into account the higher resolution for the combination layer 0 - layer 2 due to the longer lever arm, a weighting scheme is applied:

[8]The radii of the different CJC layers used for the algorithm deviate from the physical parameters and are chosen in a way to avoid binning artefacts (moiré effects).

Trigger Element	Method	Signal region
TE 154	Top Peak 40	-40 cm - 100 cm
TE 155	Top Peak 50	-50 cm - 100 cm
TE 156	Top Peak 60	-60 cm - 100 cm
TE 157	Significance	-40 cm - 100 cm

TABLE D.8: *Trigger elements provided by the z vertex trigger. They correspond to two different methods for evaluating the vertex histogram and different definitions of the signal region.*

histogram entries from this combination get a weight of three, whereas entries from the other two layer combinations are smeared to the left and right neighbour bin.
The Peakfinder Unit analyzes the vertex histogram. A peak search is performed and entries for the central, forward and backward region are counted. An asymmetric signal window is defined from bin 14 to 30 as illustrated in figure D.17. Due to secondary tracks showering in the forward region, the signal window had to be extended to the forward region.

D.3.6 Trigger Element Generator Unit

This unit processes the results from the Histogram Unit given by the number of entries for the three different histogram regions and a 40 bit array containing the peak information. Two different methods are used: For the **Significance Method** the number of entries for the signal and background regions are compared. The corresponding trigger element is enabled if the condition

$$2N_{signal} > (N_{forward} + N_{backward}) \tag{D.3}$$

is fulfilled. A similar method was used for the level 2 z vertex Trigger and the CIP trigger.
For the **Top Peak Method** the peak array is evaluated. The corresponding trigger condition is fulfilled if the position of the top peak is within the signal window. Three different asymmetric signal windows are defined.
In total four trigger elements are defined, they are summarized in table D.8. All four trigger elements are sent to the Central Trigger. To fulfill the timing requirements with respect to the central trigger and to synchronize the four trigger elements, additional individual delays are added.

D.3.7 Timing

The processing and transmission times needed for the individual steps of the algorithm are summarized in table D.9. The accumulated time is estimated to 1250 ns. As the maximal level 1 latency is 2100 ns and the maximum drift time is 1056 ns, this results in an implicit cut into the hit distribution for the outermost layer (see figure D.14). The latest hits (about three bunch crossings) for this layer are therefore not included in the processing of the vertex histogram.

Delay	Clock Cycles	time (ns)	accumulated (ns)
Analogue cable delay	-	180	180
FEM: Digitization	-	60	240
FEM: Charge Integration (FFPGA)	6	72	312
FEM: Charge Division (FFPGA)	15	180	492
FEM: Data Preparation (FFPGA)	2	24	516
FEM: Segment Finding (BFPGA)	12	120	636
Channel Link: FEM-Merger	-	70	706
Merger: Merging	12	120	826
Channel Link: Merger-z Linker	-	60	886
z Linker: Receiving, Synchronizing	6	120	1006
z Linker: Linking	6	60	1066
z Linker: Pipelining	10	100	1166
z Linker: Summing histograms	3	30	1196
z Linker: Evaluating histogram	8	80	1276
z Linker: TE Driver, delay	5	50	1326
Transmission of trigger elements to CTL	5	50	1376

TABLE D.9: *Summary of time consumption of the algorithm for the different processing and transmission steps.*

D.4 Results

D.4.1 Cosmic Runs

In the course of the commissioning phase the first test were performed using data from cosmic runs. The cosmic muon events recorded during this runs provide ideal back to back two track events. The functionality of the trigger is documented in figure D.18 where the correlation between z vertex position as determined by the H1 event reconstruction and the position of the top peak is shown.
Figure D.19 shows an overlay of many vertex histograms for ideal single track events from cosmic runs. As the vertex position of each event is distributed uniformly, each single histogram is shifted to the central bin. The overlay histogram has a small width and peaks at the central bin. This demonstrates that the FTT is able to reconstruct the vertex position reliably for single track events with small combinatorical background.

D.4.2 Luminosity Runs

The performance of the trigger with respect to the background rejection and efficiency is tested using ep data. For these dedicated test runs the filtering on trigger level 4 was switched off (transparent runs). In figure D.20 the distribution of the offline reconstructed z vertex is shown for an event sample triggered with the level 1 subtrigger s61, which requires a scattered electron (see section 5.1.2 for the trigger conditions). As the veto conditions are switched off for these runs, a background

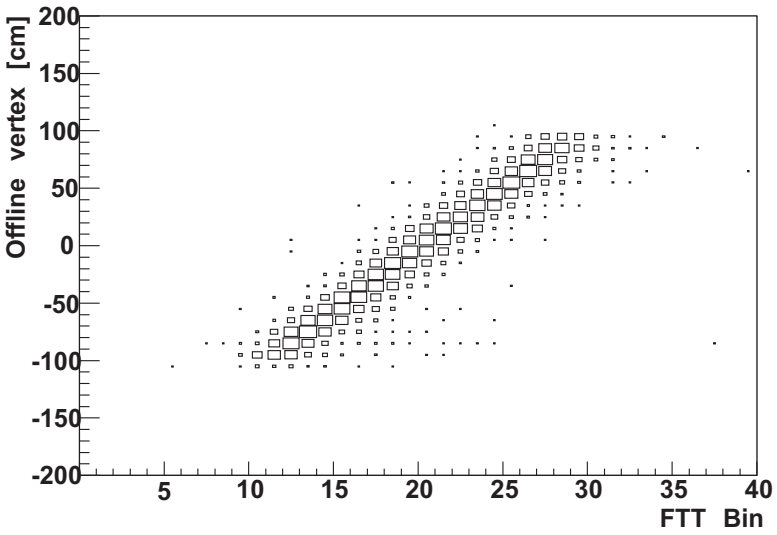

FIGURE D.18: *Correlation plot of offline measured z vertex and online measured top peak position for cosmic events.*

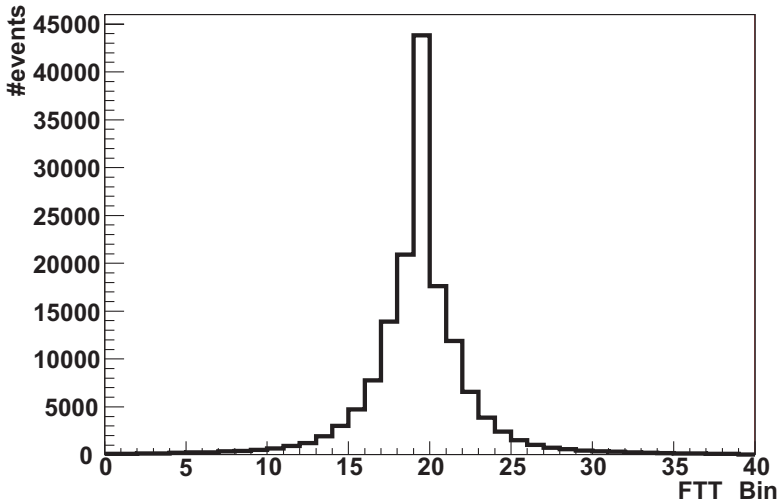

FIGURE D.19: *Overlay of vertex histograms for ideal single track cosmic events. Each individual histogram contributing is shifted to the central bin (see text). The binwidth is 11 cm.*

peak is visible in the backward region of the detector. This peak contains about the same number of events as the signal peak due to the bad background conditions. In the same plot this distribution is shown if the trigger element TE 157 (significance method) is required. A large part of the background peak is rejected (about 65%), whereas only a small fraction of about 5% of the signal peak is rejected.
This analysis was preceeded by detailed simulation studies on ep data [36]. The predicted rejection power of the z vertex trigger is shown in figure D.20 for a method very similar to the implemented significance method. A comparison to figure D.20 shows that the predicted background rejection was achieved for the implementation of the algorithm.
The implemented methods are compared in figure D.21. The maximum rejection is achieved for the significance method. The width of the signal window influences the rejection for the backward region. As expected, the largest rejection is achieved for the smallest signal window (Top Peak 40 method).
For all methods, the signal window is asymmetric and extends to +100 cm in the forward direction. The reason is a secondary vertex peak in the forward direction, which results from secondary tracks induced by particle showers. This peak often exceeds the primary vertex peak which results in a rejection of signal events if the signal window does not cover the forward region.
The efficiency for the signal region is comparable for all methods. This was checked using samples of elastic and inelastic J/Ψ events which provide an ideal ep-signal. The selection was performed using the J/Ψ finder algorithm, both tracks belonging to the J/Ψ meson are required to be identified as an electron or muon. For the elastic sample no other tracks are allowed, for the inelastic sample the inelasticity is restricted to the range $0.2 < z < 0.9$, the center of mass energy in the photon proton system to the range $50 < W_{\gamma p} < 250$ GeV. In figure D.22 the invariant mass distribution is shown for both samples and compared to the distribution with the requirement of trigger element 157 (significance method). Only minimal losses due to the z vertex condition are desirable, the measured efficiency is about 98%, which is still acceptable.
The performance of the FTT z vertex trigger is compared to the CIP z vertex trigger, again using the s61 triggered data sample. The result is shown in figure D.23. Whereas the rejection of the FTT is about 65% for the background region, the CIP trigger rejects almost every event for this region. The difference for the signal region is smaller, nevertheless the performance of the CIP z vertex trigger is superior. The FTT has a better rejection power for the forward region.

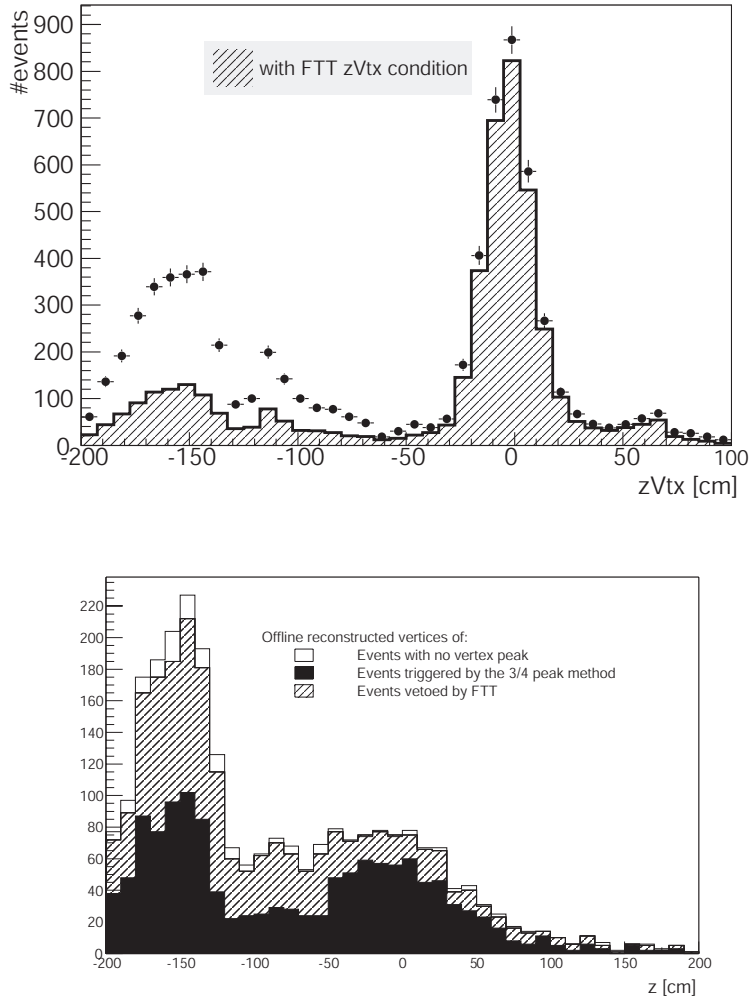

FIGURE D.20: *Upper plot: z vertex distribution for s61 triggered events and for the additional z vertex trigger requirement. This data sample was taken at the end of a fill using dedicated trigger conditions, avoiding the rejection of background at other trigger levels.*
Lower plot: z vertex distribution showing the predicted rejection power of the z vertex trigger as result of simulation studies (from [36]).

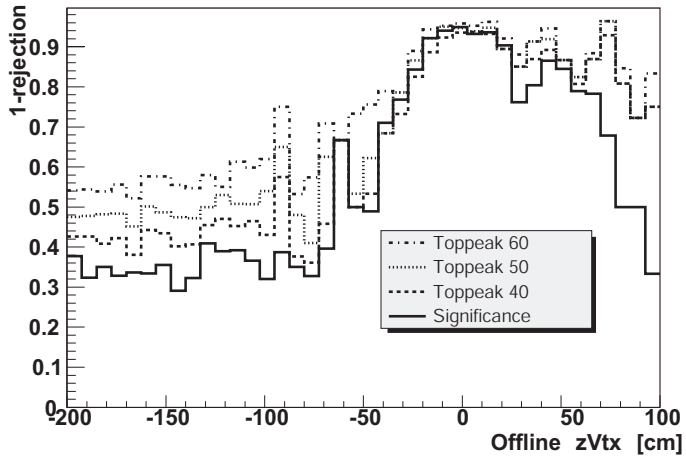

FIGURE D.21: *Comparison of the rejection power for different z vertex trigger elements.*

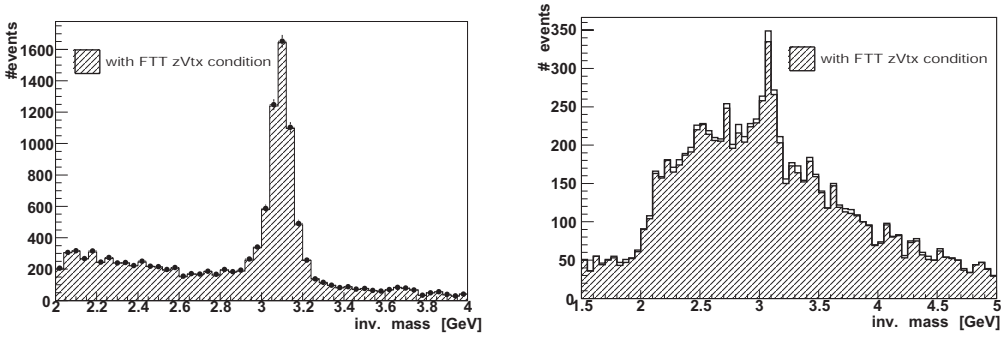

FIGURE D.22: *Invariant mass distribution of a elastic (left) and inelastic (right) J/Ψ-sample with and without requiring the z vertex condition.*

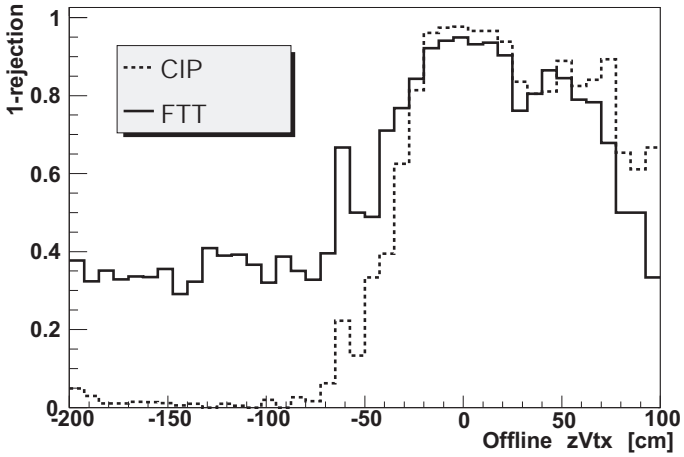

FIGURE D.23: *Comparison of the rejection power for the FTT and the CIP z vertex trigger.*

List of Figures

List of Tables

References

[1] CDF Collaboration (D. Acosta et al.), *"Measurement of the J/Ψ meson and B-Hadron Production Cross Section in $p\bar{p}$ Collisions at $\sqrt{s}$ = 1960 GeV"*, Phys. Rev. D, **71**, 2005.

[2] CDF Collaboration (D. Acosta et al.), *"Measurement of the B^+ Total Cross Section and B^+ Differential Cross Section $d\sigma/dp_T$ in $p\bar{p}$ Collisions at $\sqrt{s} = 1.8$ TeV"*, Phys. Rev. D, **65**, 2002.

[3] D0 Collaboration (B. Abbott et al.), *"Small angle muon and bottom quark production in $p\bar{p}$ collisions at $\sqrt{s}$ = 1.8 TeV"*, Phys. Rev. Lett., **84** 5478, 2000.

[4] D0 Collaboration (B. Abbott et al.), *"Cross section for b-jet production in $p\bar{p}$ collisions at $\sqrt{s} = 1.8$ TeV"*, Phys. Rev. Lett., **85** 5068, 2000.

[5] HERA B Collaboration (I. Abt et al.), *"Improved measurement of the $b\bar{b}$ cross section in 920 GeV fixed-target proton-nucleus collisions"*, Phys. Lett. B, **638** 407, 2006.

[6] HERA B Collaboration (I. Abt et al.), *"Bottom production cross section from double muonic decays of b-flavoured hadrons in 920 GeV proton-nucleus collisions"*, Phys. Rev. D, **73**, 2006.

[7] H1 Collaboration (A. Aktas et al.), *"Measurement of charm and beauty dijet cross sections in photoproduction at HERA using the H1 vertex detector"*, Eur. Phys. J. C, **47** 597, 2006.

[8] H1 Collaboration (A. Aktas et al.), *"Measurement of beauty production at HERA using events with muons and jets"*, Eur. Phys. J. C, **41** 453, 2005.

[9] H1 Collaboration (A. Aktas et al.), *"Measurement of charm and beauty photoproduction at HERA using $D^*\mu$ correlations"*, Phys. Lett. B, **621** 56, 2005.

[10] H1 Collaboration (C. Adloff et al.), *"Measurement of open beauty production at HERA"*, Phys. Lett. B, **467** 156, 1999.

[11] H1 Collarboration (I. Abt et al.), *"The Tracking, Calorimeter and Muon Detectors of the H1 Experiment at HERA"*, Nucl. Instr. Meth. A, **386** 310 and 348, 1997.

[12] H. L. Lai et al., *"Global QCD Analysis of Parton Structure of the Nucleon: CTEQ5 Parton Distributions"*, Eur. Phys. J. C, **12** 375, 2000.

[13] L3 Collaboration (P. Achard et al.), *"Measurement of the cross section for open-beauty production in photon-photon collisions at LEP"*, Phys. Lett. B, **619** 71, 2005.

[14] UA1 Collaboration (C. Albajar et al.), *"Beauty production at the CERN $p\bar{p}$ collider"*, Phys. Lett. B, **256** 121, 1991.

[15] UA1 Collaboration (C. Albajar et al.), *"Erratum: beauty production at the CERN $p\bar{p}$ collider"*, Phys. Lett. B, **262** 497, 1991.

[16] ZEUS Collaboration (S. Chekanov et al.), *"Bottom photoproduction measured using decays into muons in dijet events in ep collisions at $\sqrt{s}$ = 318 GeV"*, Phys. Rev. D, **70** 2004.

[17] ZEUS Collaboration (S. Chekanov et al.), *"Beauty Photoproduction using decays into electrons at HERA"*, to be published in Phys. Rev. D, 2008.

[18] ZEUS Collaboration (S. Chekanov et al.), *"Measurement of open beauty production at HERA in the D^* muon final state"*, Eur. Phys. J. C, **50** 299, 2007.

[19] ZEUS Collaboration (S. Chekanov et al.), *"Erratum: Bottom photoproduction measured using decay into muons in dijet events in ep collisions at $\sqrt{s}$ = 318 GeV"*, Phys. Rev. D, **74**, 2006.

[20] ZEUS Collaboration (S. Chekanov et al.), *"Measurement of beauty production in DIS at HERA II"*, submitted to the XXXIII International Conference on High Energy Physics, ICHEP06, 2006.

[21] ZEUS Collaboration (S. Chekanov et al.), *"Measurement of beauty production in deep inelastic scattering at HERA"*, Phys. Lett. B, **599** 173, 2004.

[22] ZEUS Collaboration (S. Chekanov et al.), *"Measurement of open beauty production in photoproduction at HERA"*, Eur. Phys. J. C, **18** 625, 2001.

[23] I. Akushevich and H. Spiesberger, In G. Ingelmann, A. De Roeck and R. Klanner, editors, *Proceedings, Future Physics at HERA*. DESY, 1996.

[24] T. Alexopoulos et al., *"Measurement of the $b\bar{b}$ cross section in 800 GeV/c proton-silicon interactions"*, Phys. Rev. Lett., **82** 41, 1999.

[25] G. Altarelli and G. Parisi, *"Asymptotic Freedom in Parton Language"*, Nucl. Phys. B, **126** 298, 1977.

[26] Altera, Quartus II Development Software Handbook v8.0, available from `www.altera.com`, Technical report, 2008.

[27] Altera, APEX 20K Programmable Logic Device Family Data Sheet, available from `www.altera.com`, Technical report, 2004.

[28] B. Andersson, G. Gustavson, G. Ingelman and T. Sjöstrand, Phys. Reports, **97** 31, 1983.

[29] M.-O. Bönig, *Messung des D^*-Meson-Produktionswirkungsquerschnittes in tiefinelastischer Streuung mit dem H1-Experiment*, PhD thesis, Universität Dortmund, 2007.

[30] A. Baird et al., *"A fast high resolution track trigger for the H1 experiment"*, IEEE Trans. Nucl. Sci., **48** 1276, 2001.

[31] R. Barlow and Ch. Beeston, *"Fitting using finite Monte Carlo samples"*, Comp. Phys. Commun., **77** 219, 1993.

[32] U. Bassler and G. Bernardi, *"On the kinematic reconstruction of deep inelastic scattering at HERA: The Sigma Method"*, Nucl. Instrum. Meth. A, **361** 197, 1995.

[33] O. Behnke, *"Production of Charm and Beauty Quarks at HERA"*, Habilitationsschrift, Universität Heidelberg, 2005.

[34] S. Bentvelsent, J. Engelen and P. Kooijman, The Double Angle Method, In W. Buchmüller and G. Ingelmann, editors, *Proceedings of the Workshop Physics for HERA*, volume 1, 1992.

[35] Niklaus E. Berger, *Measurement of Diffractive ϕ Meson Photoproduction at HERA with the H1 Fast Track Trigger*, PhD thesis, Swiss Federal Institute of Technology Zurich, 2007.

[36] Niklaus E. Berger, *Development of a z-vertex trigger based on drift chamber signals at H1*, Diploma thesis, Swiss Federal Institute of Technology Zurich, 2002.

[37] H. Bethe and W. Heitler, *"On the Stopping of Fast Particles and on the Creation of Positive Electrons"*, Proc. Roy. Soc. A, **146** 83, 1934.

[38] Marcello Bindi, *Measurement of charm and beauty production in deep inelastic scattering at HERA using semi-leptonic decays into muons*, PhD thesis, University of Bologna, 2008.

[39] J. D. Bjorken, *"Asymptotic Sum Rules at Infinite Momentum"*, Phys. Rev., **179** 1547, 1969.

[40] M.G. Bowler, *"e^+e^- Production of Heavy Quarks in the String Model"*, Zeit. Phys. C, **11** 169, 1981.

[41] R. Brun, ROOT: An Object-Oriented Data Analysis Framework, `http://root.cern.ch`.

[42] R. Brun et al., *"GEANT 3"*, CERN-DD/EE-84-1.

[43] L. Caminada, *Implementation of a Trigger for the Decay $b \to eX$ on the Third Trigger Level at the H1 Experiment*, Diploma thesis, Swiss Federal Institute of Technology Zurich, 2006.

[44] S. Catani, Y. L. Dokshitzer, M. H. Seymour and B. R. Webber, *"Longitudinally-Invariant k_T Clustering Algorithms for Hadron-Hadron Collisions"*, Nucl. Phys. B, **406** 187, 1993.

[45] S. Catani, F. Fiorani and G. Marchesini, *"QCD Coherence in Initial State Radiation"*, Phys. Lett. B, **234** 339, 1990.

[46] S. Catani, F. Fiorani and G. Marchesini, *"Small-x Behavior of Initial State Radiation in Perturbative QCD"*, Nucl Phys. B, **336** 18, 1990.

[47] V. Chiochia, *Measurement of beauty quark production in deep inelastic scattering*, PhD thesis, Universität Hamburg, 2003.

[48] M. Ciafaloni, *"Coherence Effects in Initial Jets At Small Q^2/s"*, Nucl. Phys. B, **296** 49, 1988.

[49] H1 Collaboration, *"A Fast Track Trigger with high resolution for H1"*. Proposal submitted to the Physics Research Committee, DESY internal report PRC 99/06 and addendum PRC 99/07, 1999.

[50] ZEUS Collaboration, *"Measurement of beauty production from dimuon events at HERA"*, submitted to the XXXIII international conference on high energy physics, ICHEP06, 2006.

[51] ZEUS Collaboration, *Precision measurements of α_s at HERA*, In *Proceedings of the DIS 2005, Madison, Wisconsin, USA*, 2005.

[52] J. C. D. Collins, D. E. Soper and G. Sterman, *"Factorisation for Short Distance Hadron-Hadron Scattering"*, Nucl. Phys. B, **261** 104, 1985.

[53] Deutsches Elektronen-Synchrotron DESY, DESY wissenschaftlicher Jahresbericht 2006, available at `www.desy.de/f/jb2006`, 2007.

[54] R. Devenish and A. Cooper-Sarkar, *Deep Inelastic Scattering*. Oxford University Press, 2003.

[55] Analog Devices, AD9218 10-Bit, 40/65/80/105 MSPS 3 V Dual A/D Converter Data Sheet (Rev. B), available from `www.analog.com`, Technical report, 2004.

[56] Analog Devices, Implementing High-Speed Search Applications with Altera CAM, Application Note, Technical report, 2001.

[57] Y.L. Dokshitzer, *"Calculation of Structure Functions of Deep-Inelastic Scattering and e^+e^- Annihilation by Perturbation Theory in Quantum Chromodynamics"*, Sov. Phys. JETP, **46** 641, 1977.

[58] S. Eidelmann and others (Particle Data Group), *"Review of particle physics"*, Phys. Rev. Lett. B, **592**, 2004.

[59] R.K. Ellis, W.J. Stirling and B.R. Webber, *QCD and Collider Physics*. Cambridge University Press, 1996.

[60] R. P. Feynman, *Photon-Hadron Interactions*. Benjamin N.Y.

[61] R. P. Feynman, *"Very High Energy Collisions of Hadrons"*, Phys. Rev. Lett., **23** 1415, 1969.

[62] R. D. Field and R.P. Feynman, Nucl. Phys. B, **136** 1, 1978.

[63] L. Finke, *Measurement of charm and beauty dijet cross sections in photoproduction*, PhD thesis, Universität Hamburg, 2006.

[64] S. Frixione, P. Nason and B. R. Webber, JHEP 0308, **007**, 2003.

[65] M. Glück, E. Reya and A. Vogt, Eur. Phys. J. C, **5**, 1998.

[66] A. Glazov, *Measurement of the Proton Structure Functions $F_2(x, Q^2)$ and $F_L(x, Q^2)$ with the H1 detector at HERA*, PhD thesis, Humboldt-Universität Berlin, 1998.

[67] V.N. Gribov and L.N. Lipatov, *"Deep Inelastic e-p Scattering in a Perturbative Theory"*, Sov. J. Nucl. Phys., **15** 438, 1972.

[68] V.N. Gribov and L.N. Lipatov, *"e^+e^- Pair Annihilation and Deep Inelastic ep Scattering in Perturbation Theory"*, Sov. J. Nucl. Phys., **15** 675, 1972.

[69] B.W. Harris and Smith. J., Nucl. Phys. B, **452** 109, 1995.

[70] S. Hellwig, *Untersuchung der D^*-π_{slow} Double Tagging Methode in Charmanalysen*, Diploma thesis, Universität Hamburg, 2004.

[71] K.C. Hoeger, The Double Angle Method, In Buchmüller W. and G. Ingelmann, editors, *Proceedings of the Workshop Physics at HERA*, volume 1, page 43, 1992.

[72] J. E. Huth et al., Proceedings of the 1990 Summer Study on High Energy Physics, Snowmass, Colorado, 1992. World Scientific.

[73] N. Isgur and M.B Wise, *"Weak Transition Form-Factors Between Heavy Mesons"*, Phys. Lett. B, **237** 527, 1990.

[74] N. Isgur and M.B. Wise, *"Weak Decays Of Heavy Mesons in the Static Quark Approximation"*, Phys. Lett. B, **232** 113, 1989.

[75] B. Schwarz J. Reichardt, *VHDL-Synthese, Entwurf digitaler Schaltungen und Systeme*. Oldenbourg, 2003.

[76] F. Jacquet and A. Blondel, Report from the study group on detectors for charged current events, In U. Amaldi et al., editors, *Proceedings, Study of an e-p Facility for Europe*, pages 377–414. DESY-Report 79-048, 1979.

[77] F. James, *Minuit, Function Minimization and Error Analysis, CERN Program Library Long Writeup D506*, CERN, Geneva.

[78] D. M. Jansen et al., *"Measurement of the bottom-quark production cross section in 800 GeV/c proton-gold collisions"*, Phys. Rev. Lett., **74** 3118, 1995.

[79] Andreas Werner Jung, Phd thesis (in preparation), Universität Heidelberg, 2008.

[80] Andreas Werner Jung, *Inbetriebnahme der dritten Stufe des schnellen Spurtriggers für das H1-Experiment*, Diploma thesis, Universität Dortmund, 2004.

[81] H. Jung, *"The CCFM Monte Carlo generator CASCADE"*, Comput. Phys. Commun., **143** 100, 2002.

[82] H. Jung, Comp. Phys. Commun., **86** 147, 1995.

[83] H. Jung and G. P. Salam, *"Hadronic final state predictions from CCFM: the hadron-level Monte Carlo generator CASCADE"*, Eur. Phys. J. C, **19** 351, 2001.

[84] V. G. Kartvelishvili, A. K. Likhoded and V. A. Perov, Phys. Lett. B, **78** 615, 1978.

[85] M. Krämer, *Measurement of Beauty Cross Sections in Photoproduction*, Phd thesis (in preparation), Universität Hamburg, 2009.

[86] M. Krämer, Tuning the vertex detector simulation of H1, In *Proceedings of the international school of subnuclear physics:* 45^{th} *course*, 2007.

[87] K. Krüger, private communication.

[88] A. Kwiatkowski, H. Spiesberger and H.-J. Möhring, *"HERACLES, version 4.0"*, Comp. Phys. Commun., page 155, 1992.

[89] H. L. Lai et al., Eur. Phys. J. C, **12** 375, 2000.

[90] U. Langenegger, *A Measurement of the Beauty and Charm Production Cross Sections at the ep Collider HERA*, PhD thesis, Swiss Federal Institute of Technology Zurich, 1998.

[91] L.N. Lipatov, *"The Parton Model and Perturbation Theory"*, Sov. J. Nucl. Phys., **20** 94, 1975.

[92] B. List, *"The H1 Silicon Tracker"*, Nucl. Instrum. Methods Phys. Res., Sect. A, **549** 33, 2005.

[93] B. List, *Diffraktive J/ψ-Produktion in Elektron-Proton-Stößen am Speicherring HERA*, Diploma thesis, Technische Universität Berlin, 1993.

[94] K. Lohwasser, *Optimisation of the selection capability of the H1 Fast Track Trigger*, Diploma thesis, Universität Dortmund, 2006.

[95] G. Marchesini, *"QCD Coherence in the Structure Function and Associated Distributions at Small x"*, Nucl. Phys. B, **445** 49, 1995.

[96] A. D. Martin, W. J. Stirling and R. S. Thorne, Phys. Lett. B, **636** 259, 2006.

[97] B. Naroska, S. Schieck and G. Schmidt, Lepton Identification in the H1 Detector at Low Momenta, H1 internal note, 1997.

[98] Jürgen Naumann, *Entwicklung und Test der dritten H1-Triggerstufe*, PhD thesis, Universität Dortmund, 2003.

[99] M. Peez, *Search for deviations in the Standard Model in high transverse energy processes at the electron-proton collider HERA*, PhD thesis, University Lyon, 2003.

[100] M. Peez, B. Portheault and E. Sauvan, An Energy Flow Algorithm for Hadronic Reconstruction in OO: Hadroo2, Internal H1 note, 2005.

[101] C. Peterson, D. Schlatter, I. Schmitt and P. M. Zerwas, Phys. Rev. D, **27** 105, 1983.

[102] J. Pumplin, D. R. Stump, J. Huston, H. L. Lai, P. Nadolsky and W. K. Tung, *"New generation of parton distributions with uncertainties from global QCD analysis"*, JHEP 0207, **012**, 2002.

[103] M. Sauter, *Beauty Production at Threshold at HERA*, Phd thesis (in preparation), Swiss Federal Institute of Technology Zurich, 2009.

[104] Andre Schöning, *"Description of the FTT Merging Scheme"*, FTT documentation 1.0.

[105] Andre Schöning and Niklaus E. Berger, *"Description of the FTT L2 Decider"*, FTT documentation 1.0, Technical report, 2006.

[106] S. Schiek, *Untersuchung der inelastischen Photoproduktion von J/Ψ-Mesonen im H1-Detektor bei HERA*, PhD thesis, Universität Hamburg, 1996.

[107] M. Seidel, *"The upgraded interaction regions at HERA"*, DESY-HERA-00-01, available at DESY Document Server, 2000.

[108] National Semiconductors, DS90CR483/DS90CR484 48-bit LVDS Channel Link SER/DES 33 - 112 MHz Data Sheet, Technical report, 2004.

[109] T. Sjöstrand, Comp. Phys. Commun., **82** 74, 1994.

[110] T. Sjöstrand, Comp. Phys. Commun., **39** 347, 1986.

[111] T. Sjöstrand et al., *"High-Energy-Physics Event Generation with PYTHIA 6.1"*, Comp. Phys. Commun., **135** 238, 2001.

[112] M. Bengtsson T. Sjöstrand, Comp. Phys. Commun., **43** 367, 1987.

[113] H1OO Project Team, *H1OO Userguide*, available at www-h1.desy.de/icas/oop/.

[114] R. S. Thorne, [hep-ph/0506251].

[115] Max Urban, *The new CIP2k z-Vertex Trigger for the H1 Experiment at HERA*, PhD thesis, Universität Zürich, 2004.

[116] B.R. Webber, Nucl. Phys. B, **238** 492, 1984.

[117] L. West, How to use the Heavy Flavour Working Group Track, Muon and Electron Selection Code, H1 internal software manual, 1997.

[118] Christoph Wissing, *Entwicklung eines Simulationsprogrammes und Implementierung schneller Spurfitalgorithmen für den neuen H1-Driftkammertrigger*, PhD thesis, Universität Dortmund, 2003.

[119] T. Wolff, *Entwicklung, Bau und erste Ergebnisse eines totzeitfreien Spurfinders als Trigger für das H1-Experiment am HERA Speicherring*, PhD thesis, Swiss Federal Institute of Technology Zurich, 1993.

Danksagung

Ich habe vielen Personen zu danken, die einen Beitrag zum Zustandekommen dieser Arbeit geleistet haben.
Frau Prof. Dr. B. Naroska, die den Abschluss dieser Arbeit leider nicht mehr erleben konnte, hat den mit Abstand größten Beitrag geleistet. Ich bedanke mich bei ihr für das Vertrauen und die Möglichkeit, die Promotion am H1 Experiment durchzuführen. Mit ihrem anhaltenden Interesse, unermüdlichen Einsatz und Verantwortungsbewusstsein bis zum Schluss wird sie mir als ein großes Vorbild in Erinnerung bleiben.

Dr. Benno List danke ich für die Betreuung der Analyse, das Korrekturlesen der Arbeit und die Übernahme des Gutachtens.
Bei Prof. Dr. Klanner bedanke ich mich für seinen Einsatz für die Abschlussfinanzierung der Arbeit, das schnelle und gründliche Korrekturlesen der Arbeit und die Übernahme des Gutachtens.
Prof. Dr. Schleper und Dr. Hannes Jung danke ich für die bereitwillige Übernahme des Disputationsgutachtens.
Bei Dr. Olaf Behnke bedanke ich mich für das Interesse an der Analyse und die beruhigenden, pragmatischen Kommentare.
Dr. André Schöning danke ich für die Möglichkeit, am FTT Projekt mitzuarbeiten. Ich konnte in dieser Zeit viel von Dr. Niklaus Berger lernen und habe von seinen Vorarbeiten profitiert.
Bei Michael und Mira bedanke ich mich für die gute Zusammenarbeit während der Datenanalyse. Miras positive Einstellung hat zu einer entspannten, positiven Büroatmosphäre beigetragen.
Bei Shiraz bedanke ich mich für das Korrekturlesen von Teilen der Arbeit.
Besonders wichtig ist es mir, Tobias und den anderen Diplomanden, Doktoranden und Post-Docs der ETH-Zürich-Gruppe in Hamburg, Giom, Lea, Michel, Nik und Ron, für die freundliche Aufnahme während des FTT-Projektes, die gute Zusammenarbeit auch danach und die vielen privaten Unternehmungen zu danken.